

THEORETICAL CHEMISTRY INSTITUTE

THE UNIVERSITY OF WISCONSIN

110-20719
(ACCESSION NUMBER)

24
(PAGES)

24
(CODE)

(THRU)

(CATEGORY)

(NASA CR OR TMX OR AD NUMBER)

FACILITY FORM 602

CROSSED MOLECULAR BEAM STUDY OF THE REACTIVE SCATTERING
OF $K + I_2$: PRODUCT KI RECOIL (VELOCITY-ANGLE) DISTRIBUTIONS
AND ENERGY DEPENDENCE OF REACTION CROSS SECTION

by

Keith Thomas Gillen

WIS-TCI-380 X

26 February 1970

MADISON, WISCONSIN

Reproduced by
NATIONAL TECHNICAL
INFORMATION SERVICE
Springfield, Va. 22151

CROSSED MOLECULAR BEAM STUDY OF THE REACTIVE SCATTERING
OF K + I₂: PRODUCT KI RECOIL (VELOCITY-ANGLE) DISTRIBUTIONS
AND ENERGY DEPENDENCE OF REACTION CROSS SECTION

by

Keith Thomas Gillen

A thesis submitted in partial fulfillment of the
requirements for the degree of

Doctor of Philosophy
(Chemistry)

at the
University of Wisconsin
1970

Crossed Molecular Beam Study of the Reactive Scattering
of $K + I_2$: Product KI Recoil (Velocity-Angle) Distributions
and Energy Dependence of Reaction Cross Section*

by

Keith Thomas Gillen

Under the supervision of Professor Richard B. Bernstein

ABSTRACT

A molecular beam study of the reaction of a velocity-selected potassium beam crossed with a thermal iodine beam is described. Velocity analysis yielded the laboratory recoil velocity-angle distribution of product KI flux. The energy dependence of this flux distribution was determined from measurements over a range of K velocities.

Computational methods have been developed which extract the center-of-mass (c.m.) differential reactive cross section functions (angular and recoil energy distributions) from the laboratory data.

The c.m. differential solid angle-recoil velocity distribution $\left(\frac{d^3\sigma(\theta, w')}{d^2\omega dw'}\right)$ is largest at small angles θ from the initial (c.m.)

- - - - -

* This work received financial support from: National Science Foundation Grant GB-16665; National Aeronautics and Space Administration Grant NGL 50-002-001; and U. S. Atomic Energy Commission Contract No. AT(11-1)-321.

K beam direction (i.e., "forward scattering" of the KI) and low KI c.m. velocities w' (i.e., high product internal excitation). However, there is also significant intensity at large θ and large w' . The product angular and recoil velocity distributions are coupled (i.e., non-separable). There appears to be a bimodal structure in the c.m. recoil velocity distributions for $\theta \gtrsim 60^\circ$. An increase in the relative collision energy from 1.9 to 3.6 kcal/mole produces only a slight change in the shape of the c.m. product differential cross section functions, accompanied by a small decrease ($\approx 20\%$) in the magnitude of the reaction cross section. Measurements were also made on the angular and velocity distributions of the non-reactively scattered K over the same energy range.

Also described are

- 1) a reactive scattering crossed molecular beam study of K + HBr, DBr, yielding angular and velocity distributions of KBr product in the laboratory and c.m. systems
- and
- 2) a selective detector, sensitive to the degree of internal excitation of alkali halides in molecular beams.

In Memoriam

Vera I. V. Dehn

(1941-1967)

ACKNOWLEDGMENTS

"with a little help from my friends" The Beatles

One man, taking this trip alone, would have lost his sanity much earlier than I did. I deeply appreciate the advice, aid, encouragement, and hard work of many fine people. Several of these "co-workers" deserve special mention:

Professor Bernstein, who channelled my energies into realistic projects and who spent a great amount of his time teaching me a sound approach to scientific research.

Clyde Riley, who taught me the use of the apparatus during the course of the $K + HBr$, DBr experiments.

Al Rulis, who worked with me closely and capably on the $K + I_2$ experiments.

The other members (past and present) of the molecular beams group, especially Art Grosser, for competent advice and assistance.

Tony Warnock for help in the early stages of the computing.

The staff of the Chemistry Department Machine Shop, especially Leo Rogers and Russ Riley, for ideas as well as execution.

A large number of people (most notably Glen Blanchar, Don Boe, Ben Schiro, Ole Walter, and Joe Wheeler of the U. W. staff), who removed some of the pain associated with moving the apparatus to the new Chemistry Building and with reassembling the pieces.

Ed O'Keefe, for a massive amount of talented drafting in an unbelievably short time.

Linda Stoltenberg, who somehow transferred my demented scratchings into a beautifully typed thesis; Jerry Carrig, for printing this thesis; the other members of the Theoretical Chemistry Institute Staff (especially Sheila Battle, Gloria Lawton and Karen Rick) for hundreds of favors.

Table of Contents

<u>Section</u>	<u>page</u>
I. Introduction	1
A. Background	1
B. Scope of the Experiments	5
C. Useful Numbers and Nomenclature	6
II. Apparatus	11
A. General	11
B. Details	23
1. Ovens	23
2. Velocity Selector	26
3. Scattering Zone	26
4. Choppers	29
5. K Beam Monitor'	29
6. Velocity Analyzer	32
7. Detector	32
III. K + HBr, DBr	37
A. "Polar (Velocity-Angle) Flux Contour Maps for KBr from the Crossed-Beam Reactions of K + HBr, DBr: Evidence for Both Forward and Backward (c.m.) Scattering," Clyde Riley, Keith T. Gillen, and R. B. Bernstein, J. Chem. Phys. <u>47</u> , 3672 (1967).	37
B. "Reactive Scattering of K by HBr, DBr in Crossed Molecular Beams: Angular and Velocity Distributions	

Table of Contents (Cont.)

<u>Section</u>	<u>page</u>
of KBr in Laboratory and c.m. Systems," Keith T. Gillen, Clyde Riley, and R. B. Bernstein, J. Chem. Phys. <u>50</u> , 4019 (1969).	41
C. After-Thoughts	57
IV. K + I ₂	61
A. Apparatus Modifications for K + I ₂ Experiments	61
B. Experimental Procedure	70
C. Data	74
1. Total Angular Distributions	74
2. Velocity Analyses	79
3. Angular Normalizations	94
4. Incident Energy Dependence Data	97
D. Comments on Detector Idiosyncracies and Methods of Processing of Raw Data	100
E. Analysis of Non-Reactive Scattering	109
F. Analysis of Reactive Scattering	121
1. Laboratory Angular Distributions and Contour Maps	121
2. "Nominal" Inversion	133
3. C.m. → Lab. Computations	136
4. Lab. → c.m. Inversion	137
5. Out-of-Plane Contributions	149
6. Total Reactive Angular Distributions (c.m.)	156

Table of Contents (Cont.)

<u>Section</u>	<u>page</u>
7. Velocity and Energy Distributions (c.m.)	156
8. Speculation on Structure in the c.m. Velocity Distributions	168
9. C.m. Contours Assumed Independent of \bar{E}	171
10. Total Reactive Cross Section, σ_R	179
11. Energy Dependence of σ_R	182
12. Summary of $K + I_2$ Reactive Scattering Results	187

V, "Selective Detector for Internal Excitation of Alkali Halides in Molecular Beams," Keith T. Gillen and R. B. Bernstein, Report WIS-TCL-377X.	189
---	-----

Appendices

A. Velocity Selector Calibrations and K Beam Characterizations	205
1. Calibrating the analyzer and selector	206
2. Velocity Distribution of the Laval K Beam	216
3. Profile of K Beam Entering Scattering Center	219
B. Computational Inversion Methods	226
1. "Nominal" Inversion	226
2. C.m. \rightarrow Lab. Computations	227
3. Linear Additivity	229

Table of Content (Cont.)

4. Lab. \rightarrow c.m. Inversion	229
5. Extensions	233
6. Narrowing Inversion	234
C. Computer Programs	236
1. DC	236
2. KICM	242
3. I2LEG	247
4. GAUSHAUS	255
D. Enlarged Views of Certain Important Figures	260
E. Coefficients for Legendre Expansion Functions	269
<u>References</u>	271

Figures

<u>Figure</u>		<u>page</u>
I-1	K + I ₂ Energetics and Kinematics	8
II-1	Apparatus Schematic	22
III-1	K + HBr, DBr Cartesian Flux Distributions	59
IV-1,2,3,4	Slit Geometry	64-67
IV-5,6,7	K + I ₂ Laboratory Angular Distributions	76-78
IV-8	Chart Recordings of Experimental Velocity Analyses	82
IV-9,10	K + I ₂ Velocity Analyses, $\bar{E} = 1.87$ kcal/mole	84-85
IV-11,12,13,14	K + I ₂ Velocity Analyses, $\bar{E} = 2.67$ kcal/mole	87-90
IV-15,16	K + I ₂ Velocity Analyses, $\bar{E} = 3.62$ kcal/mole	92-93
IV-17	KI Angular Normalizations (Laboratory)	96
IV-18	Energy Dependence Data	99
IV-19	Separation of K from KI in Velocity Analyses	106
IV-20	Angular Distributions of Non-reactive Scattering (Laboratory)	111
IV-21	Differential Cross Sections (c.m.) for Non-Reactive Scattering	115
IV-22	Reduced Plot of c.m. Angular Distribution of K	118
IV-23,24,25	KI Flux, Laboratory Angle-Velocity Distributions	123-125

Figures (Cont.)

<u>Figures</u>		<u>page</u>
IV-26	Laboratory Angular Distribution of KI	127
IV-27	KI Laboratory Polar (Velocity-Angle) Flux Contours	130
IV-28	"Nominal Inversion" c.m. Contours	135
IV-29	Uncoupled c.m. Distribution Function	139
IV-30	KI Polar c.m. Contour Maps	142
IV-31,32,33	Computed Fits to Laboratory KI Contours	146-8
IV-34,35,36	Computed Fits to Laboratory Velocity Analyses	151-3
IV-37	KI c.m. Contour Maps, Weighted by $\sin \theta$	155
IV-38	Computed c.m. Angular Distributions	158
IV-39	KI c.m. Recoil Angle-Velocity Distributions	160
IV-40	KI + I c.m. Recoil Angle-Energy Distributions	165
IV-41	KI + I c.m. Recoil Energy Distributions	167
IV-42	KI c.m. Polar Flux Contour Map (Assumed Energy Independent)	174
IV-43	KI c.m. Flux Contour Map Weighted by $\sin \theta$	176
IV-44	Computed Fits to Laboratory KI Contours (Single c.m. Map)	178
IV-45	Energy Dependence of Total Reactive Cross Section	186
V-1	Dependence of KI Detection on Internal Energy	(199), 8a

Figures (Cont.)

<u>Figures</u>		<u>page</u>
A-1	Velocity Selector Calibration	211
A-2	Analyzer Scan of Selector Transmission	215
A-3	Laval K Beam Flux Distribution	218
A-4	Angular Profile of K Beam	221
A-5	Estimation of K Beam Density in Scattering Zone	224
D-1,2,3	Enlargements of sections of Fig. IV-27	262-4
D-4,5,6	Enlargements of sections of Fig. IV-30	266-8

Tables

<u>Table</u>		<u>page</u>
II-1	Selector and Analyzer Constants	27
II-2	Typical Beam Operating Conditions	28
IV-1	K + I ₂ Apparatus Geometry	62
IV-2	Nominal Reaction Conditions	132
V-1	Dependence of Residual (Unsensitized Mode) KI Sensitivity on the Laboratory Scattering Angle, Θ , for the K + I ₂ Experiments	(203), 12
A-1	Relations of Velocity Distributions, M-B Beam	207

Photographs

<u>Photo</u>		<u>page</u>
1	Overall View of Apparatus	14
2	Two More Views of Apparatus	16
3	Accessories	18
4	Lid Lifted	20
5	Beam Ovens	25
6	Details of Scattering Center	31
7	Velocity Analyzer	34

I. Introduction.

A. Background

Since the pioneering reactive product angular distribution experiment¹ on $K + HBr \rightarrow KBr + H$ by Taylor and Datz in 1955, nearly all crossed molecular beam studies of chemical reactions in neutral species have involved alkali metals². This is due to the ease with which the alkali metals can be detected by the surface ionization technique³ and the existence of a differential detection method which can be used to distinguish alkali atoms from alkali halide molecules⁴⁻⁶. Although more general (yet less efficient) electron bombardment (with mass analysis) detection methods are now being utilized to extend dramatically the range of chemical systems studied⁷, the problems with low detector efficiency have not yet been completely overcome; and the "alkali age" has yet to end. Using the early Polanyi dilute flame experiments⁸ as both a metric and an inspiration, a few research groups have squeezed from the alkali reactions a veritable cornucopia of information on the dynamics of reaction processes².

The reactions of alkalis with halogens have received the most experimental attention; the advantages of these systems, besides efficient (and differential) detection, include large reactive cross sections ($100-300\text{\AA}^2$) and easy reactant condensibility at liquid nitrogen temperatures.

A wide variety of experimental techniques, discussed briefly below, have been applied to the study of these reactions. Total scattering cross sections as a function of energy⁹ show complete quenching of the "glory oscillations"¹⁰ due to the large reaction

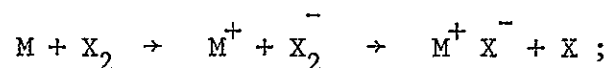
cross sections. Angular distributions of the non-reactive scattering have been measured by several groups, most notably by Greene *et al.*¹¹; the scattering is found to be sharply attenuated at large angles (relative to less reactive systems); the rainbow maximum¹² is not observed, again due to large chemical reaction probabilities.^{2b} Differential surface ionization detection⁵ has been used to determine the reactive product angular distributions (strongly forward-peaked in the c.m., but with significant intensity at all angles) by Datz and co-workers,^{13,14} Herschbach and co-workers,¹⁵⁻¹⁹ and others. Reactive product total angular distributions have also been measured using an inhomogeneous magnetic field to deflect away the paramagnetic alkali atoms before they reach the detector;²⁰⁻²³ the results confirm the reactive angular distributions obtained with differential detection.

Product KBr laboratory velocity distributions for $K + Br_2$ have been reported at a limited number of angles by Birely and Herschbach^{24,25} (for thermal beams) and by Grosser and Bernstein^{26,27} (for a velocity selected K beam at three incident energies). The results indicate low product translational energies. Estimates of product rotational energies (also relatively small) are available from experiments on deflection of the polar product molecules by an inhomogeneous electric field.^{28,29} A triple-beam experiment was carried out by Moulton and Herschbach³⁰ in which the KBr (KCl) product of a $K + Br_2$ (ICl) reaction was crossed with a Na beam to produce Na Br (Na Cl) + electronically excited K. This result demonstrated the large average vibrational excitation in the primary alkali halide, in agreement with expectations based on the diffusion

flame results of Roth and Schay for $K + I_2$ ³¹.

The reaction $K + Br_2$ has been studied by most of the techniques mentioned above and the general conclusions are typical of the other alkali-halogen reactions: The differential solid angle reactive cross section is large and is forward peaked in the c.m. (but is significant at all angles); there is severe attenuation of the large angle non-reactive scattered intensity relative to that which would be expected in the absence of reaction; the product internal energy distribution is broad, but the partitioning strongly favors high vibrational excitation of the KBr with little average rotational or translational energy.

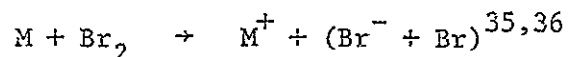
A model commonly used to correlate these properties is the electron jump ("harpooning") model of Magee^{32,33} in which the alkali atom is thought to transfer an electron to the halogen molecule at large distances and then to hook ("harpoon") a halogen atom with a strong coulomb potential



the electron transfer takes place at the "crossing" of the covalent and ionic potential surfaces, and the strong ionic attraction gives the observed large product internal excitations. The large interaction distances imply large reactive cross sections and predominantly forward scattering, in accord with the observations. A fine review of the implications of the harpooning model for beam experiments has been written by Herschbach^{2a}. A detailed study by

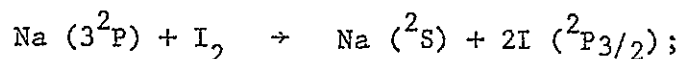
Anderson³⁴ treated the effect on the harpoon model of using the commonly invoked necessity of "overcoming the centrifugal barrier" as the criterion for reaction.

Some recent high energy beam studies have produced alkali ions from the reactions



equivalent to the first step of the electron jump mechanism ($M = K, Na, Li^{35}; Cs^{36}$).

Two important (non-beam) experiments recently accomplished are also worthy of attention. Brus³⁷ observed the quenching by iodine vapor of the fluorescence of Na (3^2P) after pulsed u.v. photodissociation of NaI and thereby determined the magnitude of the total reaction cross section σ_R for

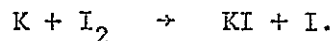


varying the wavelength of the pulse allowed a determination of the small negative velocity dependence of σ_R for the above reaction. Brodhead et al.³⁸ photodissociated CsI with a u.v. pulse in the presence of I_2 vapor and monitored the disappearance of the Cs atoms by observing the transmission of Cs resonance light through the reaction vessel; an estimate of $180 \pm 25A^{0.2}$ was obtained for the total reaction cross section for $Cs + I_2 \rightarrow CsI + I$ (at ~ 2.4 kcal/mole energy).

Theoretical approaches to alkali-halogen scattering have put strong emphasis on attempting to match the available data. Classical Monte Carlo trajectory studies³⁹ have been done on a variety of potential surfaces which simulate the effect of the postulated electron-jump mechanism; by reasonable choice of potential functions the results can be made to agree qualitatively with much of the experimental data available. More detailed experiments should further test the potential surfaces used in these calculations.

B. Scope of the Experiments

The main section of this thesis describes a detailed experimental investigation by the crossed beam technique of the reaction



The only previous beam data on this reaction are studies of the overall angular distributions of reactive and non-reactive products^{14,16,11}. The present work included re-measurements of those angular distributions; the cause for the large disparities among the non-reactive data of earlier workers was found.

Velocity analyses of non-reactive and reactive product distributions have also been taken; normalizations of the reactive product distributions at the different angles allow the determination of laboratory reactive product polar (velocity-angle) flux contour maps²⁷. Reactive product contours have previously been obtained for a number of ion-molecule reactions⁴⁰; so far the only published contour

maps for neutral-neutral reactions are the $K + HBr$, DBr ^{41,42} results (section III of this thesis).^{*} Computational techniques are also reported which extract the more fundamental center-of-mass (c.m.) differential cross sections from the laboratory data.

The laboratory contour maps have been determined over a range of relative energy; thereby, the energy dependence of the size and shape of the c.m. reactive cross section function is studied directly -- this represents the first such study for low energy neutral-neutral beam experiments.

C. Useful Numbers and Nomenclature

Figure I-1(a) indicates the approximate energetics of the $K + I_2$ reaction at a relative initial kinetic energy (\bar{E}) of 2.67 kcal/mole (the middle energy in the energy range studied). The ground state to ground state exothermicity of the reaction (ΔD_0) is 40.5 kcal/mole⁴³. This energy is much larger than the average internal energy of the thermal I_2 beam, $E_{int, I_2} = 1.1$ kcal/mole (0.7 $\frac{\text{kcal}}{\text{mole}}$ rotational, 0.4 kcal/mole vibrational); it is also much larger than the \bar{E} (2.67 kcal/mole) or the range in \bar{E} (1.87 to 3.62 kcal/mole) over which most of the experiments were carried out. The total energy

- - - - -

* The Herschbach group has determined the velocity-angle contour maps for a number of crossed thermal beam reactions, all unpublished. See: International School of Physics "Enrico Fermi" XLIV Course Molecular Beams and Reaction Kinetics - Ch. Schlier, Ed., to be published.

Fig. I-1 K + I₂ Energetics and Kinematics

a) Energetics

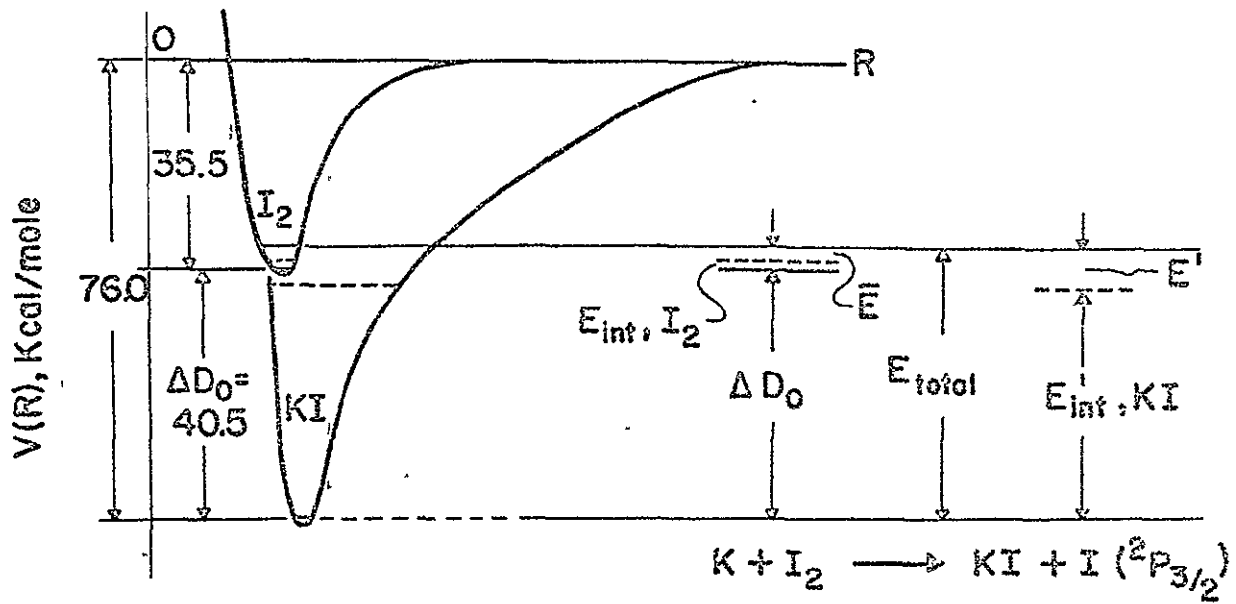
Shown are two slices through the K-I-I potential surface (shapes are only schematically represented) corresponding to reactants and products. $V(R)$ is the potential energy as a function of R .

Reactants: ΔD_0 = ground state exothermicity of reaction; E'_{int} , I₂ is an average value; $\bar{E} = 2.67$ kcal/mole.

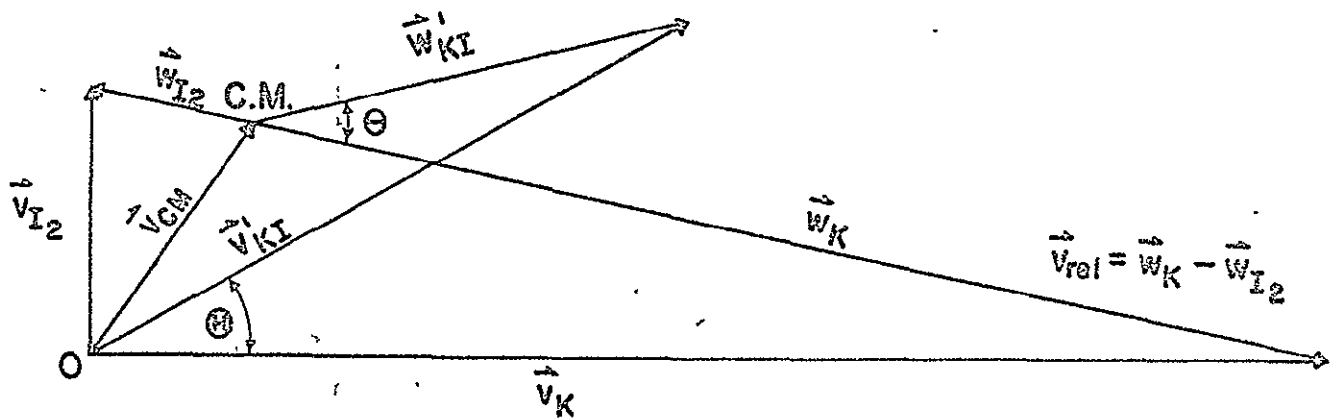
Products: A typical partitioning of the total energy (E_{total}) between E'_{int} , KI and $E'_{\text{translation}}$ is indicated (for ground state I (²P_{3/2}) atom production).

b) Kinematics

Velocity vector diagram corresponds to average velocities of K and I₂ for $\bar{E} = 2.67$ kcal/mole. The lab. velocities are denoted by v ; c.m. velocities by w . Primed symbols are for product velocities, unprimed for reactants. Capital letter angles (Θ , Φ) are laboratory quantities (z axis is perpendicular to beam plane; polar angle $\Phi = 90^\circ$); small letters (θ , ϕ) are c.m. angles (\vec{v}_{rel} is z axis; polar angle is θ); Ω and ω are, respectively, Lab. and c.m. solid angles - not shown on diagram.



(a)



In-Plane: $\phi = 0, \Phi = 90^\circ$

(b)

Fig. I-1

available to reactive products in the example shown is ~44.3 kcal/mole; this energy is partitioned between internal excitation of the 'KI (E_{int}^{\prime}, KI) (and perhaps also of the I) and relative translational energy E' of the products (an example of partitioning is shown by the dotted line in Fig. I-1(a); the corresponding KI internal energy level is shown on the schematic KI potential curve at the left).

The product I atom has an excited electronic level ($^2P_{1/2}$) which is 21.73 kcal/mole above the ground state (and hence accessible in the reaction); but the diffusion flame results of Roth and Schay³¹ on $K + I_2$ suggest that this excitation is relatively small (confirmed by comparison with the present results).

The nomenclature to be followed in subsequent sections has been delineated by Warnock and Bernstein⁴⁴. A number of the important definitions are illustrated in the "nominal" velocity vector diagram in Figure I-1(b); this "Newton" diagram for the crossed beam reaction removes the influence of beam velocity distributions by representing each beam by its average ("nominal") velocity. The vectors \vec{v}_{I_2} , \vec{v}_K , \vec{v}_{CM} represent the average values of the laboratory velocities of the I_2 beam, K beam, and c.m., respectively. Likewise \vec{w}_{I_2} and \vec{w}_K are the average vector velocities of I_2 and K relative to the c.m. For a given product KI laboratory velocity v_{KI}' and laboratory scattering angle \textcircled{H} , the corresponding velocity w_{KI}' and the angle θ relative to the c.m. can be determined*. The c.m. velocity

- - - - -

* Unfortunately there are distributions in beam velocities that produce a lack of uniqueness in the (θ, w') co-ordinates associated with a given (\textcircled{H}, v') ; this, of course, significantly complicates the job of inverting from lab. data to c.m. (relative to the simple case illustrated in Fig. I-1(b)).

of the KI (w'_{KI}) allows a calculation of the corresponding relative translational energy of products:

$$E' = \frac{1}{2} \mu' v'_{rel}{}^2$$

where $\mu' = \frac{m_I m_{KI}}{m_I + m_{KI}}$, and momentum conservation

$$m_I w'_I = m_{KI} w'_{KI}$$

yields

$$E' = \frac{1}{2} \mu' \left[\frac{m_I + m_{KI}}{m_I} \right]^2 w'_{KI}{}^2 .$$

The reaction exothermicity Q is defined by

$$Q \equiv E' - \bar{E} ,$$

the difference between final and initial relative kinetic energies for the reactive collision. For a specified E_{total} (nominal example shown in Fig. I-1(a)), the following limits are imposed:

$$0 \leq E' \leq E_{total} ,$$

and

$$-\bar{E} \leq Q \leq E_{total} - \bar{E} .$$

Most of the differential cross section functions used in this thesis are carefully defined by Warnock and Bernstein⁴⁴; the others are closely related and can be seen by analogy.

II. Apparatus

A. General

The experimental apparatus was designed and built by H. U. Hostettler^{45,46} under the guidance of R. B. Bernstein; since that time F. A. Morse, P. J. Groblicki, A. R. Blythe, A. E. Grosser, C. Riley, the author, and A. M. Rullis have all contributed to a long list of alterations^{47-54,26,42} (both improvements and degradations), while the experimental work has evolved from elastic⁴⁷⁻⁵¹ to inelastic⁵³ (briefly) and finally to reactive scattering.^{54,26,41,42}

The main vacuum chamber is a Cd-Ni plated cold rolled steel welded box (inside dimensions 14 $\frac{1}{4}$ " x 14 $\frac{1}{4}$ " x 15") pumped by one 9" and one 4" oil diffusion pump (DC 704 pump fluid). The separate detector chamber is a Ni plated brass cylinder pumped by another 4" oil diffusion pump; an adjustable slit for the beam to be detected, the "product" beam, is the only opening to the main chamber. A rotating ("goniometer") lid sealed by an O-ring fits into the main chamber from the top; it houses the ovens and collimation for both beams (as well as the velocity selector, chopper, etc). It can be rotated (manually) from the outside while the apparatus is in operation. The two beams cross at the axis of rotation of the (goniometer) lid and the detector is collimated to view this point at the axis of rotation (called the scattering center); hence rotating the lid changes the scattering angle as viewed by the detector (note: the scattering angle θ is always in the plane defined by the two crossed beams).

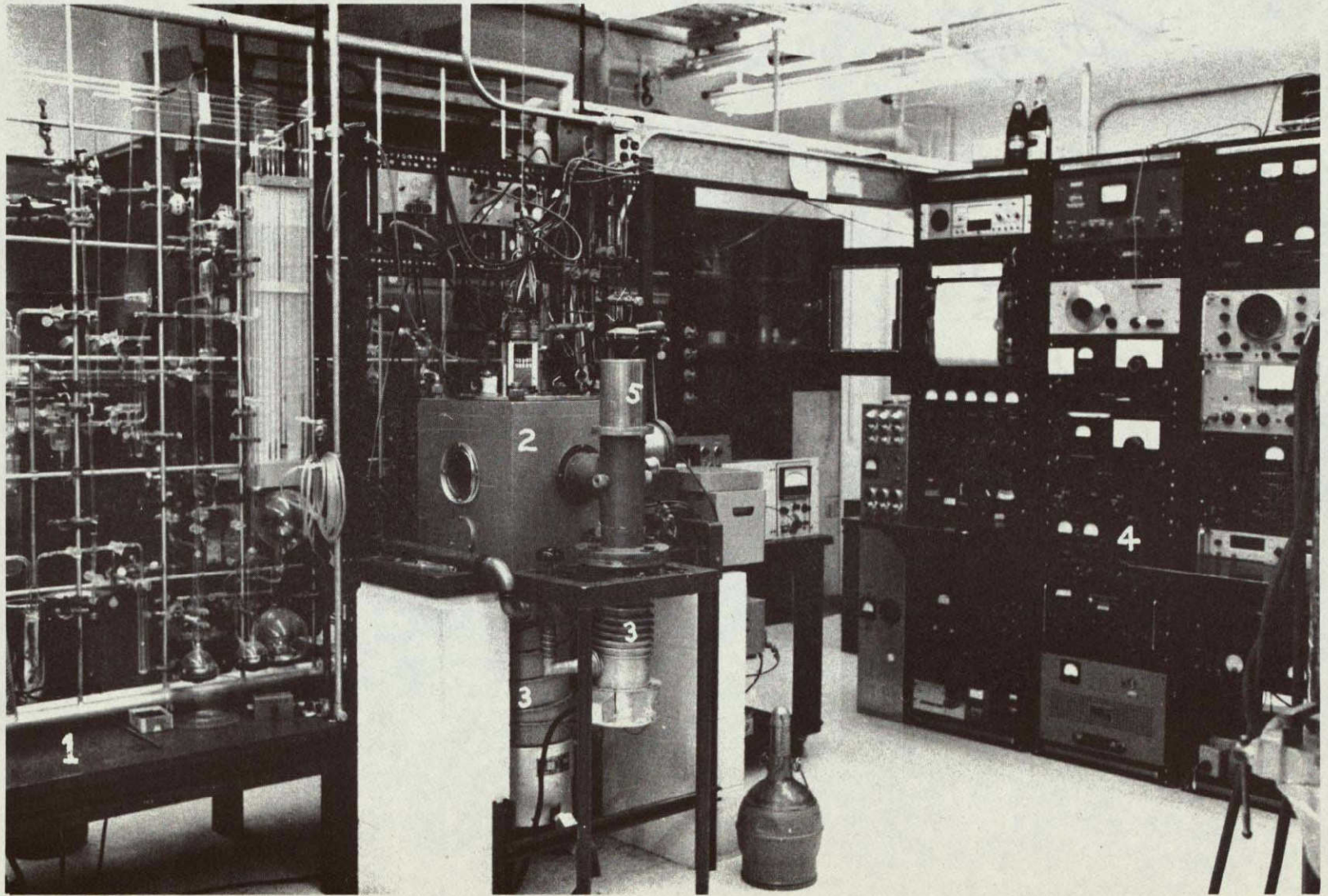
Other general features of the apparatus include:

- 1) A velocity selector (presently 14% nominal resolution) on the primary (K) beam.
- 2) Another selector⁴⁶ (5% nominal resolution) employed as a velocity analyzer for the molecules leaving the scattering center.
- 3) Surface ionization detection (Pt/W 92/8 ribbon) of alkalis and alkali halides.
- 4) A modulator (chopper) on the secondary (non-alkali) beam and a lock-in amplifier for phase-sensitive detection.
- 5) Ample cryogenic (liquid N₂) pumping of condensible species.

Photographs 1-4 and Figure II-1 aid in describing the apparatus.

Photograph 1. Overall View of Apparatus.

1. Glass gas handling rack
2. Main chamber
3. Diffusion pumps
4. Electronic racks
5. Liquid nitrogen reservoir for condensation of residual I_2 .



Photograph 1

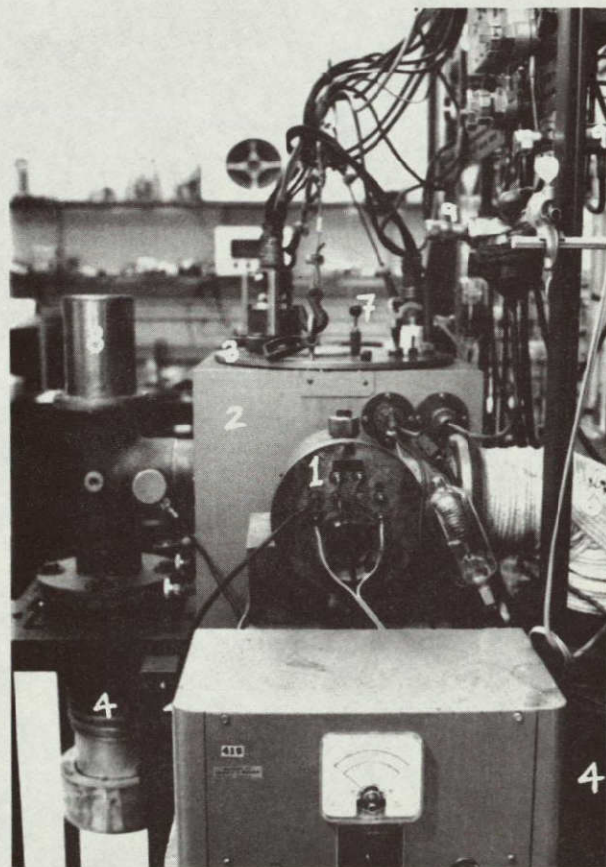
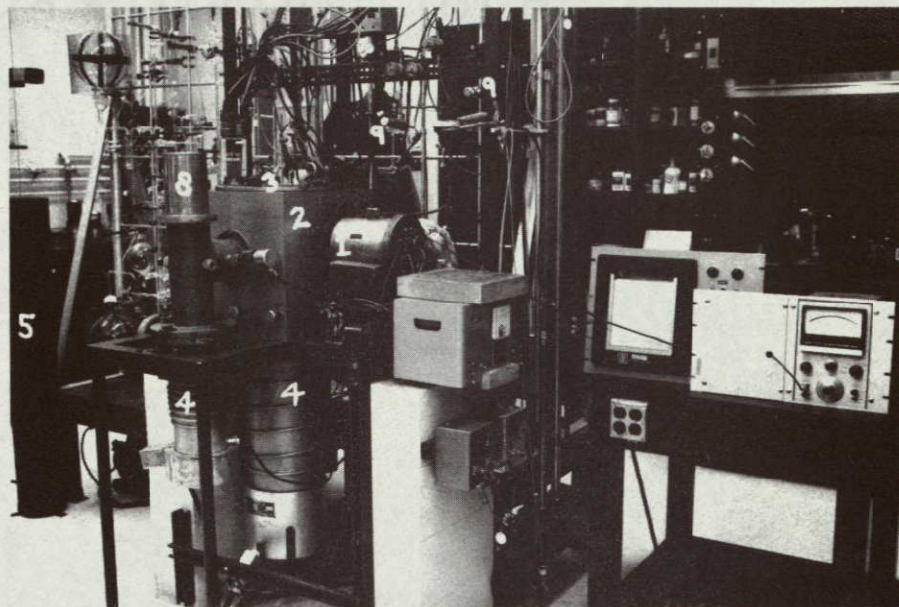
Photograph 2. Two More Views of Apparatus

1. Detector chamber.
2. Main chamber.
3. Goniometer lid.
4. Diffusion pumps.
5. Guard cylinder for counter-weight connected to goniometer lid by pulleys.
- *6. Elbow to detector diffusion pump, containing baffle fashioned out of alumina beads; these beads are outgassed before every experiment using a chromel heater wire inserted through them.
7. Control knob for secondary oven beam flag.
8. Liquid N_2 reservoir used for I_2 condensation.
9. Vactronic leak valves for regulation of gas flow.

* On right side of lower photograph (difficult to see on white background).

Neenah Bond

25% COTTON FIBER

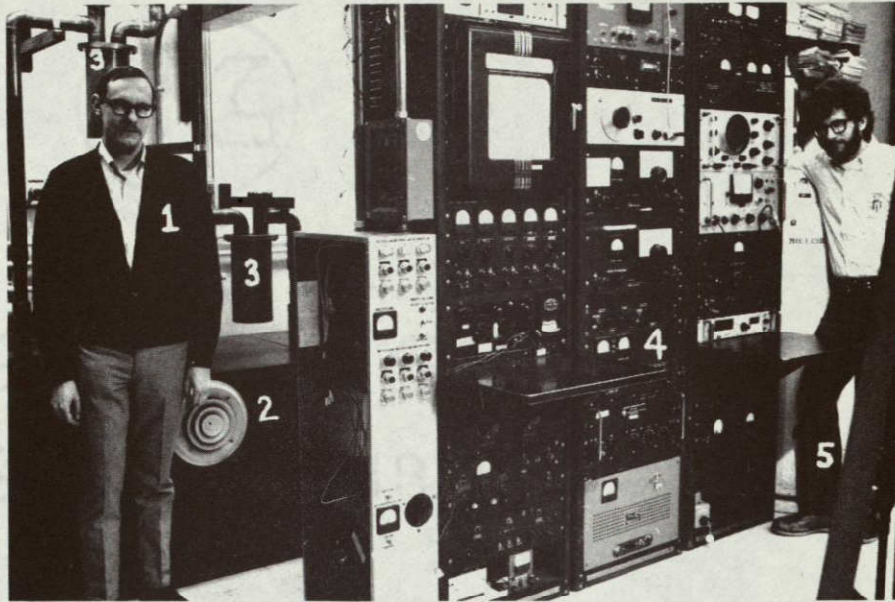


Photograph 2

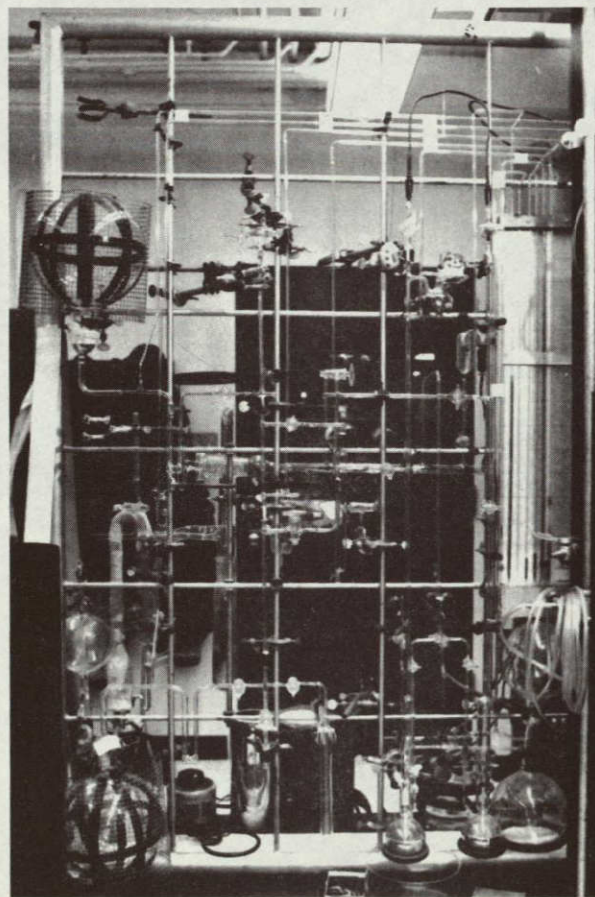


Photograph 3. Accessories

- A:
1. Alan M. Rulis.
 2. Fan-cooled, sound-insulating box for rotary pumps.
 3. Chemical traps; containing soda lime
to protect rotary pumps.
 4. Electronics racks.
 5. Keith T. Gillen.
- B: Glass gas handling rack.



A



B

Photograph 3

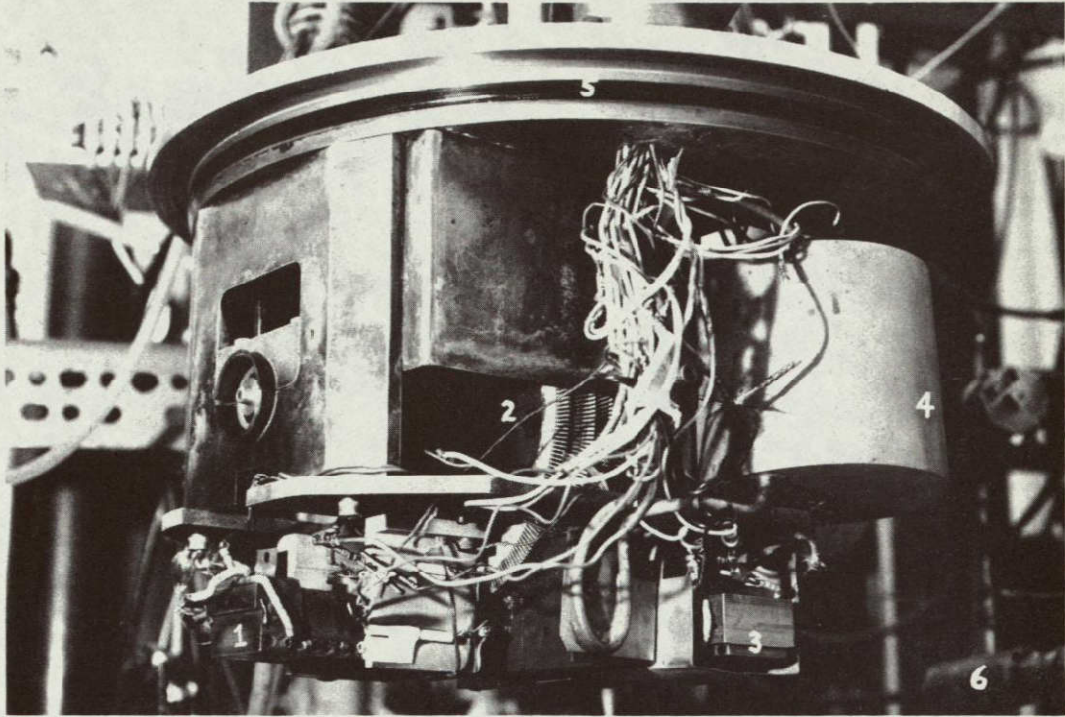
Photograph 4. Lid Lifted.

A: Goniometer lid

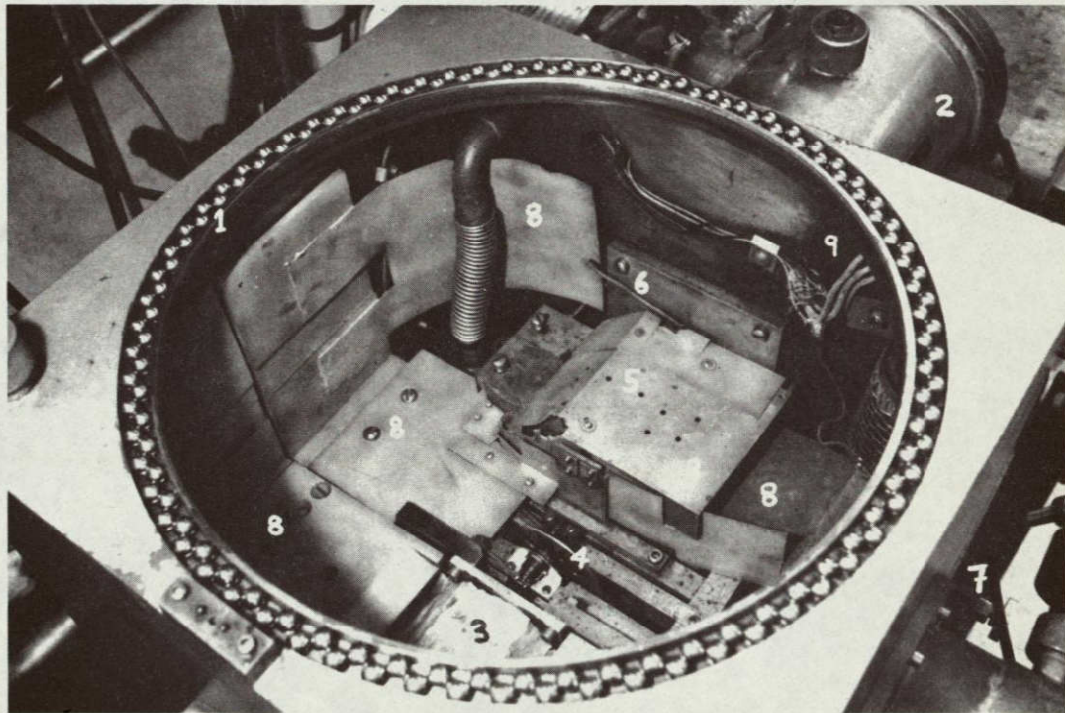
1. Primary (K) oven.
2. Primary beam velocity selector.
3. Secondary (I_2) oven.
4. Liquid N_2 reservoir.
5. Large O-ring for sealing goniometer lid.
6. Vactronic controlled-leak valve for gas admission (external to chamber).

B: Main chamber interior.

1. Bearings to support goniometer lid.
2. Detector chamber.
3. Analyzer motor under this.
4. Light-photocell tachometry (disk is on same shaft as velocity analyzer).
5. Velocity analyzer under here (see photograph 7C).
6. Tube for admitting O_2 to detector chamber.
7. Gear for raising, lowering analyzer (see Photographs 7A,B).
8. Liquid nitrogen cooled trapping surfaces. Many of these surfaces are carbonized before an experiment.
9. Corrosion.



A



B

Photograph 4

Fig. II-1 Apparatus Schematic

Dimensions along the beam directions are to scale. Limits of goniometer rotation are $\Theta \geq -15^\circ$ and $\Theta \leq 101^\circ$. Collimation, trapping surfaces, and other details omitted. S.C. denotes "scattering center."

APPARATUS (TOP VIEW)

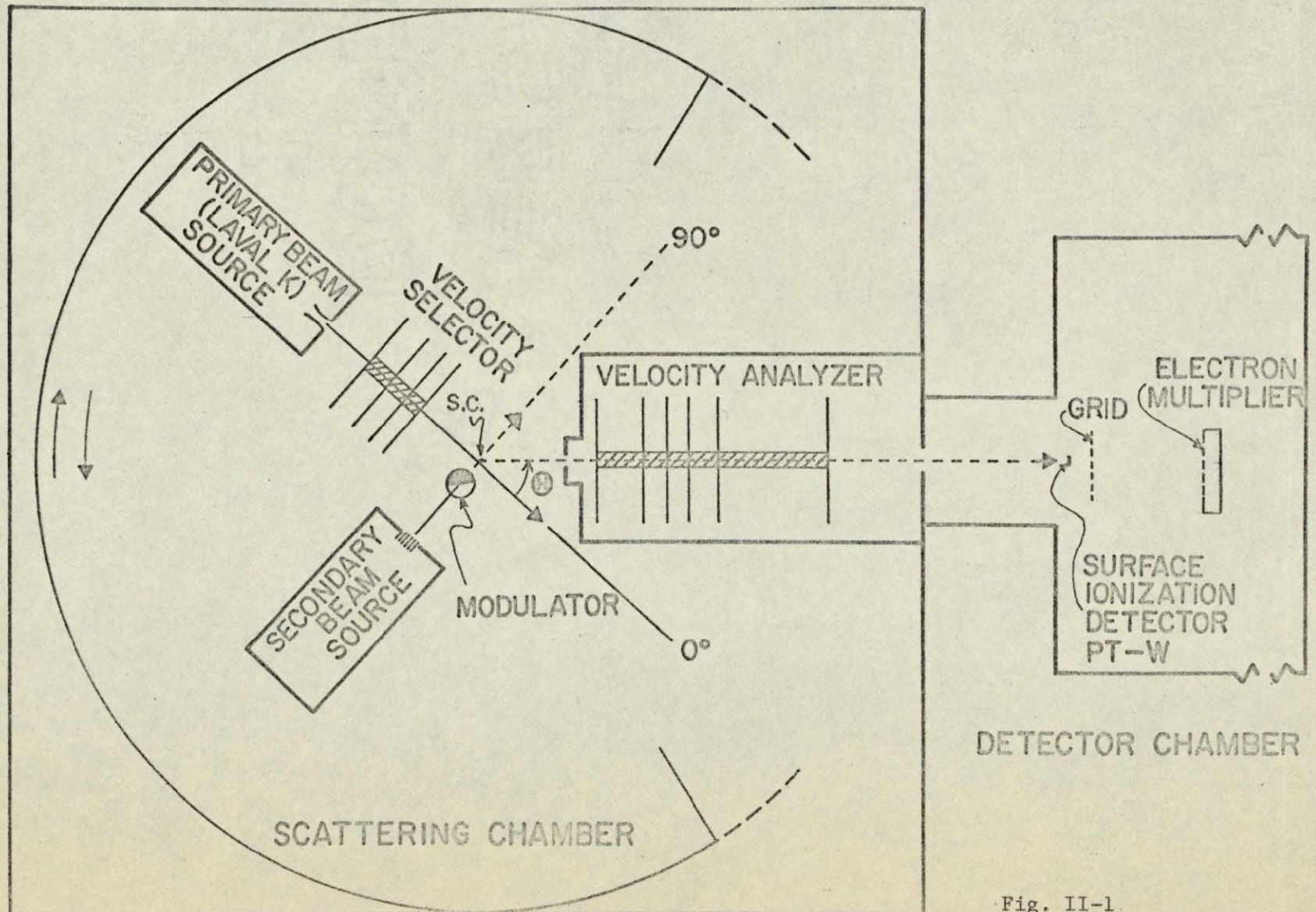


Fig. II-1.

B. Details (circa 1969) (see also Section IVA)

1. Ovens

The primary (potassium) beam oven (Photograph 5a) consists of two pieces of monel which are screwed together (finely polished surfaces make gaskets unnecessary). The larger piece has a capacity of ~ 20 ml and holds the K; the smaller piece is equipped with Laval slits^{55,30} out of which the K beam emerges. A loose nickel baffle between the two sections of the oven prevents splashing of liquid K as the oven temperature is raised. Coiled tungsten wires inserted through ceramic insulators provide the heating; a set of heater wires for each section of the oven allows one to keep the slit temperature higher than the rest of the oven in order to prevent clogging of the slits. Three chromel-alumel thermocouples attached (at various locations) to the oven are used to determine the temperature.

The secondary (I)₂ oven (~ 20 ml capacity) (Photograph 5B) is a three piece stainless steel oven equipped with multichannel Ni (Zacharias foil) slits; in other ways it is similar to the primary oven. An alternate I₂ oven equipped with Laval slits was used for a few of the early experiments.

For experiments with HBr a copper oven was used. The HBr (or DBr) can be introduced from outside the apparatus as a gas; in the K + HBr work it was fed from a Vacronic Vari-Vac leak valve through a copper line to the copper block oven, equipped with Zacharias foil slits.

Photograph 5. Beam Ovens.

A: Assembled primary (K) oven (Monel).

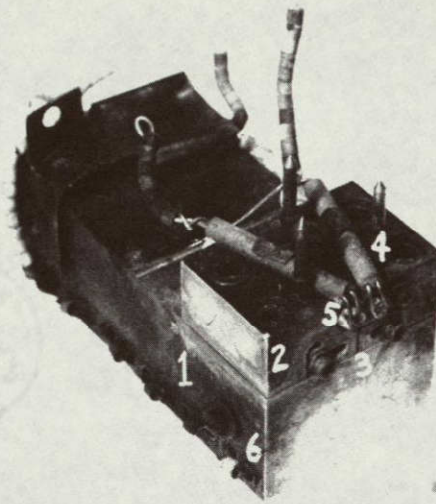
1. Main oven piece.
2. Slit piece.
3. Laval slits.
4. Alignment pins.
5. Slit heaters.
6. Main heaters.

B: Exploded secondary (I_2) oven (304 Stainless).

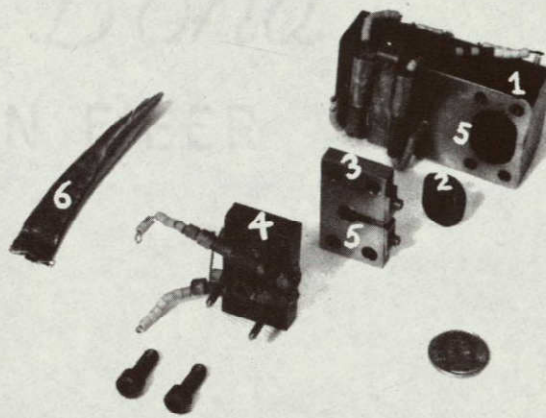
1. Main oven piece.
2. Baffle.
3. Slit piece equipped with Zacharias multichannel slits.
4. Top (slit heater) piece.
5. Lapped surfaces.
6. Specially designed tool for prying open the goniometer lid (specifications available upon request).

C: Secondary oven assembled in position. Several trapping surfaces have been removed to give a view of oven and chopper.

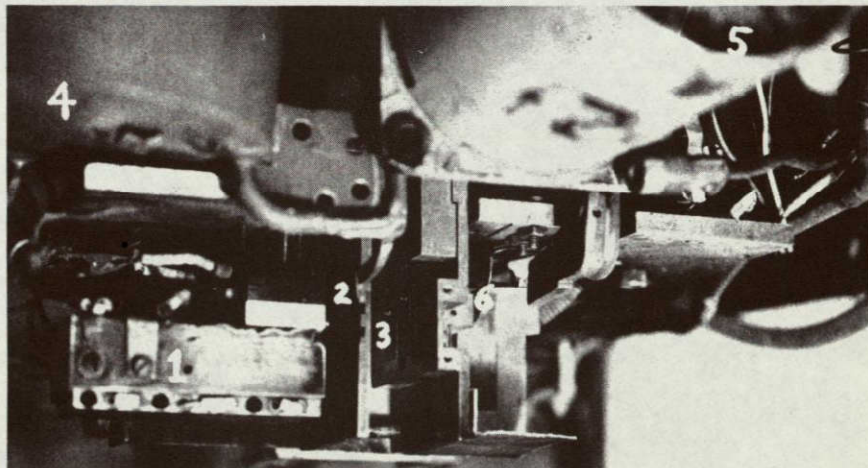
1. Oven.
2. Beam flag (mechanically controlled through rotary O-ring seal).
3. Bulova tuning-fork chopper (25 Hz).
4. Liquid N_2 reservoir.
5. Motor for primary velocity selector.
6. Support for W primary beam monitor (near scattering center).



A



B



C

Photograph 5

NOT REPRODUCIBLE

2. Velocity Selector

The primary (K) beam is velocity selected before entering the scattering zone by a mechanical slotted-disk velocity selector similar in design to the one described by Hostettler and Bernstein⁴⁶; using their notation the velocity selector parameters are given in table II-1* For reference the same information is given for the velocity analyzer⁴⁶.

The selector and analyzer are each driven by an hysteresis synchronous motor (McLean-Syntorque), powered by a variable frequency oscillator and power amplifier (120 Watts nominal output). The rotation speed of the selector is monitored by a light and photocell combination using (ten) holes through one of the selector disks; as the selector rotates, the pulses of light are counted by a digital counter.

The motor bearings (Barden S38H5) and selector bearings (Fafnir MM20EX) are lubricated with Dow-Corning DC 704 silicone pump oil.

3. Scattering Zone

Typical values of the estimated beam intensities entering the scattering zone are given in Table II-2. The K

* This selector was designed by A. E. Grosser.

Table II-1 Selector and Analyzer Constants

	Selector	Analyzer
Number of disks	4	6
Disk diameter	16.0 cm	16.0 cm
Number of slits per disk	278	278
Length of slits (radial direction)	0.8 cm	0.8 cm
Slit width, ℓ_1	0.0813 cm	0.0813 cm
Wall thickness between slits		
At base of slits	0.0814 cm	0.0814 cm
At top of slits	0.0995 cm	0.0995 cm
Average value	0.0905 cm	0.0905 cm
Disk thickness, d	0.1628 cm	0.1628 cm
Average radius, \bar{r}	7.6 cm	7.6 cm
Overall length, $L + d$	3.16 cm	10.16 cm
L	3.00 cm	10.00 cm
Helix angle, ϕ	0.0564 rad	0.1695 rad
$\gamma = \frac{\ell_1}{r\phi}$ (average)	0.190	0.0631
$\beta = d/L$	0.0543	0.01628
$\eta = \frac{\ell_1}{(\ell_1 + \ell_2)}$ (average)	0.473	0.473
Resolution, R	0.141	0.047

Table II-2 Typical Beam Operating Conditions

	K	I_2
Oven Temp. ($^{\circ}$ K)	620	310
Oven Slit Temp. ($^{\circ}$ K)	710	350
\bar{v} (cm/sec)	8×10^4	1.7×10^4
Flux into S.C. (#/sec)	$6-12 \times 10^{13}$	$1-2 \times 10^{15}$
Flux Distribution (#/cm ² /sec)	$5-10 \times 10^{14}$	$1-2 \times 10^{16}$
Density (#/cm ³)	$6-12 \times 10^9$	$5-10 \times 10^{11}$

beam intensities, estimated from the current received by the W monitor (see IIB 5), are for the velocity selected beam with the selector set near the peak in the Laval K beam distribution. The I_2 intensities were calculated assuming ideal Knudsen effusion.⁵⁶

4. Choppers

The secondary beam, crossed perpendicular to the primary K beam, was modulated at 25Hz in either of two ways:

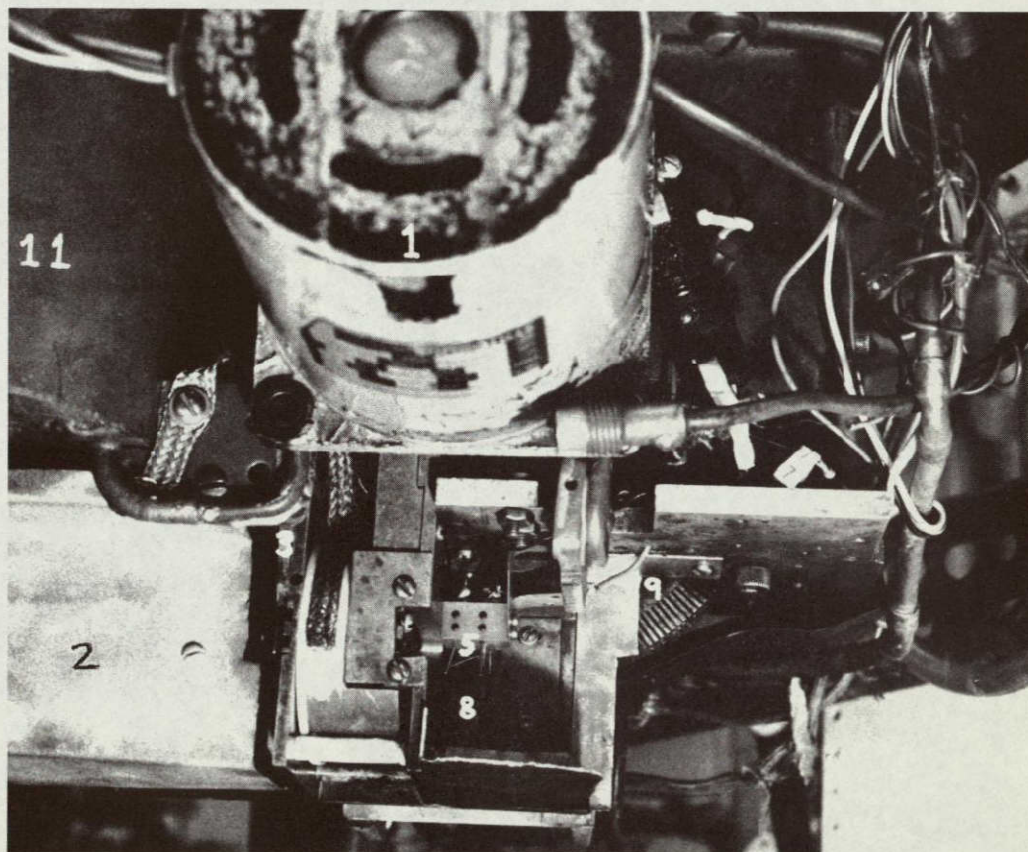
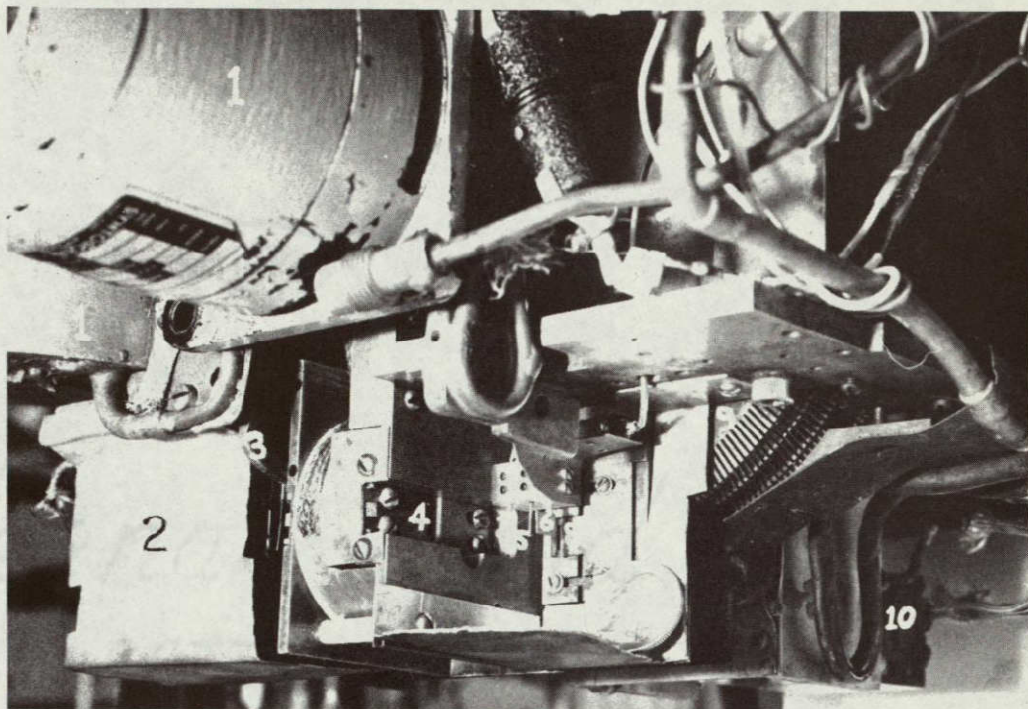
- a) A rotating, motor driven semicircular disk was used for the HBr, DBr experiments and the early I_2 experiments. Its bulk limited the goniometer angle to less than $\textcircled{H} \approx 50$ degrees.
- b) For the later I_2 experiments a very compact Bulova (model L40 with type 4A power supply) tuning fork chopper was used; its small size allowed the angular range of rotation to be extended to 101° . Photograph 5C "shows" this chopper, after removal of some collimation and trapping surfaces.

5. K Beam Monitor

A 0.01 cm diameter tungsten wire (Photo. 6) is used as a surface ionization detection monitor (continuous operation) for the K beam. The K^+ ions emitted from the W wire (biased at -22.5 v) are collected on a nearby collector (a brass rod at -90 v); the current is fed directly to a floated (-90 v) Keithley electrometer. Typical beam monitor currents for a velocity selected

Photograph 6. Details of Scattering Center.

1. Motor for primary selector.
2. Box around secondary oven.
3. Beam flag support.
4. Final secondary beam collimating slit.
5. Tungsten wire K beam monitor.
6. K^+ ion collector (from W wire).
7. Left as an exercise for the reader.
8. Final primary beam collimating slit (visible only in upper photograph).
9. Primary beam velocity selector.
10. Rear of primary beam oven.
11. Liquid N_2 reservoir. (1 in upper photograph!)



Photograph 6

NOT REPRODUCIBLE

Laval K beam were $1-3 \times 10^{-7}$ amps.

6. Velocity Analyzer

The product velocity analyzer is the original instrument described by Hostettler and Bernstein⁴⁶ (see Table II-1). The tygon tubing coupling between the analyzer and its driving motor has been replaced by a flexible metal coupling of "speedometer cable". The motor, power supply, and tachometry are the same as for the selector. The velocity analyzer can be raised or lowered (total vertical motion ~ 1 cm) by a gear system operated (using rotary O-ring seals) from outside the apparatus (see Photograph 7). Hence, in the course of an experiment it can be lowered out of the product beam path to determine the total product at a given apparatus angle, (H).

7. Detector

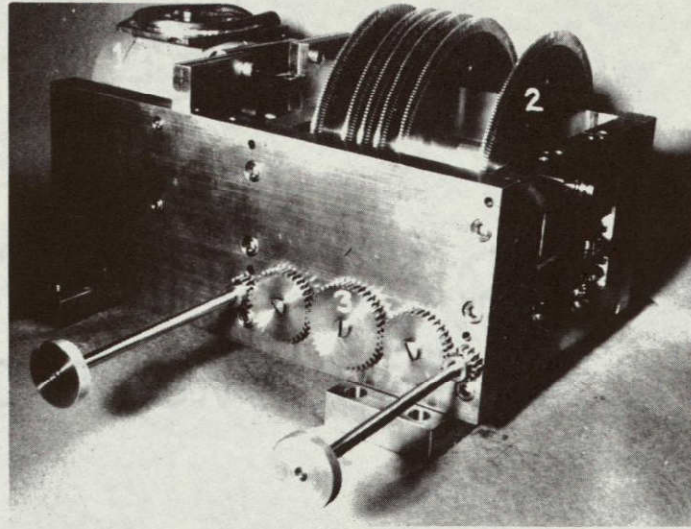
The detector filament is an ~ 1.5 cm long ribbon (.071 cm x .0025 cm) of 92% Pt-8% W alloy (Sigmund-Cohn No. 479). There are two distinct modes⁵ of operation for the detector:

- a) a low work function mode (called "unsensitized" or "desensitized") where K atoms are efficiently ionized to K^+ on the surface, but alkali halide molecules have a low probability of ionization; and
- b) a high work function mode (called "sensitized") where both K atoms and KI(KBr) molecules are ionized to K^+ with nearly unit probability.

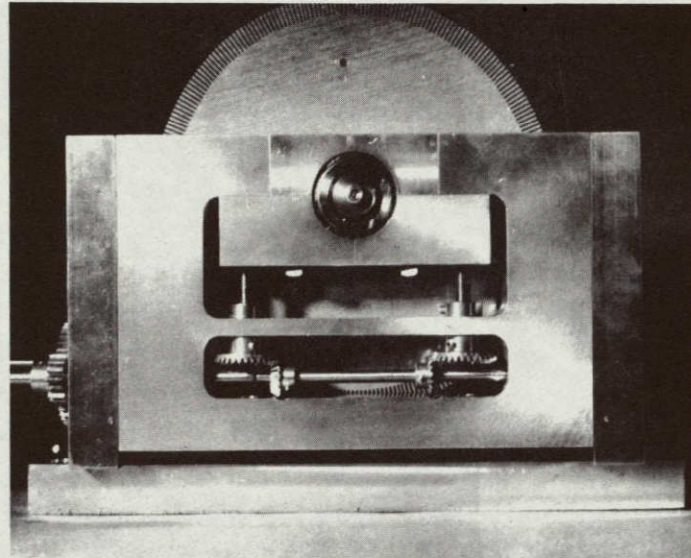
The unsensitized mode could be reached by outgassing the filament for ~ 30 minutes at $\sim 1700^\circ\text{K}$ ($I \approx 1.4$ amps); the filament operating

Photograph 7. Velocity Analyzer

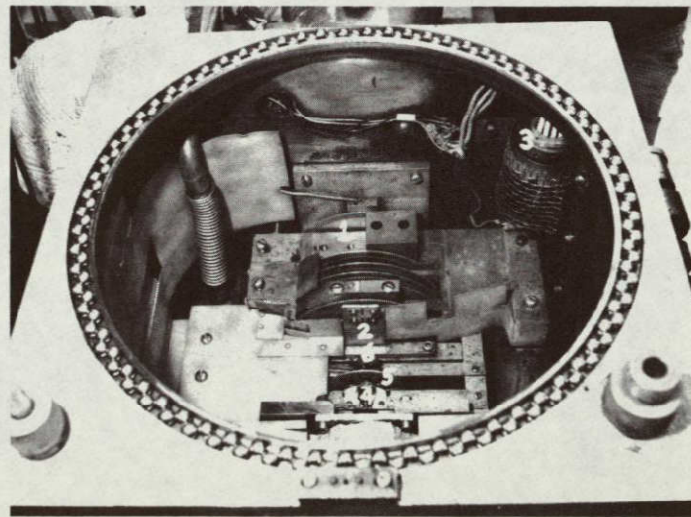
- A: Perspective view of analyzer in original form.
1. Motor.
 2. Velocity analyzer.
 3. Gear system to raise and lower analyzer.
- B: End view of same, showing details of gear system.
- C: Analyzer now in position in main chamber. Note that some cooling surfaces and collimation elements have been removed to allow every disk of the analyzer to be seen.
1. Analyzer.
 2. Analyzer entrance slit.
 3. Nude ion gauge inside vacuum chamber.
 4. Light bulb.
 5. Tachometry disk.
 6. Photocell.



A



B



C

Photograph 7

temperature for "unsensitized" experiments was 1330°K ($I \approx 0.95$). To achieve the sensitized mode, the filament was heated to $\sim 1510^{\circ}\text{K}$ ($I \approx 1.2$) for at least 10 minutes in the presence of O_2 (at a pressure of $\sim 2 \times 10^{-5}$ Torr); then the filament temperature was lowered to $\sim 1370^{\circ}\text{K}$ ($I \approx 1.0$) and the O_2 pressure was reduced to a steady value of $\sim 5 \times 10^{-7}$ Torr using a Vacronic Vari-Vac valve to regulate the leak of oxygen to the detector chamber. This oxygen "bleed" was usually sufficient to assure minimal decay in the sensitivity of detection of alkali halide molecules.

The K^+ ions produced by the filament (biased typically at 0-2 v negative) were pulled through a Pt-mesh grid (typically 40-60 v negative) to a Bendix M-306 electron multiplier (dynode strip input end at -2100 v) whose output leads to a cathode follower. The amplified current (25 Hz) was displayed on an oscilloscope and was also used as the signal input for an EMC Model RJB lock in amplifier (phase-sensitive detector). The reference for the lock-in depends on the chopping method used:

- a) With the mechanical chopper another blade on the same shaft as the modulator interrupted a light bulb beam to a photocell; the photocell output was the synchronous reference.
- b) With the tuning fork chopper, a signal from the driving oscillator network was used as the reference.

The rectified lock-in output (time constant, $\text{RC} = 1$ sec) was fed to a (Leeds and Northrup 10 mv) chart recorder. The usual limit of detection for scattered beam particles (signal-to-noise ratio of approximately

1:1 on the chart recorder) corresponded to a flux of $\sim 5 \times 10^2$ particles/sec striking the filament.

III. K + HBr, DBr

A. A reproduction of the note "Polar (Velocity-Angle) Flux Contour Maps for KBr from the Crossed-Beam Reactions K + HBr, DBr: Evidence for Both Forward and Backward (c.m.) Scattering, " Clyde Riley, Keith T. Gillen, and R. B. Bernstein, J. Chem. Phys. 47, 3672 (1967) follows. It has since been noted that photographic reduction had not been uniform for the x and y directions (1-2% difference) on Fig. 1, leading to a very slight distortion in the scattering contours of Fig. 1.

Polar (Velocity-Angle) Flux Contour Maps for KBr from the Crossed-Beam Reactions K+HBr, DBr: Evidence for Both Forward and Backward (c.m.) Scattering*

CLYDE RILEY, KEITH T. GILLEN, AND R. B. BERNSTEIN

Chemistry Department, University of Wisconsin,
 Madison, Wisconsin

(Received 26 July 1967)

We report new and detailed observations of the velocity and angular distributions of KBr from the crossed-beam reactions K+HBr and K+DBr, leading to a revised understanding of the reaction dynamics. These experiments indicate a very broad angular distribution of KBr in the center-of-mass (c.m.) system, with substantial "forward" and "backward" contributions. Thus, categorizing the differential c.m. reaction cross section $[d\sigma_r(\theta)/d\Omega]$ by such terms as "stripping," "rebound," etc., is an oversimplification.

Previous velocity analysis experiments¹ showed that the locus of maxima in the KBr flux-velocity distributions lay beyond the locus of velocities of the most-probable centroids, suggesting that the KBr was scattered predominantly in the "forward hemisphere" in the c.m. system (i.e., KBr preferring the incident K direction). Doubt as to the validity of this conclusion arises from the recent (kinematically more favorable) observations of Martin and Kinsey² of the angular distribution of tritium atoms from K+TBr. Although tritium was found at all angles,^{2b} its peak occurred in the vicinity of the K direction, implying "backward" c.m. scattering of KBr. Their results are consistent with prior indications suggestive of a "rebound" model^{3a}: the rainbow effect in the angular distribution of the nonreactive scattered K,^{3b,3c} and the moderately small reactive cross section ($\sigma_r \approx 30 \text{ \AA}^2$).^{3b,3d} Attempting to resolve the discordance, we investigated both K+HBr and K+DBr by velocity analysis (the latter reaction providing additional kinematic sensitivity), using refinements in technique to improve sensitivity and accuracy.

The apparatus is that of I,⁴ modified as follows. The "maximum angular divergence" of the secondary beam was reduced from 14° to 4.6° by positioning the source farther from the scattering center (SC). The K beam intensity was increased by utilizing "Laval slits",⁵ reducing the oven-SC distance, and using a shorter,

higher-transmission, but lower-resolution ($R=0.15$) selector.

The K beam peak intensity was set at $919 (\pm 5)$ m/sec. The secondary beam (296°K , crossed perpendicularly) was assumed Maxwellian. To minimize deviations from ideality, low secondary effusion rates were used. The observations consisted of KBr intensity-velocity distributions at various laboratory angles, normalized with respect to the peak flux in the velocity scan at 35° .

The results are presented (Fig. 1) in polar (velocity-angle) KBr flux contour maps,⁶ superimposed upon the "nominal" velocity vector triangle. The solid vertical line ("1") represents the locus of centroids corresponding to the peak K velocity combined with all possible secondary velocities. Similarly, the two parallel dashed lines ("0") show the outer limits of the centroid velocity distribution based on the velocity cutoffs imposed on the K beam by the (asymmetric, but nearly triangular) selector transmission function.

Inspection of the contour maps reveals the extent and breadth of the KBr distribution relative to centroid. Intensity at higher velocities than the high-velocity centroid cutoff arises primarily from "forward" c.m. scattering; flux at lower velocities than the low-velocity centroid "zero line" is predominantly "backward." As in I, the locus of maxima (X 's) is shifted outward from the vertical "peak-centroid" line at low angles, but the new observations differ by crossing over at higher angles. Another difference is that the peak in KBr flux appears at an angle $\approx 5^\circ$ greater than the most probable centroid angle. Both changes imply more "backscattering." As anticipated kinematically,⁷ the K+DBr velocity scans are broader (FWHM $32 \pm 1\%$) than those for HBr ($27 \pm 1\%$).

A quantitative estimate of $d\sigma_r(\theta)/d\Omega$ and $P(E_{\text{int}})$ ⁸ by data "inversion" awaits completion of a full computer analysis (including Jacobian effects⁹). Preliminary

results confirm the present qualitative conclusion, indicating the presence of both forward and backward contributions to $d\sigma_r(\theta)/d\Omega$

* Financial support from the U.S.A.E.C., Division of Research, is gratefully acknowledged

¹ A. E. Grosser, A. R. Blythe, and R. B. Bernstein, *J. Chem. Phys.* **42**, 1268 (1965), here after referred to as I

² (a) I. R. Martin and J. L. Kinsey, *J. Chem. Phys.* **46**, 4834 (1967) (b) L. R. Martin, Ph.D. thesis, Chemistry Department, MIT, (1966)

³ (a) D. R. Herschbach, *Advan. Chem. Phys.* **10**, 319 (1966), (b) E. F. Greene, A. L. Moursund, and J. Ross, *ibid.* **135** (1966), (c) D. Beck, E. F. Greene, and J. Ross, *J. Chem. Phys.* **37**, 2895 (1962), (d) J. R. Arcey, E. F. Greene, K. Kadera, G. P. Reck, and J. Ross, *ibid.* **46**, 3237 (1967).

⁴ See also (a) A. R. Blythe, A. E. Grosser, and R. B. Bernstein, *J. Chem. Phys.* **41**, 1917 (1964); (b) A. E. Grosser and R. B. Bernstein, *ibid.* **43**, 1110 (1965)

⁵ (a) E. Hundhausen and H. Pauly, *Z. Naturforschung* **20a**, 625 (1965); (b) M. C. Moulton and D. R. Herschbach, *J. Chem. Phys.* **44**, 3010 (1966).

⁶ Such maps are described by F. T. Warnock, R. B. Bernstein, and A. E. Grosser, *J. Chem. Phys.* **46**, 1685 (1967). In our Fig. 1, the "experimental points" are obtained by interpolating smooth "best-fit" curves of the velocity scans, averaging replicate experiments

⁷ From Eqs (1), (2) of I, for conditions of the "nominal" triangle, if $Q=0$, $w_{\text{KBr}}=58$ m/sec (DBr) vs 41 m/sec (HBr), if $Q=Q_{\text{max}}$ [using KBr thermochemical data from L. Brewer and E. Brackett, *Chem. Rev.* **61**, 125 (1961)], these values are, respectively, 83 and 64 m/sec

B. A reproduction of the paper, "Reactive Scattering of K by HBr, DBr in Crossed Molecular Beams: Angular and Velocity Distributions of KBr in Laboratory and c.m. Systems," Keith T. Gillen, Clyde Riley, and R. B. Bernstein, J. Chem. Phys. 50, 4019 (1969), follows.

Please note the following erratum on page 4025:

The modified (ESS) density distribution is

$$I(v) \propto (v^2/\alpha^2) \exp [-(v^2/\alpha^2) - c\bar{F}] .$$

Reactive Scattering of K by HBr, DBr in Crossed Molecular Beams: Angular and Velocity Distributions of KBr in Laboratory and c.m. Systems*

KEITH T. GILLEN, CLYDE RILEY,† AND R. B. BERNSTEIN

Chemistry Department and Theoretical Chemistry Institute, University of Wisconsin, Madison, Wisconsin 53706

(Received 18 November 1968)

Measurements of the velocity and angular distribution of KBr formed in reactive collisions between crossed molecular beams of velocity-selected K and thermal HBr (DBr) at a collision energy of 2.8 kcal/mole are described. The results have been subjected to a computer analysis to extract information about the center-of-mass (c.m.) distributions. For both isotopic systems, the c.m. recoil energy distributions are broad, and are similar in shape. The c.m. angular distributions are also broad, HBr shows relatively greater wide-angle scattering than DBr. The total reactive cross section for K+HBr is 40% larger than that for K+DBr. Measurements of the angular distribution of nonreactively scattered K agree well with the results of Airey *et al.* in the region of the rainbow angle.

INTRODUCTION

In 1955 Taylor and Datz at the Oak Ridge National Laboratory pioneered the use of crossed molecular beams to study a chemical reaction, examining the bimolecular reaction $K+HBr \rightarrow KBr+H$.¹ This system has received considerable experimental attention subsequently. Various aspects have been investigated by molecular beam methods in at least five other laboratories (Bonn University, Brown University, Harvard University, Massachusetts Institute of Technology, and the University of Wisconsin).²

Due to unfavorable kinematic factors it has been difficult to extract from the laboratory measurements of the reactively scattered KBr the more fundamental quantities in the center-of-mass (c.m.) system, e.g., the differential reactive scattering cross sections.

A better technique for obtaining the over-all shape of the c.m. angular distribution of reactive products is the method of Martin and Kinsey.³ They studied $K+TBr \rightarrow KBr+T$, detecting the tritium atoms. In contrast to the case of detection of product KBr, the laboratory angular distribution of the light tritium atom should closely mirror the c.m. distribution. They found T scattered at all angles, but with a peak in the direction of the incident K beam, implying preferential backward c.m. scattering of KBr. Since this result disagreed with the conclusions deduced from the early

KBr velocity analysis of this laboratory,⁴ an extensive and improved reinvestigation of the reaction was undertaken. The principal experimental results have been published,⁵ in the form of polar (velocity-angle) flux contour maps of KBr from the reactions $K+HBr$ and $K+DBr$. Inspection of these maps suggests a very broad angular distribution of KBr in the c.m. system.

This paper presents an elaboration of the experimental methods and results of Ref. 5, as well as further observations of nonreactive scattering in these systems. Also reported is a detailed computer analysis of the reactive scattering data in an attempt to extract the "best" c.m. functions (i.e., those c.m. functions which yield calculated scattering that is most consistent with the experimental data). The main results are semi-quantitative estimates of the shapes of the c.m. angular distributions (which appear to differ for the two isotopic systems) and of the c.m. translational energy distribution of the products, deduced in the "uncoupled" approximation. The ratio of the total reactive cross sections for the two isotopic systems has also been estimated; that for HBr is 1.4 ± 0.2 times that for DBr; this ratio agrees with one obtained from the reaction cross sections estimated by Airey *et al.*⁶

EXPERIMENTAL

The apparatus is a modification⁵ of one previously described.^{4,7} The primary Laval⁸ K beam is velocity selected⁹ (resolution, $R=14.4\%$, the full width at half-maximum, FWHM, for an "ideal" transmission tri-

* Supported by the National Science Foundation, Grant GP-7409; the National Aeronautics and Space Administration, Grant NGL-50-002-001; and the U.S. Atomic Energy Commission, Division of Research.

† Present address: Chemistry Department, University of Alabama, Huntsville, Ala.

¹ E. H. Taylor and S. Datz, *J. Chem. Phys.* **23**, 1711 (1955).

² For literature coverage, in addition to references cited in subsequent footnotes, see (a) D. R. Herschbach, in *Molecular Beams*, J. Ross, Ed. (Interscience Publishers, Inc., New York, 1966), Chap. 9, p. 319; (b) E. E. Greene, A. L. Moursund, and J. Ross, *ibid.*, Chap. 4, p. 135; (c) R. B. Bernstein and J. T. Muckerman, in *Intermolecular Forces*, J. O. Hirschfelder, Ed. (Interscience Publishers, Inc., New York, 1967), Chap. 8, p. 389; (d) J. P. Toennies, in *Chemische Elementarprozesse*, H. Hartmann, Ed. (Springer-Verlag, Berlin, 1968), p. 157.

³ (a) L. R. Martin and J. L. Kinsey, *J. Chem. Phys.* **46**, 4834 (1967). (b) L. R. Martin, Ph.D. thesis, Chemistry Dept., Massachusetts Institute of Technology, 1966.

⁴ A. E. Grosser, A. R. Blythe, and R. B. Bernstein, *J. Chem. Phys.* **42**, 1268 (1965).

⁵ C. Riley, K. T. Gillen, and R. B. Bernstein, *J. Chem. Phys.* **47**, 3672 (1967).

⁶ J. R. Airey, E. F. Greene, K. Kodera, G. P. Reck, and J. Ross, *J. Chem. Phys.* **46**, 3287 (1967).

⁷ See, e.g., A. R. Blythe, A. E. Grosser, and R. B. Bernstein, *J. Chem. Phys.* **41**, 1917 (1964).

⁸ (a) E. Hundhausen and H. Pauly, *Z. Naturforsch.* **20a**, 625 (1965). (b) M. C. Moulton and D. R. Herschbach, *J. Chem. Phys.* **44**, 3010 (1966); the slits were of the Moulton-Herschbach design.

⁹ H. U. Hostettler and R. B. Bernstein, *Rev. Sci. Instr.* **31**, 872 (1960).

TABLE I. Apparatus geometry (all dimensions in centimeters).

	Primary beam	Secondary beam		Primary	Secondary
s	0.015	0.147	s'	0.60	0.64
c_I	0.40	0.152	c_I'	0.60	0.64
c_{II}	0.076	0.152	c_{II}'	0.60	0.64
a	0.127 (0.254) ^a		a'	0.80	
d	0.071		d'	0.60	
l_{scI}	1.0	0.6	Maximum angular divergence of secondary beam (in plane) = $\pm 2.3^\circ$		
l_{scII}	5.5	3.7			
l_{ot}	8.6	4.4			
l_{to}	3.7				
l_{td}	25.3				

^a The wider analyzer entrance slit was used for the so called "angle scans," in an attempt to minimize the uncertainty in correcting for the "viewing factor."¹⁴

angle)¹⁰; an estimate of its distribution is given in Appendix A. The secondary beam (296°K, crossed perpendicularly) effuses through a Zacharias foil slit and is mechanically modulated (25 Hz) for phase sensitive detection. A second velocity selector ($R=4.7\%$) is used to analyze the velocity of the scattered products coming from the scattering center (s.c.) to the detector. The detector is a Pt-W alloy which, in the "sensitized mode", detects both K and ⁴¹KBr by surface ionization¹¹; the K⁺ ions are accelerated into an electron multiplier, followed by a cathode follower, a "lock-in" amplifier (25 Hz), and chart recorder. The laboratory detection angle is varied by rotating the beam production system around the s.c. Typical vacua during operation with HBr are 1×10^{-6} , 4×10^{-6} , 7×10^{-7} torr (uncorrected ion gauge readings) in the isolated chamber for the HBr source, the main scattering chamber, and the isolated detector chamber, respectively. HBr gas (Matheson Company, stated purity >99.8%) and DBr gas (Stohler Isotope Company, stated isotopic purity 99% D) were used without purification. Comparison experiments with a synthetic DBr (chemically purified) gave results indistinguishable from those for the commercial DBr.

Table I lists the important apparatus dimensions. The symbols s , c_I , c_{II} , a , and d are, respectively, the full widths of the oven slit, collimator slit I, collimator slit II, analyzer entrance slit, and detector; l_i is the distance between points i and j (i refers to the scattering center). Primed symbols refer to the vertical dimensions (full heights).

¹⁰ This selector is coarser in resolution than that used in Ref. 4, it represents the only degradation from the first velocity analysis experiment. There are many improvements in the present experimental arrangement, however, including lower angular divergence in the secondary beam, improved signal-to-noise ratios, more reproducible data, isotopic substitution (DBr), and much improved data analysis techniques; the present experiments as reported (in abbreviated form in Ref. 5) definitely supersede the earlier results of Ref. 4.

¹¹ For details, see T. R. Touw and J. W. Trischka, J. Appl. Phys. 34, 3635 (1963) and Footnote 3 of Ref. 4. It was found that a very small "leak" of oxygen into the detector chamber is sufficient to insure that there is no decay in the detection efficiency for KBr, once the "sensitized" mode has been obtained.

RESULTS

A single relative velocity distribution was used for all the experiments, with the peak in the velocity-selected K beam flux set at 908 ± 5 m/sec¹² and with the secondary beam oven held at $296 \pm 3^\circ$ K. The primary results are velocity analysis scans of KBr flux distributions at various apparatus angles, θ_a . Figure 1 shows seven such scans for K+HBr (corrected in the usual way⁷ for the velocity-dependent transmission of the analyzer); the curves are seen to have very similar shapes, with FWHM = $27 \pm 1\%$ for all curves. Figure 2 shows eight such scans for K+DBr; the shapes and widths are again very uniform (FWHM = $32 \pm 1\%$), but wider than those for HBr.⁵ Figure 3 shows replicate experiments for K+HBr at $\theta_a = 30^\circ$ and for K+DBr at $\theta_a = 25^\circ$, an indication of reproducibility. The flux peaks at the various angles are compared in Fig. 4, where the ratio of peak intensities is plotted vs θ_a ; these data can be combined with the velocity analysis scans to generate the polar (velocity-angle) flux contour maps of Ref. 5.

Angular distributions of the total flux of K (unsensitized filament) and of the sum of K and KBr (sensitized filament) are shown in Fig. 5. For both reactions, the curves have been normalized in the low-angle rainbow region (where there is only negligible KBr contribution to the observed flux in the sensitized mode). The fact that replicate experiments (sensitized mode) do not agree precisely in intensity for reactive (large-angle) scattering is a consequence of slight day-to-day variation in the relative sensitivity of the filament to K vs KBr. This also precludes using these data to obtain the relative reactive intensities for the two isotopes. However, other supplementary experiments were done contiguously (under conditions of constant sensitivity); they showed that the peak intensity of KBr (at $\theta_a \approx 35^\circ$) from the HBr reaction was twice as great (2.00 ± 0.05) as that for DBr. This is shown in the reactive KBr distribution of Fig. 6, where the points are obtained from

¹² The density peak, however, is at 905 ± 5 m/sec (see Fig. 17). Note, also, that this is an improved estimate which supersedes the value of 919 m/sec used in Ref. 5.

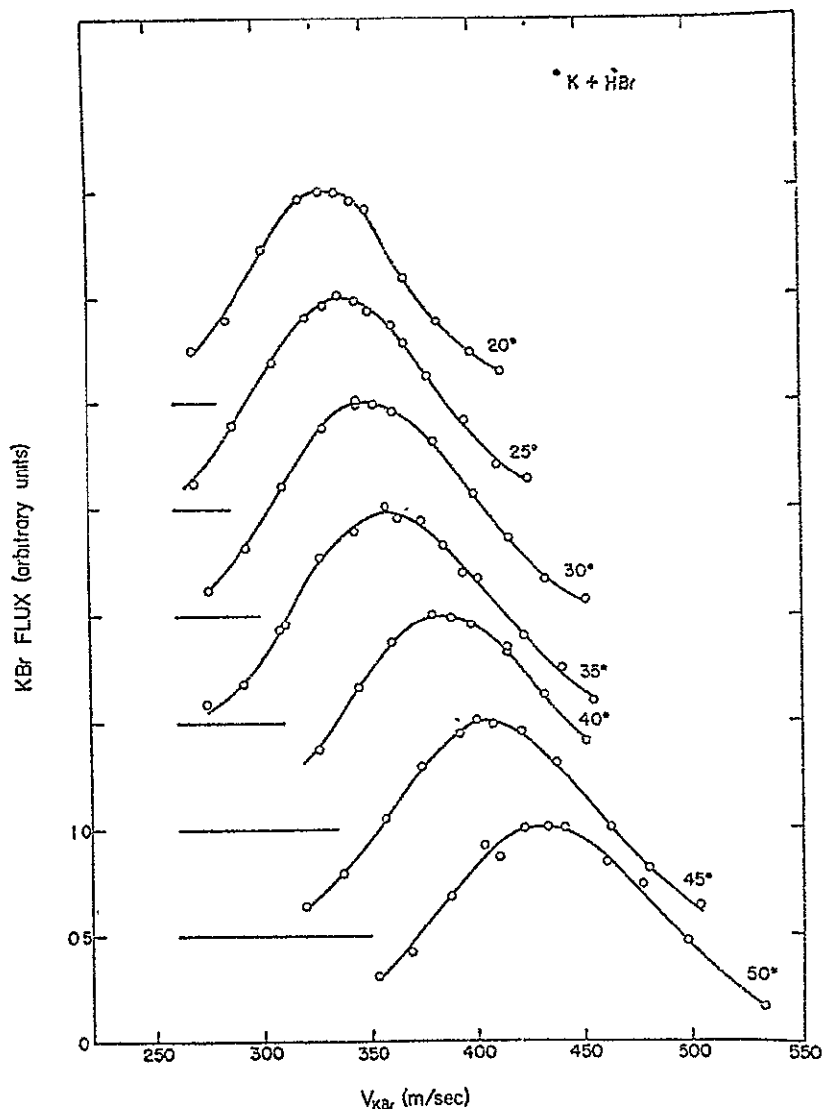


FIG 1 K+HBr Typical velocity analysis scans (KBr flux vs velocity) for $\theta_a = 20(5)50^\circ$. Each curve is scaled to unit peak flux with successive vertical displacements of 0.5. Smooth curves have been passed through the data points.

Fig. 5 by subtraction and normalization. The differential scattering cross section at angles smaller than the rainbow angle θ_r (essentially due to nonreactively scattered K) was assumed to be substantially the same for the two isotopic systems, in accord with Ref. 6. The data were normalized to the same intensity at the respective rainbow maxima.

The solid curves of Fig. 6 are obtained from the data of Fig. 4, as follows. The KBr flux peak intensity at each θ_a was multiplied by the FWHM (in meters per second) of the velocity scan at that angle; assuming that all velocity scans from K+HBr (DBr) are of a fairly uniform shape, this product should be nearly proportional to the total KBr flux at that angle. The good agreement with the data points confirms the assumption.

Figure 7 shows the angular distribution of the nonreactively scattered K on the more familiar semilog plot of $(\sin\theta_a)I(\theta_a)$ vs θ_a .

Figure 8 presents a reduced plot (as recommended by Smith *et al.*)¹³ of the intensity of nonreactively scattered K in the c.m. system. The conversion from laboratory to c.m. assumes a single (nominal) velocity vector triangle and uses the transformation equations of Morse and Bernstein.¹⁴ Also shown are the most comparable experiments of Airey *et al.*⁶ (same beam configuration, slightly lower energy). The agreement is satisfactory in the rainbow region. The results, in terms of the reduced rainbow angle parameter^{2a, 15} $J = \theta_r E$, are presented in Table II.

The maxima in Fig. 8 are slightly better resolved in the data of Ref. 6, this is probably due to the higher

¹³ F. T. Smith, R. P. Marchi, and K. G. Dedrick, *Phys Rev* 150, 79 (1966).

¹⁴ F. A. Morse and R. B. Bernstein, *J. Chem Phys.* 37, 2019 (1962).

¹⁵ The reduced rainbow angle is that angle at which the intensity has fallen to 44% of its peak value on a plot of $\sin^2\theta_{c.m.} \times I(\theta_{c.m.})$ vs $E\theta_{c.m.}$; D. Beck, *J. Chem Phys.* 37, 2884 (1962).

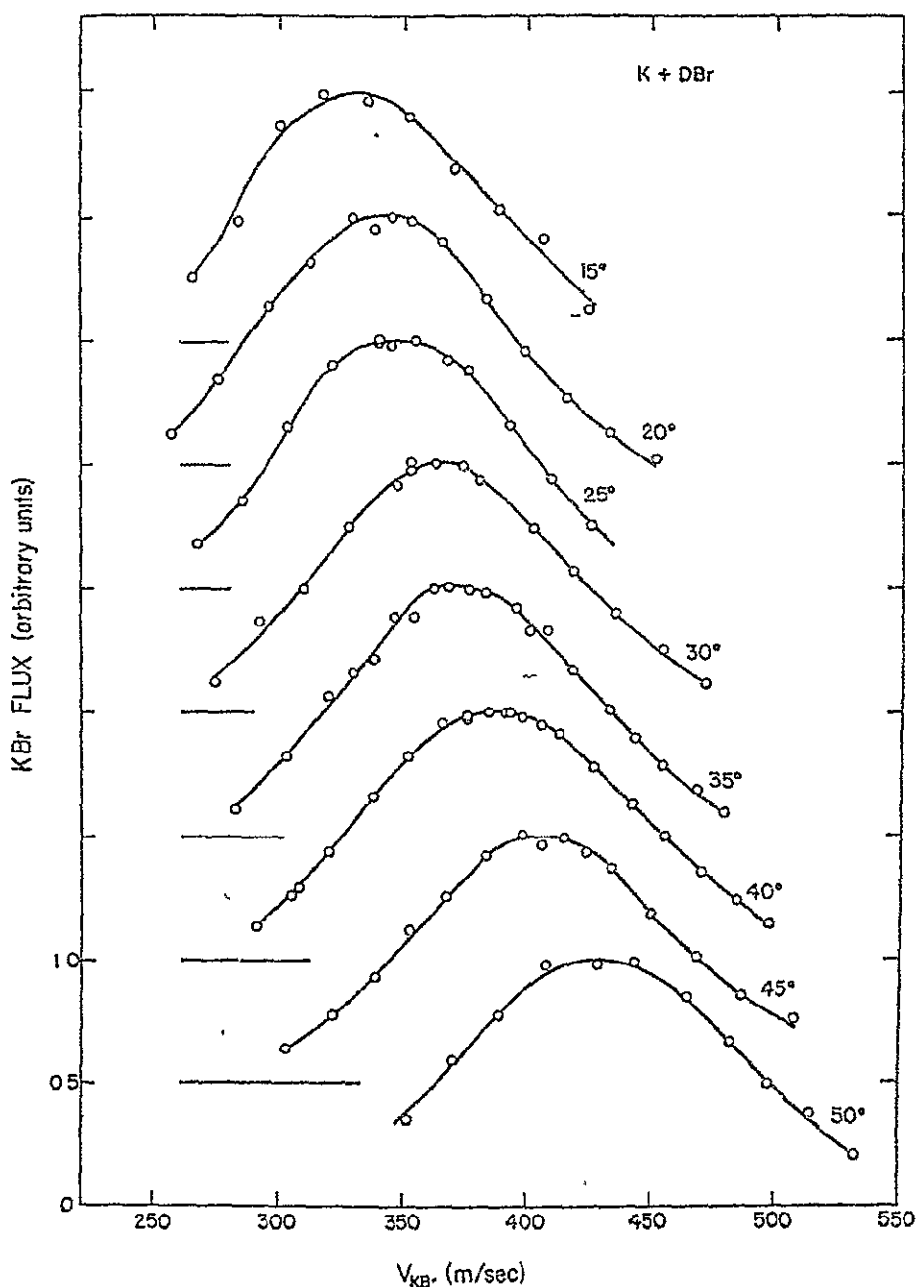


FIG. 2. K+DBr Similar to Fig. 1 for $\theta_a = 15(5)50^\circ$.

resolution primary beam velocity selector used in that work.⁵ However, the present experiments indicated lower values of the relative intensity of nonreactively scattered K in the high-angle region. This increase in the wide-angle "dropoff" of the elastic scattering implies a somewhat larger probability of reaction for collisions of low impact parameter.^{2b,16} In the study of Ref. 6, however, other experiments were done in the out-of-plane configuration (thought to be more reliable); here the wide-angle dropoff was much greater than for their in-plane data. It appears that the in-plane

¹⁶ R. B. Bernstein and R. D. Levine, *J. Chem. Phys.* **49**, 3872 (1968).

results of Ref. 6 contained a significant spurious background signal, which was largely eliminated in their out-of-plane experiments.¹⁷ The reaction probabilities reported for their out-of-plane configuration were approximately the same as those which have been deduced from the present (in-plane) results (analyzed using Ref. 16). The present data show at wide angles (i.e., $\theta_{cm} \gtrsim 50^\circ$) a nearly constant ratio, 1.7 ± 0.3 , for the nonreactive scattering of K by DBr compared to

¹⁷ Any estimate of reaction probability based on the reduced level of nonreactive scattering at wide angles is probably a lower limit, since much of the high-angle nonreactive signal may be due to scattering by the background not fully eliminated.

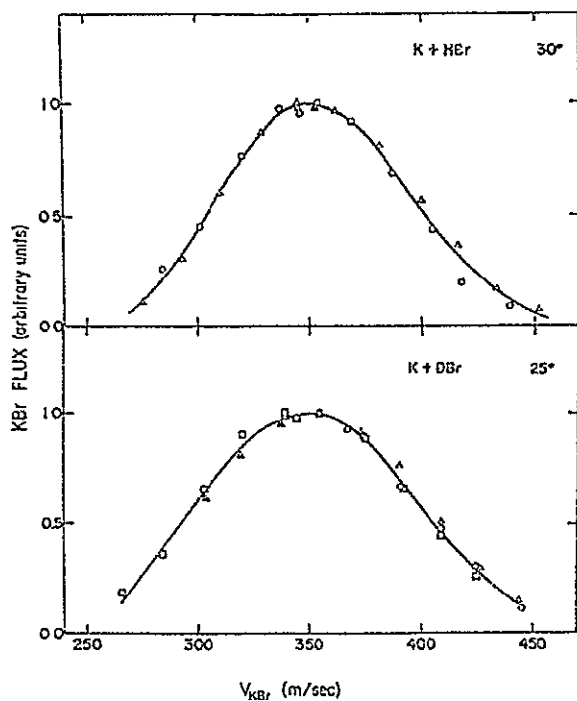


FIG 3 Replicate velocity analyses, scaled to unit peak flux. Upper: K+HBr, $\theta_a=30^\circ$. Lower: K+DBr, $\theta_a=25^\circ$; smooth curves have been passed through the data points.

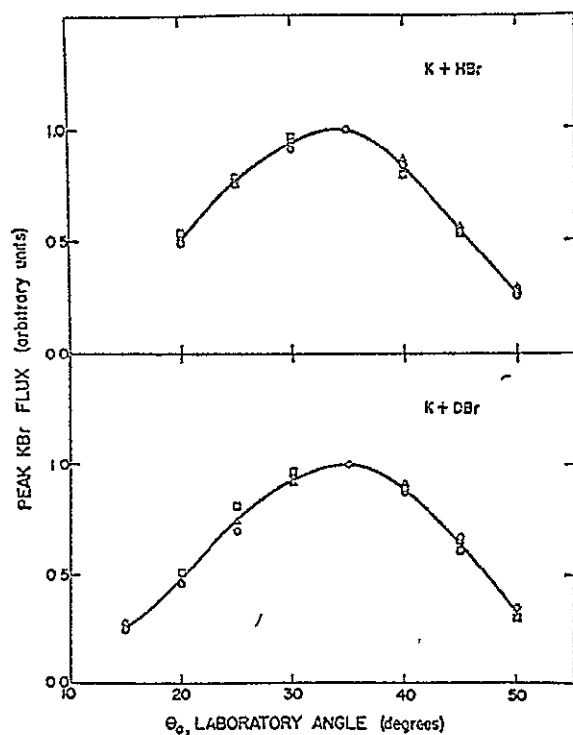


FIG 4 Angular dependence of "peak KBr flux" from comparison of velocity analysis curves at various θ_a . Upper: K+HBr, replicate experiments. Lower: K+DBr, similarly. Smoothed curves passing through the data are scaled to unity at peak.

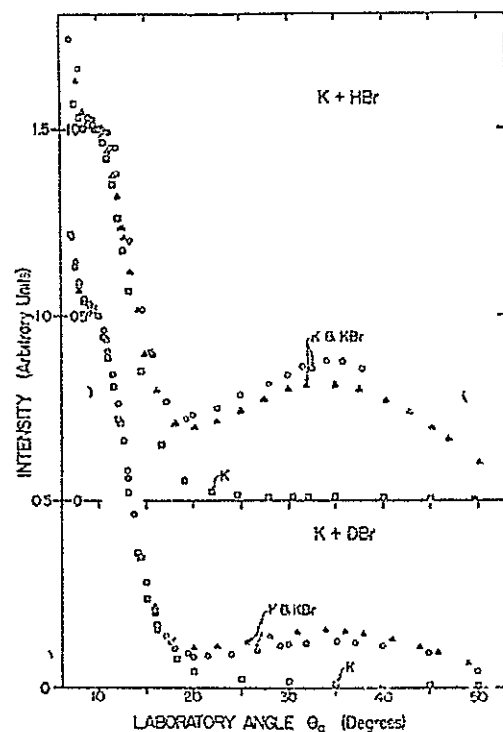


FIG 5 Angular scans of total scattered flux. Circles (O) and triangles (Δ) "sensitized" filament (detecting K and KBr). Squares (\square) "unsensitized" filament (detecting K only). The HBr data are displaced vertically upward by 0.5 units. Normalization is arbitrary for both sets of data.

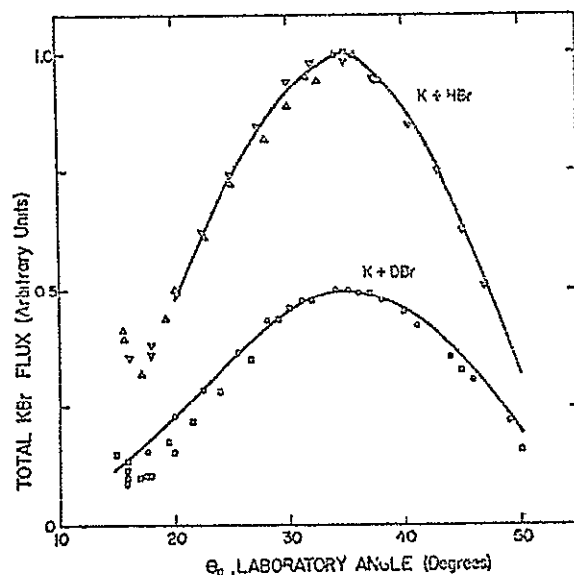


FIG 6 Total KBr flux (no velocity analysis) as a function of θ_a . The various symbols are experimental points derived from the data of Fig 5 (after appropriate subtraction of the K flux). The solid curves are derived from Fig 4; the KBr flux peak at each angle was multiplied by the FWHM of that peak, under the assumption that all velocity scans from K+HBr (or DBr) are of "similar" shape. The ordinate scale is arbitrary, but the ratio of the two curves is presented accurately (based on supplementary direct comparison experiments).

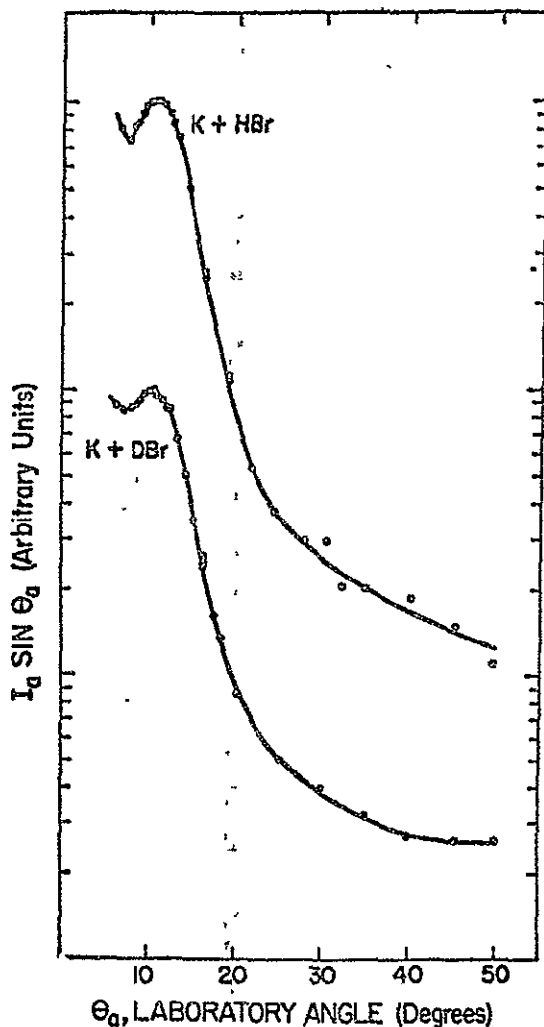


FIG. 7. Semilog plot of the angular distribution of the flux of nonreactively scattered K, $(\sin\theta_a)I(\theta_a)$. The curves have been separated by an arbitrary vertical displacement.

HBr. (However, this ratio should be considered only as a lower limit, due to the possibility of some incompletely eliminated residual background which would tend to reduce the apparent ratio.)

ANALYSIS OF REACTIVE SCATTERING DATA

Two difficulties, one fundamental to the reaction studied, and one experimental, have caused significant problems in analyzing the data:

(1) The reaction $K+HBr$ (DBr) is a particularly difficult one from the viewpoint of extracting the c.m. differential reactive cross sections and excitation functions from the KBr laboratory scattering data. This is caused by the unfavorable kinematics associated with the large mass ratio of KBr to $H(D)$; i.e., the light $H(D)$ atom takes away most of the c.m. recoil velocity, so the velocity vector of the heavy KBr is confined close to the centroid velocity. Thus very small uncertainties

in the laboratory distributions can lead to a large loss of information in the c.m.

(2) The most troublesome experimental uncertainty is associated with the lack of direct knowledge of the velocity distribution of the secondary beam. Indirect evidence suggested that under certain conditions non-ideal flow conditions could seriously affect the results. Preliminary experiments, carried out at high secondary beam flow rates [$\approx 6 \text{ cm}^3$ (STP)/min], yielded a distribution of KBr product which was sensitive to secondary beam flow, and centered at somewhat greater laboratory angles than the results presented in this paper. This indicated abnormal secondary beam effusion with velocity distributions peaked significantly higher than for ideal Knudsen flow. To minimize deviations from ideality, before the reported experiments, the flow was reduced by stages to a final value of $\approx 0.5 \text{ cm}^3$ (STP)/min, beyond which the results seemed essentially invariant to flow. Here ideal effusive flux (with a Maxwellian velocity distribution) could be assumed with reasonable confidence as a first approximation in the data analysis. However, the possibility of some modification could not be ruled out.

A computer simulation which attempted to reproduce the experimental polar (velocity-angle) flux contour maps for reactive product was made using the methods described by Warnock and Bernstein.¹⁸ The c.m. differential reactive cross section ($d^2\sigma/d\omega dw$) was assumed factorizable (the "uncoupled" approximation):

$$(d^2\sigma/d\omega dw) \propto P(\omega)P(w), \quad (1)$$

where $P(\omega)$ is the probability density (distribution) function for scattering into a given element of solid angle in the c.m., $P(w)$ is the probability distribution of flux as a function of velocity in the c.m.,¹⁹ ω is the c.m. angle (θ, ϕ), and w is the c.m. velocity of the reactive product, KBr . The reaction cross section was also assumed to have a negligible dependence on incident energy over the fairly narrow energy range encompassed by the velocity distributions in the two beams.

Initial computations assumed a Maxwell-Boltzmann (M-B) velocity distribution for the secondary beam, the "best-fit" (i.e., most consistent fit to the data) c.m. functions deduced gave an excellent representation of all of the velocity scans (e.g., Figs. 1-3), but the predicted shapes of the peak ratio curves (Fig. 4)

TABLE II. Reduced rainbow angle parameter,^{20,15}
 $J = \theta_c E$ (radian·kilocalorie/mole).

	K+HBr	K+DBr
Airey <i>et al.</i> ⁸	1.10 ₈	1.07 ₇
Present results	1.08 ₈	1.06 ₆

¹⁸ T. T. Warnock and R. B. Bernstein, *J. Chem. Phys.* **49**, 1878 (1968).

¹⁹ E. A. Entemann and D. R. Herschbach, *Discussions Faraday Soc.* **44**, 289 (1967). Their $U_f(u)$ is the present $P(w)$; their $P_f(E')$ is here termed $P(E')$.

were too broad, as seen in Fig. 9. Attempts to narrow this peak ratio curve by varying the c.m. cross section functions were unsuccessful since they generally destroyed the good fits to the individual velocity scans.²⁰ Noting from Fig. 1 of Ref. 5 that the individual angular maxima lie on an almost vertical line (where the secondary beam defines the vertical), it appears that the difficulty may be associated with the assumption of ideal M-B flow. A narrowing of the secondary beam distribution suggests itself as the cause for the narrowing of the experimental peak ratio curve. This conclusion is made plausible by the preliminary (unreported) experiments done at higher secondary beam effusion rates, experiments with definitely nonideal flow.

The simplest model which has been introduced to allow for modification of the M-B flow condition is that of Estermann, Simpson, and Stern²¹ (ESS). It attempts in a simple way to account for preferential scattering of low velocity beam molecules by "cloud" formation in front of the source slit.²² The modified (ESS) density distribution is

$$I(v) \propto (v^2/\alpha^2) \exp[-(v^2/\alpha^2) \frac{c}{k} c \bar{F}],$$

where $\alpha = (2kT/m)^{1/2}$, \bar{F} is given in Fig. 14 of Ref. 21,²³ and c is a constant that determines the magnitude of the attenuation. The constant $c=2$ was chosen because it could account nicely for the observed narrowing of the peak ratio curve. The ESS density distribution ($c=2$) is compared to the M-B ideal case in Fig. 10. The velocity of the peak in the ESS density curve, denoted by α' , is 11% greater than α , the velocity of the maximum in the M-B density function.

Using this ESS secondary beam distribution a new set of "best" c.m. distribution functions was deduced. The functions found were almost identical to the ones derived assuming a M-B secondary velocity distribution. The reproductions of the velocity scans of Figs. 1-3 were as good as before, but the peak ratio curves now fit much better for both HBr and DBr reactions (see Fig. 9). This verified the strong correlation between the shape of the peak ratio curve and the secondary beam velocity distribution and strongly implied nonideal secondary beam flow conditions.

Figure 11 shows the deduced "best" c.m. angular distributions for the two reactions. The c.m. recoil energy distributions, expressed in $P(w)$ and $P(E')$ form,¹⁹ are shown in Fig. 12. The curve in the upper part of the figure gives the best estimate of the transla-

²⁰ In the present analysis it has been considered more important to fit the individual velocity scans than the peak ratios. This is because the peak ratio curve is intrinsically subject to more systematic error, associated with the possibly different scattering volume "seen" at every angle. The analyzer entrance slit was opened to 0.254 cm (see Table I) for the peak ratio experiments in an attempt to minimize the correction for this "viewing factor."¹⁴

²¹ I. Estermann, O. C. Simpson, and O. Stern, Phys. Rev. 71, 238 (1947).

²² See also R. S. Freund and W. Klemperer, J. Chem. Phys. 47, 2897 (1967).

²³ Although \bar{F} is velocity dependent, it is fairly constant for $v \gtrsim \alpha$, increasing rapidly at lower velocities.

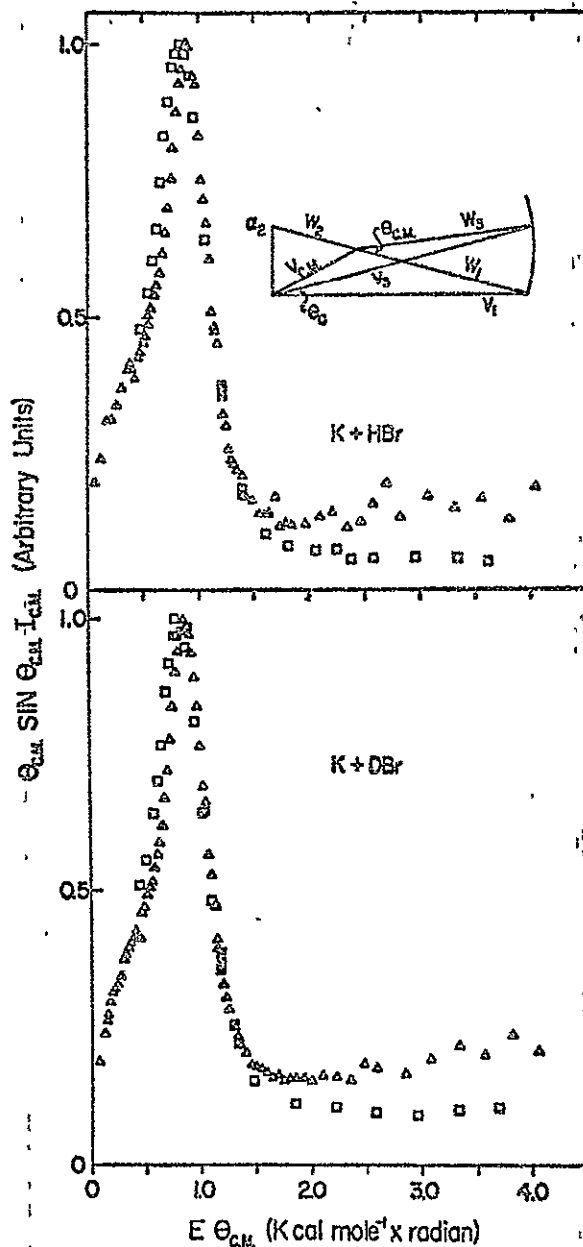


Fig. 8. Reduced plot (Smith *et al.*)¹³ of the flux of nonreactively scattered K in the center-of-mass (c.m.) system. The conversion from laboratory to c.m. was done using the "nominal velocity vector triangle" (as illustrated in the insert, where $|w_1| = |w_2|$). Laboratory velocities are denoted by v 's; c.m. velocities by w 's. The triangles (Δ) represent the data of Airey *et al.*⁴ ($v_K = 878$ m/sec, $T_{HBr} = 250^\circ K$, $T_{DBr} = 254^\circ K$), the squares (\square) are the present data ($v_K = 908$ m/sec, $T_{HBr, DBr} = 296^\circ K$). All data have been normalized to a peak of unity. Upper: K+HBr; Lower: K+DBr.

tional energy distribution of flux $P(E')$ in the c.m. system (the same for both isotopic systems); the lower curves give the corresponding translational velocity distributions of flux $P(w)$ in the c.m. system. [Note their relationship: $P(w) \propto wP(E')$.] The collision exothermicity Q is defined as usual⁴ by $Q \equiv E' - E$, where E and E' are, respectively, the relative translational

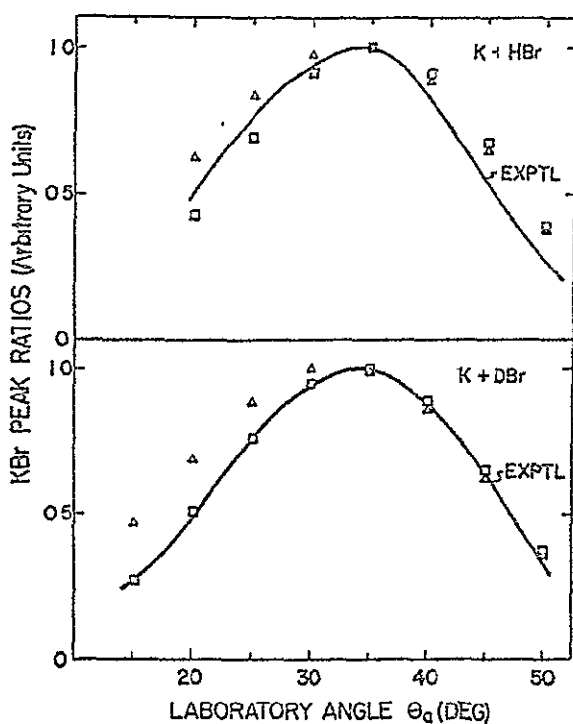


FIG. 9. Experimental KBr flux "peak ratio curves" compared with best-fit computed results for M-B secondary beam (Δ) and for ESS secondary beam (\square); all curves arbitrarily normalized to unity at peak.

collision energy before and after collision.²⁴ Shown on Fig. 12 are the points for $Q=0$ and $Q=Q_{\max}$ (all available energy going into translation) for the case of the most probable initial collision energy.²⁵ Table III lists numerical values.

The shaded zones in Figs 11 and 12 represent the

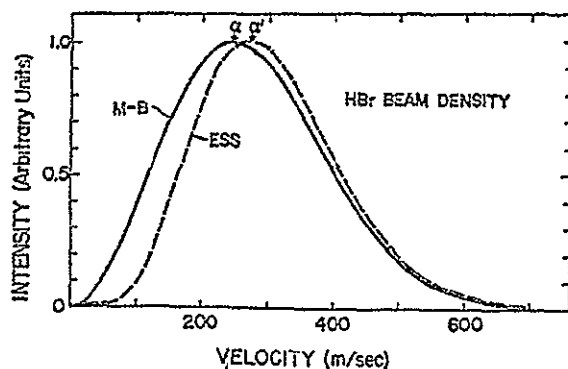


FIG. 10. Density distribution functions used to represent HBr beam (296°K). Solid curve (peak at α) M-B, dashed curve (peak at α'): ESS function. Both curves normalized to unity at peak.

²⁴ See Footnote 17 of Ref. 18 for further details.

²⁵ Use is made of KBr thermodynamic data of L. Brewer and E. Brackett, Chem. Rev. 61, 425 (1961).

limits for smooth, low-resolution functional forms that give reasonable fits to the data [many different combinations of functional forms were tried for $P(\omega)$ and $P(\omega)$, including various simple angular distributions which attempted to simulate the strong preference for "backward" c.m. scattering of the KBr reaction, $K+TBr$].³ The "best" c.m. functions (Figs 11 and 12) are summarized in Table IV.

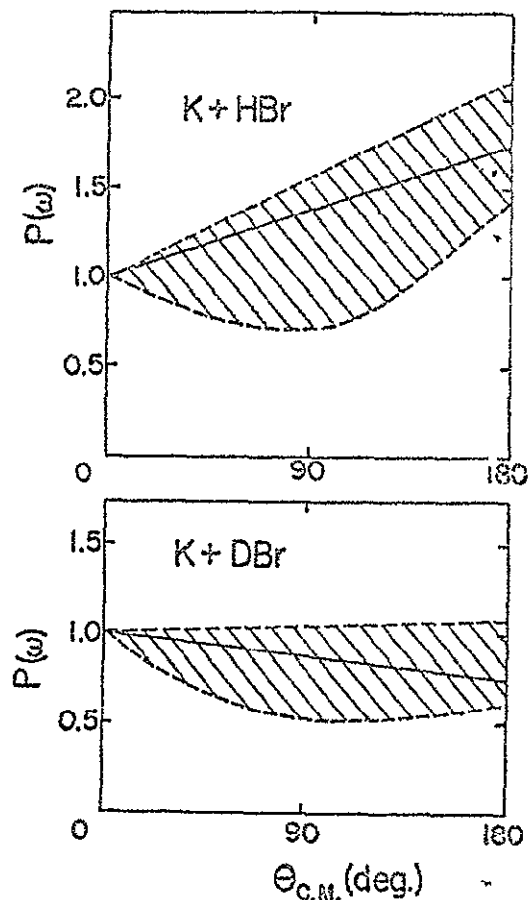


FIG. 11. Deduced c.m. angular distribution functions $P(\omega) \propto d^2\sigma(\theta_{c.m.})/d^2\omega$. The heavy solid lines are the distributions which give the "best" representation of the data, and the shaded areas encompass limits for "reasonable fits" to the data. All curves arbitrarily normalized to unity at zero degrees.

A set of curves of KBr flux vs velocity, computed by using the "best" c.m. functions and the assumed ESS velocity distribution for the secondary beam, is compared in Fig. 13 (K+HBr) and Fig. 14 (K+DBr) to the set of experimental velocity scans (the "experimental" curves are smoothed, best representations of the data). Here, both the computed points (10-m/sec intervals) and the smoothed experimental curves are normalized (for both reactions) relative to the maximum in the flux at $\theta_a=35^\circ$ (using Fig. 9). Fig. 15 pre-

sents polar (velocity-angle) KBr flux contour maps^{5,26,27} as another representation of Figs. 13 and 14; solid contours are experimental, dashed contours are calculated from the preferred c.m. functions. The "nominal" velocity vector triangles drawn [$v_K=908$ m/sec, $v(\text{HBr, DBr})=\alpha'$] correspond to the velocity of the maximum in the flux distribution of the primary beam and the velocities of the (assumed) ESS density maxima of the secondary beams.²⁸

The computed fits to the experimental contour maps (Fig. 15) are reasonable considering the kinematic difficulties and the problems with the nonideal secondary beam. Not fitted within the estimated experimental error bounds were the "peak ratio" data for HBr. Since there is such a strong link between the secondary beam velocity distribution and the peak ratio curve, the uncertainty in the secondary beam flow conditions precludes further attempts at adjusting and improving the fit to the HBr peak ratio data; as mentioned, such adjustments improve the fit, but do not appreciably change the "best" c.m. functions.

Also shown in Fig. 15 are "Cartesian" flux contour map representations of the experimental data, obtained by dividing the polar flux intensity by v^2 [Note that $1/v^2$ is part of the Jacobian (lab \rightarrow c.m.) factor w^2/v^2 .] This removes the influence of the relative position of the origin in laboratory velocity (v) space upon the size of the laboratory volume element (in v space). (Note: A volume element increases proportional to v^2 in the polar coordinate system, not so in the Cartesian reference frame.) Hence such a Cartesian flux contour

TABLE III. KBr recoil velocity for several cases.
 $E=2.8$ kcal/mole.

	Q (kcal/mole)	w (m/sec)
K+HBr	0	41
	4.2 ($=Q_{\text{MAX}}$)	64
K+DBr	0	58
	3.1 ($=Q_{\text{MAX}}$)	83

²⁶ T. T. Warnock, R. B. Bernstein, and A. E. Grosser, *J. Chem. Phys.* 46, 1685 (1967).

²⁷ See also (a) Z. Herman, J. Kerstetter, T. Rose, and R. Wolfgang, *Discussions Faraday Soc.* 44, 123 (1967); (b) W. R. Gentry, E. A. Gislason, Y. Lee, B. H. Mahan, and C. Tsao, *ibid.* 44, 137 (1967).

²⁸ The "most probable triangle" (most probable collision event) corresponds to the maximization of $v_i d_i(v) d_2(v)$, where $d_i(v)$ is the density distribution of beam i , and v_r is the relative velocity. When one beam (e.g., beam 1) is much faster than the other, then $v_r \approx v_1$ and the quantity to maximize is $v_1 d_1(v) d_2(v)$. But $v_i d_i(v) = f_i(v)$, where $f_i(v)$ is the flux distribution of beam i . Hence, in this case, the most probable triangle corresponds approximately to the velocity of the density maximum in beam 2 and the velocity of the flux maximum in beam 1. These considerations have been discussed also by J. H. Birely, Ph.D. thesis, Harvard University, 1966.

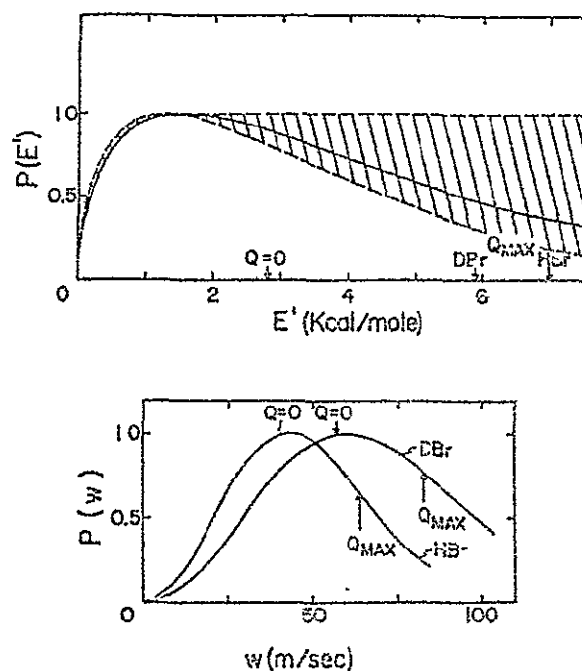


FIG. 12. Upper: Deduced c.m. flux distribution function $P(E')$. The solid curve represents the function giving the "best" reproduction of the data both for HBr and for DBr, the shaded area encompasses limits for "reasonable fits" to the data $Q=0$ and $Q=Q_{\text{MAX}}$ (for each system) refer to the "nominal" collision conditions ($v_1=908$ m/sec, $v_2=\alpha'$). (Curves are normalized to unity at peak). Lower: c.m. flux distribution functions $P(w)$ for HBr and DBr corresponding precisely to the solid $P(E')$ curve (upper), arbitrarily normalized to unity at peak in $P(w)$.

map provides a better visualization of the scattering relative to centroid.²⁹ Inspection of the Cartesian maps of Fig. 15 reveals the broad but somewhat "backward" scattering of KBr from the HBr reaction, and the tendency for "forward" scattering for the DBr system.

The observed absolute intensity ratio of scattered KBr from HBr and DBr (as shown in Fig. 6) has been used with the "best" c.m. functions to deduce a ratio for the total reactive cross sections of the two systems. The procedure was as follows. The c.m. functions were normalized to the same total integral [$I_t = \iiint P(w)P(\omega)dw d\omega^2$] for the two systems [corresponding to (temporarily assumed) identical magnitudes for the total reactive cross sections]. These functions were used to compute scattering maps in the laboratory system. The ratio of total KBr flux at $\theta_a=35^\circ$ for the two isotopic reactions was then computed. This ratio was compared to the experimental ratio in Fig. 6, and the integrals I_t adjusted so as to recover the experimental ratio of laboratory flux. The total reaction cross section thus evaluated is

$$\sigma^r(\text{K}+\text{HBr})/\sigma^r(\text{K}+\text{DBr})=1.4\pm 0.2.$$

²⁹ (a) W. R. Gentry, E. A. Gislason, B. H. Mahan, and C. Tsao, *J. Chem. Phys.* 49, 3058 (1968), (b) R. Wolfgang and R. J. Cross (private communication).

TABLE IV. Preferred ("best fit") c m distribution functions, not normalized. E' (kilocalories per mole), w (meters per second), θ (degree in c m).

	K+HBr	K+DBr
$P(\omega) [= P_s(\theta)]$	$1 + \frac{1}{2}(\theta/180)$	$1 - \frac{1}{2}(\theta/180)$
$P(E')$	$E'^{1/2} \exp(-0.325E')$	(same as K+HBr)
$P(w)$	$(w/42.6)^2 \exp[-(w/42.6)^2]$	$(w/60)^2 \exp[-(w/60)^2]^a$

* This functional form is used by W B Miller, S A Safran and D R Herschbach, Discussions Faraday Soc 44, 108 (1967) See also Ref. 19 They (appear to) use this as a density function rather than as a flux function, hence their corresponding flux function would be multiplied by w (see Ref 19)

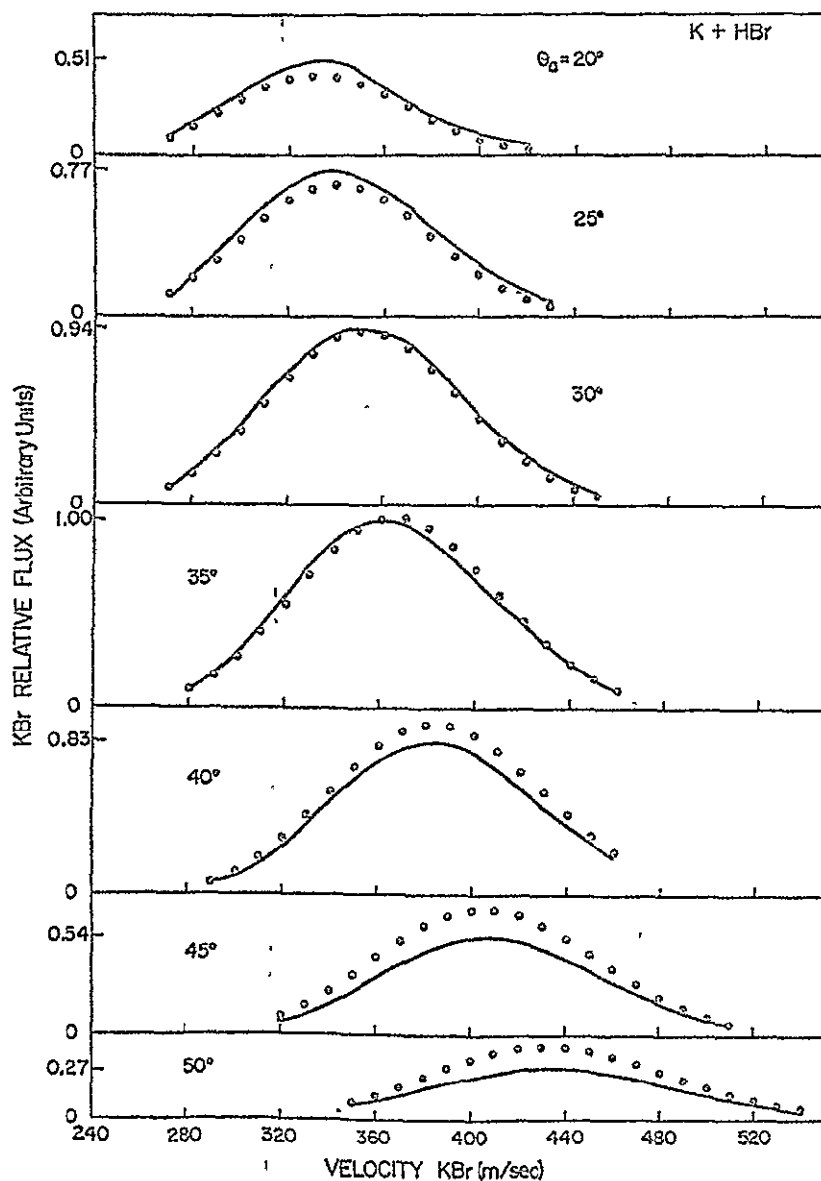


FIG 13. K+HBr Best computer reproductions of the experimental velocity scans of KBr flux Note that here the solid curves are best smooth representations of the data, the normalizations (numbers along the ordinate), relative to the peak in the flux at 35°, are from the peak ratio curves of Fig 9. The points are computed results (at 10-m/sec intervals in v_{KBr}).

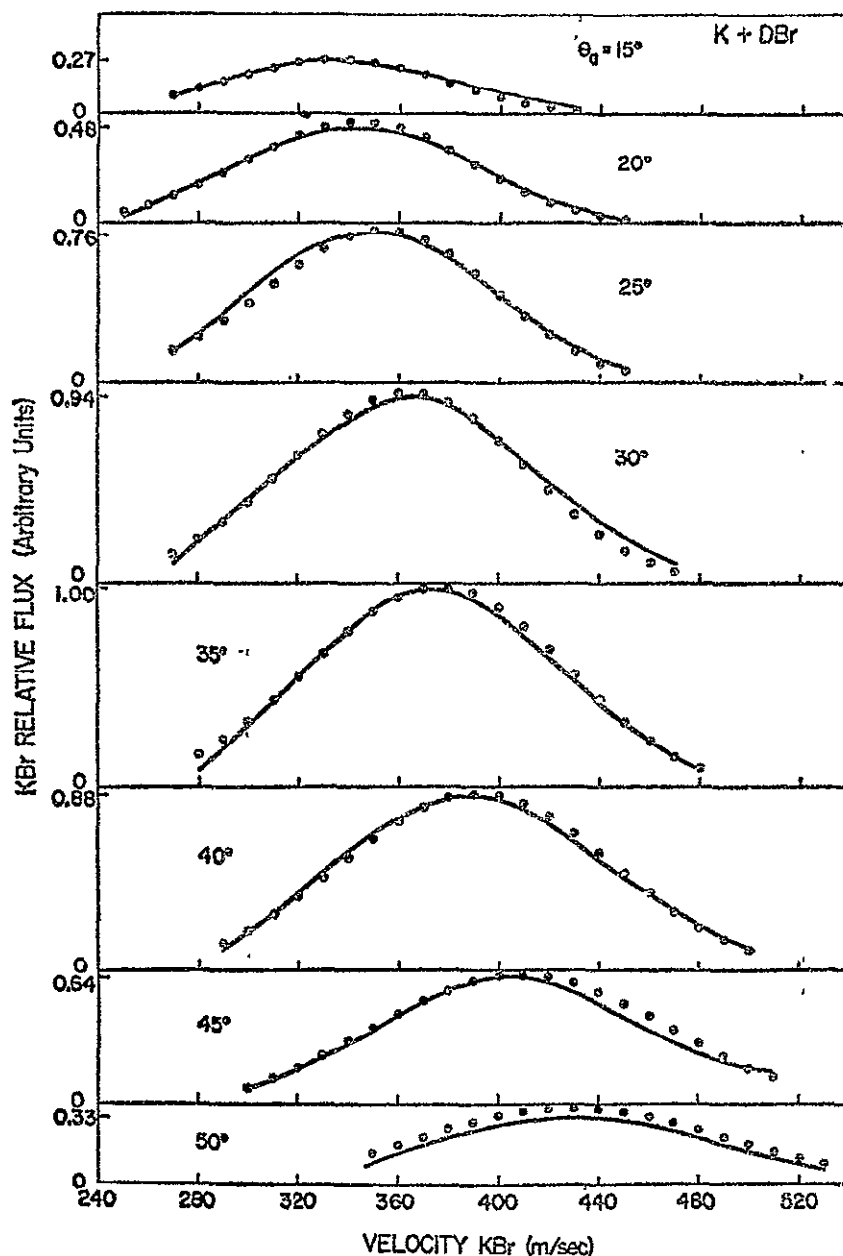


FIG. 14. K+DBr. Similar to Fig. 13.

This number may be compared with the (less precise) ratio of the estimates of total reactive cross sections (based on the optical model analysis of the wide-angle nonreactive scattering), reported by Airey *et al.*⁶: $\sigma^r(\text{K}+\text{HBr}) = 35 \pm 9 \text{ \AA}^2$ and $\sigma^r(\text{K}+\text{DBr}) = 26 \pm 8 \text{ \AA}^2$, which gives the ratio 1.3, with considerable uncertainty.

COMMENTS ON THE REACTIVE SCATTERING RESULTS

The c.m. angular and recoil energy distribution functions are broad. Fundamental kinematic restrictions and an uncertainty in the secondary beam velocity

distribution seem to preclude the possibility of extracting fine details of the distribution functions $P(\omega)$ and $P(w)$ (for example, any coupling between the two distributions). Nevertheless, a "low-resolution," uncoupled [i.e., Eq. (1)] set of functions can be found which reproduces the main features of the data. The choice of functions, fortunately, is nearly independent of assumptions as to the secondary beam distribution. The recoil energy distribution function $P(E')$ (Fig. 12) is similar for both the HBr and DBr reactions and indicates a large range of product internal excitation energies. The angular distribution (Fig. 11) is more forward for K+DBr than for K+HBr; this trend is not consistent (at least in a trivial sense) with the pre-

4030

GILLEN, RILEY, AND BERNSTEIN

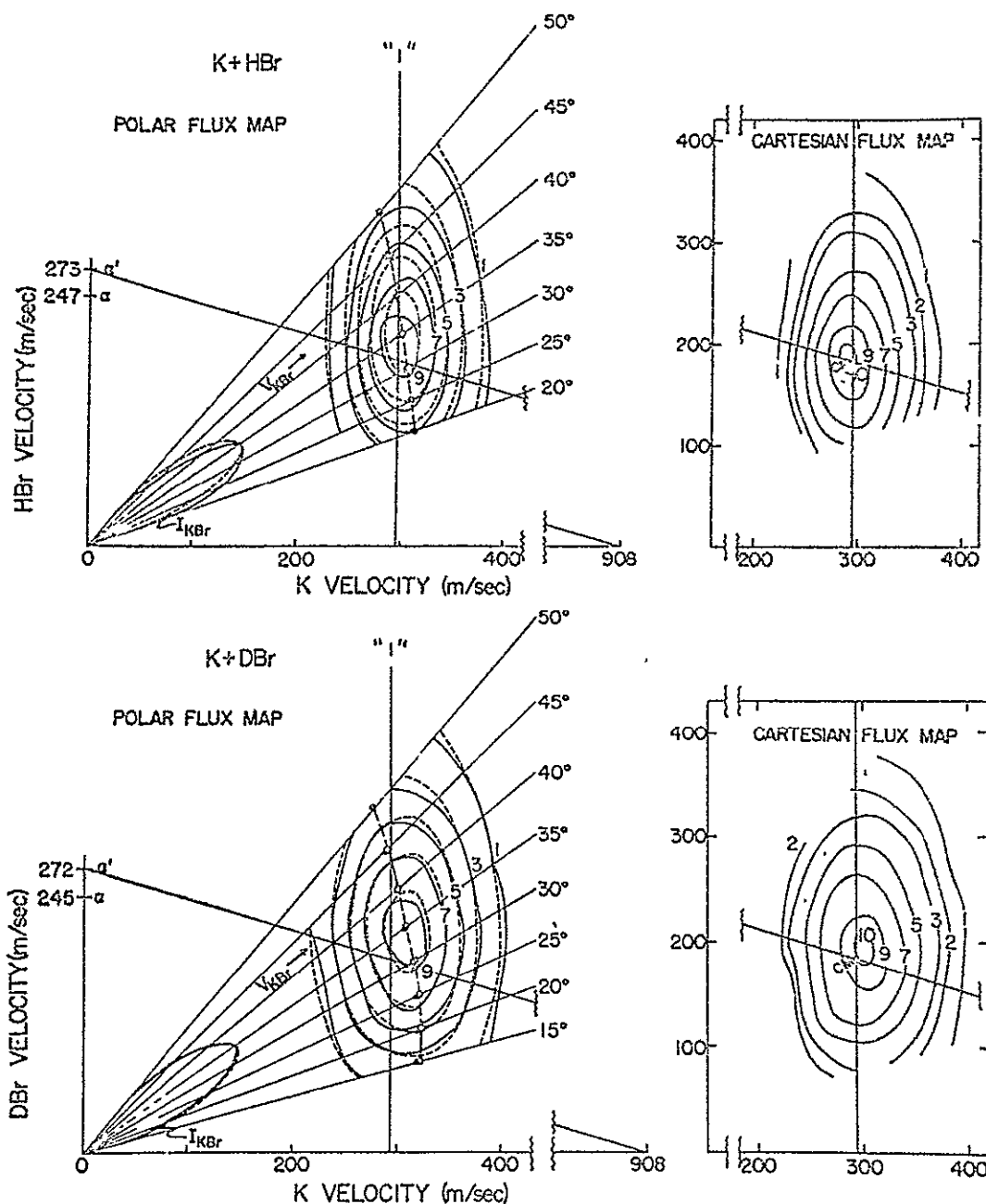


FIG. 15. Left: KBr polar (velocity-angle) flux contour maps for reactions $K+HBr$ and $K+DBr$ at a nominal initial relative kinetic energy of 2.8 kcal/mole. The solid contours are the experimental data.⁵ The dashed contours are the computed curves. At a given angle, experimental flux maxima are denoted by solid triangles (Δ), computed flux maxima by open circles (O) (sometimes overlapping). The open circles are connected by a dashed line. The solid vertical line ("1") is the peak centroid locus. The polar curves $I_{KBr}(\theta_s)$ display peak KBr intensities (cf. Fig. 9). Right: KBr Cartesian flux contour maps of experimental data, derived from polar maps by dividing flux by v_{KBr}^2 . Peak centroid locus lines and nominal relative velocity lines are drawn as at left. The cm points correspond to the nominal triangle with α' and v_{KBr} as at left.

dominantly backward scattering of KBr from the K , $Cs+TBr$ experiments of Martin and Kinsey.³ The larger total reactive scattering cross section for the $K+HBr$ system compared with $K+DBr$ agrees with the deductions of Airey *et al.*⁶ from their phenomenological analysis of the nonreactive scattering. This result is however, not in accord with the usual correlation

found^{2a} to apply for a number of other chemical systems, namely, that a reaction with more "forward" scattering usually has a larger total reactive cross section.

THEORETICAL CONSIDERATIONS

The present paper will not attempt to review or elaborate on the various theoretical treatments which have

been applied to the reactive scattering of alkalis by hydrogen halides.²⁰ Indeed, it seems premature to draw any serious conclusions from these treatments in view of the rapid development of new theoretical-computational methods for dealing with the reactive scattering problem.²¹

Much of the attention in the literature has been devoted to the purely phenomenological description of the scattering²² via the optical model, which is intended to account in a simple way for the elastic scattering in potentially reactive systems. As mentioned earlier, the present study essentially confirms the nonreactive data on K+HBr (DBr) of Airey *et al.*⁶ and the main features of their analysis. Their data and the present results suggest an opacity function $P(b)$ with limiting values (i.e., for very small impact parameters) $P(0) \gtrsim 0.9$ and 0.8 for HBr and DBr, respectively. Their results indicate that the shape of the function can be fairly well approximated by a "rounded" step function characterized by a threshold impact parameter b_{thr} corresponding to a "critical" K-Br separation of about 3.6 Å.

However, as pointed out in Ref. 32(k), because of shape-sensitivity considerations it is very difficult to deduce a unique opacity function even from very reliable data. An even more serious limitation on the optical model interpretation was brought out in Ref. 32(b), where it was shown that the existence of a deep attractive well at small K-Br separations, superimposed on the usual van der Waals (vdW) well at large distances, would also lead to suppression of the wide-angle scattering. This result was obtained using a two-body central force model, involving only a semi-classical analysis of the pure elastic scattering, i.e., no

chemical reaction per se was necessarily introduced by the deep "chemical" well. In many respects the differential elastic scattering expected from the two-well potential resembles that from the vdW well alone; the usual analysis would give an r_m characteristic of the shallow outer well. The effects of the deep inner well might be wrongly interpreted as due to chemical reaction, with significant *apparent* opacity for $b < b_r$, [where $b_r(\theta_r)$ is the rainbow impact parameter for the vdW well].

Thus one must be cautious about prediction of the reactive scattering behavior from the nonreactive scattering data via an optical analysis. However, as pointed out in Ref. 33, the simple model appears reasonably successful for a number of alkali-halogen compound systems (especially for K+CH₃I),^{33b} in that observed total *reactive* cross sections are fairly well predicted by suitable integration over the opacity function $P(b)$ derived from the *nonreactive* data.

Among the many treatments³⁰ of the reactive scattering per se, one of the more promising appears to be that of Eu, Huntington, and Ross.^{30c} They have presented a simple formulation based on the Butler-Tobocman direct interaction theory and applied it to the calculation of orientation-averaged differential reaction cross sections. They treated a number of systems, including those of interest here. A form for the potential energy surface was chosen which contains a step function to represent "bond switching," occurring at a critical M-X separation (chosen to be 3.6 Å for K+BrH). For a collision energy of 1.5 kcal/mole, and considering a *fixed* $Q = -1$ kcal/mole, they calculated the angular distribution for several values of the rotational angular momentum value l for the KBr product ranging from 100-112, with $l = 104$ "preferred" from an analysis^{32a} of the elastic scattering. The resulting angular distributions were broad and somewhat "backward" weighted, but a change of 8% in l sufficed to bring the maximum from the backward to the forward direction. Unfortunately their model does not predict Q or l distributions for isotopic reactions. Thus it is not fully predictive in character, but it may well be helpful in correlating the grosser features of the results for reactions of related systems. At present there appears to be no *ab initio*, theoretical prediction of the differential scattering cross sections and internal excitation function for the systems K+HBr, DBr to compare with the present observations.

ACKNOWLEDGMENTS

The authors appreciate a number of valuable discussions with Professor J. L. Kinsey, Professor E. F. Greene, Professor D. R. Herschbach, and Professor J. Ross. We thank Professor Ross especially for supplying us with the original data from the experiments of Ref. 6. We are also grateful to Mr. A. Rulis, who

²⁰ See, for example: (a) N. C. Blais and D. R. Bunker, *J. Chem. Phys.* **39**, 315 (1963); (b) P. Pechukas, J. C. Light, and C. Rankin, *ibid.* **44**, 794 (1966); (c) J. Lin and J. C. Light, *ibid.* **45**, 2545 (1966); (d) R. E. Olson and C. R. Mueller, in Ph.D. thesis of R. E. Olson, Purdue University, 1967; (e) R. J. Suplinskas and J. Ross, *J. Chem. Phys.* **47**, 321 (1967); (f) J. C. Light, *Discussions Faraday Soc.* **44**, 14 (1967); (g) B. C. Eu, J. H. Huntington, and J. Ross (to be published). Also J. H. Huntington, Ph.D. thesis, Brown University, 1968.

²¹ See, for example: (a) M. Karplus, R. N. Porter, and R. D. Sharma, *J. Chem. Phys.* **43**, 3259 (1965); (b) P. J. Kuntz, E. M. Nemeth, J. C. Polanyi, S. D. Rosner, and C. E. Young, *ibid.* **44**, 1168 (1966); (c) L. M. Raff and M. Karplus, *ibid.* **44**, 1212 (1966); (d) R. A. Marcus, *ibid.* **45**, 2630 (1966); **46**, 959 (1967); *Discussions Faraday Soc.* **44**, 7 (1967); (e) M. Karplus and K. T. Tang, *ibid.* **44**, 56 (1967); (f) M. S. Child, *ibid.* **44**, 68 (1967); (g) E. E. Nikitin, *Chem. Phys. Lett.* **1**, 266 (1967).

²² See, for example: (a) D. Beck, E. F. Greene, and J. Ross, *J. Chem. Phys.* **37**, 2895 (1962); (b) D. R. Herschbach and G. H. Kwei, in *Atomic Collision Processes*, M. R. C. McDowell, Ed. (North-Holland Publ. Co., Amsterdam, 1964), p. 972; (c) E. Hundhausen and H. Pauly, *Z. Physik*, **187**, 305 (1965); (d) R. B. Bernstein, in *Molecular Beams*, J. Ross, Ed., (Interscience Publishers, N.Y., 1966), Chap. 3, p. 75; (e) E. F. Greene, A. L. Moursund, and J. Ross, Ref. 2(b); (f) D. R. Herschbach, Ref. 2(a); (g) J. L. Rosenfeld and J. Ross, *J. Chem. Phys.* **44**, 188 (1966); (h) H. Y. Sun and J. Ross, *ibid.* **46**, 3306 (1967); (i) B. C. Eu and J. Ross, *Discussions Faraday Soc.* **44**, 39 (1967); (j) C. Nyeland and J. Ross, *J. Chem. Phys.* **49**, 843 (1968); (k) R. B. Bernstein and R. D. Levine, Ref. 16; (l) R. D. Levine, *Quantum Mechanics of Molecular Rate Processes* (Oxford University Press, to be published); (m) D. A. Micha, *J. Chem. Phys.* (to be published).

³⁰ (a) J. R. Airey, E. F. Greene, G. P. Reck, and J. Ross, *J. Chem. Phys.* **46**, 3295 (1967); (b) E. F. Greene and J. Ross, *Science* **159**, 587 (1968).

checked a number of the calculations, and to Professor A. E. Grosser, who was involved in the early stages of the experiments.

APPENDIX A: CALIBRATION OF VELOCITY SELECTOR AND VELOCITY ANALYZER

The velocity analyzer was calibrated using a direct, low-temperature potassium beam under Knudsen effusive conditions. The experimental curves of intensity vs analyzer rotational speed are compared to a calculated Maxwell-Boltzmann (M-B) distribution at the K oven temperature. Figure 16 shows a typical result comparing the experimentally determined flux entering the analyzer with an ideal M-B flux distribution, $I \propto v^3 \exp[-(mv^2/2kT)]$. The excellent fit confirms the ideal effusive flow conditions; in this way, absolute velocities can be determined to within 0.6% at the peak of the analyzer transmission triangle. (Of course, the analyzer, has an appreciable transmission width, i.e., FWHM = 4.7%.)

The velocity selector was calibrated similarly; but there is an added difficulty to be noted. Being of lower resolution, the selector has a transmission "triangle" (shown in Fig. 17) which exhibits a significant bias to high velocities (i.e., there is a somewhat greater flux transmitted at velocities greater than the velocity of the peak in the transmission curve than there is at lower velocities). The shift in the K beam calibration curve caused by this bias must, therefore, be accounted for in achieving a correct match to an ideal M-B form. The best estimate of the actual distribution of K transmitted by the velocity selector is given in Fig. 17, here the reduced velocity v^* is defined to be $v/908$ (meters per second). The spreading from the nearly triangular "ideal" function is caused by angular divergence in the potassium beam, due to the well-known dependence of transmission velocity on the angle relative to the selector axis.²⁴ The angular spread in the K beam was determined experimentally by scanning near $\theta_a = 0^\circ$. The change in the selector transmission as a function

of angle through the selector was determined by scanning and comparing the selector transmission with the velocity analyzer transmission for various angular settings (e.g., $\theta_a = 0.0^\circ, +0.5^\circ, -0.5^\circ$) of the K beam. One such scan is shown in Fig. 17 along with a computational simulation. This type of comparison scan indicates the relative consistency of calibration of the selector and analyzer; they agree to better than $\pm 1\%$ in velocity. The velocity of the flux peak of the selector transmission at 908 m/sec, however, is known to $\pm 0.6\%$. The estimated density distribution transmitted (solid curve, Fig. 17, which supersedes the "0," "1," "0" lines of Ref. 5, that were based on the "ideal" transmission triangle) is appreciably broader (18.8% FWHM) than that expected for the "ideal" triangle (14.4%).

It is also important to note that the Laval potassium beam has a significantly narrowed velocity distribution²⁵; if, therefore, the selector is set to transmit a velocity range well below the region of peak intensity of the Laval curve, then the steep variation of flux vs velocity incident upon the selector will cause an enhancement of the high velocity portion of the density transmission function. This suggested operating the selector near the peak of the Laval curve, where this effect was small and readily accounted for in the calibrations, and also where the transmitted intensity was nearly a maximum.

APPENDIX B: COMMENT ON ELASTIC VELOCITY ANALYSIS

In Ref. 4, velocity analyses of the nonreactively scattered ("elastic") K were made at 5° laboratory intervals from $\theta_a = 5^\circ$ to 40° . At all but one of the angles the positions of the peaks of these scans were within $\approx 1\%$ of the velocities predicted for elastic scattering using the nominal vector triangle (Fig. 4 of Ref. 4). The exception was at $\theta_a = 25^\circ$, where three separate experiments gave peaks in the intensity of the scattered K at a velocity some 5% lower than that

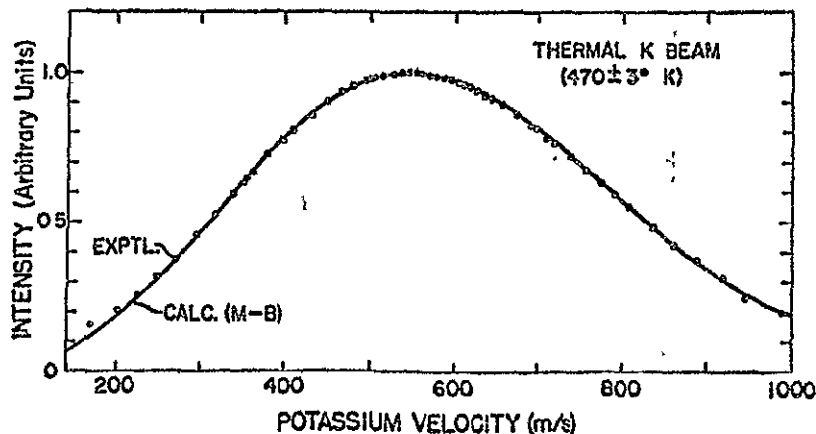


FIG. 16 Calibration of a thermal K beam with the high-resolution velocity analyzer. The calculated, ideal M-B curve is shown superimposed upon the experimental points.

²⁴ M. Ackerman, E. F. Greene, A. L. Moursund, and J. Ross, *J. Chem. Phys.* 41, 1183 (1964); see Appendix IV.

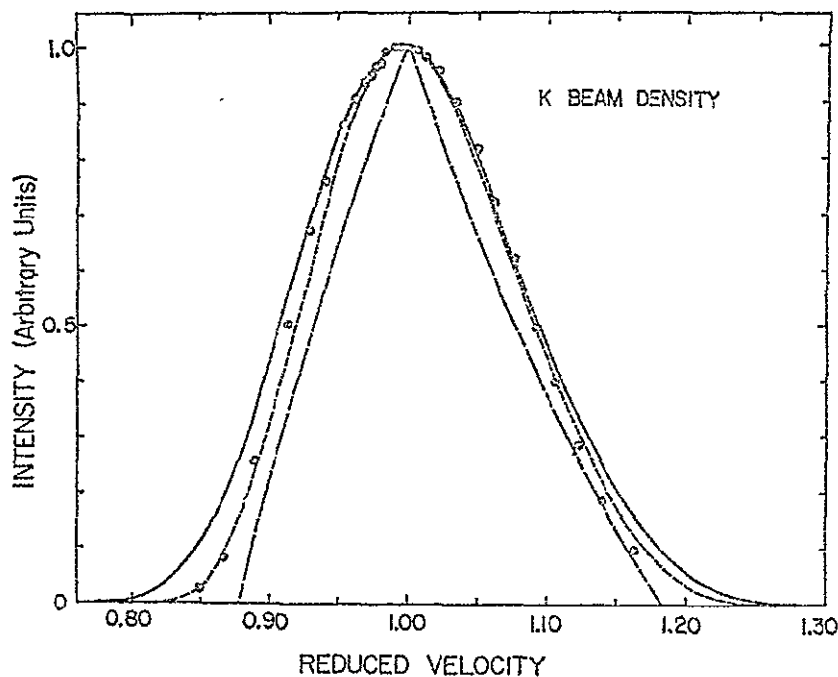


FIG 17. Density distribution in the K beam vs reduced velocity $v^* = v/908$ (m/sec). The dot-dash curve (— · — · —) is the near-triangular ideal selector transmission function, assuming negligible angular divergence in the beam. The solid curve is the best estimate of the actual beam distribution, taking account of angle spread. The points are the experimental density distribution through the low-resolution selector as seen by the high-resolution analyzer, and the dashed curve is a computed curve intended as a theoretical simulation of these observations.

predicted. This anomaly can now be explained on the basis of the steep slope of the angular distribution at the edge of the rainbow and the significant range in incident relative energy. The selector used in the earlier experiments had a velocity FWHM of 4.7%, and hence an energy FWHM of $\sim 9\%$; the secondary beam causes an even greater spread in the energy range for collisions. Since the rainbow "edge" shows an inverse relationship between incident energy and angle (hence the use of the reduced variable $E\theta_{c.m.}$ in Fig 8),¹³ it follows that at a given angle the elastic scattering will show a strong energy dependence (greatest in regions of large logarithmic derivative of the elastic scattering curve). The size of the effect is enough to explain the observed 5% peak shift, and also accounts for significantly greater shifts in elastic scattering results found (but not reported) in the course of the present study with a selector of lower resolution.

APPENDIX C: COMMENT ON IMPROVING THE COMPUTER ANALYSIS

Velocities for the KBr flux contours in this study are secure to better than 1% (see Appendix A); thus, these data are extremely accurate relative to other reported velocity analysis results, yet the kinematic difficulties still prevent the use of much detail in the c.m. functional fits. Were it not for the fact that the K+HBr system is kinematically very unfavorable, many of the assumptions used in the analysis could have been removed by taking advantage of improvements in data analysis and computational techniques

now being used both at Wisconsin²⁶ and at Harvard.²⁶ For this system, however, the kinematic difficulties preclude even the obvious extension to relatively more complex [but still "uncoupled," as in Eq (1)] c.m. functions. For example, based on knowledge of the TBr results,³ a sharp backward c.m. peak in the angular distribution can be added to a fairly isotropic angular distribution, and, as long as the sharp peak does not become too intense, one can obtain a fairly good fit to the HBr data. This method of "educated guessing" is too subjective and cannot, of course, be applied generally.

A better extension of the analysis would involve no assumption of functional form and no guessing of trial functions. The computer should be free to find a general best representation, for instance, by minimizing a least squares fit to the data using general functional forms (e.g., orthogonal polynomials, or histograms) for the c.m. angular and recoil energy distributions. These extensions have been made,²⁶ and a least-squares polynomial analysis of the K+HBr (DBr) system has even been carried out in the general case²⁶ in which the angular and energy functions are allowed to be coupled. The method, unfortunately, is better than the data warrant, the results are dependent on assumptions as to the (unknown) secondary beam distribution, and are perhaps of questionable value. The application of these methods to kinematically more favorable reactive systems is in progress.^{26,26}

²⁶ K. T. Gillen and R. B. Bernstein (unpublished work).

²⁶ P. Siska and D. R. Herschbach (private communication).

C. After-Thoughts

There are a couple of reasons to suspect that the use of the modified (ESS) velocity distribution for the secondary beam was unnecessary, and that an assumption of a simple Maxwellian velocity distribution was reasonable. First, the necessary narrowing of the calculated angular distribution in Fig. 9 (p.4026) can be accomplished without losing the good fit to the velocity distributions if one generalizes to a "coupled" (angle-velocity) c.m. distribution function⁵⁷.

Secondly, test calculations have since been made on assumed c.m. distributions which show that the nominal relative velocity vector (collision axis) around which there is an approximate symmetry in the c.m. system is the one defined by the average velocity in both beams (rather than the most probable velocities, v_{mp}). For HBr (DBr) under the standardized experimental conditions of the paper $\bar{v} = \left(\frac{8}{\pi} \frac{kT}{m} \right)^{1/2} = 279$ (277) m/sec. The Cartesian flux maps^{40e} of Fig. 15 allow a test of this symmetry condition⁵⁸; if \bar{v} of the secondary beam is used (instead of v_{mp}) to define the collision axis, the symmetry is satisfied approximately for HBr, but not very well for DBr (see Figure III-1). Perhaps the experimental "peak ratio curves" (Fig. 4 of paper IIIB) for K + DBr were done at slightly too high a flow, causing a small deviation from ideal M-B conditions (but smaller than the ESS model used); yet the K + HBr experiments appear to have a reasonably ideal secondary beam velocity distribution. It must be noted once again that the assumption

Fig. III-1 K + HBr, DBr Cartesian Flux Distributions

Enlarged view of cartesian data flux maps of Fig. 15 of Ref. 42 (section III B). The "nominal" relative velocity vector has been shifted slightly to correspond to the average (rather than most probable) velocity in both beams (assuming a Maxwellian velocity distribution for the secondary beam).

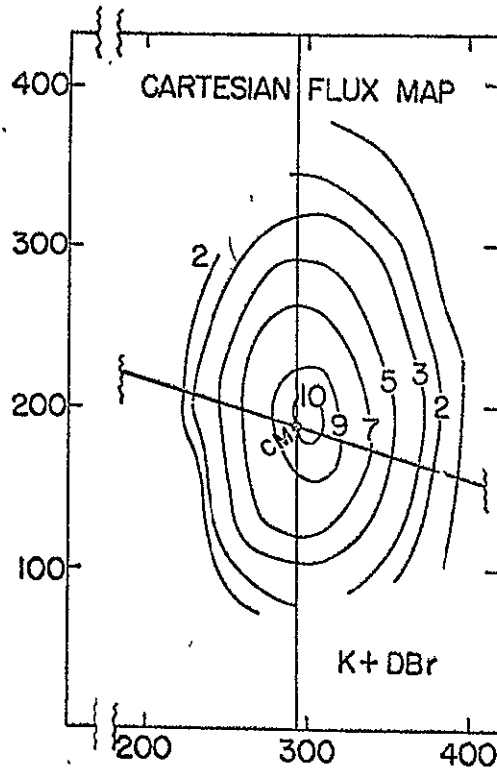
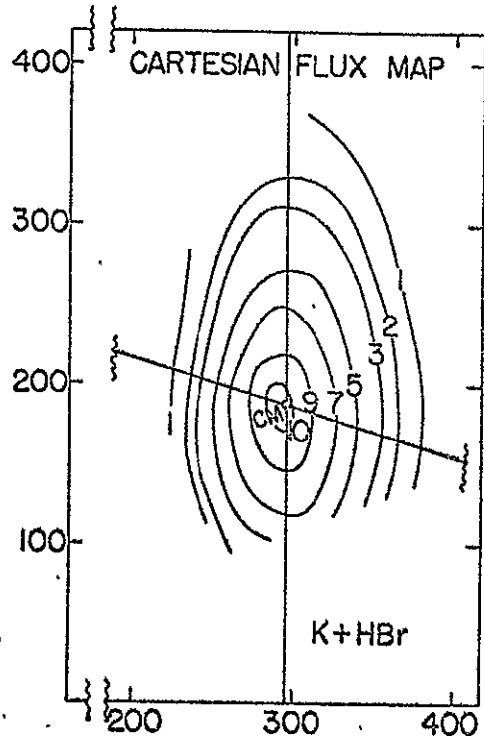


Fig. III-1

(used in the paper) of non-ideal flow for the secondary beam hardly influences the final best uncoupled c.m. distribution found (Figs. 11,12); this assumption was only used in an attempt to get a better fit of the computations to the experimental data. Coupling of the angle and velocity distributions may be a better approach to improving the match to the data.

IV. K + I₂

A. Apparatus Modifications for K + I₂ Experiments

Table IV-1 lists some important apparatus dimensions for the K + I₂ experiments; it is the analogue of Table I in Chapter III (p. 402C). The full heights are all unchanged and are therefore not listed in Table IV-1; the dimensions which have changed since the K + HBr, DBr work are underlined in the table. All widths are "full-widths".

With the mechanical modulator the angular range possible in the laboratory was only from $\Theta \sim 0^\circ$ to 49.5° (where $0^\circ \cong$ K beam direction; $90^\circ \cong$ I₂ beam direction); using the tuning fork chopper, $\Theta_{\text{lab}} = 101^\circ$ was obtained; a simultaneous slight alteration of the chopper support and the last collimation slit for the I₂ beam (as noted in Table IV-1) allowed the possibility of reaching $\Theta = -15^\circ$.

The collimating slits were generally wider than for K + HBr, DBr; in this way intensity was increased with only a small sacrifice in resolution. The lower resolution is unimportant here since the kinematics of the K + I₂ system are so favorable; this decreases the laboratory resolution requirements necessary for obtaining meaningful c.m. results. Figures IV-1,2,3,4 show the slit geometries and beam profiles. The ideal limit of the umbra is marked by line "u"; the extent of the penumbra is denoted by line "p"; "h" is the half-intensity line. Note that in every case the vertical and horizontal scales are not the same. As in the earlier work, all meaningful angular distributions were done with a wider analyzer entrance slit in order to eliminate the possibility

Table IV-1 K + I₂ Apparatus Geometry
(all dimensions in cm)ⁱ

	Primary Beam (K)	Secondary Beam (I ₂)	
s	0.015	<u>0.076(0.015)</u> ^{iv}	
c _I	0.40	<u>0.51(0.254)</u>	
c _{II}	<u>0.127</u>	0.152	All heights same as
a	0.127(<u>0.51</u>) ⁱⁱ		for K + HBr, DBr;
d	0.071		See Chapter III B,
l _{scI}	1.0	0.6	Table I.
l _{scII}	5.5	(3.7), <u>3.1</u> ⁱⁱⁱ	
l _{st}	8.6	4.4	
l _{ta}	3.7		Maximum Angular Divergence of
l _{td}	25.3		Secondary Beam (in-plane) =
			<u>(± 1.8), ± 2.1</u> ⁱⁱⁱ

- (i) When two numbers are given, the one in parenthesis denotes the less common configuration. The underlined numbers are the only changes from the K + HBr, DBr experiments.
- (ii) Angular normalizations and total angular distributions used a wider analyzer entrance slit in order to view the entire scattering zone at all angles and eliminate any viewing factors.
- (iii) The "new" support piece for the tuning fork chopper had a collimating slit slightly closer to the I₂ oven than the old piece used with the mechanical modulator.
- (iv) A few early experiments used a set of Laval slits on the I₂ beam oven with results hardly distinguishable from the experiments which used Zacharias foil slits.

Figs. IV - 1,2,3,4 Slit Geometry

Details of the slit collimation for the two beams (subscript 1, K; subscript 2, I_2) and for the detector. All dimensions in cm. In all figures the vertical and horizontal scales are different.

S: oven slit
 c: collimator slit
 a: analyzer entrance slit
 d: detector
 S.C.: scattering center
 u: ideal beam umbra limit
 h: ideal beam "half intensity"
 p: ideal beam penumbra limit

} Primes refer to beam heights

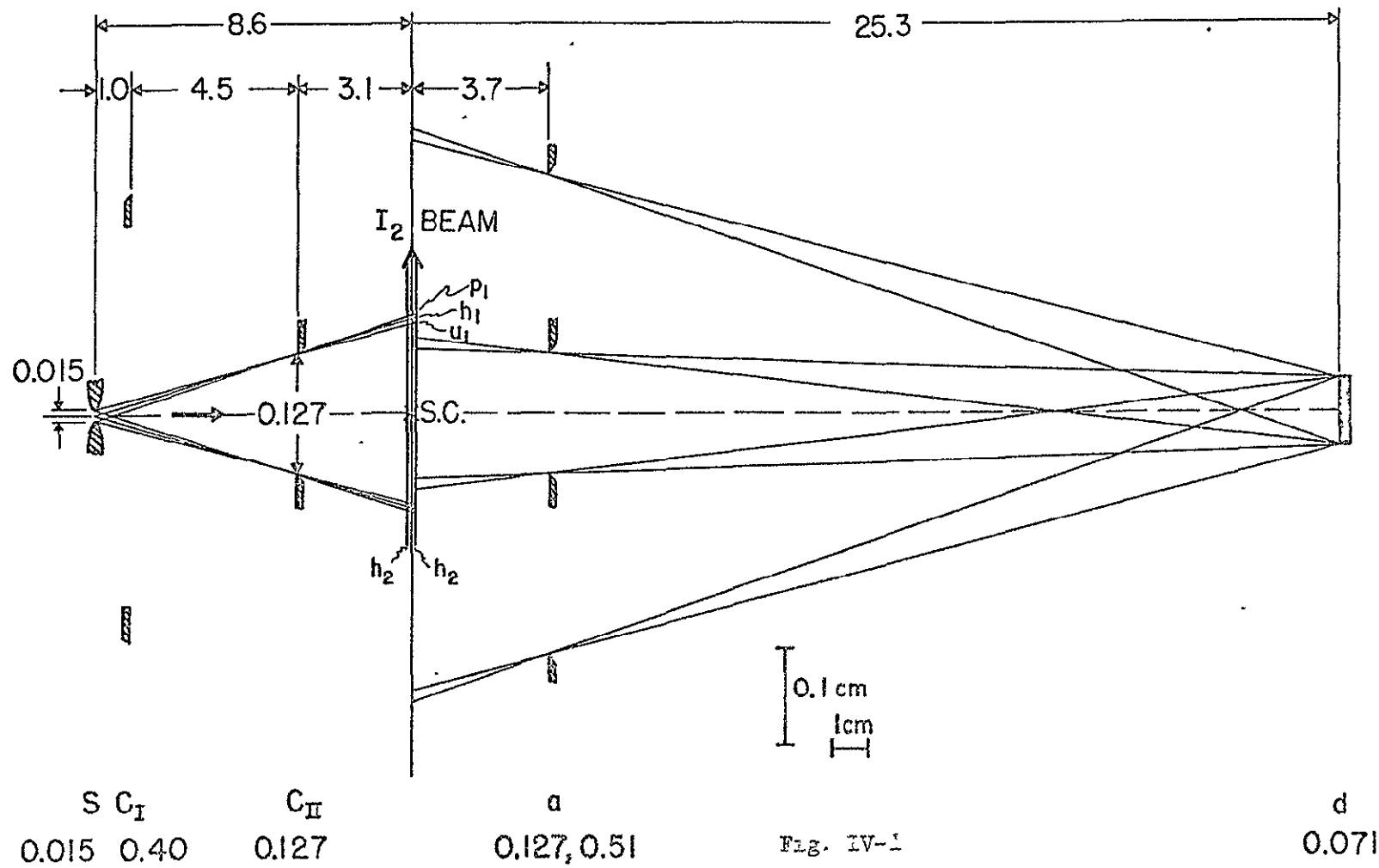
Alternate positions of slits are indicated with dashed outlines referring to the alternative arrangement, less frequently employed.

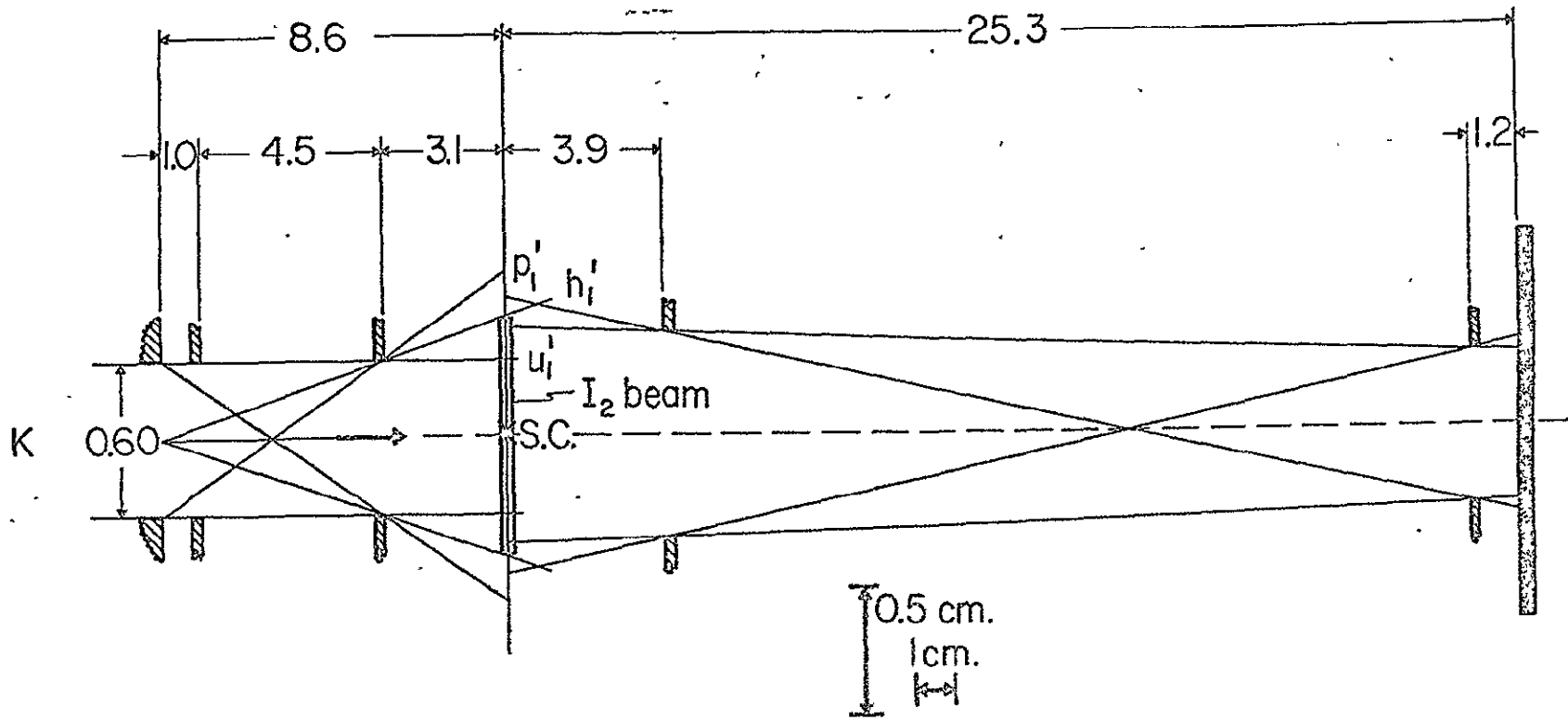
Figure IV -1 K beam and detector widths.

Figure IV-2 K beam and detector heights.

Figure IV-3 I_2 beam width.

Figure IV-4 I_2 beam height.





S	C_I	C_{II}	a	d
0.60	0.60	0.60	0.80	0.60

Fig. IV-2

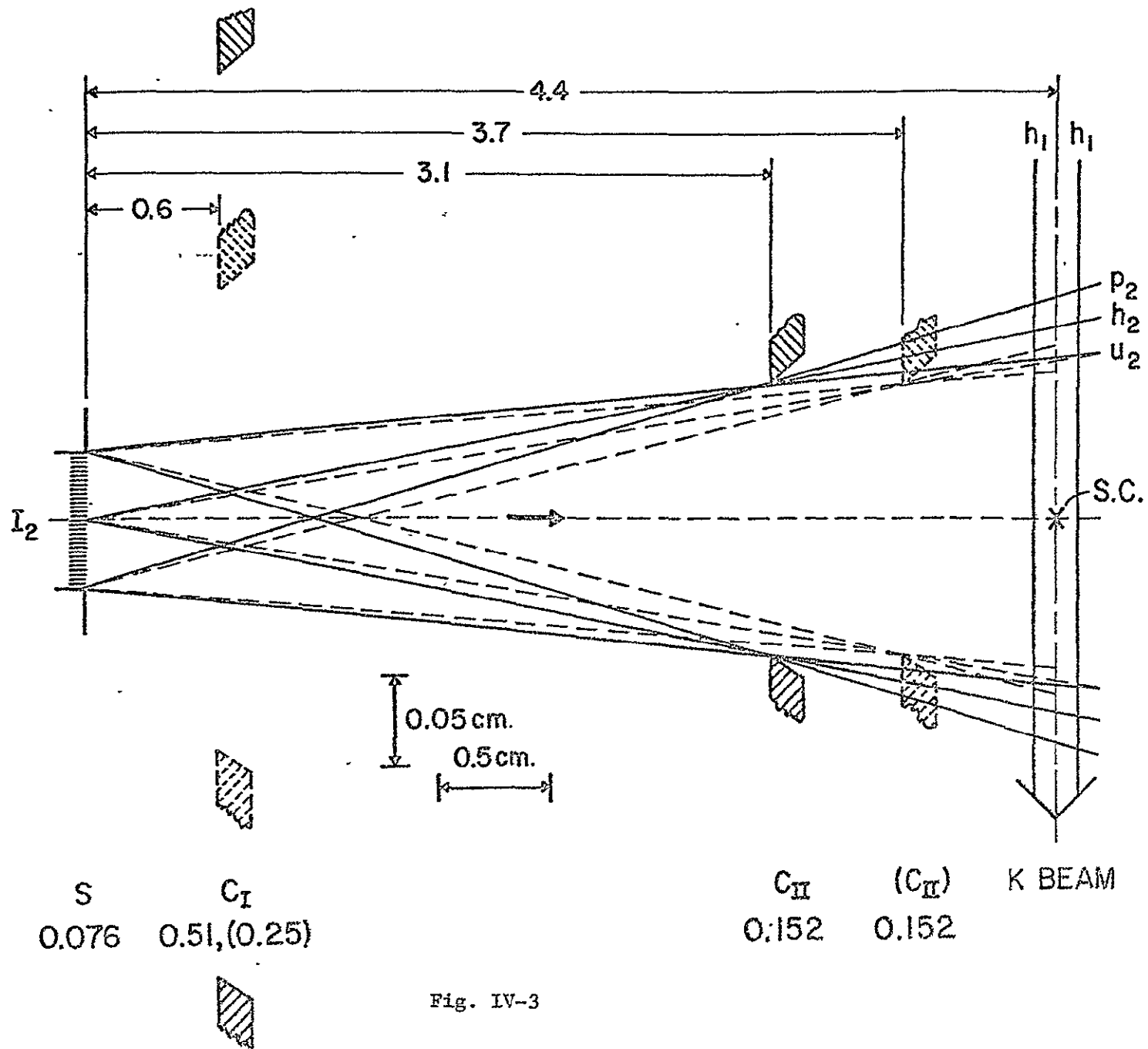
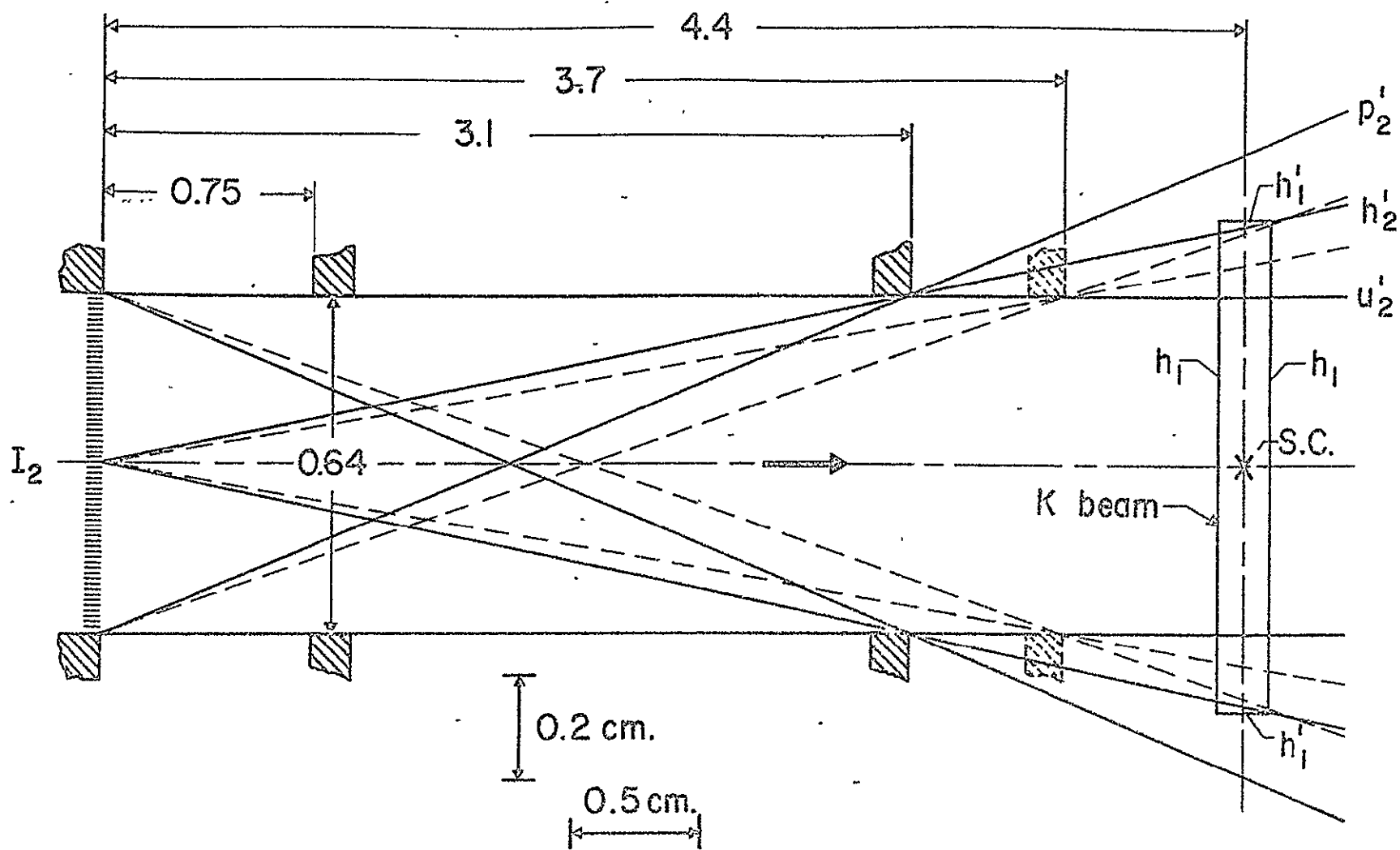


Fig. IV-3



S	C_I	C_{II}	(C_{II})
0.64	0.64	0.64	0.64

Fig. IV-4.

that the scattering volume viewed was dependent upon the apparatus angle. Velocity analyses (unreported) with the wider analyzer slit had slightly broadened velocity distributions relative to the ones reported here (section IV-C). This is due to the larger angular range through the analyzer, which causes a broadening in the velocity distribution transmitted at a given rotation speed. (The dependence of the transmission on the angle through the analyzer can be calculated using the general transmission equation (A-1) of Appendix A.)

Iodine, unlike HBr, has too low a vapor pressure to be introduced conveniently as a gas; hence a reservoir interior to the apparatus had to be used. The differential pumping of the secondary beam chamber was also eliminated and replaced with more cryogenic surfaces near the beam oven.

The tungsten wire beam monitor for the K beam was installed specifically for the purpose of monitoring the variation in the K flux entering the scattering zone during the course of studies of the dependence of scattering on the relative incident kinetic energy, \bar{E} ; however, even in experiments done at a constant \bar{E} , the W wire proved to be a valuable monitor of beam stability.

The last modification to be noted, both unplanned and unpleasant, was a gradual thinning of the disk and widening of the slots of the selector disk closest to the K oven. This was caused by the large amount of K deposited on this disk during the course of the Laval K beam experiments, followed by hydrolysis and attack upon the aluminum during cleanup of the apparatus. At the end of the I_2 experiments (three years after the first Laval K beam with HBr) the slots on

this disk were $\sim 20\%$ wider than their original dimension. This leads to a slightly wider velocity distribution transmitted through the selector; it is not at present serious and has been accounted for in the beam calibrations of Appendix A; but eventually this disk will have to be replaced.

IV. K + I₂B. Experimental Procedure

Before each experiment the bearings for the selector and analyzer motors were cleaned with benzene, lubricated with pump oil (Dow-Corning 704), and if necessary, discarded and replaced; these bearings caused the premature end of a large number of experiments; the selector and analyzer bearings, in contrast, lasted almost indefinitely.

The night before an experiment the two ovens were loaded. The primary oven was first filled with benzene; pieces of K were cut under benzene and placed in the oven, which was then screwed shut (lapped surfaces, no gasket) and inserted into the apparatus. With the two ovens in place (typical loads: ~ 14 grams of K, ~ 45g of I₂), the machine was pumped down overnight (to ca. 25 μ) with the roughing pumps.

Early the next morning the diffusion pumps were turned on and the potassium oven was gradually heated to beam conditions (typical conditions: oven ~ 620^oK, slit ~ 710^oK, reached after ~ 7 hours of heating; ~ 140 watts of power required to maintain temperature at operating conditions). Meanwhile, as soon as the liquid nitrogen traps could be filled, the outgassing of the Pt-W detector was commenced (usually for 3-4 hours at temperatures up to 1700^oK). At 1700^oK the positive ion emission from the filament is typically 10⁻¹² amps; the A.C. noise produced on the chart is equivalent to ~ 10⁻¹⁵ amps at 25Hz, ten times the equivalent noise at the sensitized operating conditions. While bringing the K oven up to its operating temperature, the selector was rotated at a slow speed (~2000rpm) to insure uniform

deposition of K on the first selector disk; the selector was not allowed to come to a complete stop for the duration of the experiment (to avoid the possibility of unbalancing it).

While the K oven temperature was stabilizing, the I_2 oven was rapidly brought up to beam conditions (oven $\sim 310^\circ\text{K}$, slit $\sim 350^\circ\text{K}$; <20 watts power to maintain conditions). If the plans called for no "unsensitized" experiments, the oxygen filament "sensitization" procedure was followed (see II B7) and a small O_2 leak established (the early outgassing is sufficient to cause an unsensitized filament).

The analyzer was lowered out of the beam path, the goniometer set to a convenient apparatus angle (e.g., $\textcircled{H} = +20.0^\circ$), the selector was brought up to operating speed (e.g., 15000 rpm) and the signal: noise ratio displayed on the chart recorder. This ratio was maximized by adjusting lock-in phase, filament bias, grid voltage, and electron multiplier voltage.

The experimental angular distributions and KI angular normalizations were all done with frequent checks of a reference angle to monitor and adjust for changes in flow conditions; all signals were taken relative to a zero defined by placing a beam flag in front of the I_2 oven.

The great majority of the velocity analyses were done as "translational spectra" (see IV C.2). Beam flag zeros were not used, since a few supplementary velocity analyses taken "point-by-point" agreed exceedingly well with the corresponding spectra whether electronic or beam flag zeroes were used. Other verification came from the results of a number of ghost "spectra" taken with the beam flag blocking the I_2 beam (in principle, no modulated alkali signal); these "spectra" were identical

in shape to the corresponding "unblocked" spectra, but of much lower intensity (the remaining signal was undoubtedly from I_2 that successfully bypassed the beam obstacle, reaching the modulator by deceitful and devious routes).

During the course of an experiment the chamber pressures and oven temperatures were periodically recorded. In sensitized experiments, occasional total angular distributions were done as a monitor for any decay in sensitivity to KI. Increases in the O_2 leak rate sometimes successfully counteracted losses in sensitization; otherwise the normal sensitization procedure was repeated after a fast outgassing (~ 10 minutes) of the filament at 1.4 amps. The detector chamber pressure was usually $5-10 \times 10^{-7}$ Torr with an O_2 leak for sensitization; unsensitized, the pressure was $\sim 1-3 \times 10^{-7}$; the main chamber pressure during an I_2 experiment was typically 2×10^{-6} (uncorrected ion gauge).

At the end of an experiment, calibrations of the direct K beam (e.g., Laval beam characterizations, angular profiles) were done; the Pt/W filament was biased at -22.5v; the grid was set at -90v to collect the K^+ ions (with the electron multiplier turned off) which were then fed directly to a Keithley electrometer. The current from the peak of a velocity selected K beam was $\sim 2 \times 10^{-7}$ amps. These calibrations were always done at the end of an experiment, since deposition from an intense K beam caused a large increase in filament noise; direct beam must not be allowed to strike the filament during the course of a scattering experiment. When turning the goniometer through 0° (the K beam direction) the analyzer was always in the blocking position, "up."

At the end of an experiment, the I_2 oven was heated to $\sim 500^\circ\text{K}$ to remove any remaining I_2 , the rotary pumps were valved shut as soon as the diffusion pumps cooled sufficiently, and one large, easily removable liquid nitrogen trap was kept filled for ~ 12 hours (using an ICC Cryogenics Inc. Model 100L LN_2 Cryotrol). Most of the I_2 distilled over to this trap, which could be removed while still cold after opening the apparatus to dry nitrogen. The K oven was removed along with many of the K-covered trapping surfaces. Potassium was destroyed with copious amounts of t-butyl alcohol and ethanol, followed by H_2O . Occasionally, alcohol fires were avoided.

IV. K + I₂C. Data

The experimental data for $K + I_2^*$ fit into five general categories: total angular distributions, velocity analyses, angular normalizations at a specific product velocity, incident energy dependence experiments, and K beam characterizations. The K beam characterization work is detailed in Appendix A; all scattering results are presented in this section.

1. Total angular distributions

Figures IV-5,6,7 show the primary data at three different relative initial kinetic energies^{**} \bar{E} for the total angular distributions (analyzer lowered out of the beam) of the detected scattered signals. The "unsensitized" curves (U) and "sensitized" curves (S) can be normalized at low angles where essentially all of the scattering is due to elastically scattered K. The sensitized filament detects both K and KI with high efficiency; but as will be noted later, the "unsensitized" filament detects an appreciable (and variable) fraction of the reactively scattered KI; at large angles this yields a much larger (U) signal intensity than that due to K alone. An alternative method of scaling of the pairs of S and U curves is to use the velocity analysis data

* A. M. Rulis (p. 18) ably assisted in the execution of these experiments.

** The nominal energy \bar{E} is calculated from a relative velocity based on the average velocity in the K beam flux distribution and the average velocity in the I₂ beam density distribution. See Footnote 28 in Reference 42 and Section III C.

Figs. IV-5,6,7 $K + I_2$ Laboratory Angular Distributions

Angular distributions of scattered flux in the laboratory at three different values of \bar{E} . Open symbols: sensitized filament; closed symbols: unsensitized filament. The three data sets are consistently scaled to each other (for the same incident K beam flux); but the overall normalization is arbitrary.

Figure IV-5 $\bar{E} = 1.87$ kcal/mole

Figure IV-6 2.67

Figure IV-7 3.62

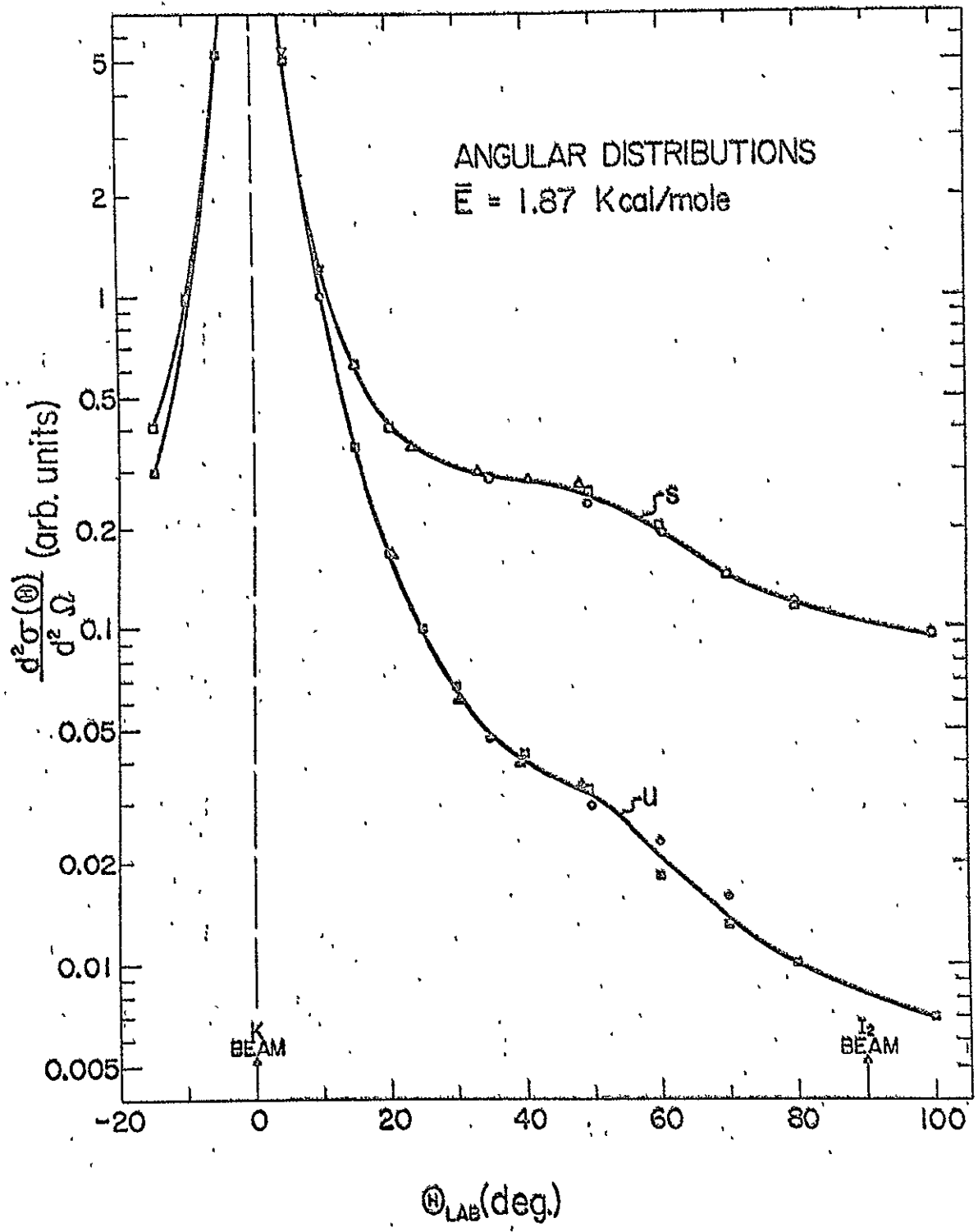


Fig. IV-5

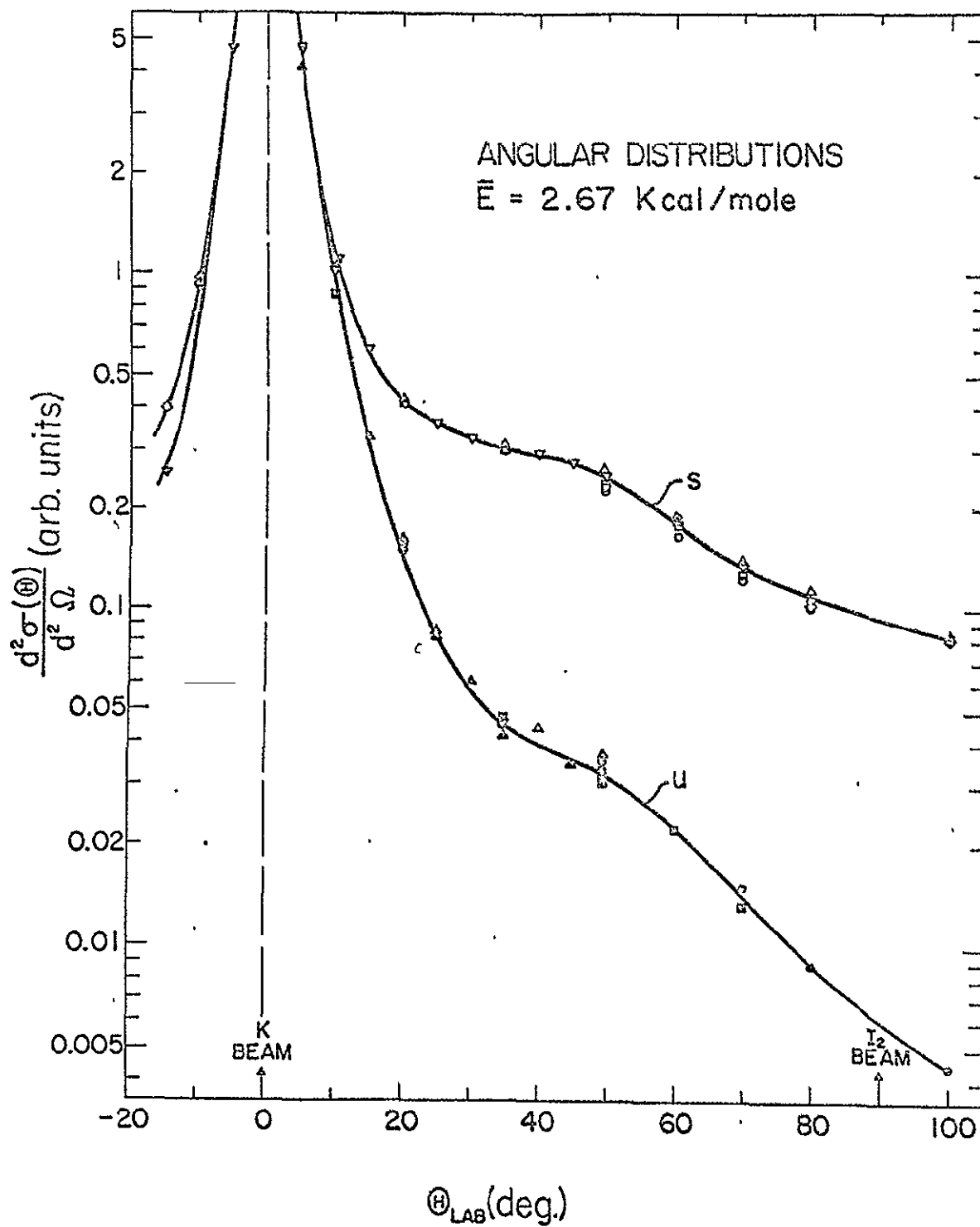


Fig. IV-6

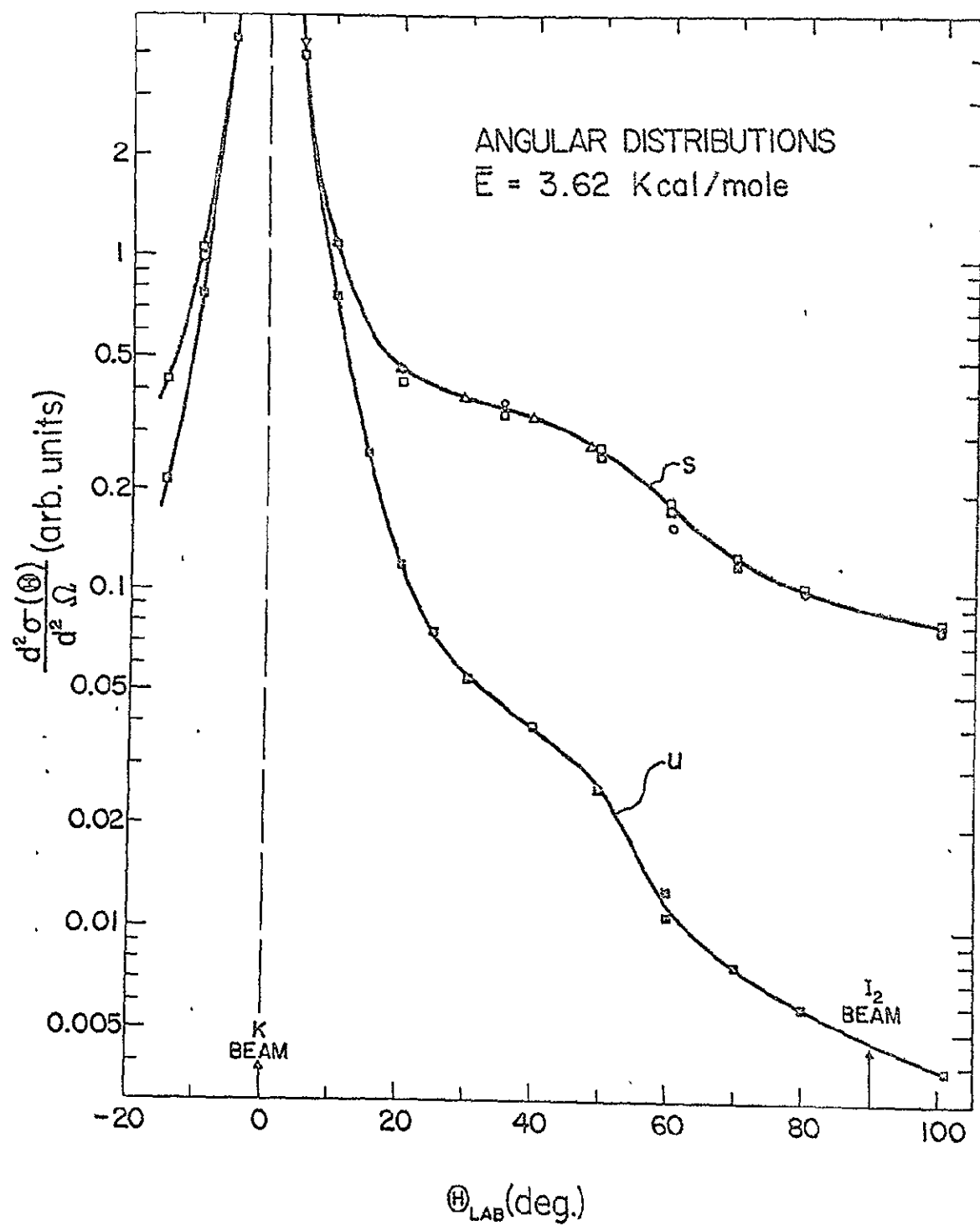


Fig. IV-7

(Sec. IV C2) to find the relative amounts of K and KI at a specified laboratory angle and adjust the angular distributions to be consistent with that finding; the velocity analyses at $\Theta = 10^\circ$ have been used to normalize the curves in this way.

Additional small angle data have been obtained in this same energy range. By monitoring the K beam intensity at the various energies, it has been possible to normalize the distributions at different \bar{E} to each other. This has been done in Figures IV-5,6,7. Much of the low-angle data is not shown here but will appear in a later section after a transformation to the c.m. Most of the angular distribution measurements (Sec. IV C 3 also) were done with a large analyzer entrance slit which viewed the entire scattering center and eliminated the necessity of correcting for an angle-dependent viewing factor; a couple of the total angular distribution curves were obtained with a smaller slit and had to be so corrected.

2. Velocity Analyses

The "translational spectrum" method was developed to handle the large number of velocity analyses anticipated in the K + I₂ experiments. The analyzer is turned at a high rotation speed (typically > 18000 rpm) which corresponds to a transmitted beam velocity ($v' > 1100$ m/sec) at or near the thermodynamic limit for reactively scattered KI (which also is at or near and sometimes beyond the stress limit of the analyzer motor bearings); it is then allowed, at reduced power, to coast gradually to a stop while the signal intensity and rotation speed are dynamically recorded. A

reference intensity taken before and after the spectrum allows one to correct for variations in beam intensities (usually $<10\%$ during the spectrum). Fig. IV-8 shows chart recordings of three "typical" sensitized spectra taken at $\bar{E} = 2.67$ kcal/mole. The time for one complete velocity analysis (0-1100 m/sec) using this technique is usually less than 15 minutes (reference-spectrum-reference). In analyzing the chart recordings, lines which smooth out the filament noise⁵⁹ are drawn through the spectrum and then the intensity is recorded for nearly uniformly spaced rotation speeds (sometimes certain regions of the spectrum are emphasized by scanning the region slower, by scanning the region more than once, or by closer spacing of the points chosen). Each intensity is then divided by the corresponding velocity to account for the usual velocity-dependent transmission of the analyzer (see Appendix A), yielding the velocity distribution of laboratory product flux at the particular apparatus angle. All of the $K + I_2$ velocity analysis flux distribution data (each spectrum normalized arbitrarily to unity at its peak) are shown in Figures IV-9 to IV-16; there are up to six spectra at a particular experimental condition. Large symbols represent expanded scales for data of low relative intensity. The spectra at large Θ are of lowest quality because the signal levels are the smallest (see 3. Angular Normalizations).

Nearly all of these velocity analyses were done as spectra; three exceptions, all sensitized and at $\bar{E} = 2.67$ kcal/mole (Θ at $20^\circ, 49.5^\circ$, Ξ at 35°), were done "point-by-point". This involved

Fig. IV-8 Chart Recordings of Experimental Velocity Analyses.

Shown are three velocity analysis spectra for the $K+I_2$ experiments, all at $\bar{E} = 2.67$ kcal/mole. For the lower two ($\theta = 25^\circ$, $\theta = 30^\circ$) the detector was fully sensitized to KI. For the upper one ($\theta = 25^\circ$) the detector was 70% sensitive to KI (see section IV D2). Variations in beam intensity during the course of a spectrum were accounted for by checking the intensity at a reference velocity before and after recording the spectrum; linear interpolation of these reference signals (and the corresponding velocity on the spectrum itself) served as a monitor for correction (REF.). Arrows mark the start of the spectra; several velocities are indicated for each spectrum. The zero line is marked by Z. The time required for the velocity analyzer to coast to a stop (at reduced power) was approximately seven minutes. The noise is from the detector and does not represent any resolved fine-structure in the curves (compare the two spectra at $\theta = 25.0^\circ$).

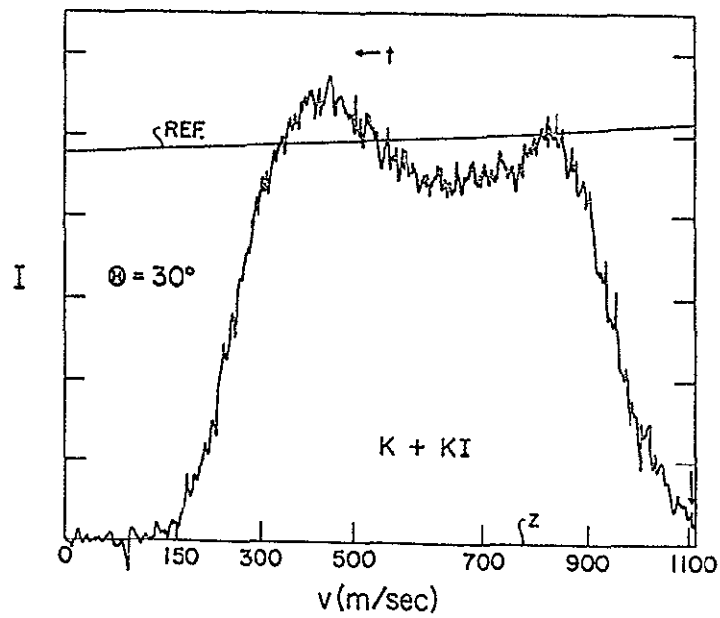
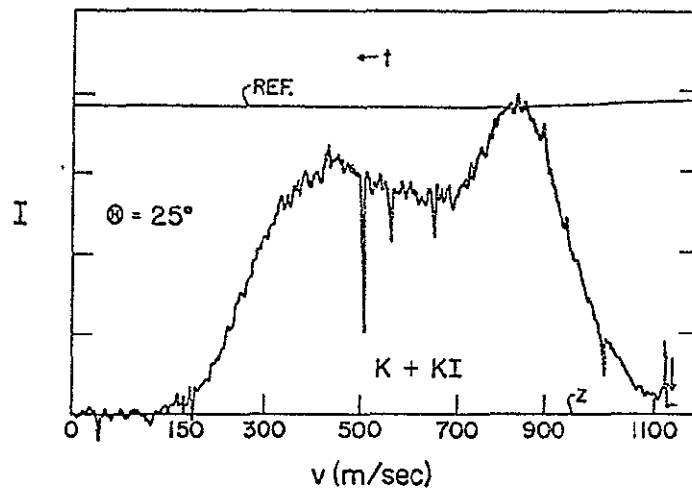
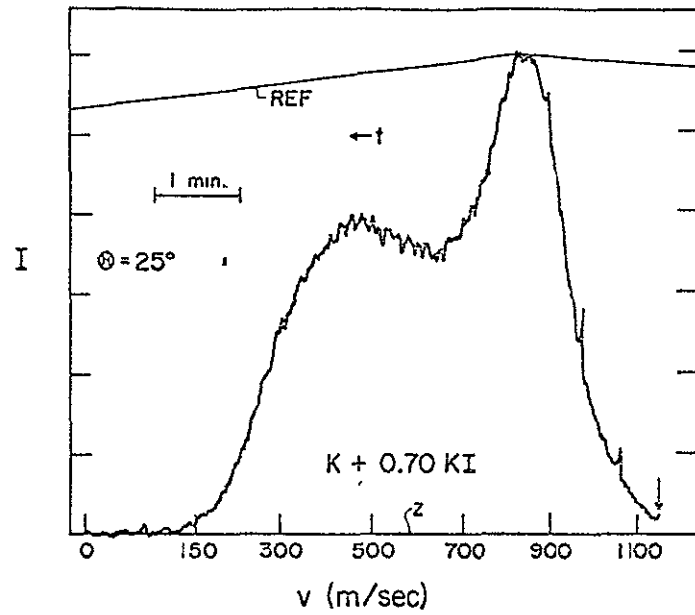


Fig. IV-8

Figs. IV-9,10 $K + I_2$ Velocity Analyses, $\bar{E} = 1.87$ kcal/mole

Velocity analysis data at 1.87 kcal/mole grouped by angle and filament condition (sensitized or unsensitized). Plotted is laboratory flux (chart intensity divided by velocity, to account for velocity-bandwidth of analyzer: $\Delta v \propto v^2$) vs. velocity; multiple sets of experiments at the same conditions are indicated by different symbols for the data points. Each curve is scaled to approximately unity at the peak. Some of the data sets have regions of low relative intensity which have been expanded for better viewing. The expanded regions are plotted with the same type, but larger, symbols. An arrow on each data set indicates the "nominal" velocity of elastically scattered K, calculated assuming a single velocity (the peak in the velocity distribution) for the K and the I_2 beams.

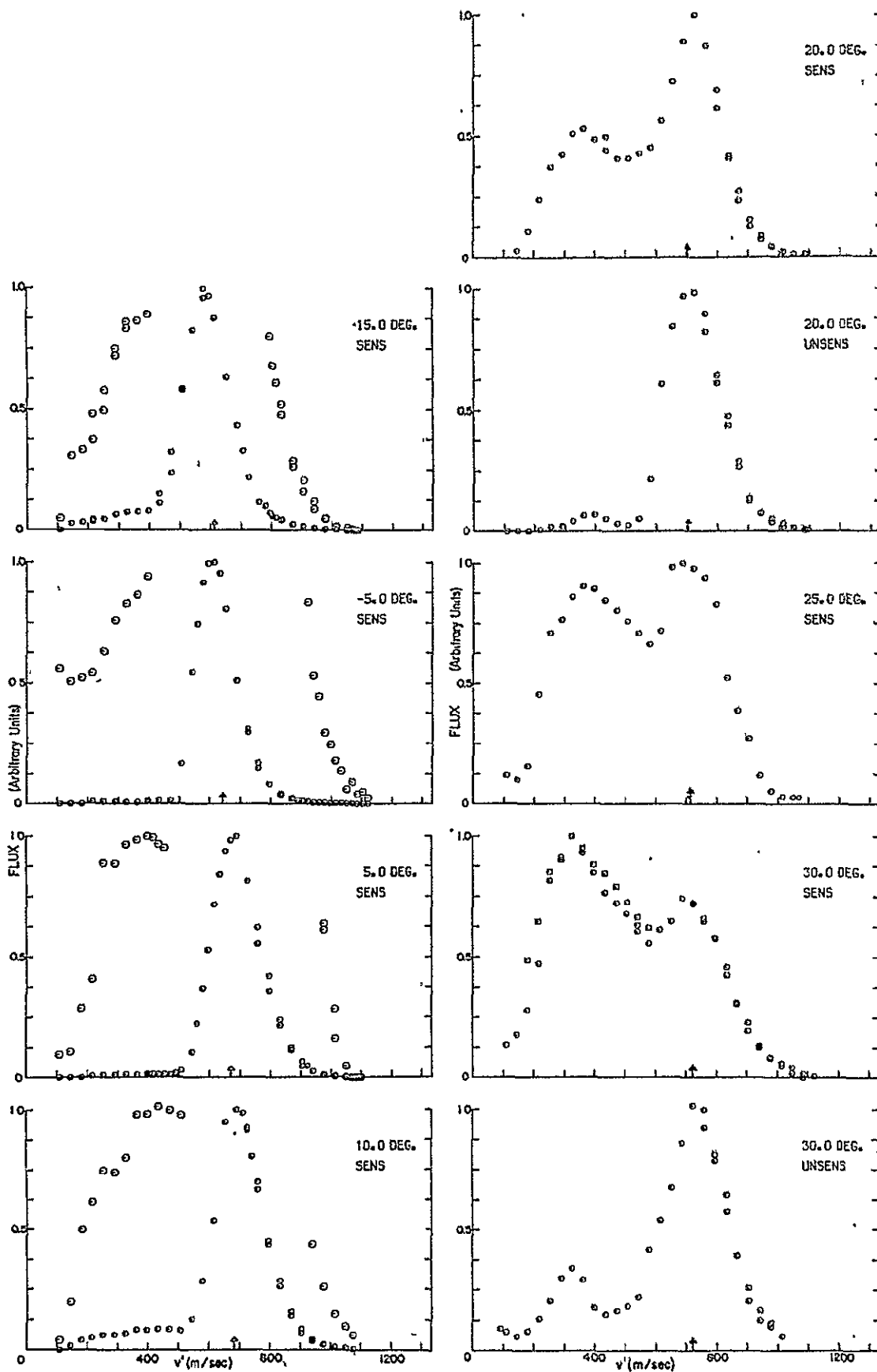


Fig. IV-9

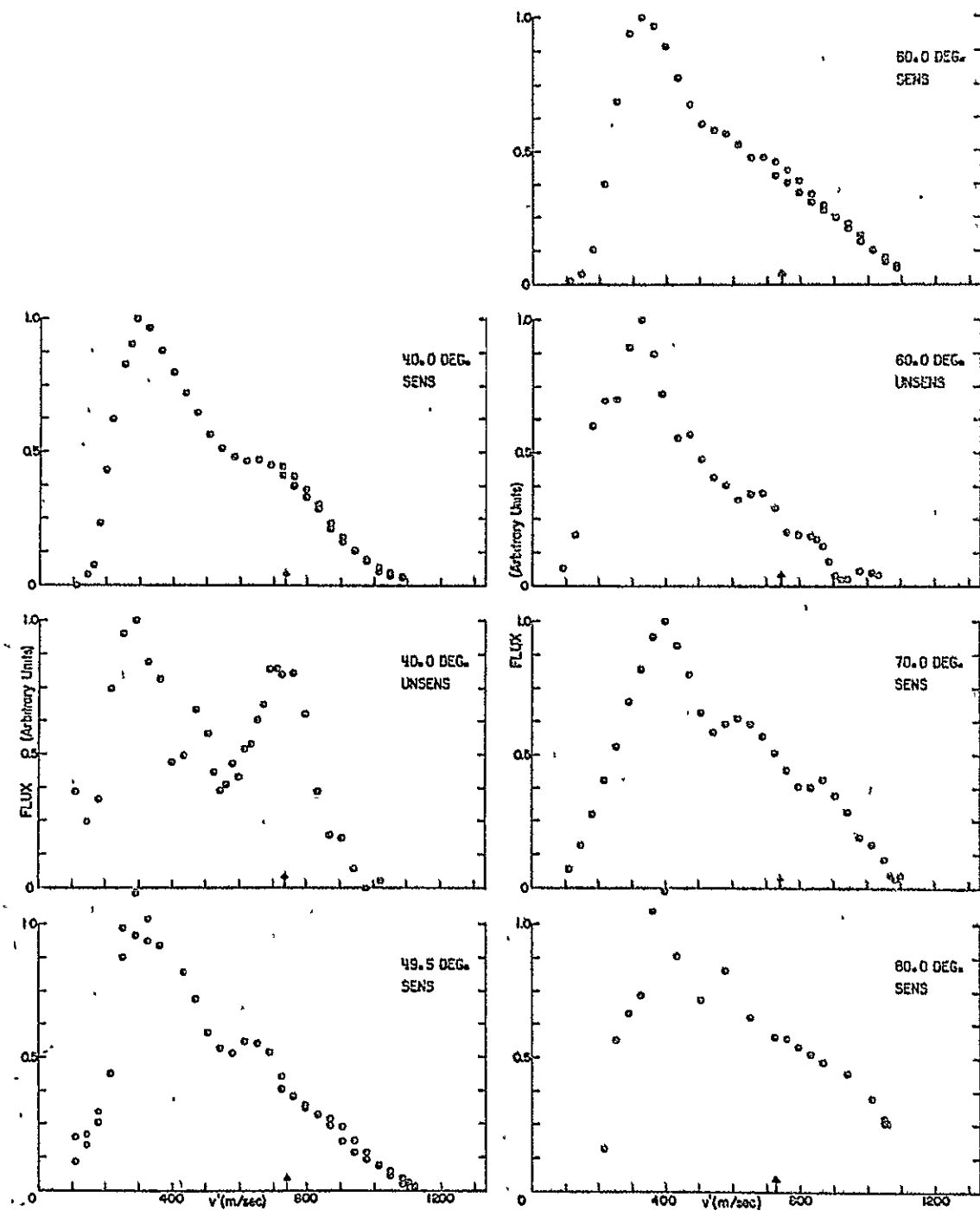


Fig. IV-10

Figs. IV-11,12,13,14 K + I₂ Velocity Analyses, $\bar{E} = 2.67$ kcal/mole

Similar to IV-9,10

Fig. IV-11 Note: Several errata on the expanded scale data,
as follows:

1) -15° SENS

The expanded scale squares (\square) plot two different spectra, only one of which corresponds to the small squares (unexpanded).

2) -5° SENS

The expanded scale circles (\ominus) plot two different spectra, as for the squares above.

3) +5° SENS

Please note that the small squares (\square) and large circles (\ominus) should be interchanged.

4) +10° SENS

Both the expanded scale circles (\ominus) and the expanded scale squares (\square) plot two different spectra, similar to 1) and 2) above.

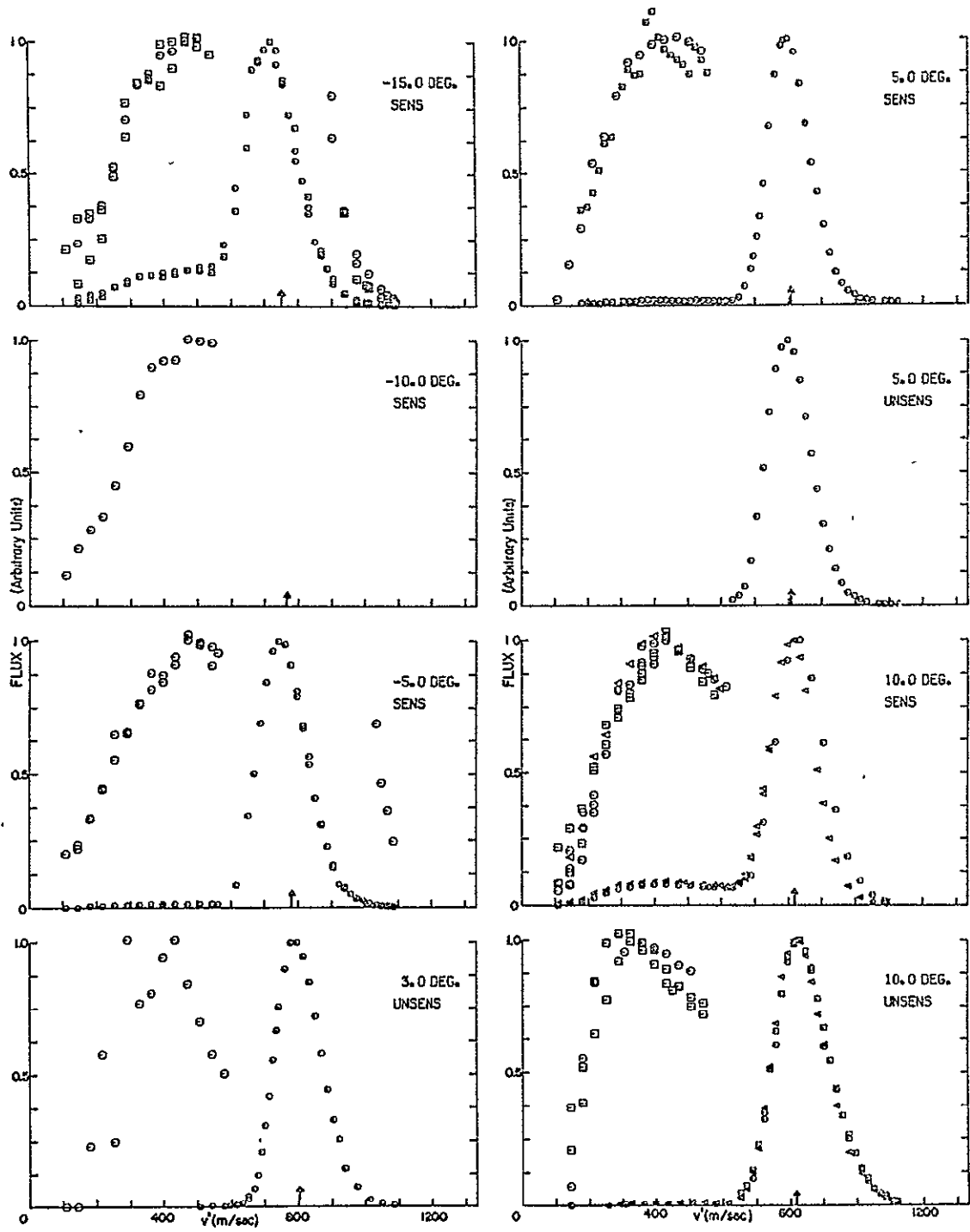


Fig. IV-11

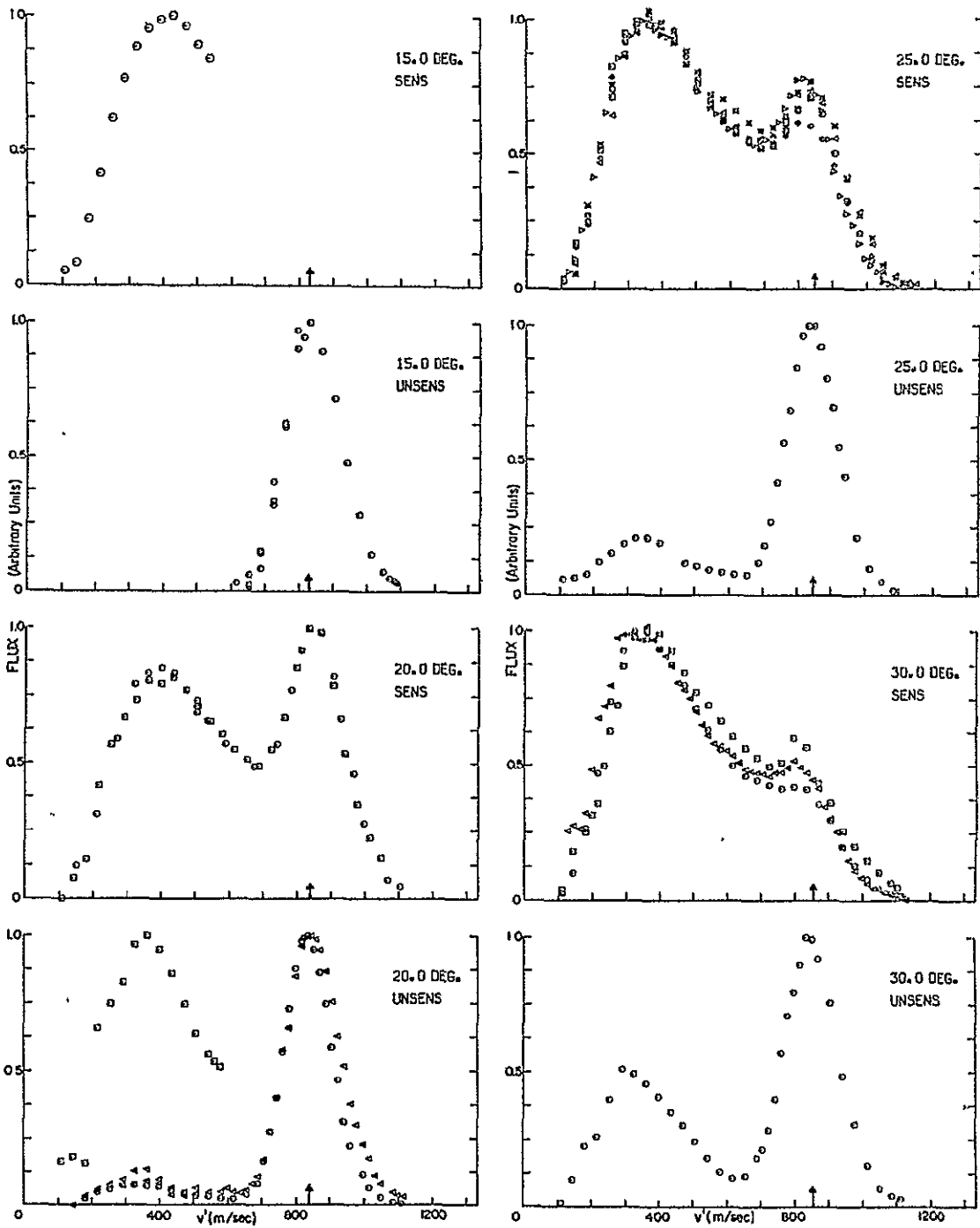


Fig. IV-12

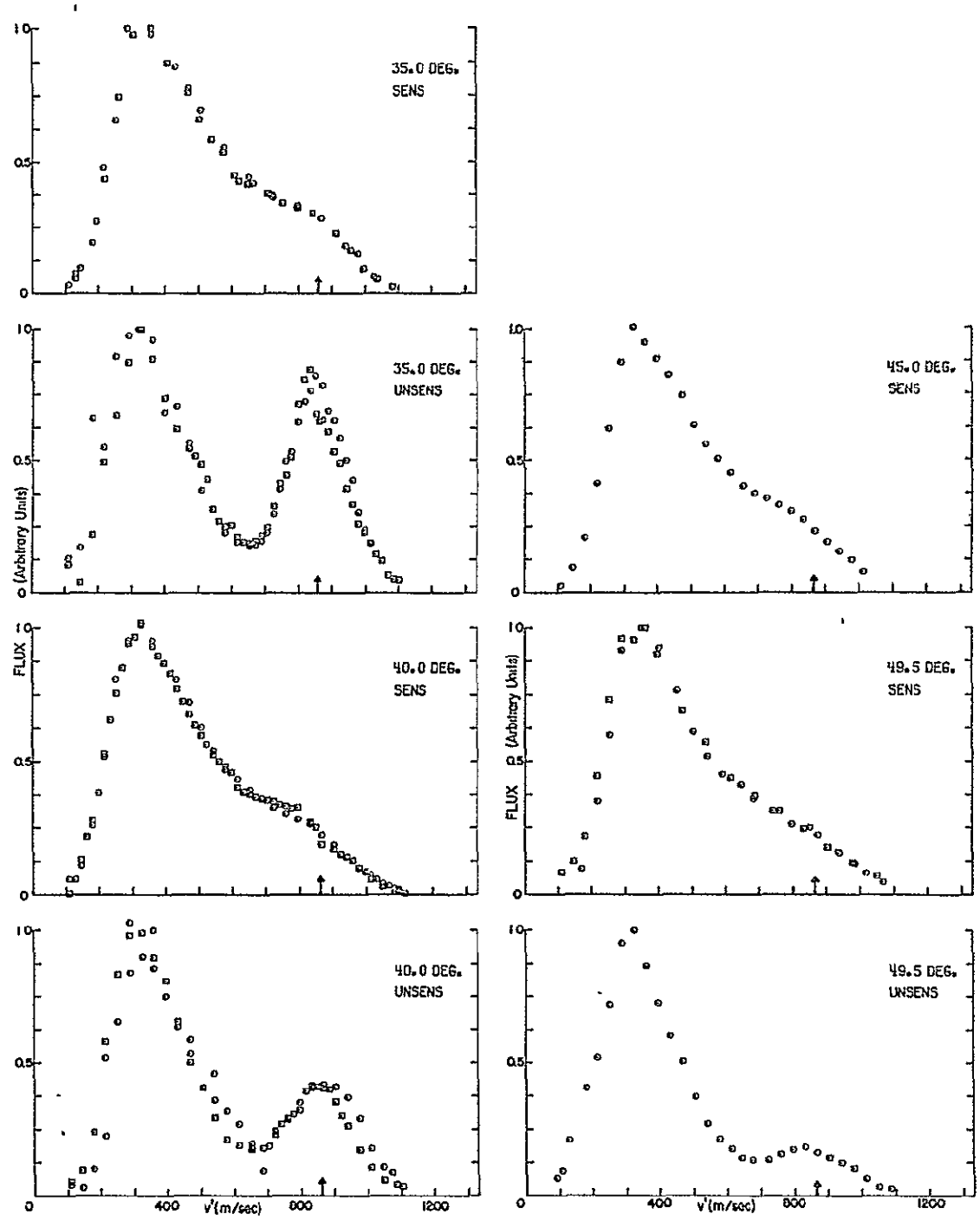


Fig. IV-13

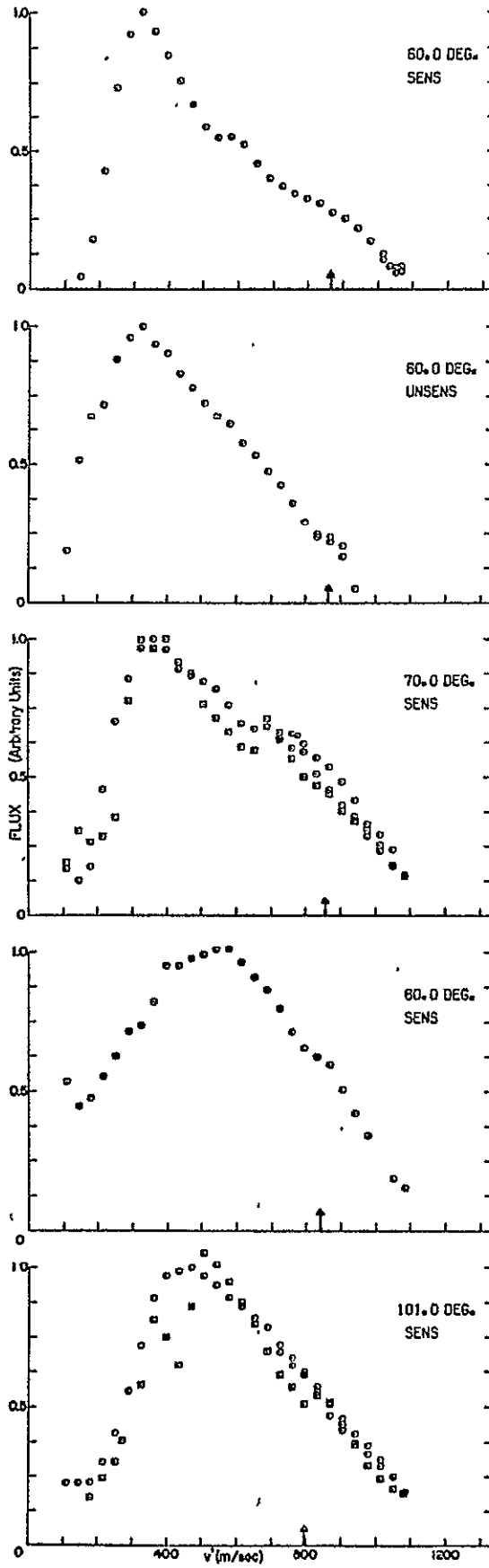


Fig. IV-14

Figs. IV-15,16 $K+I_2$ Velocity Analyses, $\bar{E} = 3.62$ kcal/mole

Similar to IV-9,10

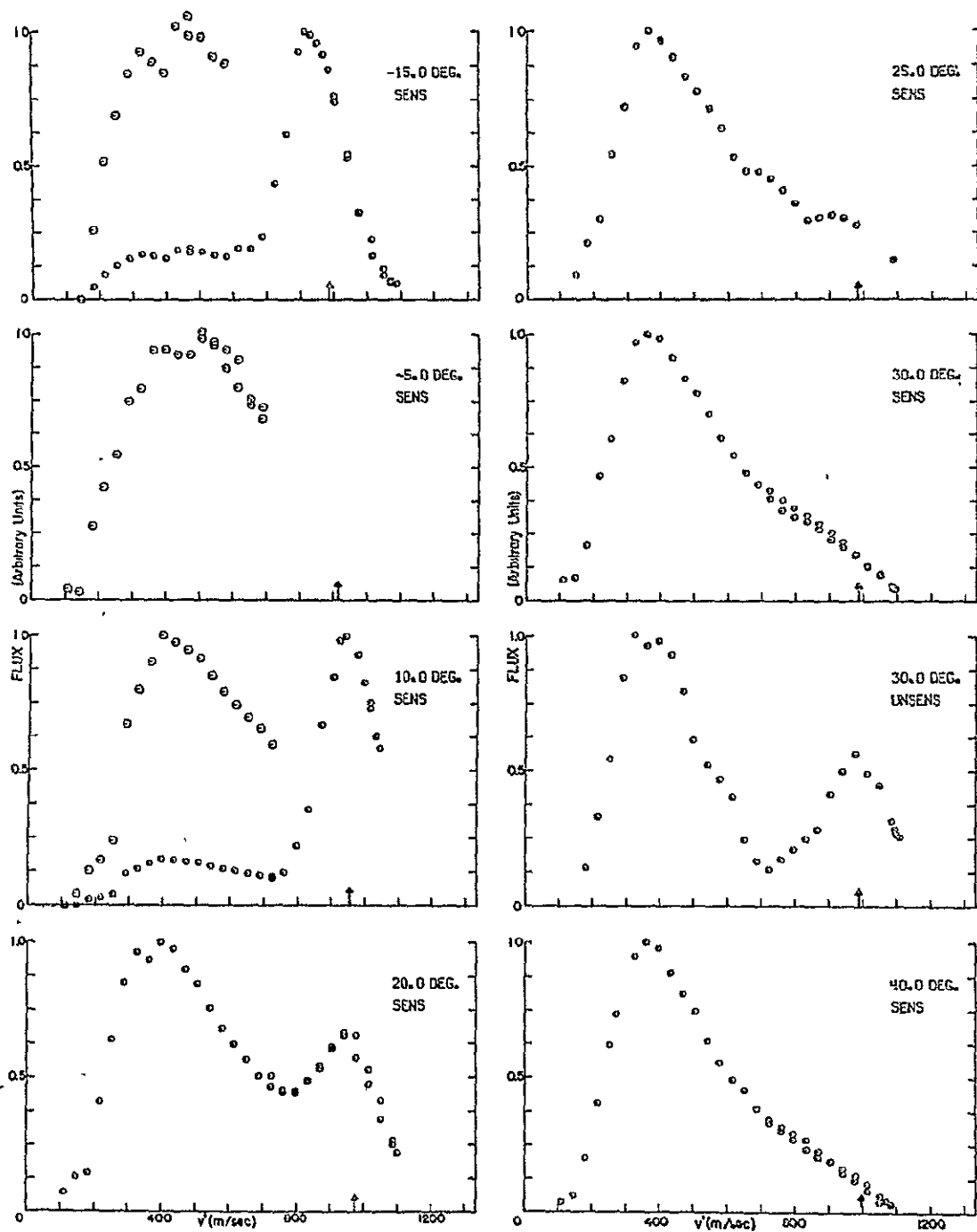


Fig. IV-15

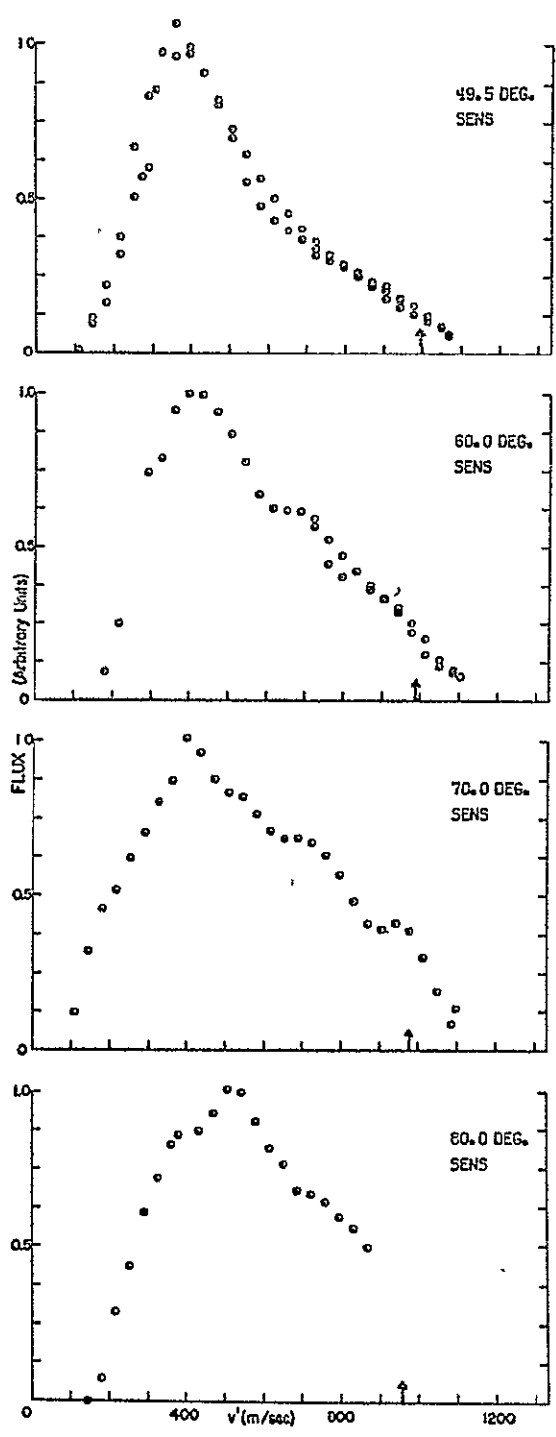


Fig. IV-16

taking data by integrating the intensity at a specified analyzer rotation speed for >30 sec, then changing to another rotational velocity; with occasional checks of a reference velocity, the entire "scan" takes 30 to 50 minutes and is operationally much more demanding than a spectrum. A comparison of the three "scans" with the corresponding spectra in Figs. IV-12,13 shows that they are essentially indistinguishable (using a metric established by comparing other pairs of spectra corresponding to supposedly identical conditions). The major worry is not small differences but rather the possibility of a bias in the spectra caused by some systematic delay in reading the rotation speed associated with a given intensity; this appears not to be the case in these three spectrum-scan comparisons, and most other spectra were taken at even slower rates.

3. Angular Normalizations

To develop a laboratory (velocity-angle) contour map of product flux,^{40,41} the various velocity analyses are properly scaled using an angular distribution measurement for the KI at a specified laboratory velocity. The velocity chosen for this normalization should be low enough that there is no "contamination" by possible elastic K; ideally, it should also be near the maximum in the KI intensity at each angle. The velocity analysis normalizations for the three different energies are shown in Fig. IV-17; all were done with a wide analyzer entrance slit which eliminated the possibility of any angular variation in the size of the scattering center viewed.

Fig. IV-17 KI Angular Normalizations (Laboratory)

Angular normalizations of the KI laboratory flux intensity for the three different relative energies. At each \bar{E} , the various experimental points (replicate experiments are denoted by different symbols) indicate the angular distribution of KI flux at a specified laboratory velocity. Smooth curves, each normalized to unity at the peak, have been passed through each data set.

Upper:	$\bar{E} = 1.87$ kcal/mole,	$v'_{KI} = 362$ m/sec
Middle:	2.67	362
Lower:	3.62	471

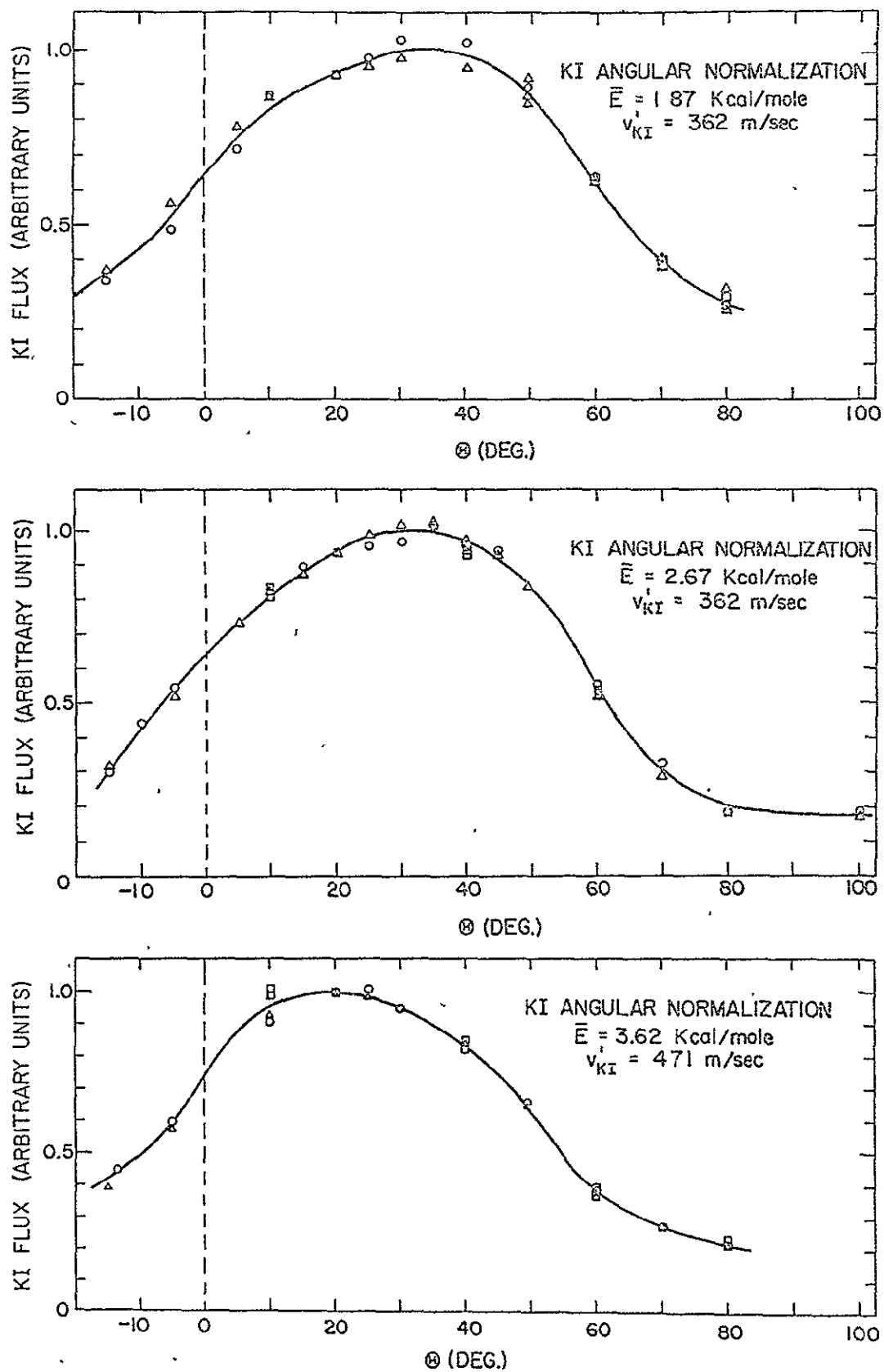


Fig. IV-17

4. Incident Energy Dependence Experiments

For an eventual estimation of the energy dependence of the magnitude of the total reactive cross section, some data were taken which measured the dependence on incident energy of the scattered KI at a specified laboratory velocity and angle (chosen to be near the peak in the laboratory KI intensity contour map); simultaneous measurements (with the W filament monitor) of the K beam flux as a function of K velocity were also necessary. The ratios of the scattered flux (at θ, v') to the total K beam flux for three experiments (each normalized to unity at $\bar{E} = 2.67$ kcal/mole) are shown in Figure IV-18.

Fig. IV-18 Energy Dependence Data

This figure plots the ratio of KI laboratory flux intensity at a specified (H , ν') to the total beam flux of K as a function of the relative energy. These data allow normalization of the laboratory flux contour maps at different \bar{E} .

The triangles are considered the most reliable data; the squares are preliminary data and are the least reliable. All three data sets are arbitrarily normalized to unity at 2.67 kcal/mole. An estimated "best" line has been passed through the data.

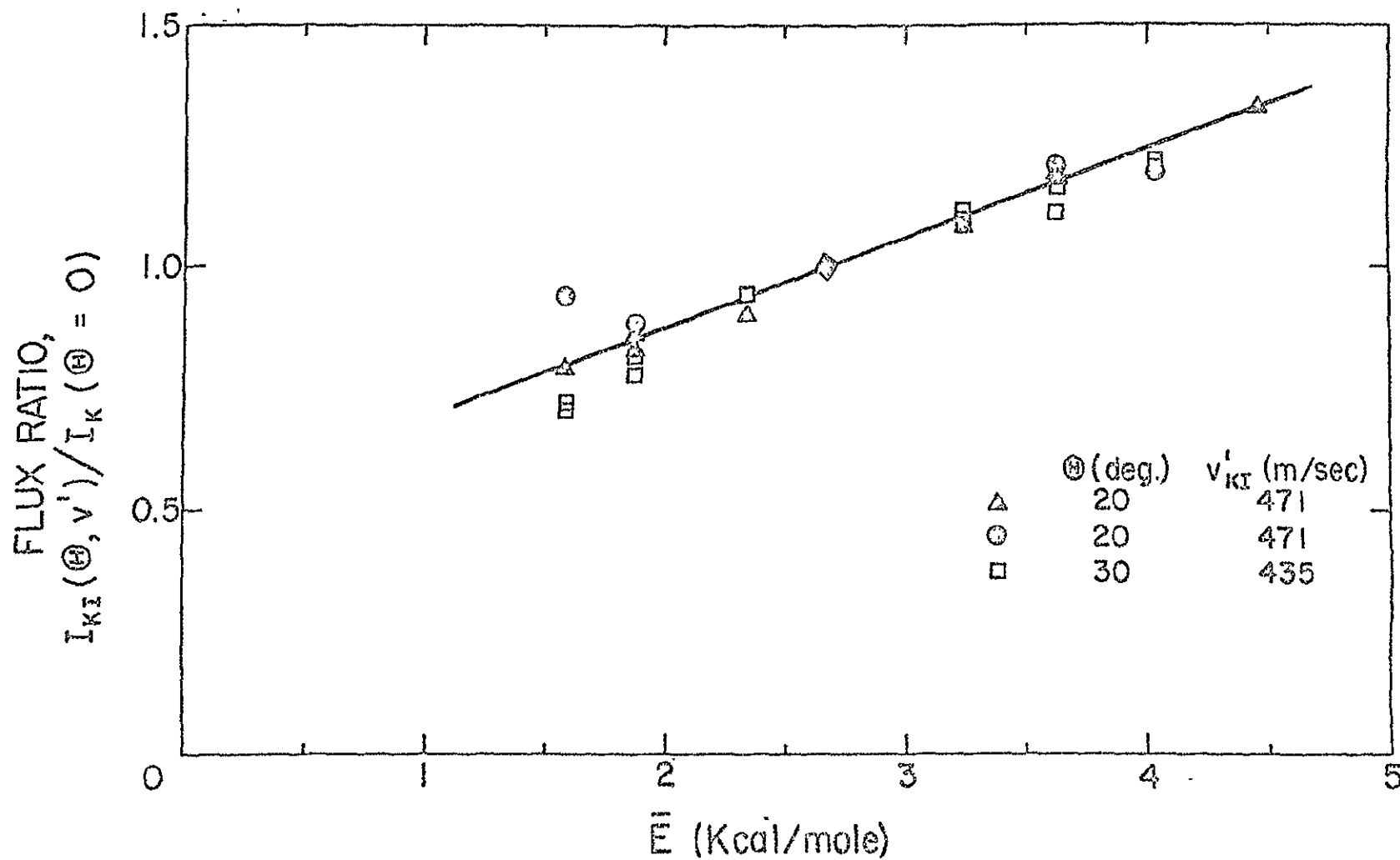


Fig. IV-18

IV. K + I₂D. Comments on Detector Idiosyncracies and Methods of Processing of Raw Data

1. In Figures IV-9 to IV-15 it is quite evident that the flux-velocity curves obtained with the Pt/W detector in the unsensitized mode, i.e., the "unsensitized" velocity analyses, show significant intensity at low laboratory velocities (100-600 m/sec). These broad peaks in the flux vs. velocity distributions cannot be caused by elastically scattered K due to the velocity limits imposed on the K beam by the selector. Inelastic scattering of K is hardly a reasonable explanation for a number of reasons:

- a) The relative incident kinetic energy is too small to excite electronic transitions.
- b) Rotational energy levels of I₂ are much too close together and the intensity at low velocities would have to imply a very implausible penchant for very large multi-quantum jumps.
- c) Vibrational spacings in I₂ (0.61 kcal/mole) are also too close. At $\bar{E} = 2.67$ kcal/mole, the low velocity peaks would correspond to $\Delta v = 4$ transitions.
- d) The (low velocity) intensity peaks do not change position as \bar{E} is varied (in contrast to the observed (and expected) shift in the high velocity elastic peak intensity position as a function of \bar{E}).

Any inelastic excitation mechanism proposed would, therefore, imply a remarkable change with \bar{E} in the preferred transition. The $\Delta v = 4$ transition mentioned in (c) for $\bar{E} = 2.67$ kcal/mole would be energetically unattainable at $\bar{E} = 1.87$ kcal/mole; likewise at $\bar{E} = 3.62$ kcal/mole, the excitation would have to represent 5 or 6 quanta of vibrational energy. Such efficient conversion of translational to vibrational energy in non-reactive collisions is unreasonable.

It is thus clear that the intensity found at low velocities in the unsensitized velocity analyses is due to some fractional (residual) detection of the reactively scattered KI. First, the general shapes and positions of all the low velocity peaks are quite similar to the reactively scattered KI distributions measured (with the sensitized Pt/W filament) at the same conditions of \bar{E} and \textcircled{H} . Also, the intensities of the low-velocity unsensitized peaks are all ~ 5 -15% of the comparable sensitized intensities. In addition, experiments on $K + I_2$ with a pure Pt filament (which does not detect alkali halides) yield non-reactive angular distributions¹¹ that drop off much more rapidly with angle than the present unsensitized results (Figs. IV-5,6,7); a reasonable conclusion is that most of the difference is due to residual detection of KI in the present results. The origin of this effect and its implications upon "K" scattering are discussed in Chapter V.

This residual sensitivity to KI adds significant spurious intensity to the present "unsensitized" angular distributions of the

non-reactive scattering. Fortunately the velocity analyses at the various angles allow a determination of the proper partitioning of the unsensitized angular distributions between true non-reactively scattered K and spurious residual KI intensity at each angle.

2. Although there are two distinct reproducible modes of the filament ("unsensitized" and sensitized), there is also a continuous gradation of filament conditions between these two standard cases. Oxygen serves to sensitize the Pt/W filament; traces of I_2 appeared to desensitize it. Depending on I_2 pressure, O_2 "leak" flow rate, and conjunction of the planets, a filament in the fully sensitized condition can gradually deteriorate in its efficiency of KI detection, eventually reaching the normal unsensitized mode. If this deterioration ensues, sometimes it can be abated by increasing the O_2 flow rate; otherwise the full sensitization procedure must be repeated. In practice, when the decay in sensitivity was gradual (typically $\lesssim 5\%$ /hour), sensitized experiments were often run at conditions corresponding to as low as 70% of full sensitivity to KI. In Fig. IV-8 two raw data chart recordings are shown at $\bar{E} = 2.67$ kcal/mole and $\textcircled{H} = 25^\circ$; the lower one is fully sensitized to KI, the upper corresponds to only 70%. The important thing to note is the change in the relative intensity of the K and KI peaks. Variations in sensitivity also show up in Figs. IV-9 to IV-16, again most easily seen as differences in K:KI ratios (e.g. in Fig. IV-12).

All of the velocity analyses have been evaluated to determine the % sensitivity to KI. Occasional checks of the total angular

distribution proved to be the best way to monitor changes in KI detection efficiency during an experiment. The relative sensitivities are needed below in properly partitioning the various velocity analyses between non-reactively scattered K and reactively scattered KI.

3. A major task in evaluating the data is determining for every velocity analysis the best curve separating the KI from the K. The pure non-reactive K curve shapes can be seen in the low angle unsensitized (U) spectra. In every velocity analysis a smooth "reasonable" line is drawn separating the K and KI contributions, such that the separated K distribution has both reasonable shape and a reasonable velocity for the intensity maximum based on kinematics. "Structure" in the separated KI distributions is avoided unless the data necessitate it (e.g., in the large angle sensitized (S) spectra where there is almost no K to subtract). For angles at which there are both S and U curves, measured areas of the separated K and KI can be combined (after correction of the KI in the S curves to 100% sensitized -see 2) above) to give the ratio of signals S/U in the total angular distributions at the given θ (note that the intensity of K is assumed to be the same in the U or S condition). This is compared to the experimental ratio in Fig. IV-5,6 or 7; any disagreement is removed by adjusting slightly the lines separating K from KI until there is reasonable agreement. Sensitized velocity analyses at angles containing no U data are divided between K and KI in a similar way; but it is additionally necessary to assume a number for the fractional residual sensitivity

to KI in the U mode. This number is not constant (as noted below), but usually can be approximated by interpolation or mild extrapolation from other data. A few iterations on the positioning of the line usually suffice to give distributions that are consistent with all the criteria listed above. The errors in the curve separations (example in Fig. IV-19) are probably not much larger than the size of the random errors evident in the raw data distributions of Figs. IV-9 to IV-16. The only major shortcoming of the separation method involves the requirement of smooth curves if possible; any structure in the KI distributions which is present near the velocity region of the non-reactively scattered K may be lost due to the assumed smooth form.

4. The existence of a small residual sensitivity of the "unsensitized" Pt/W alloy to the alkali halides is well known⁴⁻⁶; yet in the present experiments the residual sensitivity to KI is surprisingly large, ranging up to $\sim 16\%$ of the reactively scattered KI at certain laboratory (v' , \textcircled{H}) positions. Measurements with the Pt/W detector on a direct beam of KI from an effusive (748°K) oven showed a signal ratio of $\sim 500:1$ for the sensitized vs. the unsensitized condition. These effusive KI molecules have low internal excitation ($\bar{E}_{\text{int}} \approx 2.7$ kcal/mole). It is concluded that the increased U-mode sensitivity to reactively scattered KI^\dagger is due to the known high internal excitation of the scattered KI^\dagger molecules.

Interference due to non-reactively scattered K (and associated

Fig. IV-19 Separation of K from KI in Velocity Analyses.

An example of the separation of the non-reactive K from the reactive KI in the velocity analyses. The data are from Figure IV-13 at $\bar{E} = 2.67$ kcal/mole.

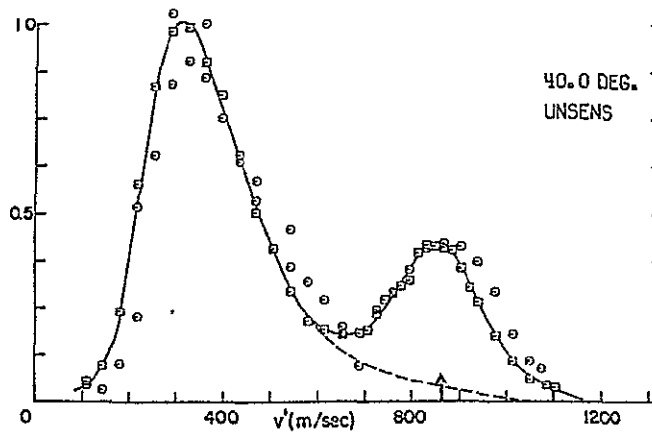
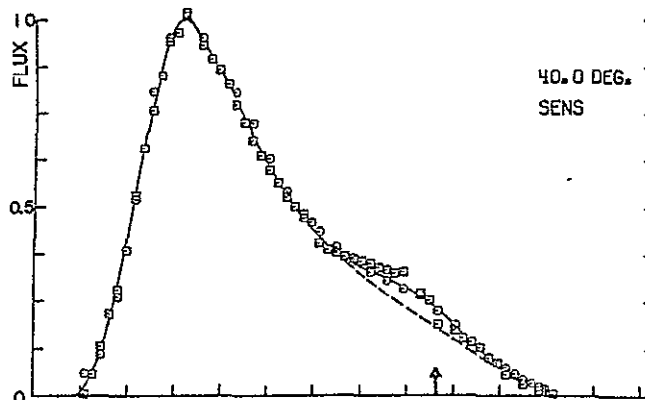
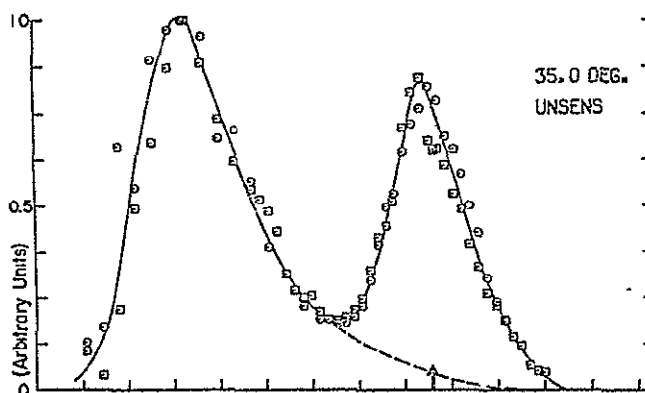
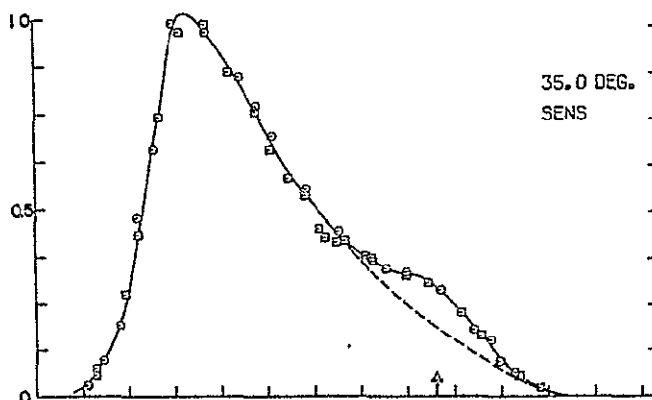


Fig. IV-19

ambiguities in achieving separation of the K from the KI) limits the laboratory velocity range at which meaningful comparisons can be made for the detection ratio of the two filament conditions. This in turn limits the internal energy range of KI that can be studied; approximately 44 kcal/mole of internal energy is available to the KI at positions near centroid (with the assumption of only ground state $I(^2P_{3/2})$ production) and it is difficult to deal with KI with $E_{exc} \lesssim 30$ kcal/mole due to the interference from K at large velocities. Nevertheless, the change in detection ratio in this energy range is very striking. To verify the existence of the effect at $\bar{E} = 2.67$ kcal/mole one can simply compare the shapes of the lab. distributions (Figs. IV-12,13) for U and S modes at 30,35,40, and 49.5°. At each of these angles the U mode KI signals drop off much faster with increasing velocity (and thus decreasing E_{exc} of the KI) than the corresponding S curves in the laboratory velocity range 300-700 m/sec.* A graph of the effect and other details are given in Chapter V.

It may be noted that previous experiments in several laboratories, some employing a velocity selector^{13,14} and others, a velocity analyzer,²⁴ individually failed to reveal the phenomenon of internal excitation-dependent surface ionization. However, with the present combination

* The velocity analysis results at $\theta = 60^\circ$ are not considered to be a contradiction of this observation, since the U-mode 60° curve had a signal: noise ratio lower than any other velocity analysis reported here.

of a velocity selector and velocity analyzer, the limits of the elastically scattered K could be sufficiently well defined as to demonstrate clearly the enhanced KI^\dagger detectability on the low work function surface.

It has already been stated that residual sensitivity to KI in the U mode necessitates a correction in the angular distributions in order to obtain the true non-reactively scattered K angular distribution. This correction must be done properly, i.e., by accounting for the enhanced KI detection due to internal excitation. Minturn et al.¹⁴ attempted to make this correction using results on detection efficiencies for thermal beams of (essentially ground state) alkali halides; the actual residual detection of scattered reactive product is much greater, yielding a spurious KI contribution to the large angle "non-reactive" scattering intensity.

IV. K + I₂E. Analysis of Non-Reactive Scattering

The largest body of data were acquired at $\bar{E} = 2.67$ kcal/mole, near the peak in the Laval K beam flux distribution incident upon the selector (see Appendix A). A large number of unsensitized velocity analysis experiments (see Figs. IV-11,12,13) allow the corresponding "unsensitized" angular distribution to be converted to a "corrected" non-reactively scattered K angular distribution by subtracting out the residual KI sensitivity using the methods described in IV-D. In Fig. IV-20 are presented the $\bar{E} = 2.67$ kcal/mole unsensitized laboratory angular distributions. They are plotted with an ordinate weighted by $\sin^4 \theta$ ^{12a,51}. The method of plotting emphasizes deviations from the classical low-angle dependence for an asymptotic R^{-6} potential and allows a comparison of results at different incident energies. The uncorrected laboratory data agree well with the data of Birely et al. ¹⁶ and demonstrate clearly that their "desensitized" 92% Pt/8% W filament suffered from comparable KI residual sensitivity. In contrast, the present data, when corrected for KI contributions, agree much better with the data of Greene et al. ¹¹ who used a Pt filament, essentially non-detecting for KI. The data of Greene et al. still drop off somewhat faster than the present results at large angles (this statement continues to have validity in the c.m. system). Their data were obtained in the out-of-plane geometry ⁶⁰, and comparisons of K + HBr, DBr elastic scattering results ^{61,42} had indicated that the out-of-plane geometry is superior in the elimination of unwanted background.

Fig. IV-20 Angular Distributions of Non-Reactive Scattering (Laboratory).

Log-log plot of the angular distributions of the flux of non-reactive scattering.

Present results: $\bar{E} = 2.67$ kcal/mole, "in-plane" geometry

- a) Uncorrected: raw data on "unsensitized" Pt/W filament, contains much residual KI at large angles.
- b) Corrected: KI contribution has been subtracted, leaving only the non-reactive K intensity.

Birely et al¹⁶ : crossed Maxwellian beams, nominal $\bar{E} = 1.58$ kcal/mole, "in-plane" geometry. Unsensitized Pt/W filament, detects significant residual KI.

Greene et al¹¹ : $\bar{E} = 2.41, 3.54$ kcal/mole, "out-of-plane" geometry. Pt filament, detects K only.

Normalization is arbitrary for all curves.

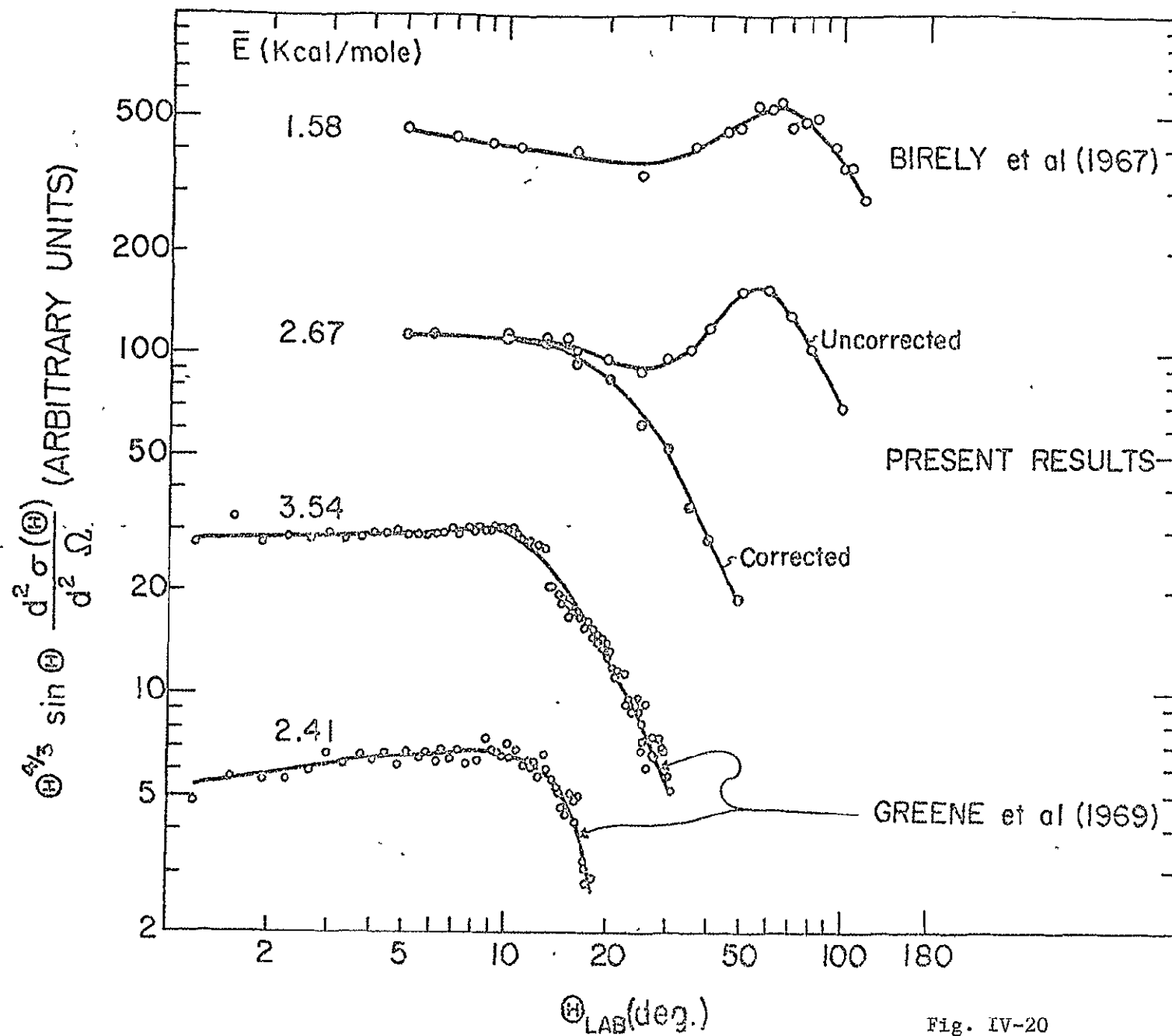


Fig. IV-20

Hence their data are probably still more reliable than the present corrected results (in this game, like golf, the lowest usually wins) due to our less complete background elimination (K!); yet the alkali halide correction is obviously the major explanation for the discrepancies in elastic scattering between the Harvard¹⁶ and Brown-MIT¹¹ groups. At $\Theta = 49.5^\circ$, 88% of the unsensitized (Pt/W) intensity is due to residual detection of KI; at 60° the K is such a small fraction of the total U signal that its size cannot be estimated.

Transformation of the non-reactive scattering data to the c.m. system makes use of the transformation Jacobian appropriate to elastic scattering angular distributions^{49,44}

$$\frac{d^2\sigma(\theta)}{d^2\omega} \propto \frac{w'^2}{v'^2} |\cos \xi| I(\Theta) \quad (1)$$

$$= J \times I(\Theta),$$

where $\frac{d^2\sigma(\theta)}{d^2\omega}$ is the c.m. differential solid angle elastic cross section;

v' , the scattered K lab. velocity; w' , its velocity w.r.t. the c.m.;

ξ , the angle between \vec{v}' and \vec{w}' ;

J, the Jacobian; and

$I(\Theta)$, the measured detected flux of K, proportional to $\frac{d^2\sigma(\Theta)}{d^2\Omega}$.

Assuming a long range potential of the pure R^{-6} form, $V(R) = -C^{(6)}/R^6$, one can predict an absolute elastic scattering cross section (cm^2/sr) using the equation^{62a}

$$\frac{d^2\sigma(\theta)}{d^2\omega} = \frac{1}{6} \left(\frac{15\pi}{16}\right)^{1/3} \left(\frac{C^{(6)}}{E}\right)^{1/3} / (\theta^{4/3} \sin\theta) \quad (2)$$

The $C^{(6)}$ has been estimated by Birely et al.¹⁶ as $C^{(6)} = 1.30 \times 10^{-57}$ erg cm^6 . In Figure IV-21 log-log plots of $\frac{d^2\sigma(\theta)}{d^2\omega}$ vs. $\theta_{\text{C.M.}}$ are shown for the uncorrected Birely et al. results, the present corrected results at 2.67 kcal/mole, and the Greene et al. (Pt filament) results at 2.41 kcal/mole; each was normalized at a reference angle of $\theta = 7$ deg. An inverse sixth power attractive potential would imply a slope of $-7/3$ on this plot; the results agree reasonably with this slope in the low angle region. Again it must be noted that the Birely et al. results are raised significantly at large angles, due to contributions from reactive scattering.

The total scattering cross section in the Schiff-Landau-Lifshitz approximation (Q_{SLL}) is given for the asymptotic $C^{(6)} R^{-6}$ potential by^{62b}

$$Q_{\text{SLL}}^{(6)} = 8.083 \left[C^{(6)} / \hbar v_{\text{rel}} \right]^{2/5}$$

At 2.67 kcal/mole the result is $Q = 920 \text{ \AA}^2$.

For elastic scattering in systems that have very small reactive cross sections it has been found that a reduced plot of

Fig. IV-21 Differential Cross Sections (c.m.) for Non-Reactive
Scattering.

Log-log plots of absolute values $\frac{d^2\sigma_{nr}}{d^2\omega}$ ($\text{\AA}^2/\text{sr}$) of the differential non-reactive scattering cross sections (c.m.) corresponding to three of the curves of Fig. IV-20. Each curve has been normalized at θ_{ref} using the assumed small angle dependence associated with an inverse sixth power attractive potential (see text). The slope of $-7/3$ is that expected classically at low angles for the inverse sixth power attractive potential.

Note: The three curves are at different \bar{E} ; this is, of course, the reason that they don't intersect at the reference angle.

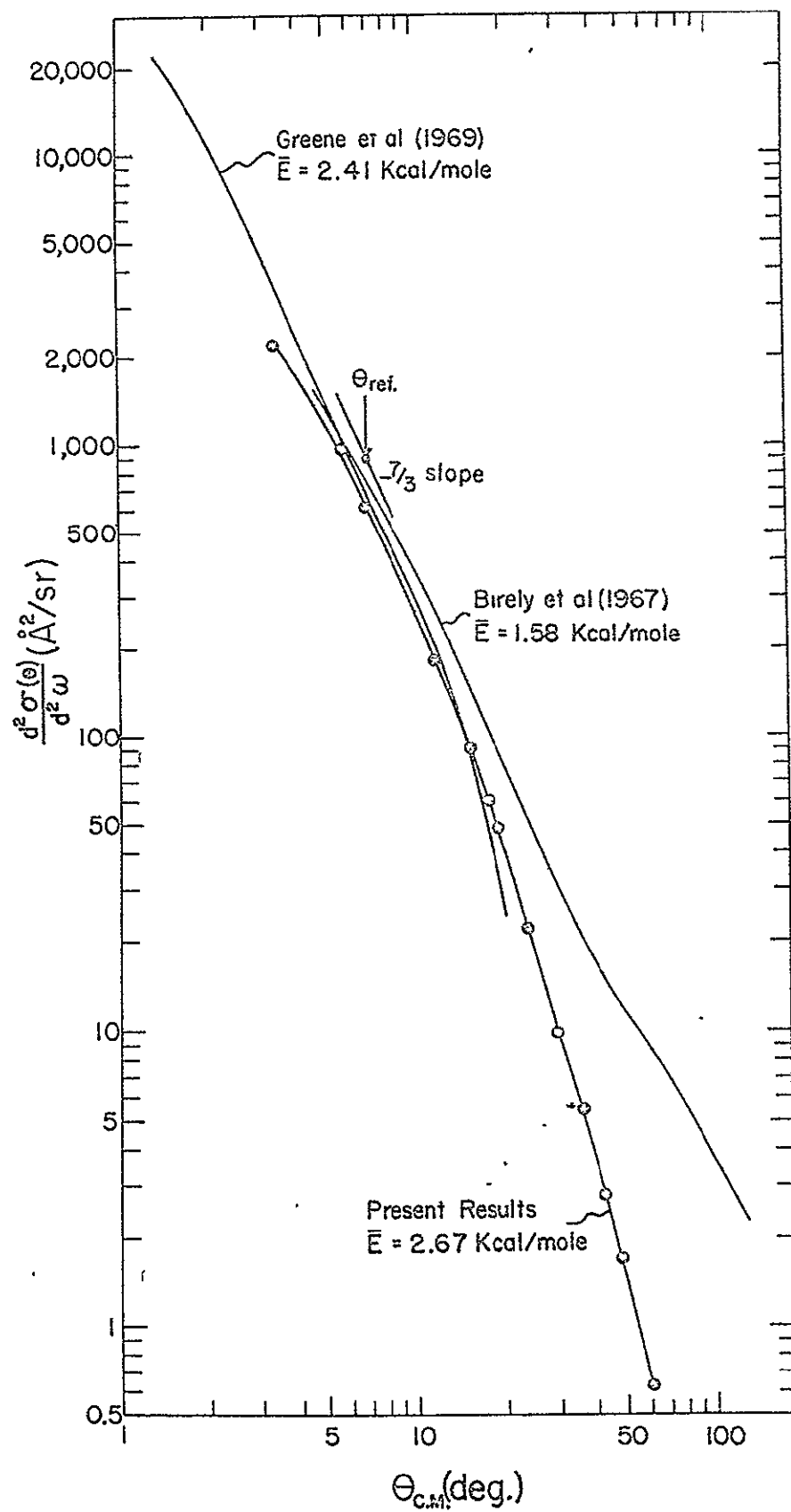


Fig. IV-21

$(E\theta)^{1/3} \theta \sin\theta \frac{d^2\sigma(\theta)}{d^2\omega}$ vs. $E\theta$ (proportional to the impact parameter, b) removes the incident energy dependence of the scattering and causes non-reactive angular distributions at different energies to become essentially degenerate⁶³. An R^{-6} attractive potential (at large distances) yields a line horizontal at low angles in this method of plotting and the "rainbow"¹² shows up as a large-angle disturbance.

For reactive systems with large cross section (e.g., $K + I_2$), reaction at large impact parameter eliminates the rainbow. On the reduced plot a horizontal portion at small angles is followed by a sharp drop-off caused by reactive attenuation ensuing at distances at which the potential is still attractive. The abscissa $E\theta$ gives a set of curves at which the "drop-off" changes with energy¹¹; the choice of an alternative abscissa, θ , serves to line up the angular distributions at different energies much better than the normal reduced plot (abscissa $\propto b$). This is demonstrated for $K + I_2$ in Fig. IV-22 for the results of Greene et al.^{11*} at four different energies and for the present (partially) confirmatory results. Again the (out-of-plane) results of Greene et al. drop off faster at large angles and are generally considered to be the more reliable.

- - - - -

* We would like to express thanks to Professor Ross for kindly supplying the laboratory and c.m. results.

Fig. IV-22 Reduced Plot of c.m. Angular Distribution of K.

A reduced log-log plot of $(E\theta)^{1/3} \theta \sin \theta \frac{d^2\sigma}{d^2\omega}$ (abscissa: $\theta_{\text{c.m.}}$) of non-reactive c.m. scattering on which the data at different \bar{E} superimpose.

Open symbols: Greene et al. (1967)¹¹

Closed symbols: Present results

Arbitrary relative normalization of the open and closed symbols.

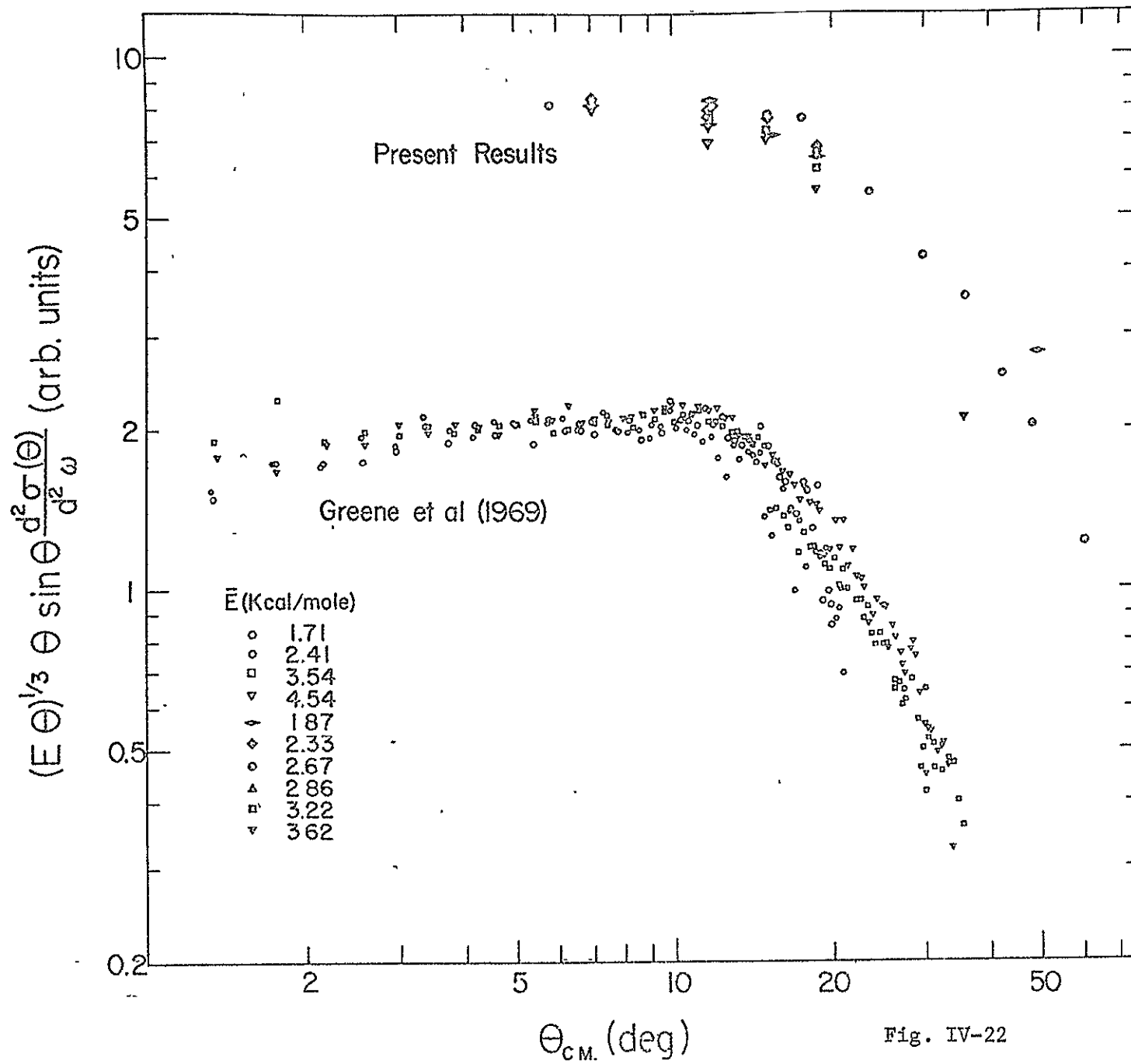


Fig. IV-22

To proceed further in the analysis of the non-reactive scattering results, it is convenient to introduce a simple fairly conventional optical model. Suppose that there is a critical impact parameter, b_{crit} , inside of which the reaction probability is unity; outside, zero. This yields a total reactive cross section πb_{crit}^2 and also a sharp cut-off in the elastic angular distribution at the angle θ_{crit} . For systems with large total reaction cross section exhibiting horizontal reduced plots (Fig. IV-22) for elastic scattering up to the "cut-off" angle, the small angle approximation relating θ to b^{62c} may be used at the critical cut-off angle

$$\theta_{\text{crit}} = \frac{15\pi}{16} \frac{C^{(6)}}{Eb_{\text{crit}}^6} \quad (3)$$

$$\text{But } \sigma_R = \pi b_{\text{crit}}^2; \quad (4)$$

$$\text{therefore } \sigma_R \propto (E/\theta_{\text{crit}})^{-1/3}.$$

Two extreme cases are of interest. If $\theta_{\text{crit}} = \text{constant}$, as suggested by the $K + I_2$ results of Greene et al. (Fig. IV-22), then $\sigma_R \propto E^{-1/3}$. If $E\theta_{\text{crit}} = \text{constant}$,

corresponding to a lining up of the various curves on the usual reduced plot*, then $\sigma_R = \text{constant}$, independent of relative

* Note that the $K + Br$, Cl_2 , ICl results of Greene et al., at higher energies than the $K + I_2$ data, seem to change to a form closer to the $E\theta_{\text{crit}} = \text{constant}$ case.

energy. Between these two extremes, an "intermediate" negative energy dependence less than $E^{-1/3}$ would be expected. As Fig. IV-22 shows, the present results might be thought to indicate such an "intermediate" case, yet the results of Greene et al. are probably more reliable than the present results. Using $\theta = 13^\circ$ (quite arbitrarily) as the experimental cut-off angle, b_{crit} (and thus σ_R) can be estimated from Eqs. (3) & (4) respectively. The result at 2.67 kcal/mole is $b_c = 6.7 \text{ \AA}$, $\sigma_R = 140 \text{ \AA}^2$. Alternatively selecting $\theta_{\text{crit}} = 19^\circ$, the angle at which Greene's scattering has dropped to approximately half the "horizontal" line, the resultant total reactive cross section would be 125 \AA^2 . There exist a number of more sophisticated treatments of the optical model^{2b,11,64}, and there are more general approaches to estimating total reactive cross sections both from reactive product intensity estimates¹⁶ and from fitting large angle non-reactive scattering data.³⁴ The present simple model gives a total reaction cross section smaller than other estimates available (Sec. IV F 10) perhaps due to lack of knowledge of the potential involved³⁴; but the possibility of a simple correlation of the energy dependence of a reaction with the energy variation of a "critical angle" is worth noting.

IV. K + I₂F. Analysis of Reactive Scattering

1. Laboratory Angular Distributions and Contour Maps

After subtracting the K contributions from the velocity analyses (by the method described in Sec. IV D3) and properly scaling the flux-velocity curves at the various angles Θ using the angular normalization data (IV C 3), one obtains a set of velocity analyses (in Figs. IV-23,24,25) representing the best estimate of the laboratory KI flux (velocity-angle) distributions. At each \bar{E} the set of curves is normalized to unity at the peak. Generally the curves of largest intensity are the most reliable; but there are exceptions (the $\Theta = 25^\circ$ curves at 1.87 and 3.62 kcal/mole are of low quality). It should also be noted that the experiments at 1.87 kcal/mole are of generally lower quality than those at other energies; this is due to the lower incident K beam flux at this energy.

With the various velocity analyses of KI properly normalized it becomes possible to integrate under the curves to obtain the relative intensities of KI at the various laboratory angles. This is one way of obtaining the laboratory angular distribution of reactive product; the results are shown (∇) in Fig. IV-26. The angular distributions at the three different energies have been made self-consistent (normalized across energy by use of the direct energy-dependence experiments, IV C 4). The more standard method of obtaining laboratory angular distributions of KI subtracts the U mode intensity at every angle from the corresponding S mode signal in the total angular

Figs. IV-23,24,25 KI Flux, Laboratory Angle-Velocity Distributions

Smoothed KI velocity analyses (after removal of K) as a function of laboratory angle for three different \bar{E} ; each curve is labelled with the lab. angle \textcircled{H} in degrees. For each \bar{E} , the various velocity analyses have been normalized to each other using the data of Fig. IV-17; in each figure the peak is set to unity.

Figure IV-23 $\bar{E} = 1.87$ kcal/mole

Figure IV-24 2.67

Figure IV-25 3.62

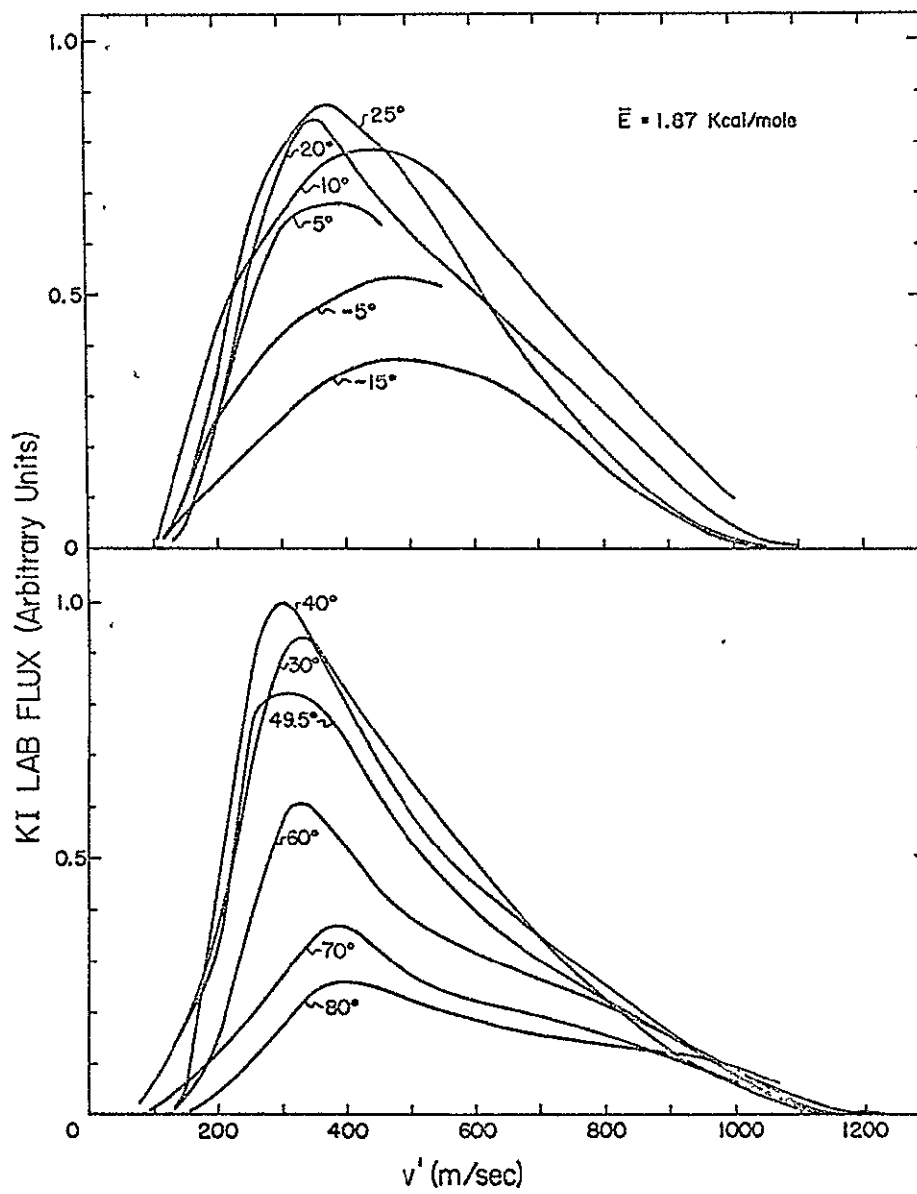


Fig. IV-23

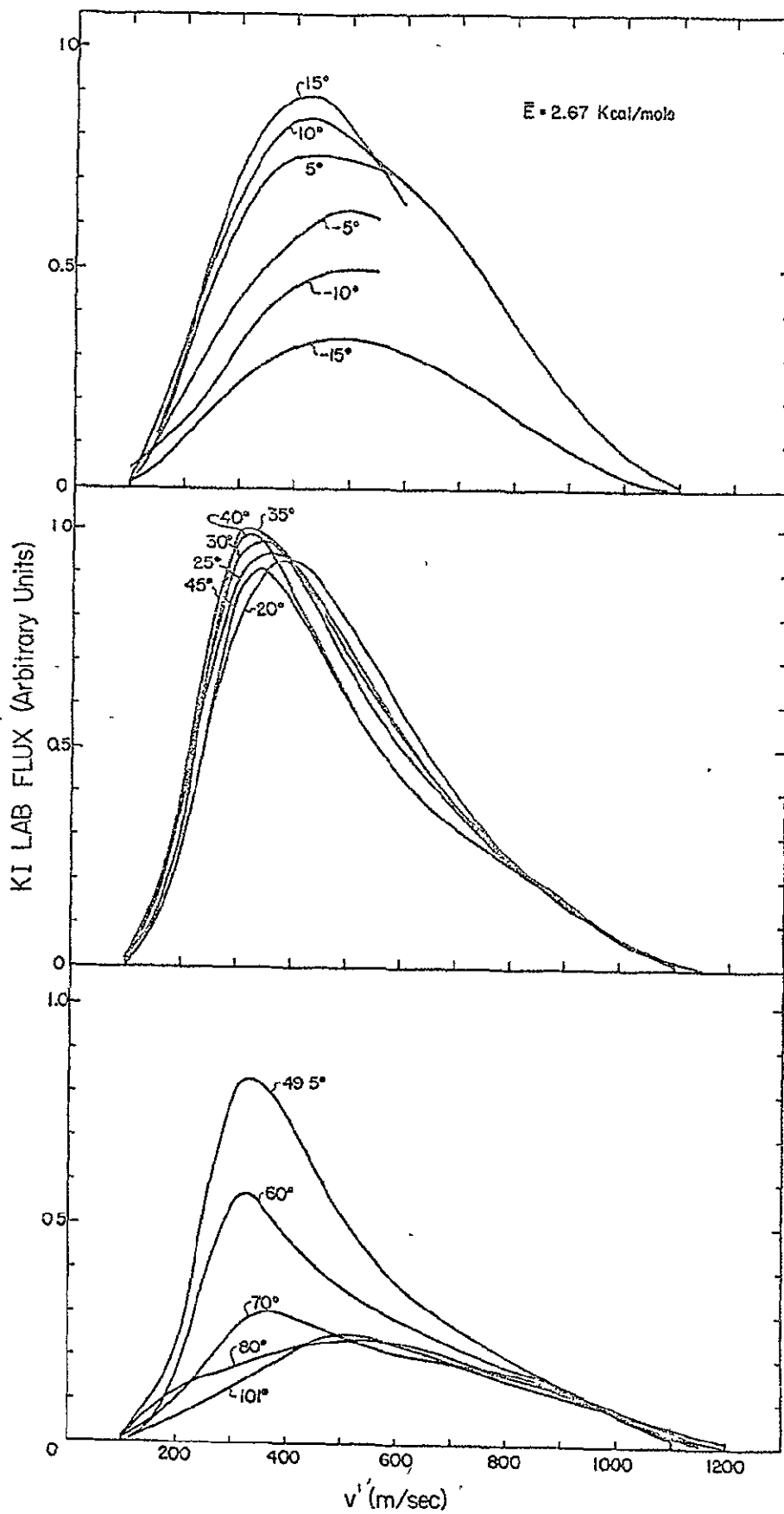


Fig. IV-24

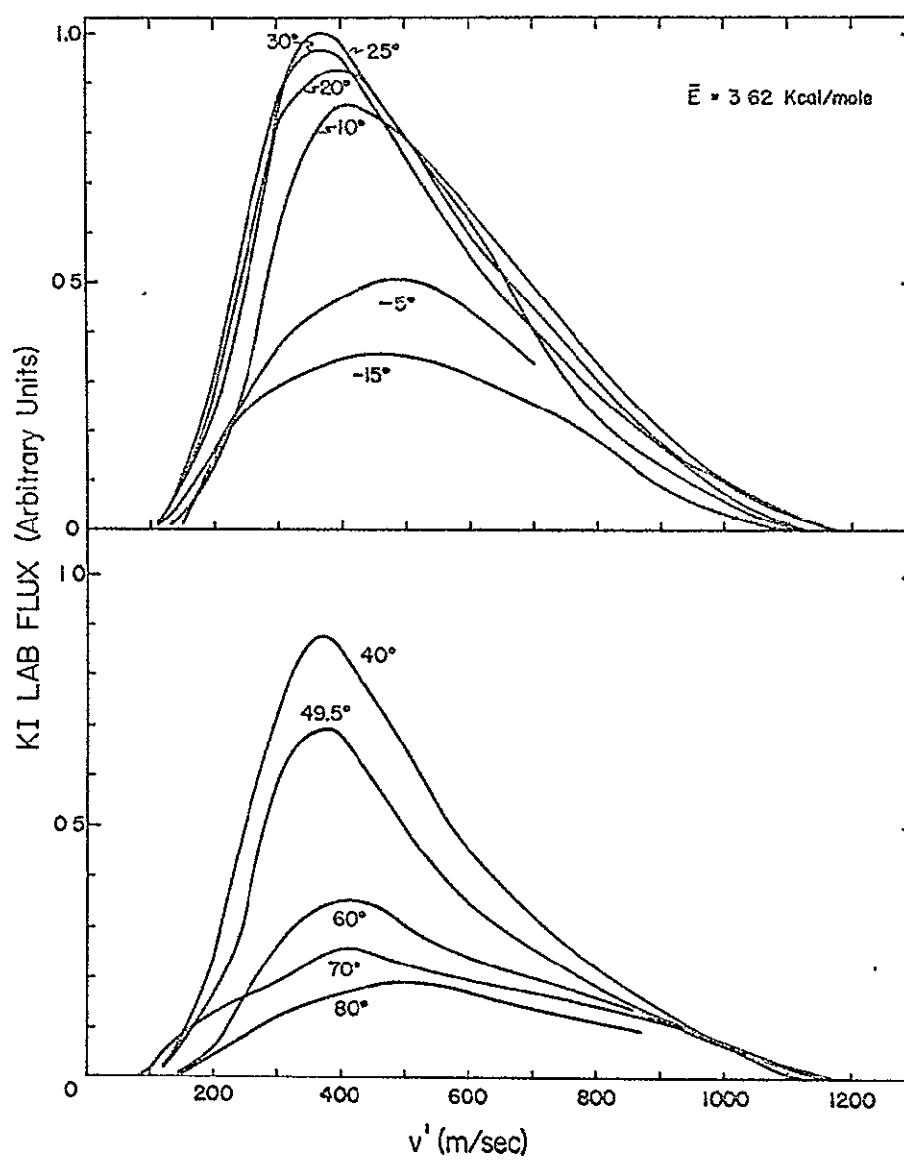


Fig. IV-25

Figure IV-26 Laboratory Angular Distribution of KI

Total laboratory angular distributions of KI reactive product.

Upper: Results of Birely et al.¹⁶ (crossed Maxwellian beams, nominal $\bar{E} = 1.58$ kcal/mole) by subtraction of "unsensitized" angular distributions from sensitized angular distributions. Arbitrarily normalized to unity at peak. Errors (as shown) become large at angles near the K direction.

Lower: Present results at three \bar{E} . Data at $\bar{E} = 2.67$ kcal/mole arbitrarily normalized to unity at $\Theta = 25^\circ$; data at other energies normalized to the same incident K beam flux. Circles (O) are derived from angular distributions as above (Figures IV-5,6,7); triangles (∇) are obtained by integrating the KI product velocity distributions of Figures IV-23,24,25 and normalizing the three different data sets to the same incident K beam flux. As above, errors are largest at small Θ .

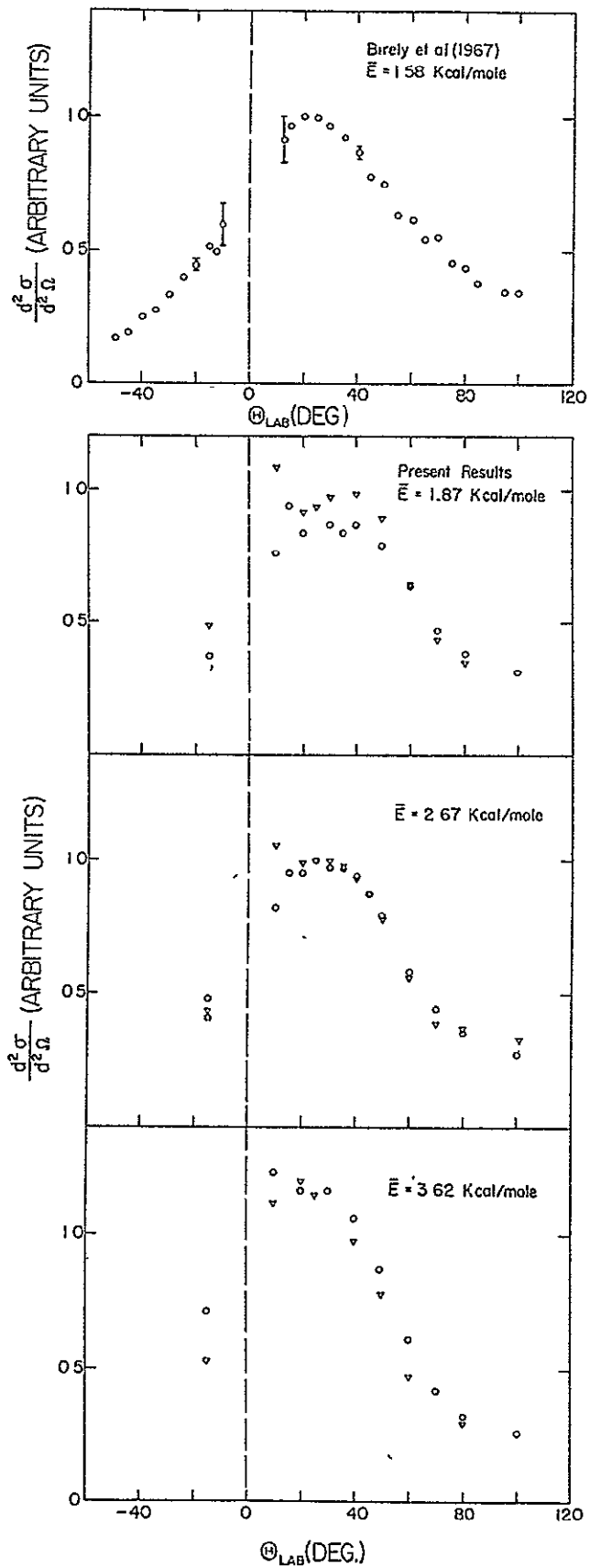


Fig. IV-26

distributions. The present results which have been corrected for residual KI sensitivity in the U mode, are shown (O) in the same figure; again the three curves are normalized to the same total incident K beam flux. The laboratory angular distribution of KI changes very little with incident energy, moving slightly towards lower angles at the highest energy. That effect results from the shift of centroid with energy; the centroid shift is also responsible for the higher laboratory intensities at 3.62 kcal/mole (this will not be the case in the c.m. system after proper transformation). Shown for comparison are the results of Birely et al.¹⁶ who used two thermal (non-selected) beams at a nominal $\bar{E} = 1.58$ kcal/mole. The distributions are quite comparable; all become quite uncertain in the vicinity of the K beam due to interference from the very large non-reactive K scattering.

Another way of presenting the results of Figs. IV-23,24,25 is in the form of laboratory polar (velocity-angle) flux contour maps^{27,40-42} of reactive KI product. Figure IV-27 gives these contour maps at the three different incident relative energies (each separately normalized). Note again the lack of data near the K beam, necessitating interpolation of the contours through the zero degree line. Also indicated on each contour map are:

- a) a cross hatched "half-intensity" centroid ellipse that indicates approximately the range of centroids around the nominal value;
- b) the angles at which velocity analysis data of KI exist (the length of each line indicates approximately the velocity range of the KI data at that angle);

Fig. IV-27 KI Laboratory Polar (Velocity-Angle) Flux Contours

Contour maps of KI laboratory flux distributions, $\frac{d^3\sigma}{d^2\Omega dv'}$, superimposed upon the "nominal" Newton diagrams at three \bar{E}' 's. Each distribution normalized to 10 in the peak region. The dashed contours represent interpolations of the data into regions where the K intensity was too large to obtain reliable reactive product data. The angles labelled are those at which velocity analyses for KI were taken; the length of the line at each angle indicates approximately the velocity range of the data at that angle. E'_{\max} is the thermodynamic limit for KI product from a collision with "nominal" incident energy. The cross-hatched ellipse specifies the "half-range" of centroids; the perimeter of the ellipse is the half-intensity contour for the centroid distribution. Enlargements of the three separate laboratory contour maps are given in Figures D-1,2,3.

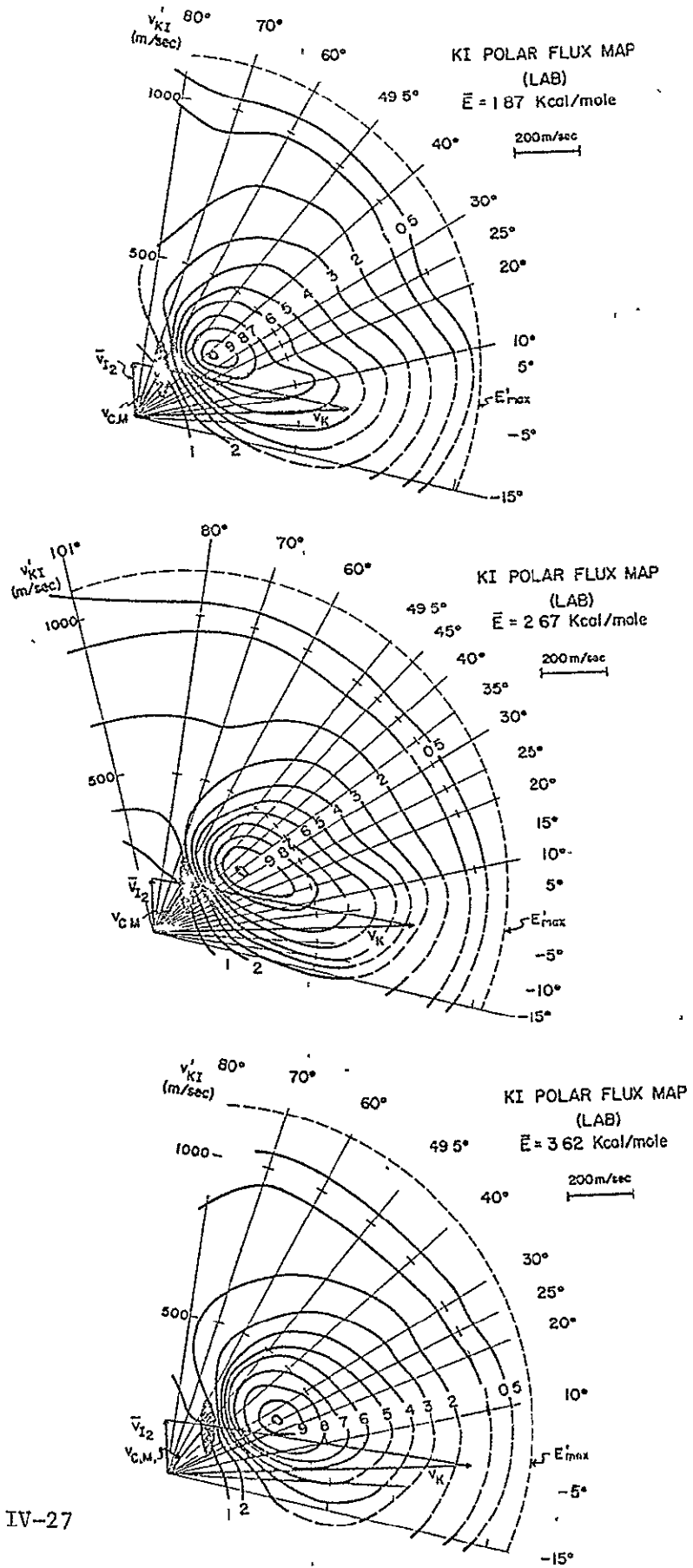


Fig. IV-27

- c) A dashed circle (origin at the nominal centroid) which indicates the laboratory velocity limits corresponding to the (nominal) maximum possible translational product energy E'_{\max} .

Table IV-2 illustrates the calculations involved in determining E'_{\max} .

The total energy (see Fig. I-1) available to the KI + I products is

$$E_{\text{total}} = \bar{E} + \bar{E}_{\text{int}}(I_2) + \Delta D_0 .$$

This energy is distributed between internal energy (E'_{int}) and translational energy (E') of the products

$$E_{\text{total}} = E'_{\text{int}} + E' .$$

If all the energy is released as relative translation (i.e., $E'_{\text{int}} = 0$), the KI reactive product would be found on the dotted circle E'_{\max} of Fig. IV-27, with a c.m. velocity

$$w'_{\max, KI} = \frac{m_I}{m_{KI} + m_I} \left(\frac{2E'_{\max}}{\mu'} \right)^{1/2}, \text{ where } \mu' = \frac{m_I m_{KI}}{m_I + m_{KI}} . \text{ The}$$

collision exothermicity Q , defined by $Q = (E'_{\text{translation}} - \bar{E})$, is the difference in relative translational energy of the reactants and products. The c.m. velocities corresponding to $Q = 0$ ($E' = \bar{E}$) are also indicated in Table IV-2 (again for the energies corresponding to the average velocities in the two beams).

Table IV-2 Nominal Reaction Conditions

(Energies in kcal/mole;

velocities in m/sec)

\bar{v} (I_2)	172		
\bar{E}_{rot} (I_2)	0.68		
\bar{E}_{vib} (I_2)	0.42		
\bar{E}_{int} (I_2)	1.10		
D_o (I_2)	35.54	^{43a}	
D_o (KI)	76	^{43b}	
ΔD_o	40.5		
<hr/>			
\bar{v}_K	657	794	930
v_{rel}	679	812	946
\bar{E}	1.87	2.67	3.62
E_{total}	43.5	44.3	45.2
$w'_{\text{KI,MAX}}$	975	984	994
$w'_{\text{KI,Q=0}}$	202	242	281

The laboratory flux contour maps are proportional to $\frac{d^3\sigma}{d^2\Omega dv'}$, the differential scattering cross section into a laboratory (solid angle-velocity) volume element; the quantity of fundamental interest is the equivalent expression in the c.m. system, $\frac{d^3\sigma}{d^2\omega dw'}$. Various approaches to extracting the differential c.m. cross sections are described in detail in Appendix B. The results for $K + I_2$ are presented here.

2. "Nominal" Inversion

The simple nominal inversion involves a Jacobian transformation to the c.m. using a single "nominal" c.m. location defined by use of a "most probable" vector triangle. This specifies (w', θ) for every (v', θ) (as illustrated in Fig. I-1b), giving $\left(\frac{d^3\sigma}{d^2\omega dw'}\right) = \frac{w'^2}{v'^2} \left(\frac{d^3\sigma}{d^2\Omega dv'}\right)$. Although beam velocity distributions are neglected, the c.m. differential cross sections obtained (Fig. IV-28) are reasonably good as a first approximation.

The results in Fig. IV-28 are also useful in determining whether the assumption of ideal effusive flow conditions for the I_2 beam is justifiable. There is necessarily an axial symmetry in the c.m. scattering around the "nominal collision axis"; supplementary calculations have shown that use of the average velocity for both beams defines a relative velocity around which there is approximate axial symmetry even when including the effects of beam distributions; the axis so defined is thus the proper "nominal collision axis". The vector diagrams of Fig. IV-28 are drawn using the average beam velocities $\bar{v}_{I_2} = \left(\frac{8}{\pi} \frac{kT}{m}\right)^{1/2}$ assuming a M-B secondary beam; the

Fig. IV-28 "Nominal Inversion" c.m. Contours

Polar c.m. contour maps $\left(\frac{d^3\sigma}{d^2\omega dw'}\right)$ of KI flux obtained by a "nominal inversion" from the lab. data at each \bar{E} . Included are the laboratory velocity vector (Newton) diagrams used for the inversion; w' and v' are shown for a typical point. Each distribution normalized to 10 in peak region. Dashed contours are interpolations as in Figure IV-27. Indicated angles and velocities are relative to the c.m. coordinate system.

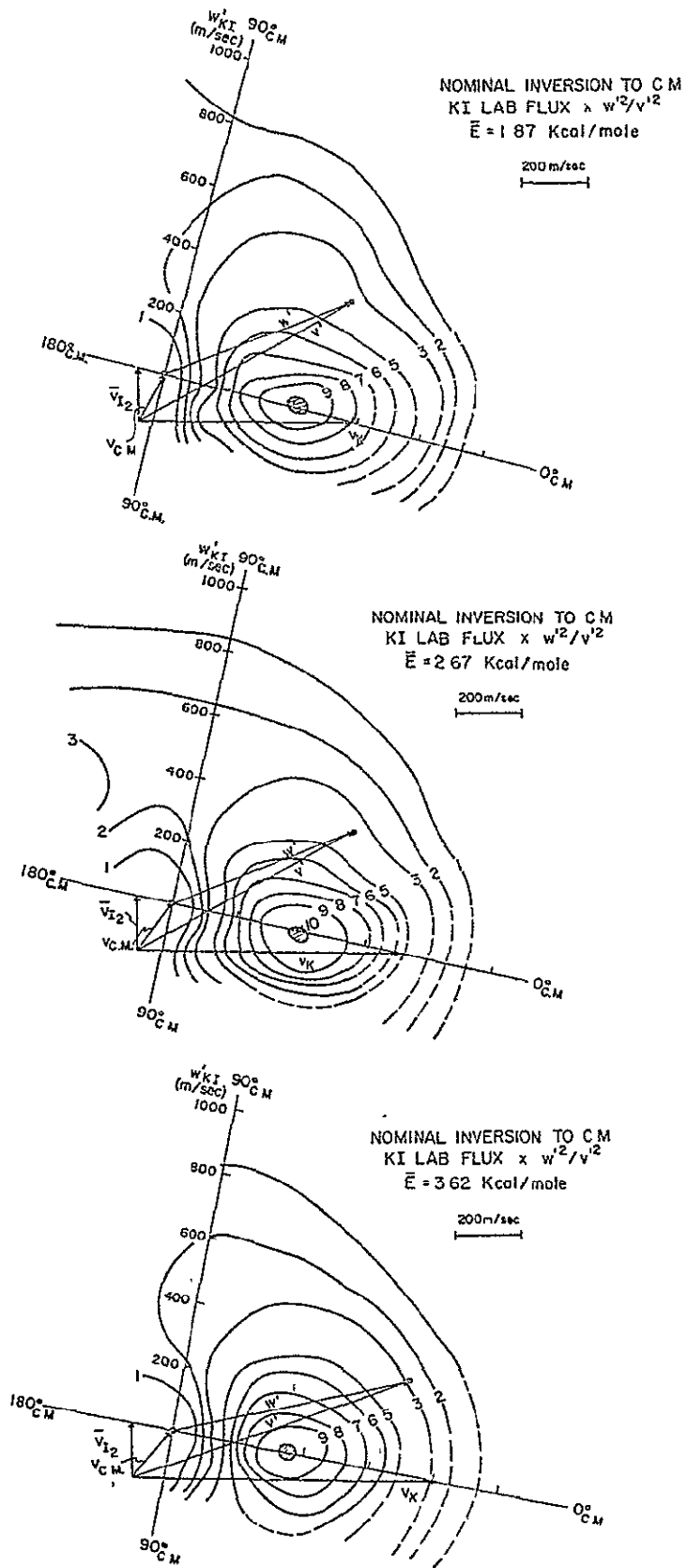


Fig. IV-28

symmetry evident around 0° c.m. confirms the assumption of effusive flow for the I_2 beam. In other work^{40,42} cartesian flux maps $(\frac{1}{v})^2 \frac{d^3\sigma}{d^2\Omega dv'}$ have been used in presenting data; the transformation from laboratory to cartesian data removes the dependence on laboratory framework (as do the nominal inversion contours), but without making any assumptions as to the c.m. location^{40e,42}. Hence the same test of symmetry can be made in the cartesian presentation,⁵⁸ with the added convenience that the "proper" nominal collision axis can be located graphically rather than by assumption followed by verification as in the nominal inversion. A difficulty arises with the cartesian presentation in cases where the scattering intensity peaks rather far from centroid; the cartesian plot (equivalent to $\frac{1}{w} \frac{d^3\sigma}{d^2\omega dw'}$) puts strong emphasis $(\frac{1}{w})^2$ on scattering near centroid where the intensity is changing very rapidly $(\frac{1}{w} \frac{d\sigma}{dw'})$ peaks at a velocity where $\frac{d\sigma}{dw} \propto w'^2$ in the c.m. (and in the laboratory). Since this is a region of relatively unreliable data, difficulties arise in checking the zero degree symmetry condition; in these instances (e.g., $K + I_2$) nominal inversions, which properly emphasize the relatively intense data, prove to be more helpful.

3. C.m. \rightarrow Lab. Computations.

The c.m. \rightarrow lab. inversion scheme⁴⁴ involves guessing a c.m. function, averaging over the beam velocity distributions to produce a map of the associated laboratory distribution, comparing with the data, and adjusting the c.m. function to obtain a better fit.

The c.m. map of Fig. IV-29 is an uncoupled (factorized)

$\left(\frac{d^3\sigma}{2 d\omega d\omega'}\right) = P_\omega(\theta) \times P_f(\omega')$ angle-velocity distribution function; this

function was, however, not obtained by the "guess and adjust" method

of the c.m. \rightarrow lab. inversion technique, but was extracted from the full

polynomial inversion methods illustrated below. It serves to illustrate

the c.m. \rightarrow lab. transformation method (in the uncoupled approximation).

Fig. IV-29 also shows the laboratory scattering contours produced by this uncoupled c.m. function (after averaging over the beam distributions at $\bar{E} = 3.62$ kcal/mole; see program KICM in Appendix C) along with the corresponding experimental data contours (this calculation was only done for the 3.62 kcal/mole data). The lack of laboratory scattering data beyond $\Theta = 80^\circ$ implies an almost complete lack of knowledge of the c.m. results beyond $\theta \sim 90^\circ$ (except at low velocities); this is why the c.m. angular distribution and contour map in Fig. IV-29 have dashed regions at high angles.

The $\theta = 180^\circ$ peak is a purely mathematical consequence of the expansion functions used in describing the angular distribution at angles below 90° ; this in no way implies the existence of a "backward" rise in the angular distribution since there are no data relevant to $\theta \gtrsim 90^\circ$. The computed laboratory contours (Fig. IV-29) seem to be a reasonably good fit to the data. However, results (below) with a general coupled c.m. function will be seen to be superior.

4. Lab. \rightarrow c.m. Inversion

The general coupled two-dimensional (velocity-angle) Legendre basis function expansion method is described in Appendix B

Fig. IV-29 Uncoupled c.m. Distribution Function

Upper: An uncoupled ($P(\theta, w') = P_f(w') P_\omega(\theta)$) c.m. distribution function used as an example in the c.m. \rightarrow lab. averaging program (Program KICM, Appendix C). This function is also the starting guess $I_o(\theta, w') = F_o(w') G_o(\theta)$ used in the iterative lab. \rightarrow c.m. inversion (Program I2LEG, Appendix C). The c.m. contour map is normalized to 10 in the peak region. Inserts show the uncoupled c.m. velocity, $P_f(w')$, and angle, $P_\omega(\theta)$, functions. Dashed contour lines are for portions of c.m. map outside range of experimental data (see below).

Lower: Comparison of experimental lab. data $\frac{d^3\sigma}{d^2\Omega dv'}$. (Solid contours, long dashed interpolations through K beam region) at $\bar{E} = 3.62$ kcal/mole with computed distributions (dashed contours, short dashed interpolations through K beam region) obtained by use of the uncoupled c.m. map (upper) in averaging program KICM. Both distributions normalized to 10 at peak. Angles indicated are limits of range of experimental data.

UNCOUPLED C.M. MAP

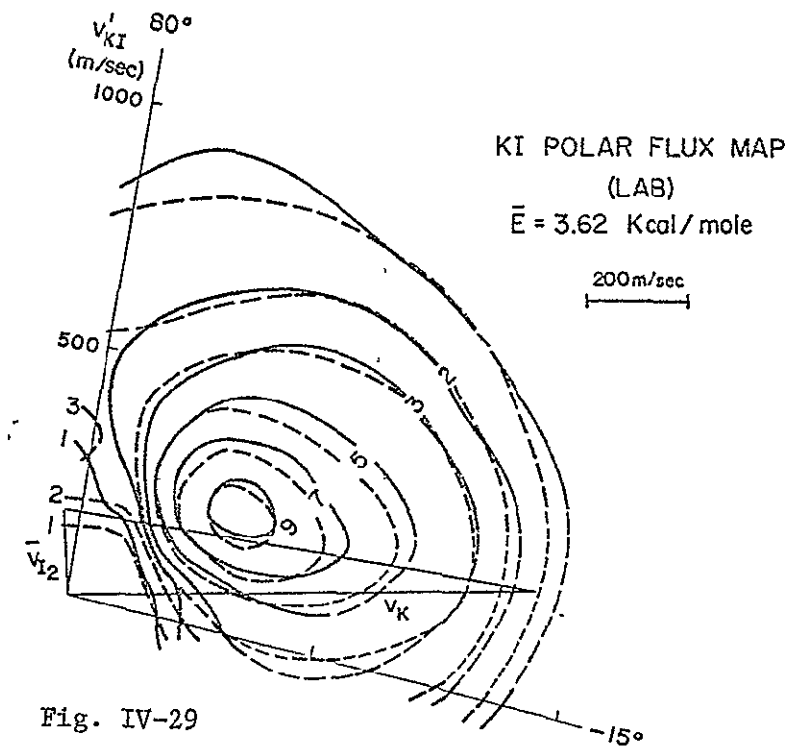
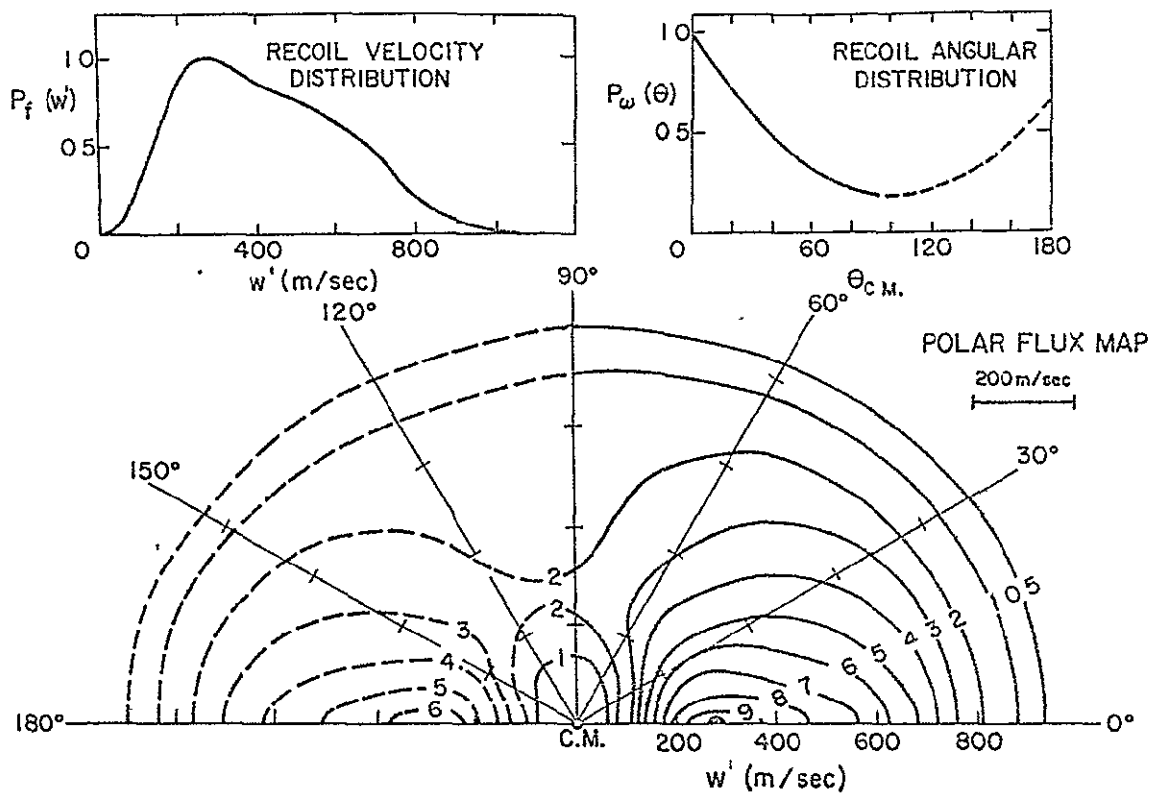


Fig. IV-29

(see Eqn.B2). In the best set of Lab. \rightarrow c.m. inversion results (example: Program I2LEG in Appendix C) the uncoupled c.m. function shown in Fig. IV-29 was used as a starting guess, $F_0(w') G_0(0)$, which was then altered by 30 term Legendre expansions to produce three coupled c.m. functions compatible with the three different laboratory data sets. The three different c.m. differential cross sections, $\frac{d^3\sigma}{d^2\omega dw'}$ are shown in Fig. IV-30 each one labelled with the \bar{E} of the experimental data from which the c.m. function was obtained. These c.m. polar flux distributions are considered the best estimates obtained for the shapes of the c.m. differential cross sections at the three different \bar{E} .

Several aspects of the results are now discussed:

- a) The $0^\circ - 180^\circ$ line is the relative velocity vector and there must be perfect axial symmetry around this line. Laboratory data "on both sides" of this line have been averaged in the computations producing the c.m. distribution. The full distribution would show an identical reflection of the contours through this $0^\circ - 180^\circ$ line; an example showing the redundant reflected contours can be seen in a c.m. contour map on page 174.
- b) Although the polynomial expansion gives values for the c.m. function beyond the reach of any experimental data, this extrapolated function is an artifact having only mathematical significance. The extrapolated c.m. data have no constraints imposed since

Fig. IV-30 KI Polar c.m. Contour Maps

Best KI c.m. differential cross section functions, $\frac{d^3\sigma}{d^2\omega d\omega'}$, obtained from the three different laboratory data contour maps. Each was obtained by data inversion from lab. to c.m. using the iterative Program I2LEG (Appendix C). All three normalized to 10 in peak region. The vectors \vec{w}_{I_2} and \vec{w}_K are the nominal c.m. values; the dashed energy circles E_{\max} are the thermodynamic limits for nominal collision conditions at each \bar{E} . Enlargements of the three separate c.m. contour maps are given in Figures D-4,5,6. Expansion coefficients are given in Appendix E.

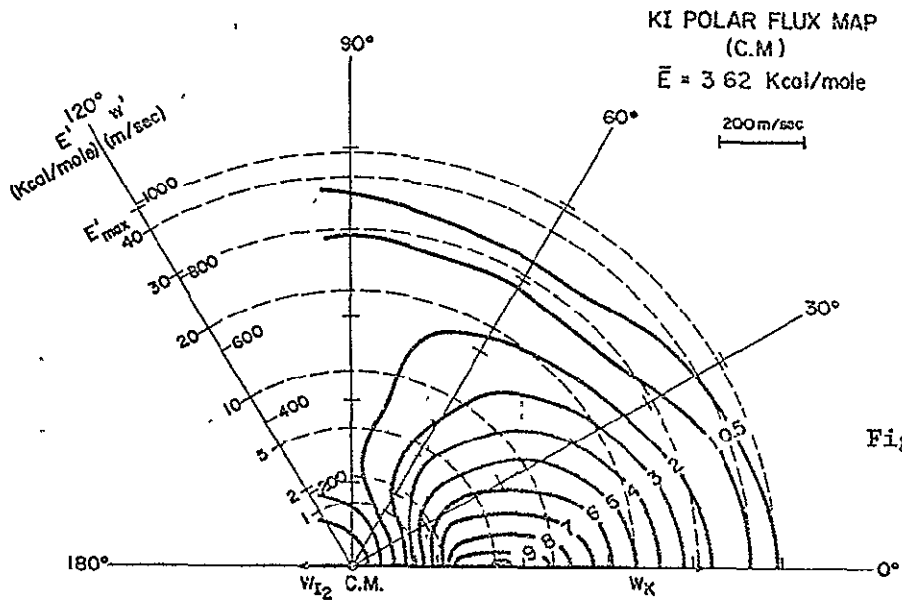
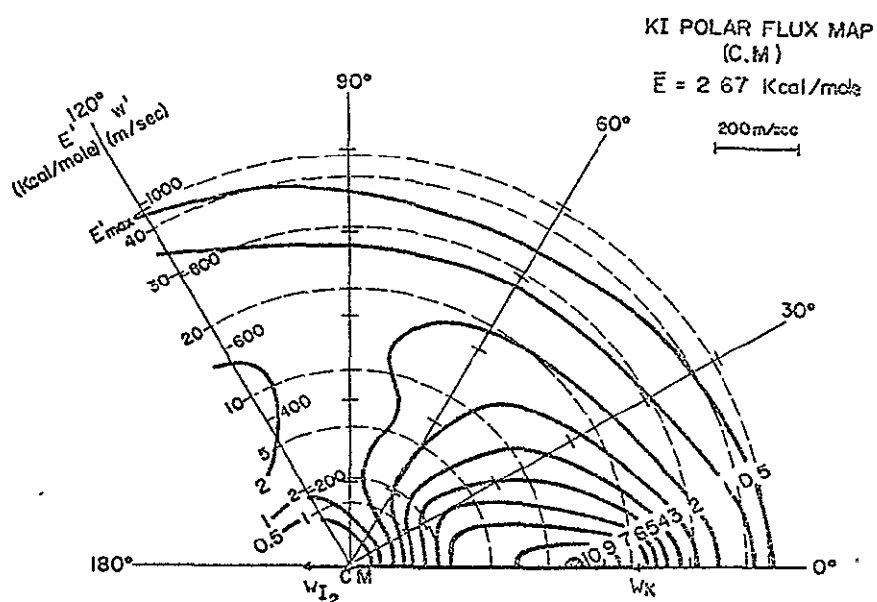
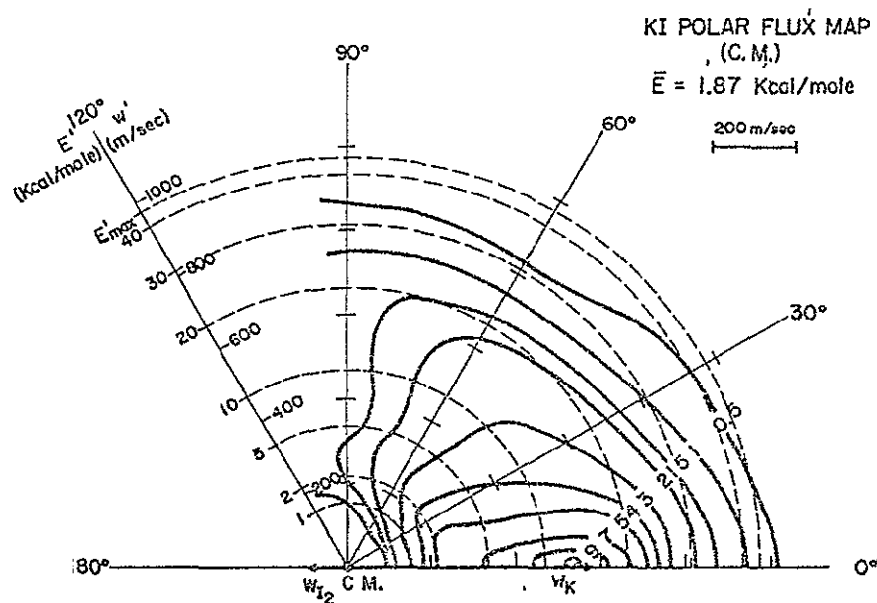


Fig. IV-30

there are no data to match; hence the extrapolation blows up wildly (and quite differently for each set of trial functions) outside the regions of experimental data. For this reason the c.m. flux maps give little valid information beyond $\theta \sim 120^\circ$ at 2.67 kcal/mole and $\sim 90^\circ$ at the two other energies; therefore the contours are not shown beyond these angles.

- c) It should also be noted that the large intensity, forward scattered K beam interfered with data near the $\theta = 0^\circ$ region (see dashed portions of contours on data maps, Fig. IV-27); the data matched by the computer did not include any data in this uncertain region. In consequence, the contours in the $0^\circ - 10^\circ$ region in the c.m. represent an extrapolation similar to the one at high angles. This yields some uncertainty in the contour maps near the 0° line.
- d) Velocity and energy scales are included for convenience in estimating product excitation; the E'_{\max} circles are the same nominal ones shown in Fig. IV-27.

Comparison of the c.m. functions at the three different incident energies shows more similarities²⁴ than differences associated with variation of the relative kinetic energy:

- i) The general overall shapes of the three functions are quite similar with the possible exception of the zero degree region at high velocities (this region contains

a mild extrapolation (see (c) above) of the contours due to the large K intensities interfering with any direct KI product intensity measurement; hence the effect may not be real).

- ii) All three functions peak strongly "forward" in angle, yet still have a significant tail at $\theta = 90^\circ$ (the large angle data at 2.67 kcal/mole suggest a possible smaller backward peak in the c.m. distribution).
- iii) The velocity distributions indicate low product translational energies for each experiment; this implies large internal excitation of the products. Product c.m. energy (rather than velocity) distributions, needed for quantitative determinations of energy partitioning, will be shown later.
- iv) The double-humped contours at large angles (found at each \bar{E}) are extremely provocative; these show up even more prominently in (w') velocity distributions (cuts through these contour maps at various c.m. angles).
- v) There exists a significant coupling of the c.m. velocity-angle distribution functions; this also is demonstrated more clearly in the velocity cuts.

Figs. IV-31,32,33 show the three calculated laboratory flux contour maps (based on the three best c.m. functions of Fig. IV-30) superimposed on the corresponding sets of laboratory data. The most satisfactory fits are at the two higher energies (where the data are

Figs. IV-31,32,33 Computed Fits to Laboratory KI Contours.

Best fits produced to the three sets of laboratory flux contour maps, $\frac{d^3\sigma}{d^2\Omega dv'}$, using the three c.m. differential cross section functions of Fig. IV-30. At each energy the lab. contours are solid lines (long dashed interpolations through 0° line); the computed contours are dashed (with short dashed interpolations through 0°). Lab. contours normalized to 10 at peak; computed contours normalized for best least squares fit to lab. data. Angles indicated are limits of range of experimental data.

Fig. IV-31 $\bar{E} = 1.87$ kcal/mole

Fig. IV-32 2.67

Fig. IV-33 3.62

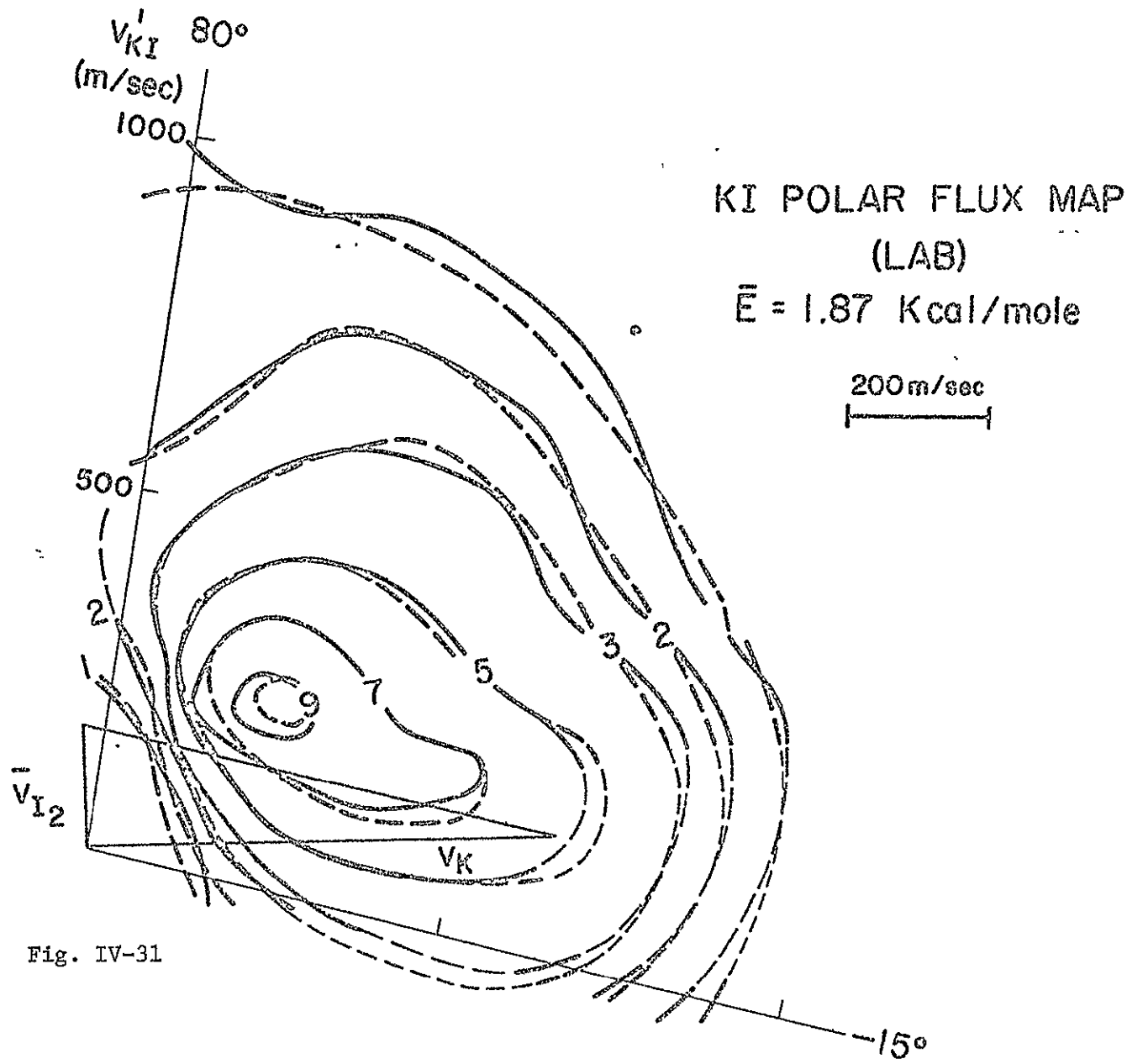


Fig. IV-31

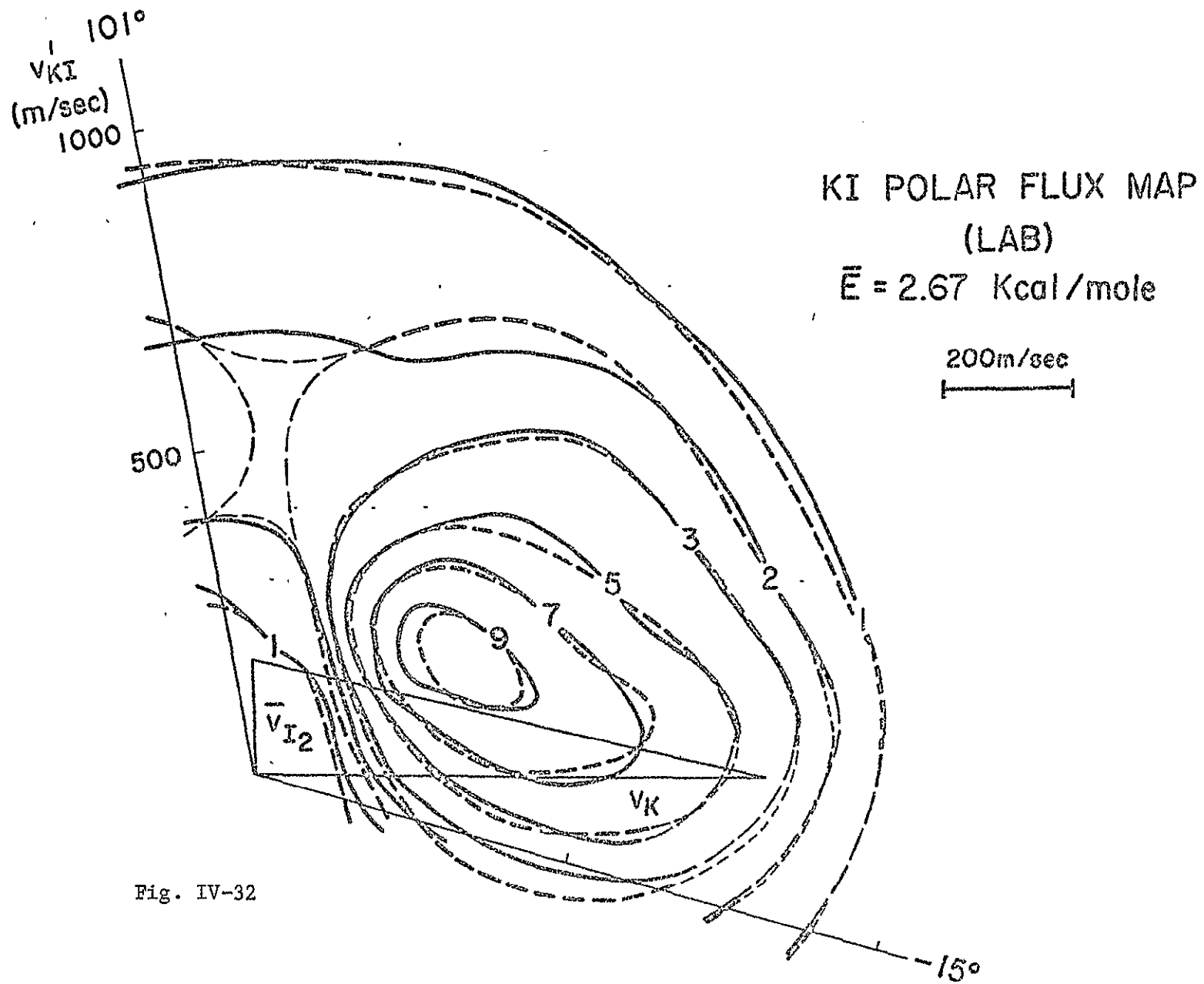


Fig. IV-32

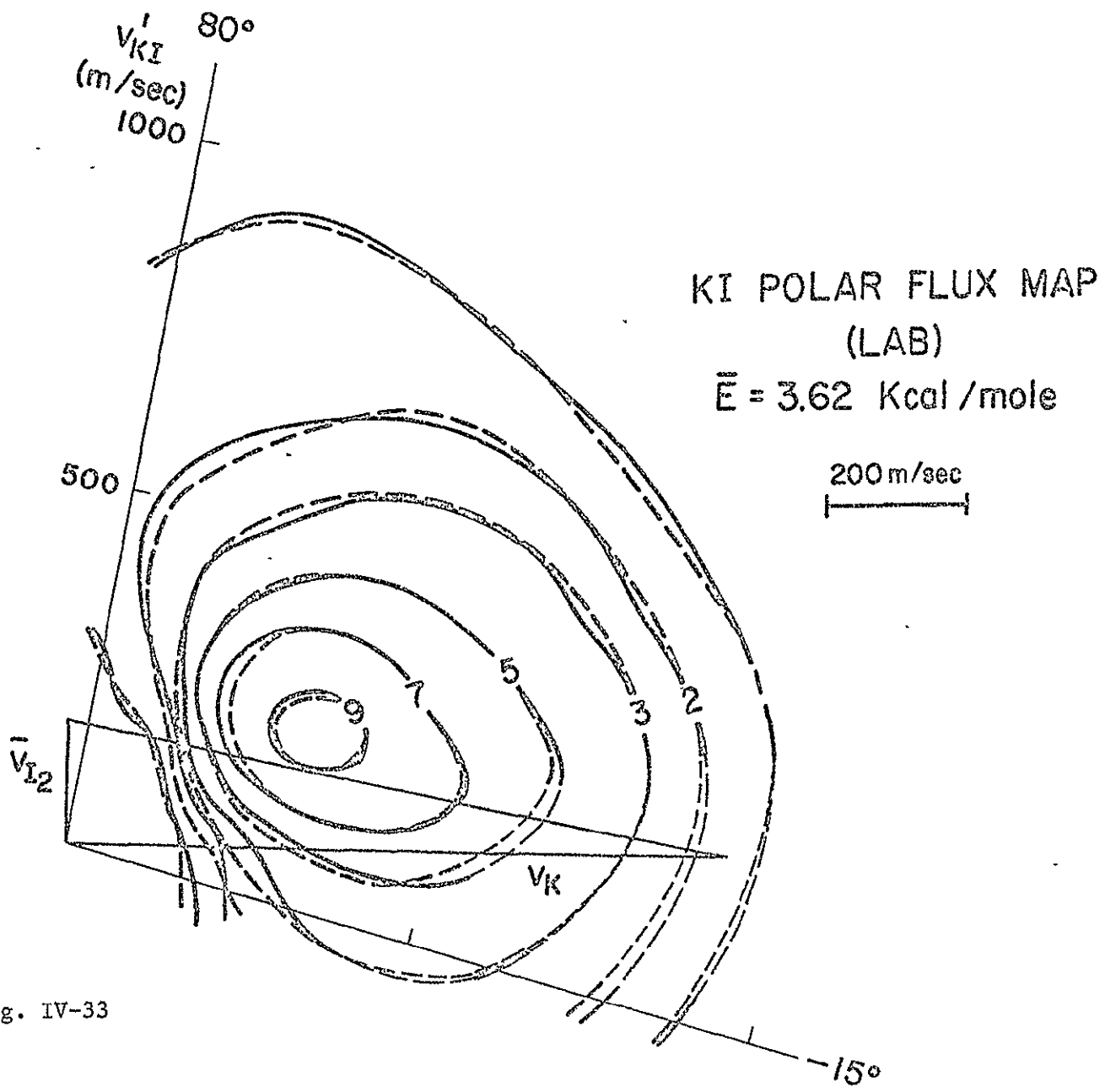


Fig. IV-33

considered superior). The computed maps appear generally "smoother" than the data contours, but are otherwise good fits.

The laboratory velocity-angle co-ordinates at which the computations attempted to match the experimental intensities are shown in cuts through the laboratory data maps in Figs. IV-34,35,36. The (smoothed) data to be matched are the points (all properly normalized at a given \bar{E}); the best computer fits to these points are represented by the (computer-generated) velocity analysis cuts. The agreement also appears satisfactory in this representation for all three experiments; yet a slight inability to match the data points of highest intensity (at all three energies) appears more clearly in these "cuts" than in the data contour maps of Figs. IV-31,32,33.

5. Out-of-Plane Contributions

Returning to the best c.m. contour maps (Fig. IV-30) one observes that the quantity plotted is $\propto \frac{d^3\sigma}{d^2\omega dw'}$. The necessity of azimuthal symmetry (around the relative collision axis) allows one to account for the out-of-plane contributions to the reactive scattering by integrating over ϕ ;

$$\frac{d^2\sigma}{d\theta dw'} = \int_0^{2\pi} \frac{d^3\sigma}{d^2\omega dw'} \sin \theta d\phi = 2\pi \sin \theta \frac{d^3\sigma}{d^2\omega dw'} \quad (5)$$

In Fig. IV-37 are shown the $\sin \theta$ - weighted c.m. flux contours, $\frac{d^2\sigma}{d\theta dw'}$ of Eq. (5). This presentation, in accounting for all of the out-of-plane intensity, weights each angle according to

Figs. IV-34,35,36 Computed Fits to Laboratory Velocity Analyses

Best fits produced to the laboratory velocity analysis flux data (i.e., cuts through contour maps) using the three c.m. distribution functions of Fig. IV-30. The symbols indicate the set of smoothed data points at which the computations attempted a best least squares fit to the data. The resultant best computed fits to the velocity analyses are represented by the (point-wise connected) solid lines. Linear scales on all curves.

Fig. IV-34 $\bar{E} = 1.87$ kcal/mole

Fig. IV-35 2.67

Fig. IV-36 3.62

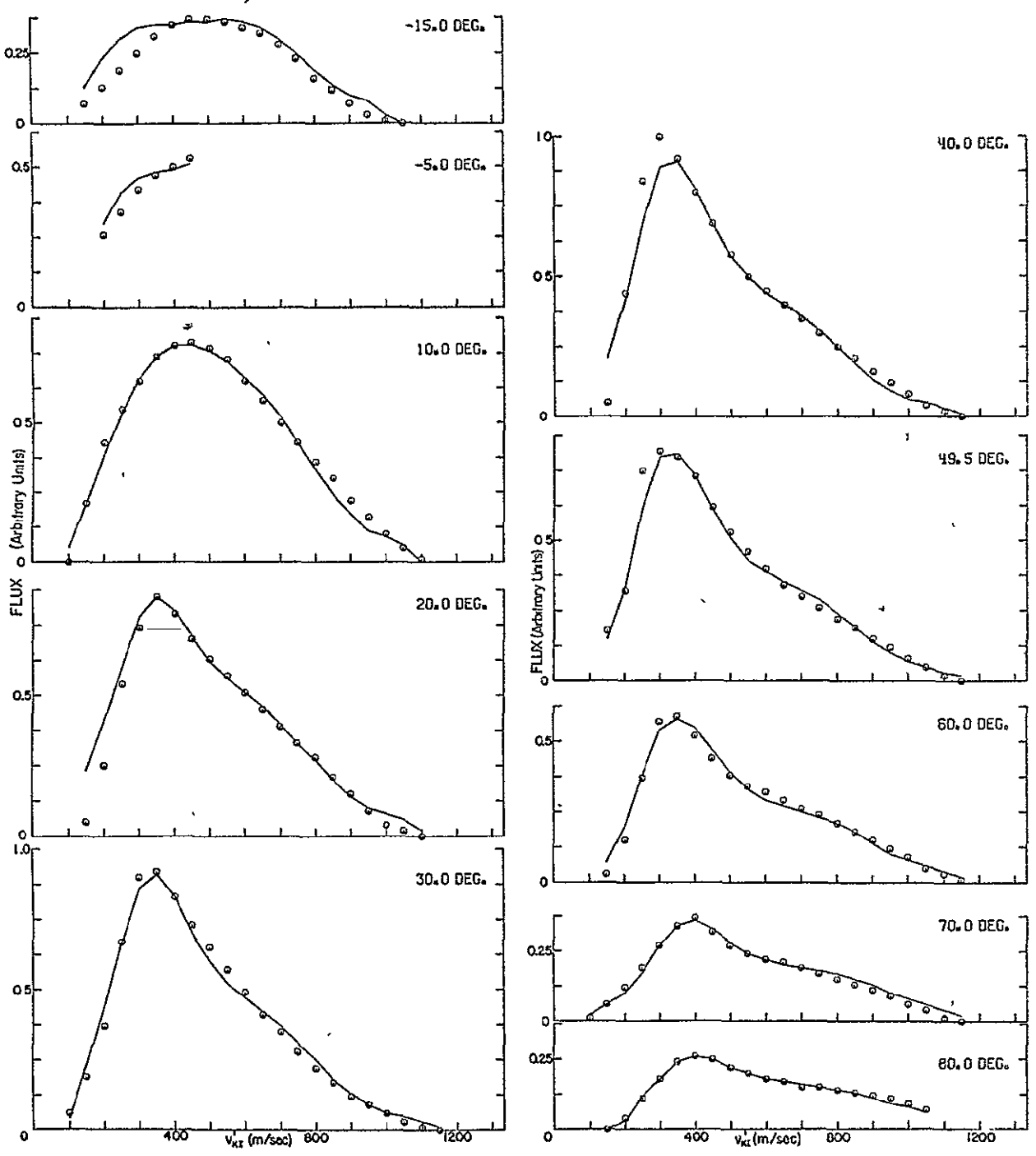


Fig. IV-34

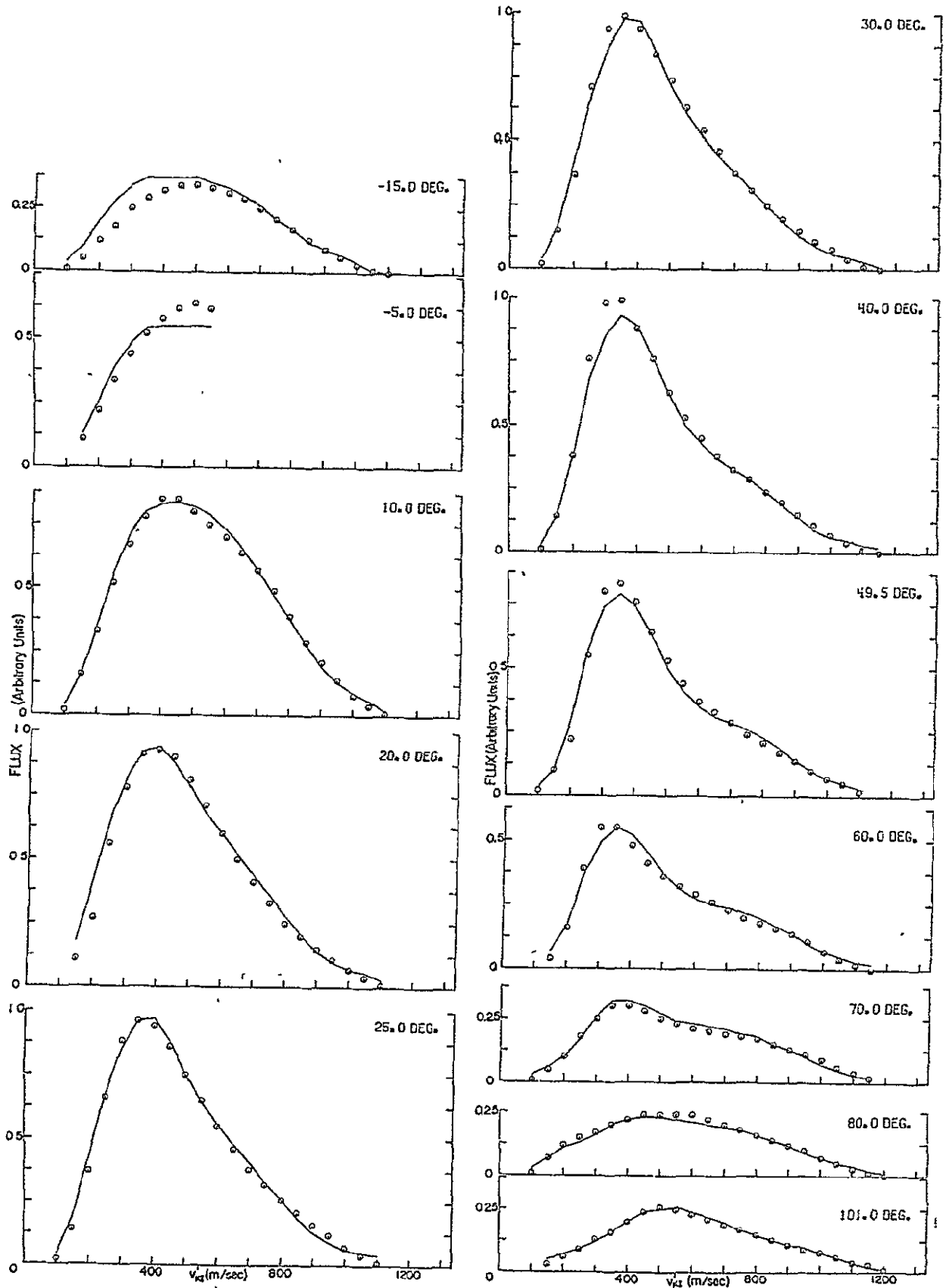


Fig. IV-35

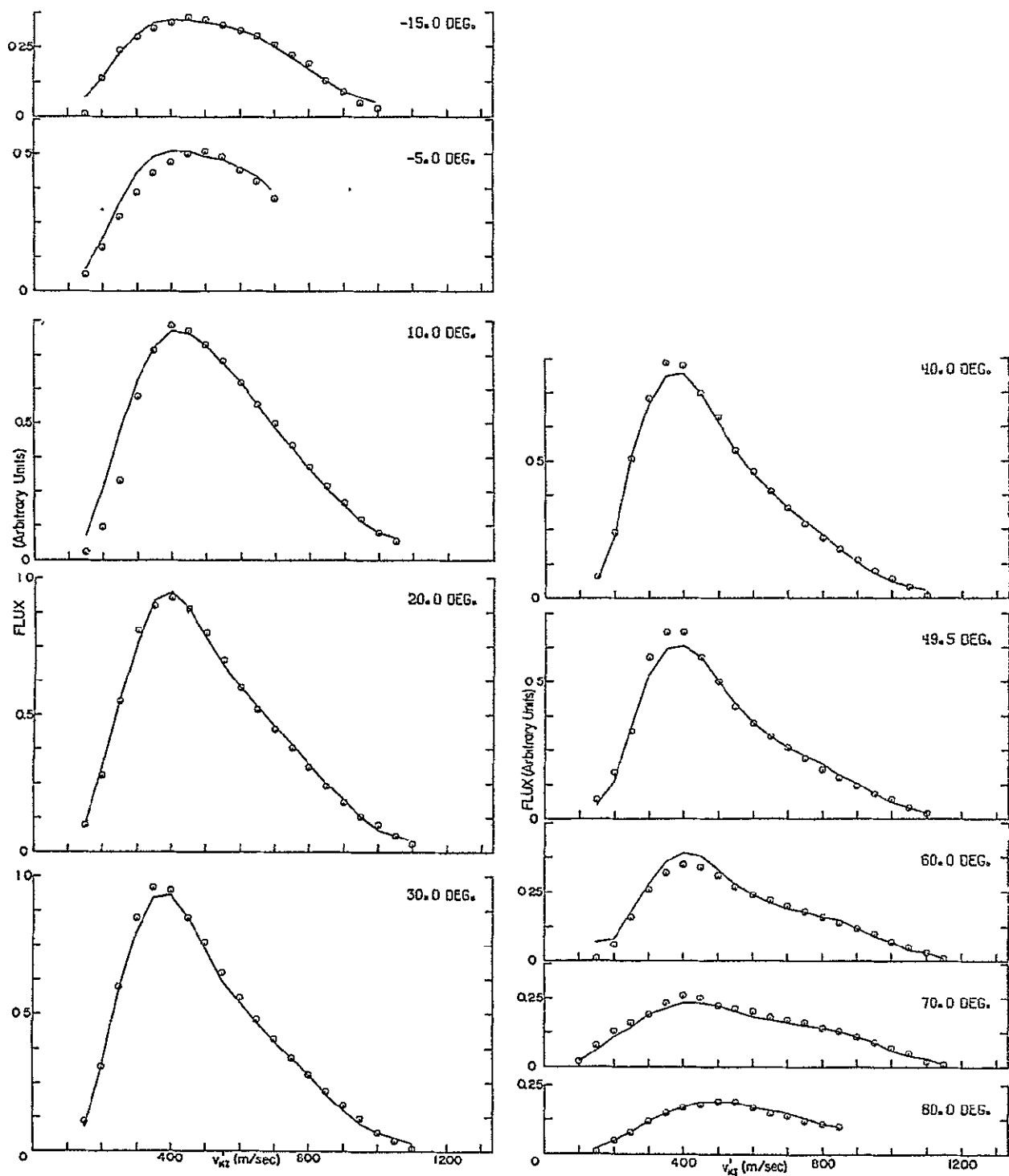
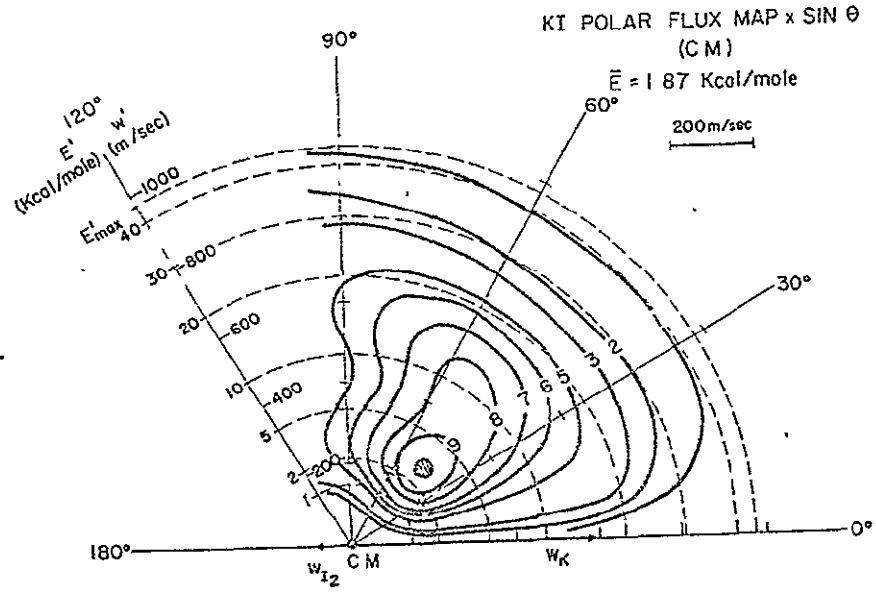


Fig. IV-36

Fig. IV-37 KI c.m. Contour Maps, Weighted by $\sin \theta$.

Best KI c.m. differential cross section functions $\frac{d^2\sigma}{d\theta dw'} \propto \sin\theta \frac{d^3\sigma}{d^2\omega dw'}$, obtained from the distributions shown in Fig. IV-30. These distributions account for out-of-plane scattering contributions and show the relative contributions to the total reactive cross section at every (θ, w') co-ordinate. Each contour map normalized to 10 in the peak region. The vectors \vec{w}_{I_2} and \vec{w}_K are the nominal c.m. values; the dashed circles E'_{\max} are the thermodynamic limits for nominal collision conditions at each \bar{E} .



its relative contribution to the total reactive cross section.

Again the similarities among the $\frac{d^2\sigma}{d\theta dw}$ contour maps at the three different energies are more striking than the differences. The $\sin \theta$ factor removes the perhaps undue emphasis normally placed on the low angle region; the worries about extrapolation to $\theta = 0^\circ$ are conveniently removed in this presentation.

6. Total Reactive Angular Distributions (c.m.)

Fig. IV-38 also emphasizes the effect of the out-of-plane contributions; it gives the total c.m. angular distributions obtained by integrating over w' . The top portion of the figure shows the conventional differential reactive cross section $\frac{d^2\sigma(\theta)}{d^2\omega} (= \int \frac{d^3\sigma}{d^2\omega dw'} dw')$, forward peaked, with all three curves (at the three different energies) normalized to unity at $\theta = 0^\circ$. The bottom, $\sin \theta$ -weighted curves of $\frac{d\sigma(\theta)}{d\theta} (= \int \frac{d^2\sigma}{d\theta dw'} dw')$ account for the out-of-plane scattering; each curve is set equal to unity at its peak. The dashed extension of the 2.67 kcal/mole distribution is an estimate based on the conclusion of Birely et al.¹⁶ that the c.m. angular distribution $\frac{d^2\sigma(\theta)}{d^2\omega}$ is approximately flat at c.m. angles beyond 120° .

7. Velocity and Energy Distributions (c.m.)

Another way of viewing the c.m. velocity-angle contour maps is by taking cuts through the maps at different c.m. angles, as shown in Fig. IV-39. At each angle the cut is weighted by $\sin \theta$; hence the curves are equivalent to slices through the c.m. function $\frac{d^2\sigma}{d\theta dw}$, and the intensities are proportional to relative contributions

Fig. IV-38 Computed c.m. KI Angular Distributions

Upper: Angular distributions of reactive KI product

$\frac{d^2\sigma(\theta)}{d^2\omega}$ obtained by integration over the best c.m. velocity distributions (e.g. Fig. IV-39). Different symbols for each of the three \bar{E} . All three normalized to unity at 0° .

Lower: Weighted c.m. angular distributions of reactive KI product

$\frac{d\sigma(\theta)}{d\theta} \propto \sin\theta \frac{d^2\sigma(\theta)}{d^2\omega}$. These distributions account for out-of-plane scattering contributions;

intensity at any angle is directly proportional in this representation to its relative contribution to the total reaction cross section. Each curve normalized to unity at its peak. The $\bar{E} = 2.67$ kcal/mole distribution has been extrapolated to 180° based approximately on the large angle c.m. reactive KI results of Birely et al.¹⁶

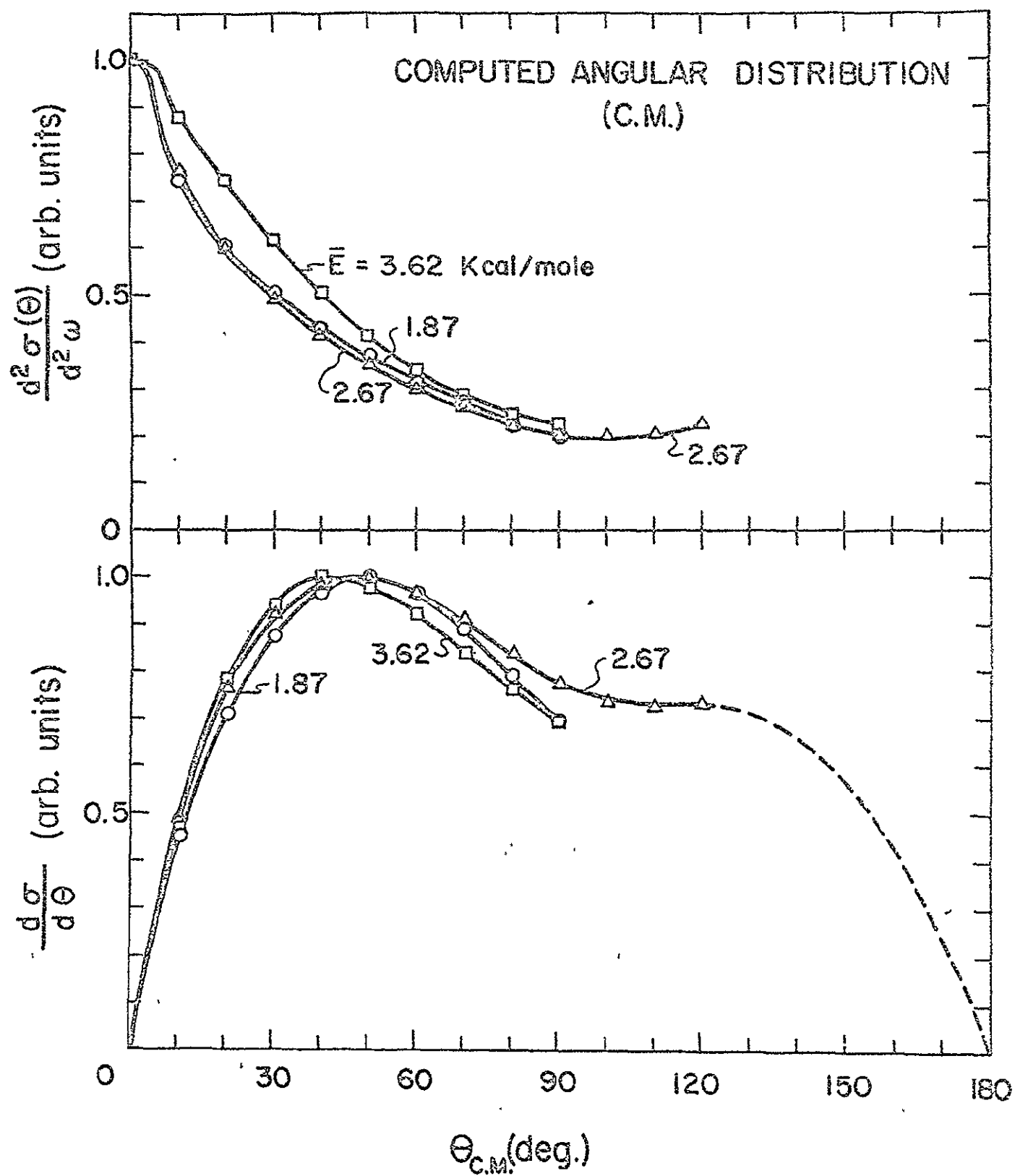


Fig. IV-38

Fig. IV-39 KI c.m. Recoil Angle-Velocity Distributions

Slices at various (designated) c.m. angles θ through the $\frac{d^2\sigma}{d\theta dw'}$ c.m. contour maps of Figure IV-37. At each \bar{E} , the nominal velocities corresponding to $Q = 0$ ($E' = \bar{E}$) and $Q = Q_{\text{MAX}}$ ($E' = E'_{\text{max}}$) are indicated. Each set of curves is normalized to unity at its peak (which may be slightly less than the peak of the entire distribution at the given \bar{E}).

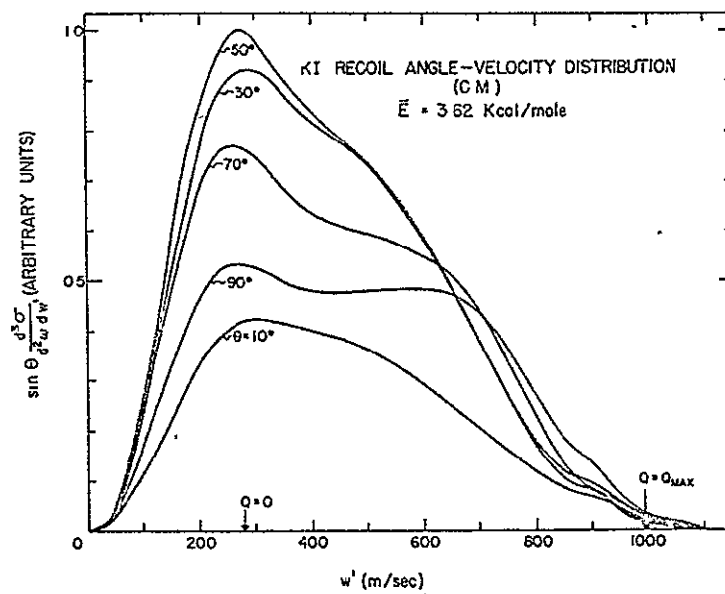
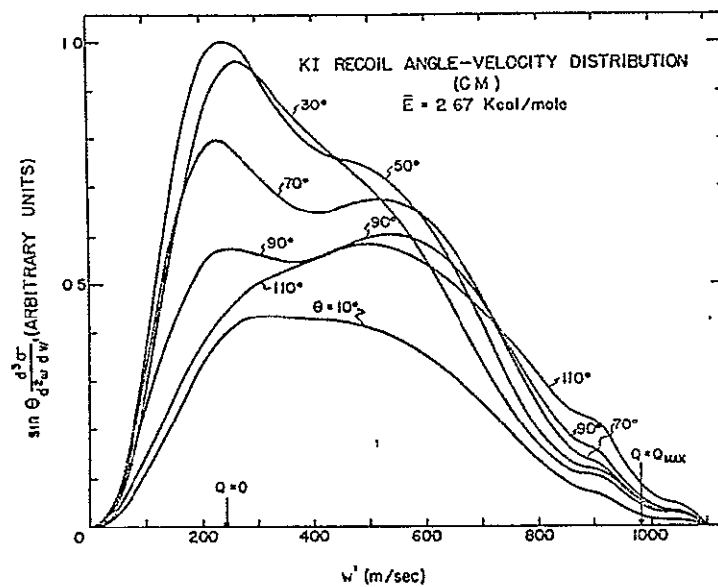
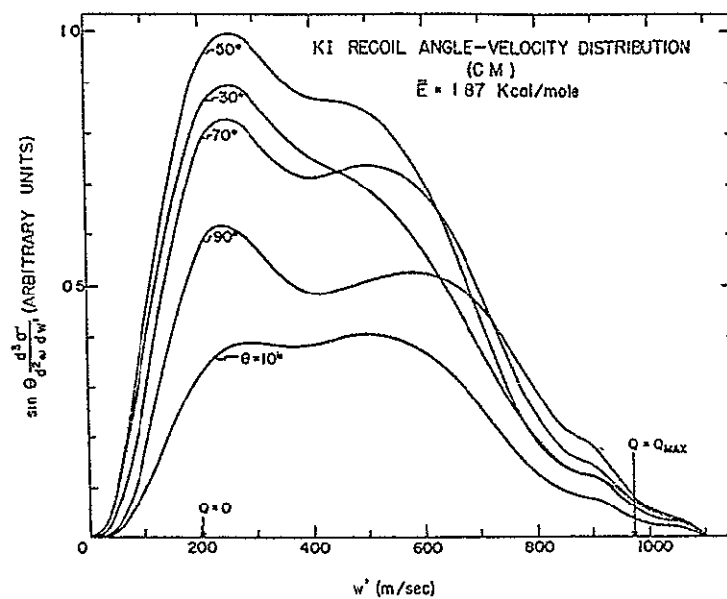


Fig. IV-39

to the total reaction cross section. In this presentation the previously-mentioned double peaked structure shows up clearly at large c.m. angles* for all three \bar{E} . The modest, but definite, velocity-angle coupling in each contour map is clear from the change in the curve shapes with angle. As before the line $Q = 0$ is the c.m. velocity at which $E'_{\text{trans}} = \bar{E}_{\text{trans}}$; the $Q = Q_{\text{MAX}}$ line is set at the same velocity that corresponds to E'_{max} as labelled elsewhere. The resolved "structure" at velocities beyond $w' = 800$ m/sec is believed to be an artifact of the expansion method caused by using only a small number of basis functions (6 velocity functions and 5 angle functions). Intensity found beyond the thermodynamic limit ($Q = Q_{\text{MAX}}$) (a reflection of a small amount of "forbidden" KI flux) may perhaps be background not completely eliminated.

One more transformation is necessary before the energy partitioning between translational and internal modes can be examined quantitatively. Recoil velocity was a convenient independent variable for the laboratory

- - - - -

* There are indications in the computed fits to the data (Figs. IV-34,35,36) that there is slightly too much weight given to the high-velocity hump: at a number of angles the computational fits have higher intensities in the pertinent regions than the experimental data. A larger number of terms in the polynomial expansion would probably remove this slight bias. Improved computations are in progress.

contour maps because the data were taken as a function of velocity; it also proved to be helpful in the c.m. differential cross section functions, especially in demonstrating the double-peaked velocity cuts at large angles. Yet recoil velocity (w') distributions are somewhat peculiar to beam experiments; recoil energy (E') is a more general independent variable; most results on reaction product internal state distributions⁶⁵ are more conveniently⁶⁶ reported as a function of energy.

The transformation from velocity to energy distributions involves more than just a change in the scale on the abscissa axis. The ordinate scale is affected also; this is a consequence of the non-linear relationship between differential elements in the two frameworks:

$$E' = \frac{1}{2} \mu' v_r'^2 = \frac{1}{2} \mu' \left(\frac{m_{KI} + m_I}{m_I} \right)^2 w_{KI}'^2 \propto w_{KI}'^2 ;$$

where $\mu' = \frac{m_{KI} m_I}{m_{KI} + m_I}$.

Thus

$$dE' \propto w' dw' ; \quad (6)$$

but

$$\frac{d^2\sigma}{d\theta dE'} dE' = \frac{d^2\sigma}{d\theta dw'} dw' , \quad (7)$$

which combines with (6) to give

$$\frac{d^2\sigma}{d\theta dE'} = \frac{d^2\sigma}{d\theta dw'} \left(\frac{dw'}{dE'} \right) \propto \frac{1}{w'} \frac{d^2\sigma}{d\theta dw'} \quad (8)$$

Transformation to a differential cross section as a function of energy thus requires that a Jacobian factor ($1/w'$) be applied to the ordinate intensities. This implies that $\frac{d^2\sigma}{d\theta dw'}$ unduly emphasizes intensity at high c.m. velocities relative to $\frac{d^2\sigma}{d\theta dE'}$ 25,44.

The transformed c.m. cuts, $\frac{d^2\sigma}{d\theta dE'} \propto \sin\theta \frac{d^3\sigma}{d^2\omega dE'}$, are shown in Fig. IV-40. The main feature to be noted is the tendency for all of the distributions to peak at $1 \lesssim E' \lesssim 2$ kcal/mole (i.e., $Q \lesssim 0$), corresponding to a very high internal energy (41-44 kcal/mole) in the products. Each distribution, though, has a long tail that spans the entire range of possible translational energy (ideal limits are $Q = Q_{MAX}$ lines on Fig. IV-40). The angle-energy coupling is evident in each of the three distributions, especially as an angular variation in the energy breadth of the differential cross section. The secondary humps of Fig. IV-39 are reduced in this presentation (Fig. IV-40) to such an extent that they are quite hard to resolve from the tails of the main peak.

Spectroscopic results of chemiluminescence experiments yield distributions of internal states⁶⁵ but no angular dependence of these distributions; the present translational energy distributions, once integrated over angle, give results that could be compared to chemiluminescence product state distributions⁶⁶. Fig. IV-41 presents

Fig. IV-40 KI + I c.m. Recoil Angle-Energy Distributions

Cuts at various specified c.m. angles θ through the c.m. differential cross sections $\frac{d^2\sigma}{d\theta dE'} \propto \sin \theta \frac{d^3\sigma}{d^2\omega dE'}$. Obtained from Figure IV-39 by use of the Jacobian transformation $\frac{d^2\sigma}{d\theta dE'} \propto \frac{1}{w'} \frac{d^2\sigma}{d\theta dw'}$ and $E' = \frac{1}{2} \mu' \left(\frac{m_{KI} + m_I}{m_I} \right)^2 w'^2$, where $\mu' = \frac{m_{KI} m_I}{m_{KI} + m_I}$. The $Q = 0$ and $Q = Q_{MAX}$ energies correspond to the similarly labelled velocities in Fig. IV-39. Each set of curves is normalized to unity at its peak (which may be slightly less than the peak of the entire distribution at the given \bar{E}).

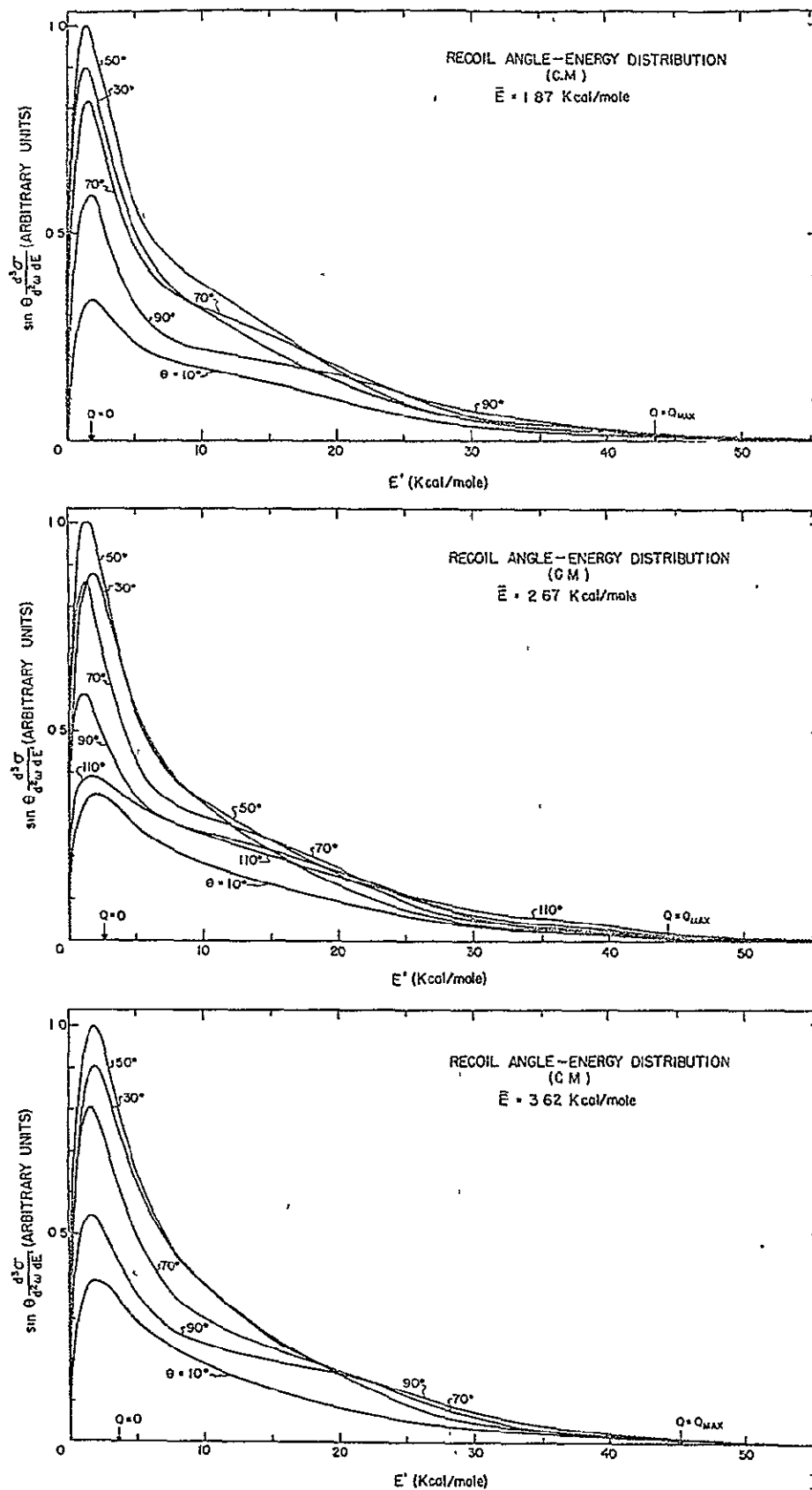


Fig. IV-40

Fig. IV-41 KI + I c.m. Recoil Energy Distributions

Distributions of c.m. translational recoil energy $\frac{d\sigma}{dE'}$ for the reactive products, where the integration $\frac{d\sigma}{dE'} = \int_0^{\theta_{\text{lim}}} \frac{d^2\sigma}{d\theta dE'} d\theta$ was only done over the forward hemisphere (i.e., $\theta_{\text{lim}} = 90^\circ$). The three curves are labelled with their respective incident relative energies, \bar{E} . The $Q = 0$ and $Q = Q_{\text{MAX}}$ energies are indicated (as in Fig. IV-40). Each distribution is normalized to unity at its peak.

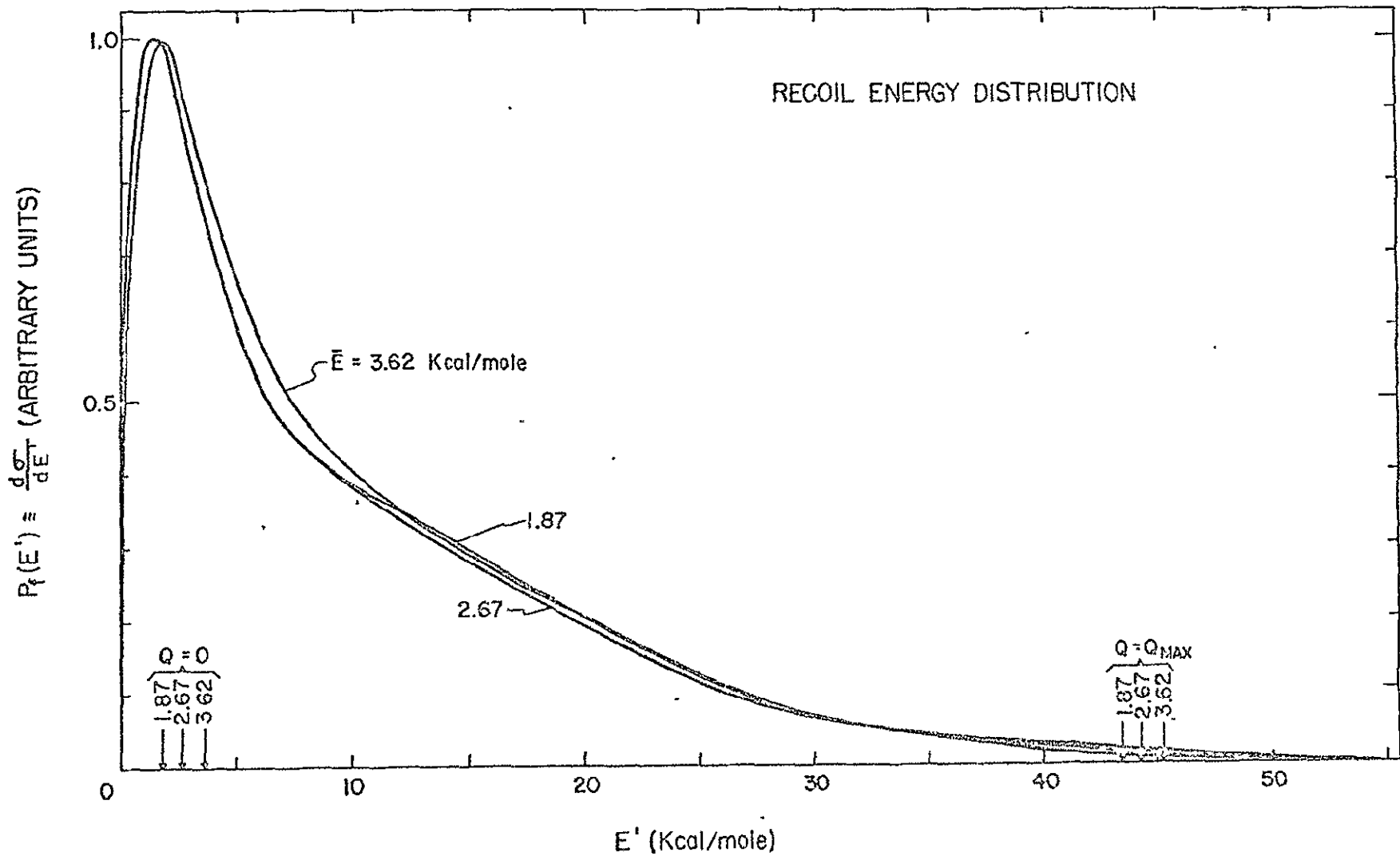


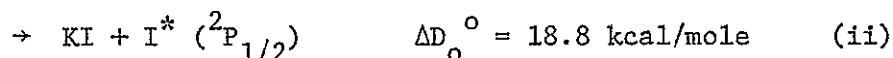
Fig. IV-41

the three distributions $\frac{d\sigma}{dE'}$, (each normalized to unity at its peak) where the integration $\int_0^{\pi/2} \frac{d^2\sigma}{d\theta dE'} d\theta$ could be properly integrated only over the forward hemisphere. The limit $\theta = 90^\circ$ was the largest angle at which results were available for all three \bar{E} ; hence, this cut-off angle is the limiting angle at which a valid comparison of the product translational energy distributions at the three different incident energies can be made. The three distributions are overall quite similar with perhaps a slight shift to higher E' at the higher \bar{E} . As in Fig. IV-40, the distributions peak at slight negative values of Q (i.e. $E' < \bar{E}$) yet have very broad tails extending to slightly beyond E'_{\max} . The corresponding internal energy distributions are directly obtained by use of $E'_{\text{int}} = E_{\text{total}} - E'$, where E_{total} is indicated by the Q_{\max} line for each incident energy.

8. Speculation on Structure in the c.m. Velocity Distributions

The existence of two separate groups of internal product states separated by some 20 kcal/mole is an interesting observation on which to speculate. There are at least three explanations that might be considered.

a) The product iodine atom has a $^2P_{1/2}$ electronic energy level 21.73 kcal/mole above the ($^2P_{3/2}$) ground state. Hence the $K + I_2$ reaction could be partitioned



Reaction (ii) would limit the sum of E' and $E'_{\text{int,KI}}$ to 24.7, 25.5, 26.4 kcal/mole (see Table IV-2) for $\bar{E} = 1.87, 2.67, 3.62$ kcal/mole. This model would associate the peaks at low E' (Figs. IV-39,40) with (ii) having a limit of 24.7-26.4 kcal/mole for E' . The secondary peak would be from reaction (i); this would include all intensity beyond the energy limit for I^* production; it could also conceivably extend to low E' , yielding a very broad distribution of internal energies associated with reaction (i). One could even hypothesize that the product KI associated with I^* production yields a relatively narrow hump at low E' resting on a broad shoulder associated with the $^2P_{3/2}$ state. This could make reaction (i) the predominant one even at low E' values.

This latter assumption would be consistent with the results of Moulton and Herschbach³⁰ on reactive scattering of K by Br_2 and ICl where there was a large amount of product (KBr or KCl) excited with enough internal energy (41 kcal/mole) to allow the endothermic (by ~41 kcal/mole) secondary reaction



to proceed, followed by fluorescence of the electronically excited K^* . Their results do not, of course, rule out the production of some X^* in the primary reaction.

The diffusion flame results of Roth and Schay³¹, however, are strongly suggestive of a very small contribution from I^* . They estimate that approximately 58% of the product KI from the $\text{K} + \text{I}_2$ reaction has enough internal energy to excite $\text{K} (^2S) \rightarrow \text{K} (^2P)$ in

a subsequent collision. The required internal energy is 37.10 kcal/mole (assuming no use is made of the available relative collision energy). Using Fig. IV-41 the fraction $(\int_0^{7.2} \frac{d\sigma}{dE'} dE' / \int_0^{\infty} \frac{d\sigma}{dE'} dE')$ of KI produced (at $\bar{E} = 2.67$ kcal/mole) with relative translational energy less than 7.2 kcal/mole is ≈ 0.50 ; this implies that $\approx 50\%$ of the reactive collisions yield product excitation of greater than 37.1 kcal/mole. If a significant fraction of these reactive encounters produced I^* , the results would be in definite contradiction to the conclusions of Roth and Schay³¹. There is, of course, some uncertainty in this deduction due to lack of knowledge of the backscattering product energy distributions; yet the overall large angle contribution to the KI intensity (i.e., that not experimentally accessible) is small and would have to be very sharply peaked at low E' values to cause any change in the above conclusion.

Other strongly exothermic reactions studied by Polanyi and co-workers gave little, if any, excited halogen atom production^{65c,67}:

	Reaction		ΔD_0 (kcal/mole)
H + Br ₂	→ HBr + Br (² P _{3/2})	> 90%	-41
	→ HBr + Br* (² P _{1/2})	< 10%	-30.5
Cl + HI	→ HCl + I	> 99%	-31.7
	→ HCl + I*	< 1%	-10.0
H + HI	→ H ₂ + I	> 98%	-32.8
	→ H ₂ + I*	< 2%	-11.1

Yet Cadman and Polanyi⁶⁷ found, very tentatively:



(with the possibility of other mechanisms being responsible for the intense I^* emission that was observed).

b) Another possible "two state" explanation would involve the formation of a bound excited electronic state of KI. A recent paper of Berg and Skewes⁶⁸ reports observation of an excited electronic state of NaI, bound by at least 22 kcal/mole relative to the ground state dissociation limit. Unfortunately KI is not thought to have any strongly bound excited states^{69,70} and a state bound by greater than 35 kcal/mole (relative to $\text{K} ({}^2\text{S}) + \text{I} ({}^2\text{P}_{3/2})$) is necessary to explain its accessibility by this reaction. Hence this mechanism also seems to be an unlikely explanation.

c) A third explanation for translational structure in the product KI recoil energy distribution involves some type of Franck-Condon-factor controlled "bunching" of transition probabilities to a certain band of vibrational-rotational states in the ground electronic state of KI. Provided that the "two state" structural feature in $\frac{d\sigma}{dE}$, is not just an artifact of the data analysis* then this may be the most reasonable explanation at present.

9. C.m. Contours Assumed Independent of \bar{E}

Although the three c.m. differential cross sections at the three different \bar{E} show minor differences, the similarities are more obvious, suggesting that there is little or no change in the c.m.

- - - - -

* See Footnote, page 161.

contour map over the small range of relative energy studied ($1.87 < \bar{E} < 3.62$ kcal/mole). This conclusion appears reasonable in light of the small percentage differences in total energy available caused by a variation in \bar{E} from 1.87 to 3.62 kcal/mole (see Table IV-2) and the fact that there is no activation "barrier" to reaction.

Under the assumption that the c.m. map does not change shape as the incident energy varies over the range considered, one can obtain a best average c.m. differential cross section for the three experiments. A computed c.m. function has been produced (20 term Legendre expansion) which gives the best compromise fits to the shapes of all three experimental contour maps. It is shown in Fig. IV-42 with a reflection through the $\theta = 0^\circ$ line (the "collision axis") to emphasize the "forward" peaking of the distribution. The shape is quite similar to the three separate contour maps for the three different \bar{E} ; all important features of the distribution are as before, including the hint of significant "backward" c.m. scattering. Fig. IV-43 once again emphasizes the effect of out-of-plane scattering, which causes the angular range $\theta = 40-50^\circ$ to be the largest contributor to the total reactive cross section.

This single "best average" c.m. function yields the computed laboratory scattering maps shown (for the three different \bar{E}) in Fig. IV-44. In compromising the c.m. function to try to fit the entire body of data, one is more restricted in the fits one can obtain to the data at each of the three energies; hence, the compromised c.m. function cannot fit the data as well as the three individual c.m. distributions (of Fig. IV-30). Yet the fair success of the data-matching suggests

Fig. IV-42 KI c.m. Polar Flux Contour Map (Assumed Energy Independent)

Plot of polar (velocity-angle) KI product c.m. contour map $\frac{d^3\sigma}{d^2\omega dw'}$ produced from all the data at the three \bar{E} , with the assumption that the shape of the c.m. differential reactive cross section is independent of \bar{E} . Normalized to 10 in peak region. Note that there is (enforced) symmetry about the $0^\circ - 180^\circ$ line; the bottom portion of the contour map is therefore redundant.

Expansion coefficients for this contour map are given in Appendix E.

KI POLAR FLUX MAP (C.M.)

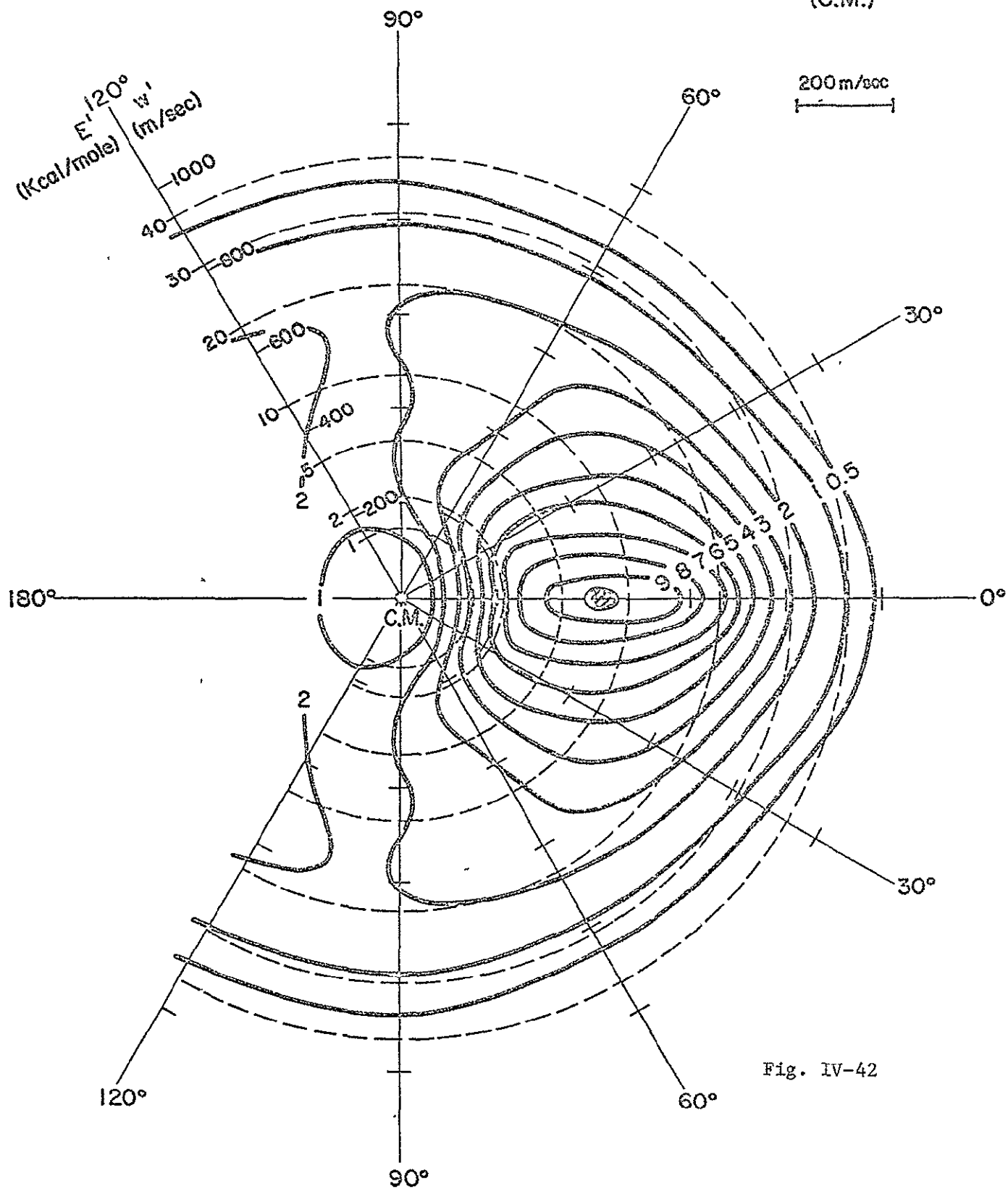


Fig. IV-42

Fig. IV-43 KI c.m. Flux Contour Map Weighted by $\sin\theta$.

KI c.m. differential cross section function $\frac{d^2\sigma}{d\theta dw'}$ (accounting for out-of-plane scattering) corresponding to the contours of $\frac{d^3\sigma}{d^2\omega dw'}$ in Fig. IV-42. Contours correspond to the assumption that the shape of the differential cross section is independent of \bar{E} over the range considered. Normalized to 10 in the peak region.

KI POLAR FLUX MAP x SIN Θ
(C.M.)

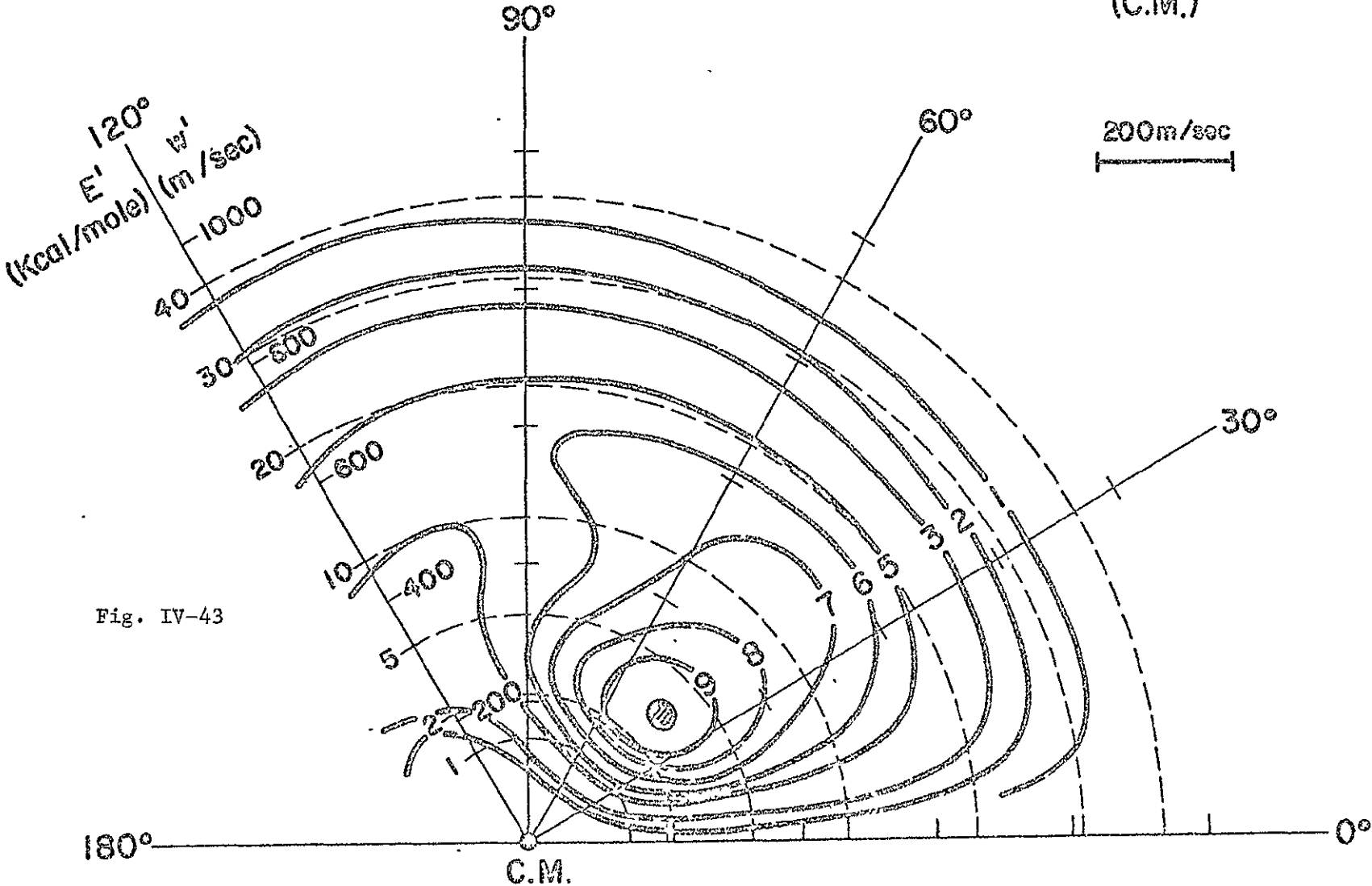


Fig. IV-43

Fig. IV-44 Computed Fits to Laboratory KI Contours (Single c.m. Map)

Fits to the three sets of laboratory flux contour maps, $\frac{d^3\sigma}{d^2\Omega dv'}$, from the one c.m. function (assumed to have a shape independent of \bar{E}) of Figs. IV-42,43.

At each energy the lab. contours are solid lines (long dashed interpolations through 0°); the computed lab. distributions are the dashed contours (with short dashed interpolations through 0°). Lab. contours at each energy are normalized to 10 in the peak region; computed contours are normalized for best least squares fit to all of the data. Angles indicated on each contour map are the limits of the experimental data.

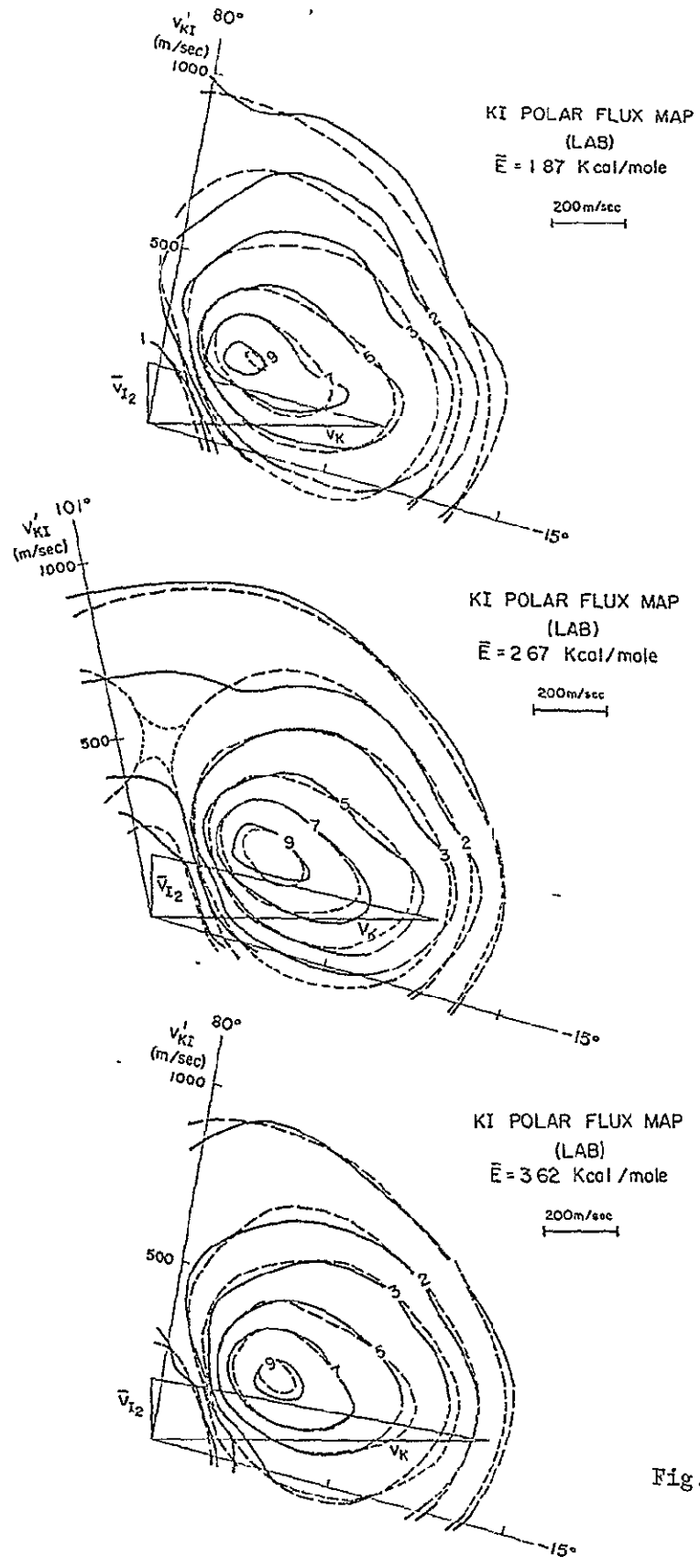


Fig. IV-44

that there may be some success in treating the cross section as being independent of incident relative energy^{24*}.

10. Total Reactive Cross Section, σ_R

An estimate of the total reactive cross section was made (section IV-E) from the sharp cut-off in the angular distribution of the non-reactive scattering (optical model method); at 2.67 kcal/mole, $\sigma_R \approx 125-140 \text{ \AA}^2$, with an energy dependence $\bar{E}^{-1/3}$. Other more direct methods of estimation based on reactive product intensities in crossed beam experiments, have been devised by Birçely et al.¹⁶. Their Method A compares the measured reactive KI intensities to the low-angle intensity of non-reactively scattered K. The absolute value of this K intensity can be calculated assuming classical low-angle elastic scattering behavior (see Eqn. (2) Section IV E) and thus the reactive product intensities deduced; their result for $K + I_2$ was $\sigma_R = 220 \text{ \AA}^2$.

Since the data used in their analysis consisted only of total angular distributions of KI, a number of assumptions had to be made concerning the transformation to the angular and energy distributions

- - - - -

* The above assumption, however, when used in a calculation of the energy dependence of the magnitude of the total reactive cross section (Sec. 11, below), gives a result in disagreement with the energy dependence suggested by the non-reactive scattering analysis (Sec. IV-E).

of reactive product in the c.m. Their "fixed-velocity approximation" neglects high-velocity product contributions and would therefore underestimate out-of-plane contributions.

The present results allow an improvement upon Method A based on a better knowledge of the c.m. distribution (an obvious weakness, the necessity to extrapolate in the region $120^\circ < \theta < 180^\circ$, is shared by the analysis of Ref. 16). The resultant total reactive cross section (at 2.67 kcal/mole) is 290 \AA^2 , somewhat larger than that of Ref. 16 (as anticipated). Unfortunately, the cross section 290 \AA^2 is more than twice the estimate based on the optical analysis of the non-reactive K scattering (Sec. IV E).

Method A is assumed to give an upper limit (as suggested by Birely et al.¹⁶) to the cross section due to the possibility of reactive attenuation of the elastic K intensities even at low angles. Anderson³⁴ points out, in addition, the importance of knowing the exact form of the potential function in calculations of this kind; he evaluates the influence of higher inverse power attractive terms in the long range potential between alkali atoms and halogen molecules and shows the significant alterations in the non-reactive angular distributions that would be caused by these terms. Hence, the scaling of reactive intensities to the low angle non-reactive scattering data has large uncertainties associated with a lack of knowledge of the potential involved.

The rate constants from the Polanyi dilute flame' results⁸ for Na reactions can be used to estimate $\sigma_R \approx 100\text{-}150 \text{ \AA}^2$ for $\text{Na} + \text{X}_2$. A beam study of the reactive product angular distributions for $\text{Na} + \text{Br}_2$

and IC₂ by Birely et al.¹⁹ gave values of σ_R (100 and 90 Å^{o2}, respectively, using Method A) in reasonable agreement with the diffusion flame data.

An increase in σ_R for the sequence Na → K → Rb → Cs is expected from the electron jump model. The crossing point, R_c , of the potential curves for $M-X_2$ and $M^+ - X_2^-$ is the radius at which the electron jump occurs. In the simplest model³², R_c is the radius at which the coulomb attraction, $-\frac{e^2}{R_c}$, of the ionic curve equals the difference between the alkali atom ionization potential (IP) and the halogen vertical electron affinity (EA):

$$\frac{e^2}{R_c} = IP(M) - EA(X_2)$$

A smaller ionization potential (e.g., Cs) would yield a larger R_c and thus a larger σ_R . Results in Herschbach's laboratory⁷¹ confirm the expected increase in reactivity in the sequence Na → K → Rb → Cs.

Yet the (Method A) estimates of σ_R (≈ 220 Å^{o2} for K + I₂) by Birely et al.¹⁶ are approximately 30% larger than the values deduced by Greene et al.¹¹ from an optical analysis of the non-reactive scattering. An even smaller estimate of σ_R (≈ 100 Å^{o2}) for K + I₂ was made by Minturn et al.¹⁴.

Comparing the various values of σ_R deduced for K + I₂, it is not difficult to accept the existence of a factor of 2 uncertainty⁷¹ in the absolute values of σ_R obtained by flame experiments⁸, optical analysis of non-reactive scattering¹¹, and reactive product estimation¹³⁻²³.

A study of the time decay of Cs atom concentration in a vapor of I_2 allowed Brodhead et al.³⁸ to estimate a total reactive cross section of $180 \pm 25 \text{ \AA}^2$ (at a nominal average energy, $\bar{E} = 2.4 \text{ kcal/mole}$) for $Cs + I_2$; this is somewhat lower than the estimate made by Birely et al.¹⁶. The estimated 15% accuracy of the value for σ_R suggests that the method of Brodhead et al.³⁸ is a better one for obtaining total reactive cross sections; an extension of the experiments to other alkali-halogen systems will be a significant test of the systematic variations in reactivity expected from the electron jump model. The system $K + I_2$ should have a smaller σ_R than $Cs + I_2$ due to the higher ionization potential of the K atom.

With a larger "weight" given to the Brodhead et al. data than to the beam results, a best estimate of the $K + I_2$ total reactive cross section (at $\bar{E} = 2.67 \text{ kcal/mole}$) would be (in the author's judgement):

$$\sigma_R = 170 \pm 50 \text{ \AA}^2 .$$

11. Energy Dependence of σ_R

The energy dependence of the total reactive cross section can be estimated from the data on variation with incident energy of the laboratory KI distributions (section IV C4). The relative normalizations of the three best c.m. differential cross section functions (Fig. IV-30) are adjusted until they yield ratios of scattered laboratory KI flux at (θ, v') which are in agreement with the experimental results; adjustment of the beam intensities to

equal values of $n_1 n_2 v_r$ is necessary to insure that the results are directly proportional to $\sigma_R(\bar{E})$:

$$I_{\text{lab}}(\bar{H}, v', \bar{E}) \propto n_1 n_2 v_r \Delta V \frac{v'^2}{w'^2} \frac{d^3 \sigma(\bar{E})}{d^2 \omega dw'} \quad (9)$$

where n_1, n_2 are the primary and secondary beam densities in the scattering zone; v_r is the relative velocity; and ΔV is the scattering volume. Equation (9) assumes mono-energetic beams (and hence a single v_r); in the calculations, use was made of the more general form (integration over the beam velocity distributions and over the volume element (\bar{H}, v')), which is given by Warnock and Bernstein⁴⁴ (their Eqn. (8)).

With the three c.m. differential cross section functions $\frac{d^3 \sigma}{d^2 \omega dw'}$ properly scaled, it is possible to obtain the forward hemisphere total reactive cross section ratios by comparing the integrals

$$\Delta \sigma_R(\bar{E}) = \int_0^\infty \int_0^{2\pi} \int_0^{\theta_{\text{max}}} \left(\frac{d^3 \sigma(\bar{E})}{d^2 \omega dw'} \right) \sin \theta \, d\theta d\phi dw' .$$

Lack of knowledge of the shape of the backward scattering region necessitates stopping the integration at an angle $\theta_{\text{max}} = 90^\circ$. The energy dependence determined in this way is only for a "partial total reactive cross section" (from Fig. IV-38 the forward hemisphere contribution should be some 58% of the total).

The results are shown in Fig. IV-45(a). The energy dependence effect is anything but dramatic over the small range of \bar{E} studied. A small negative energy dependence might be construed. The error limits unfortunately do not exclude either (i) an $E^{-1/3}$ energy dependence consistent with the present analysis (Sec. IV E) of the non-reactive data of Greene *et al.*¹¹, or (ii) a nearly energy-independent total reactive cross section. A small negative energy dependence ($\sigma_R \propto E^{-a}$, with $a \leq 1/3$) is consistent with the non-reactive scattering analysis (Sec. IV E); i.e., the reactive results offer no contradiction. The best estimate of "a" from the reactive scattering data is $a = 0.25 \pm 0.1$.

The c.m. angular distributions $\frac{d\sigma}{d\theta}$ vs. θ (Fig. IV-38) allow an estimation of the fraction of σ_R from angles beyond $\theta = 90^\circ$; this fraction (at $\bar{E} = 2.67$ kcal/mole) is 0.42. Changes with incident energy of the forward-backward partitioning of the total reactive cross section are possible; this could result in an energy dependence of σ_R which is in disagreement with the forward hemisphere energy dependence of Fig. IV-45(a).

Another (less valid) attempt at determining the energy dependence involves using the single compromise c.m. contour map which best accounted for all the data at different \bar{E} (Fig. IV-42) and repeating the calculation done above. The advantage inherent in this approach is that it is possible to extrapolate the results to energies outside of the range of the experimental flux contour maps since the shape of the c.m. function is (assumed to be) independent of energy. The results are shown in Fig. IV-45(b); the error bars are comparable in size to those of Fig. IV-45(a). As is seen, if one assumes no

Fig. IV-45 Energy Dependence of Total Reactive Cross Section

Log-log plot of partial total reactive cross section, $\bar{\sigma}_r$ ($\theta = 0$ to 90°), as a function of the relative collision energy.

(a): Based on three best c.m. differential cross section functions of Figs. IV-30,37; uses the best line through the energy dependent normalization data of Fig. IV-18. Arbitrarily normalized to unity at $\bar{E} = 2.67$ kcal/mole. A line of slope $-1/3$, corresponding to an $E^{-1/3}$ energy dependence, is shown for comparison. Error bars are approximate 90% confidence limits for the three points.

(b): Based on the assumption of energy independence of shape of c.m. differential cross section function, using c.m. contours of Figs. IV-42,43. Points correspond to data points of Fig. IV-18; the triangles are the best data; the squares were preliminary results and are of lowest quality. Arbitrarily normalized to unity at $\bar{E} = 2.67$ kcal/mole. Experimental uncertainties are comparable to those shown in (a).

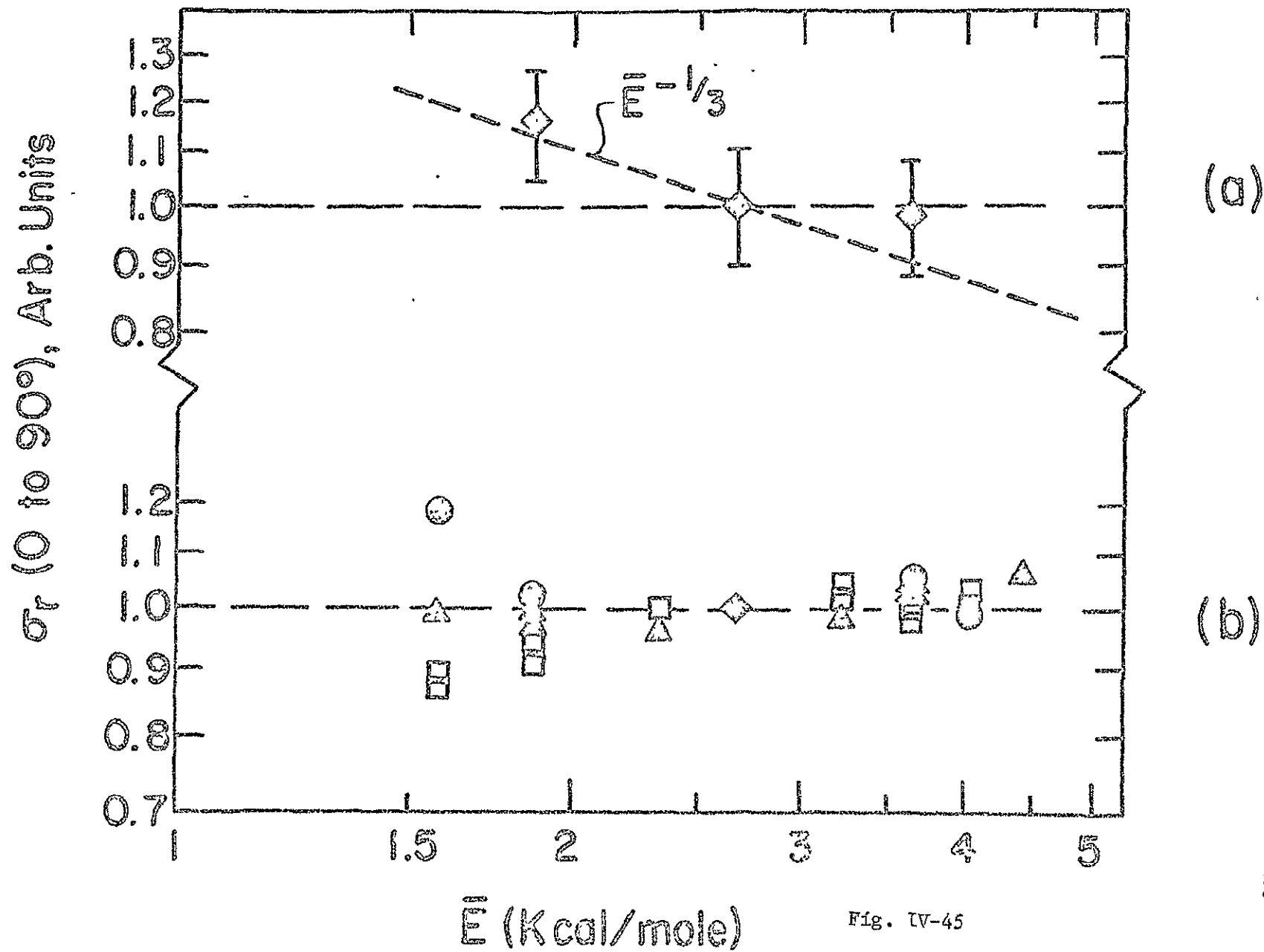
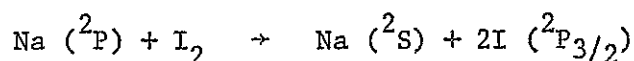


Fig. IV-45

dependence upon \bar{E} of the shape of the c.m. cross section, one also obtains little or no energy dependence for the magnitude of the total reaction cross section.

The best estimate of energy dependence $\sigma_R = E^{-a}$, $a = 0.25 \pm 0.1$ agrees with the approximate functionality found by Brus³⁷ for a quenched fluorescence study of the reaction



with σ_R varying from 190 to 140 \AA^2 in the range $4.6 \leq \bar{E} \leq 19.6$ kcal/mole. Plotting $\log \sigma$ vs. $\log \bar{E}$ for the Brus data yields $a = 0.21$.

A recent comprehensive analysis of the magnitudes of reactive cross sections for the alkali-halogen systems was done by Anderson³⁴. He considered the influence of other factors in the long-range attraction of $M + X_2$ and developed a more complete optical model. The criterion for reaction was the rather standard one of overcoming the centrifugal barrier. He found a negative energy dependence ($a \approx 0.27$) and reasonable sizes ($\approx 150 \text{\AA}^2$ at $\bar{E} = 2.67$ kcal/mole) for the reaction cross sections for $\text{K} + \text{Br}_2$ and $\text{K} + \text{ICl}$; but the "non-reactive data" used in the analysis included a significant amount of spurious residual alkali halide intensity at large angles (see Chapter V). Hence the results may need to be re-examined; in any case they cannot be considered quantitative.

12. Summary of $\text{K} + \text{I}_2$ Reactive Scattering Results

The total reaction cross section is large ($\sigma_R = 170 \pm 50 \text{\AA}^2$ at $\bar{E} = 2.67$ kcal/mole) and has a very small (negative) dependence on relative translational energy (Fig. IV-45). The

differential c.m. reaction cross section $\frac{d^2\sigma}{d^2\omega}$ (Fig. IV-38) peaks at $\theta = 0^\circ$ (forward scattering), but still has a significant value at large c.m. angles with the possibility of a smaller backward peak. The energy partitioning strongly favors high internal excitation of the product KI (with little electronically excited I^* product); the most probable value of E' is ≈ 1.5 kcal/mole (corresponding to ≈ 43 kcal/mole of KI excitation energy). The recoil energy distribution (Fig. IV-41) has a broad high energy tail; thus, a small fraction of the product molecules has low internal excitation energies. There is significant coupling (Fig. IV-39) between the product angular and recoil energy distributions, the most important manifestation being a poorly resolved double-peaked structure (Fig. IV-40) in the translational recoil distributions (best resolution at $\theta > 60^\circ$). The dependence of the shape of $\frac{d^3\sigma}{d^2\omega d\omega'}$ upon \bar{E} (Fig. IV-30) is not very large over the energy range studied.

The present results for the $K + I_2$ system fit in well with the general conclusions deduced from reactive product angular distributions for the whole family of alkali-halogen reactions^{2a,13-19}. They are also in qualitative agreement with the predictions of several Monte Carlo trajectory calculations based on various assumed potential forms³⁹. This is not surprising since the "best" potentials were not determined from ab initio calculations; rather, the comparative merits of the various potentials examined were deduced solely from their relative abilities to reproduce the general aspects of the available experimental data. The extra experimental details now available (in the form of the various detailed cross section functions) will necessarily provide a stiffer test of future potential surface calculations.

V. Selective Detector for Internal Excitation of Alkali Halides in
Molecular Beams

A reproduction of the note "Selective Detector for Internal
Excitation of Alkali Halides in Molecular Beams," Keith T. Gillen
and R. B. Bernstein, WIS-TCI-377X, Univ. of Wisconsin, Madison,
Wisconsin, 1970 follows.

All references in this section are numbered independently
of the rest of this thesis; the references are found on pages 6, 7,
and 13 of this section.

Selective Detector for Internal Excitation of
Alkali Halides in Molecular Beams^{*}

by

Keith T. Gillen and R. B. Bernstein

Chemistry Department and Theoretical Chemistry Institute
University of Wisconsin, Madison, Wisconsin 53706

The sensitivity, or ionization efficiency, f , of a low work-function ("desensitized") Pt/W (92/8%) surface ionization detector for alkali halide (MX) beams increases strongly with the internal energy, E_{exc} , of the MX. For excited KI (formed in crossed beam chemical reaction), $f \propto \exp[\gamma E_{exc}/kT]$ with $\gamma \approx 1/4$.

- - - - -

* Work supported by National Science Foundation Grant GB-16665.

Introduction

The suitability of a 92% Pt/8%W alloy as a differential surface ionization (SI) detector for alkali/alkali halide beams was established by Datz and Taylor [1] and employed in a multitude of crossed beam scattering experiments involving reactions of alkali atoms with halogen-containing molecules [2]. The present note reports a new application of such a SI beam detector as a discriminator for extent of internal excitation of alkali halide molecules.

The possibility of a variation in the rate of an overall tungsten surface reaction $\text{LiCl}(v) \xrightarrow{W(1400^\circ\text{K})} \text{Li}^+ + \text{Cl} + e^-$ with the alkali halide vibrational state v ($v = 0, 1, 2, 3$) was suggested by Klemperer and Herschbach [3] on the basis of their analysis of some molecular beam resonance experiments of Marple and Trischka [4]. Unfortunately, subsequent careful measurements by Moran and Trischka [5] negated the earlier experimental results and no measurable (i.e., $\pm \sim 1\%$) discrimination in SI efficiency with vibrational state could be found. It was recognized [6] however, that sufficiently highly excited states (e.g., $v \gg 3$) of alkali halides might well be selectively ionized under favorable SI conditions. Such conditions were found, somewhat by chance, in this laboratory in the course of a detailed study of the velocity analysis of the reactive scattering of K by I_2 .

The present experiments involved the chemically excited KI molecules, with known internal (excitation) energies in the range 1-2 eV. A Pt/W (92/8) SI filament was employed in the low work-function or "desensitized" mode [7], such that it had a very low

sensitivity to a thermal KI beam. The ionization efficiency of the detector was found to depend exponentially upon E_{exc} , the excitation energy of the KI. This effect is not expected to be limited to this particular alkali halide; indeed, qualitative confirmation of the enhancement in sensitivity of such a SI detector for other excited alkali halides is available from a number of sources.

Experimental

The present data were obtained in the course of a crossed beam study [8] of the reaction of a velocity-selected K beam with a thermal I_2 beam at 90° incidence. The product KI and K scattered at various laboratory angles passed through a velocity analyzer to the SI detector. This consisted of a Pt/W (92/8) ribbon 0.7 mm wide, 0.025 mm thick, ca. 1 cm in length, DC heated (by ca. 1 amp) to operate at ca. 1330°K . Under these conditions (the desensitized mode), the ionization efficiency for a thermal KI beam was in the range 0.1 - 0.4%, based on comparative measurements with the filament in the sensitized (oxidized) mode at ca. 1370°K , where it is essentially 100% efficient.

With the knowledge of the translational velocity of the chemi-excited KI and conventional conservation considerations commonly applied [9] to crossed-beam velocity analysis experiments, the average internal excitation energy of the KI molecules striking the detector could be calculated:

$$E_{exc}(KI) = E_{tr} + E_{int}(I_2) - \Delta D_o - E'_{tr}$$

where E_{tr} and E'_{tr} are, respectively, the incident and final (c.m.) relative translational (kinetic) energies. E_{tr} is, typically, 0.12 eV; $E_{int}(I_2) \approx 0.05$ eV, and $\Delta D_0 = -1.80$ eV assuming the other reaction product, I, to be in its ground ($I^2P_{3/2}$) state. The velocity analysis results [8] combined with the results of a diffusion flame study by Roth and Schay [10] of the $K + I_2$ reaction indicate that there is little, if any, excited $I(^2P_{1/2})$ product [8].

Fig. 1 shows the logarithm of the ionization efficiency f vs. the internal excitation E_{exc} of the KI. Each connected set of points represents data at the same laboratory angle Θ but different laboratory velocities v' . Provided there is negligible translational energy effect, different points at the same calculated E_{exc} (arising from different Θ and v') should yield the same f . Within the estimated $\pm 20\%$ uncertainties in the points this appears to be the case. Also shown on the graph at low E_{exc} are the results for a thermal KI beam, which accord well with a linear extrapolation from the main body of data for the excited KI.

Interpretation

The process of surface ionization of alkali halides has received considerable study [11] but is not yet thoroughly understood. Adopting either of the thermodynamic or the kinetic models commonly invoked to explain the large body of SI experimental data for alkali halides, it can readily be shown that the dependence of the ionization efficiency upon the excess (excitation) energy of the MX should be of the form $f = f_0 \exp[\gamma E_{exc}/kT]$, where f_0 is the efficiency of the detector for ground state MX ($f_0 \ll 1$), T is the surface temperature, and γ is a fraction

characterizing the effectiveness of the internal excitation (whether vibrational or electronic) to the reduction in the free energy barrier for dissociative ionization. For the present detector and chemi-excited KI, the slope of Fig. 1 yields $\gamma = 0.25 \pm 0.05$.

Concluding Remarks

The slope of the line in Fig. 1 (i.e., the value of γ obtained) implies that an increase of as little as 0.02 eV (the spacing between adjacent low-lying vibrational levels of KI [12]) would produce a 5% increase in the fraction f . The question arises as to the failure of the experiments of Ref. [5] to observe vibrationally selective detection for the various LiX molecules. This may be due to either of two distinct differences in their work. They used a tungsten filament for ionization, and the mechanism of ionization may vary considerably with filament material. Also, their low efficiency experiments were done at higher temperatures than those corresponding to the maximum ionization efficiency; the high temperature decrease in sensitivity is undoubtedly caused by a different mechanism than that which lowers efficiency in the low temperature region.

There exist a number of observations which confirm that this qualitative behavior is somewhat general. The f values on desensitized Pt/W are usually low for all alkali halides, but there is a considerable span which correlates well with MX ionization potentials [13]. The CsX molecules are most efficiently ionized;

f usually increases from Cl to Br to I. Datz and Minturn [14] reported a value of $f \approx 0.08$ for a CsBr beam on desensitized Pt/W; (this increased detection sensitivity over KI suggests that CsBr might be better from the viewpoint of detection of excitation). An analysis [8] of literature data and experiments from this laboratory on the wide-angle (supposedly non-reactive) scattering of alkalis by several halogen-containing molecules (using desensitized Pt/W detectors) has provided evidence for interference due to selective (enhanced) detection of internally excited MX product (for $X = \text{Cl}, \text{Br}, \text{and I}$).

In order to make use of this type of selective detector for use as an internal energy monitor (i.e., for estimating average internal excitation of chemi-excited alkali halides, MX) one must evaluate (calibrate) γ for the alkali halide in question; then the set of reactions $M + XY \rightarrow MX + Y$ (for all Y) may be studied.

The implications of the present findings alter the interpretation of the $M + X_2$ scattering data obtained with Pt/W "differential" detectors (see Appendix).

Acknowledgment

The authors appreciate the valuable advice and assistance of Mr. A. M. Rulis in connection with these experiments.

References

- [1] S. Datz and E. H. Taylor, J. Chem. Phys. 25, 389, 395 (1956).
- [2] (a) E. Taylor and S. Datz, J. Chem. Phys. 23, 1711 (1955).
See reviews of later work by: (b) J. P. Toennies, in Chemische Elementarprozesse, Ed. by H. Hartmann et al., Springer, Heidelberg (1968), p. 157, and (c) Ber. Bunsen. f. phys. Chem. 72, 927 (1968); (d) H. Pauly and J. P. Toennies, in Methods of Experimental Physics, Ed. by L. Marton, Vol. 7 of Atomic and Electron Physics; Atomic Interactions, Part A, Ed. by B. Bederson and W. L. Fite, Academic Press, N. Y. (1968), p. 227; (e) D. R. Herschbach, Adv. Chem. Phys. 10, 319 (1966).
- [3] W. Klemperer and D. Herschbach, Proc. Nat. Acad. Sci. 43, 429 (1957).
- [4] D. T. Marple and J. W. Trischka, Phys. Rev. 103, 597 (1956).
- [5] T. I. Moran and J. W. Trischka, J. Chem. Phys. 34, 923 (1961).
- [6] D. R. Herschbach, private communication (Oct., 1968).
- [7] T. R. Tow and J. W. Trischka, J. Appl. Phys. 34, 3635 (1963).
- [8] K. T. Gillen, Ph.D. thesis, University of Wisconsin (1970);
K. T. Gillen, A. M. Rulis and R. B. Bernstein, to be published (1970).
- [9] A. E. Grosser, A. R. Blythe and R. B. Bernstein, J. Chem. Phys. 42, 1268 (1965); K. T. Gillen, C. Riley and R. B. Bernstein, J. Chem. Phys. 50, 4019 (1969).
- [10] E. Roth and G. Schay, Z. physik. Chem. B28, 323 (1935).

- [11] See, for example, in addition to Refs. 1, 3, 7:
B. H. Zimm and J. E. Mayer, J. Chem. Phys. 12, 362 (1944);
G. E. Cogin and G. E. Kimball, J. Chem. Phys. 16, 1035 (1948);
K. R. Wilson and R. J. Ivanetich, U.C.R.L. Report 11606 (1964)*
N. I. Ionov, J. Exptl. Theoret. Phys. (U.S.S.R.) 18,
96, 174 (1948).
- [12] S. A. Rice and W. Klemperer, J. Chem. Phys. 27, 573 (1957).
- [13] J. W. Hastie and J. L. Margrave, Fluorine Chemistry
Reviews, to be published.
- [14] S. Datz and R. E. Minturn, J. Chem. Phys. 41, 1153 (1964).
- [12b] J. R. Rusk and W. Gordy, Phys. Rev. 127, 817 (1962).

Legend for Fig. 1

Dependence of the logarithm of f , the apparent fraction of KI ionized, (in the unsensitized mode) on E_{exc} , the (average) internal excitation (in eV) of the KI. Each set of connected points is derived from data at specified relative kinetic energy and laboratory angle but different laboratory velocities (corresponding to different c.m. recoil energies and thus different E_{exc} for the KI). Open symbols denote less reliable data.

f, APPARENT FRACTION KI IONIZED

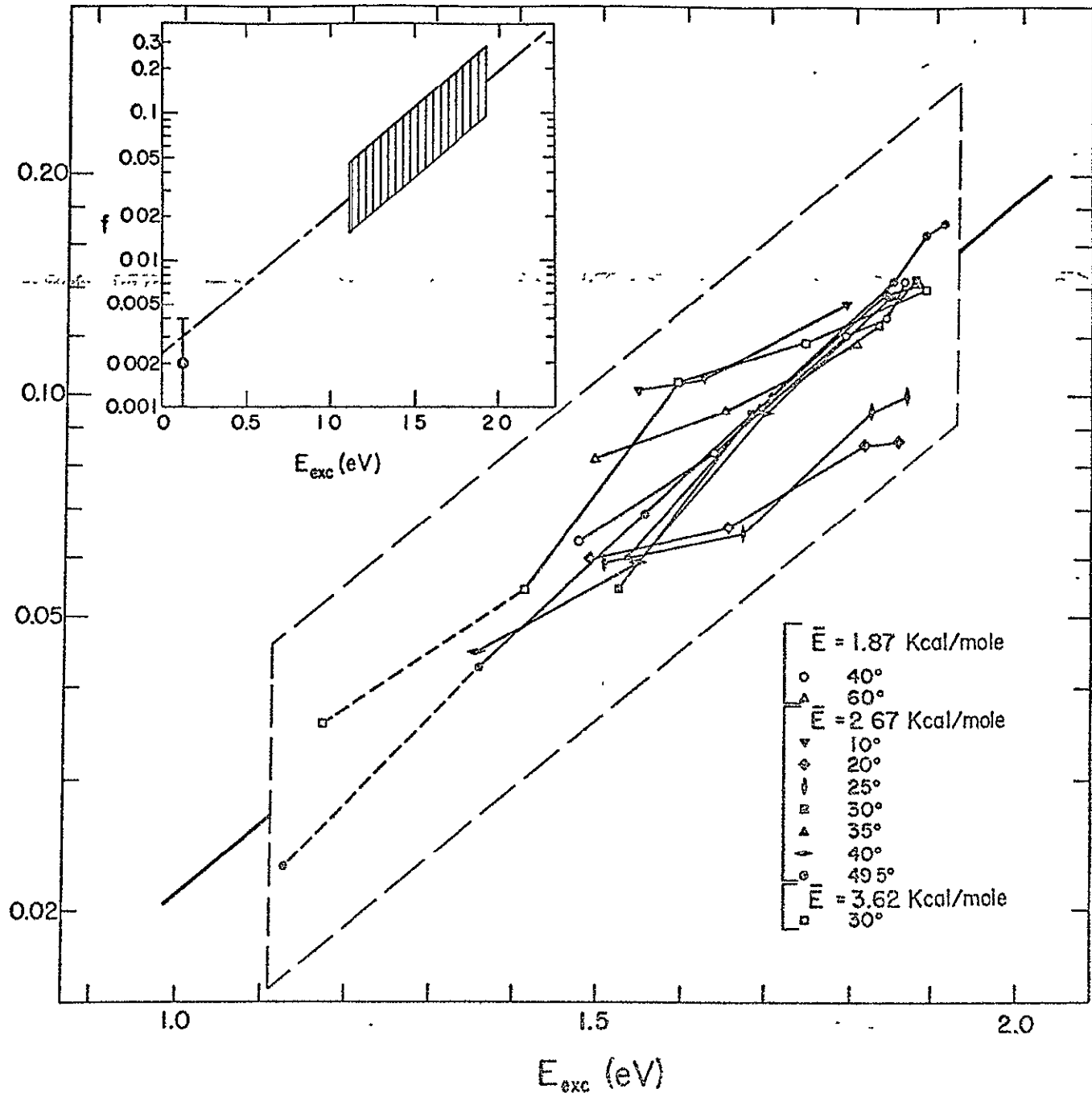


Figure I

APPENDIXRelevance to Interpretation of Alkali-Halogen Scattering Experiments

The magnitude of the residual detection sensitivity (of the nominally unsensitized Pt/W alloy) for highly excited alkali halide (MX^{\dagger}) molecules vitiates the common assumption that the Pt/W alloy is an ideal differential detector. Greene et al. [15] use a pure Pt filament (essentially non-detecting to alkali halides) in measuring angular distributions of non-reactively scattered alkali atoms. For a number of alkali + halogen reactions their measured intensity distributions drop off much faster at large angles than the distributions (for the same systems) reported by other workers using "unsensitized" Pt/W detectors.

In the $K + I_2$ system [8] measurements of the residual sensitivity of the Pt/W filament to excited KI^{\dagger} made it possible to correct the observed "intensities" to obtain an angular distribution of scattered K which was in reasonable accord with that of Ref. [15]. The importance of this correction may be judged by noting that at the largest angle where the correction could be made ($\theta = 49.5^\circ$), the residual KI signal represented some 90% of the total intensity (K + KI).

The $K + Br_2$ system provides another example. Minturn et al. [16] and Birely et al. [17] (both using Pt/W detectors) reported significantly greater wide-angle non-reactive scattering than that observed by Greene et al. [15], presumably due to residual sensitivity to KBr^{\dagger} . Minturn et al. [16] attempted to subtract out the residual KBr

contribution to their angular distributions, but used the much smaller residual detection efficiency as measured for a thermal KBr beam, thereby accounting for only a small fraction of the residual KBr^\dagger contribution to the apparent non-reactive scattering.

The reaction of K with HBr (DBr) produces KBr with a maximum excitation of only ≈ 0.25 eV (less than 15% of that for the $\text{K} + \text{Br}_2$ reaction); hence the residual detection should be much lower than that for KBr^\dagger from $\text{K} + \text{Br}_2$. Indeed, the uncorrected Pt/W results [18] for the non-reactive angular distributions were found to agree quite satisfactorily with the data of Airey *et al.* [19] obtained with a Pt detector.

Kwei and Herschbach [20] have reported angular distributions of alkalis scattered by ICl and IBr with distinctly higher wide-angle scattering for Cs than for K or Rb. Residual sensitivity may have contributed significantly to the unsensitized angular distributions for all three alkalis; but thermochemically the CsX^\dagger product has more internal energy available and, even at the same excitation energy, it should have a higher detection efficiency than the other alkali halides.

Product MX molecules scattered into regions of negative laboratory angle Θ usually have relatively larger translational energy and correspondingly less internal excitation; this implies that the residual sensitivities to MX^\dagger will be much smaller at negative Θ . Also, the total MX found at negative angles is lower. There are numerous examples [17,20] of angular distributions measured with an unsensitized Pt/W detector where the c.m. angular

intensity distribution deduced from the negative Θ "branch" is somewhat lower than that from the positive branch. It may be that data from the negative angles more closely approximate the true non-reactive angular distribution.

Any observed residual detection will not directly mirror the MX^\ddagger (angular) distribution since molecules whose velocities lie closest to centroid are those with the highest internal excitation (and residual detection sensitivity increases exponentially with internal energy). For the $\text{K} + \text{I}_2$ experiments [8], the average residual sensitivity to KI at a number of laboratory angles ($\Theta > 0$) has been measured; the results are given in Table I. The effect shows a (broad) maximum near the angle of the centroid, as anticipated. It is possible that these "weighted-average" observed residual sensitivities might be used as a rough indicator of the degree of product excitation as a function of Θ .

Table I Dependence of Residual (Unsensitized Mode) KI Sensitivity on the Laboratory Scattering Angle, Θ , for the $K + I_2$ Experiments.

\bar{E} (kcal/mole)	1.87	2.67	3.62
Centroid Angle (degrees)	60	55	50
Θ lab (degrees)	f, fraction ionized (± 0.02)		
10.0		0.07	
20.0		0.07	
25.0		0.08	
30.0	~ 0.07	0.09	0.11
35.0		0.10	
40.0	0.10	0.11	
49.5		0.12	
60.0	0.09	~ 0.12	
70.0		<0.10	<0.06
80.0	<0.08	<0.08	<0.06
101.0	<0.07	<0.05	<0.05

References for Appendix

- [15] E. F. Greene, L. F. Hoffman, M. W. Lee, J. Ross, and C. E. Young, J. Chem. Phys. 50, 3450 (1969).
- [16] R. E. Minturn, S. Datz, and R. L. Becker, J. Chem. Phys. 44, 1149 (1966).
- [17] J. H. Birely, R. R. Herm, K. R. Wilson, and D. R. Herschbach, J. Chem. Phys. 47, 993 (1967).
- [18] K. T. Gillen, C. Riley, and R. B. Bernstein, J. Chem. Phys. 50, 4019 (1969).
- [19] J. R. Airey, E. F. Greene, K. Koder, G. P. Reck, and J. Ross, J. Chem. Phys. 46, 3287 (1967).
- [20] G. H. Kwei and D. R. Herschbach, J. Chem. Phys. 51, 1742 (1969).

Appendix AVelocity Selector Calibrations and K Beam Characterization

The equations of Hostettler and Bernstein⁴⁶ for a velocity selector transmission function $B(v)$ assumed no misalignment of the selector axis with respect to the beam axis. A generalization of their calculations to include the effect of a small misalignment angle is presented here. The notation is that of Ref. 46. The generalized extensions of equations (10 a,b) of Ref. 46 are:

$$B(v) = \eta \left[1 - \left\{ \frac{(1+\beta)}{(1+\delta)} \frac{V_0^*}{v} - 1 \right\} / \gamma' \right] \quad \text{for } V_0^* > v > V_{\min} \quad (\text{A-1})$$

and

$$B(v) = \eta \left[1 + \left\{ \frac{(1-\beta)}{(1-\delta)} \frac{V_0^*}{v} - 1 \right\} / \gamma'' \right] \quad \text{for } V_{\max} > v > V_0^*$$

where

$$\begin{aligned} \gamma' &= \frac{l_1}{(L+d)\alpha + \phi r} = \gamma \left[1 + \frac{(L+d)\alpha}{\phi r} \right]^{-1}, \\ \gamma'' &= \frac{l_1}{(L-d)\alpha + \phi r} = \gamma \left[1 + \frac{(L-d)\alpha}{\phi r} \right]^{-1}, \\ V_0^* &= \frac{L\omega r}{\phi r + L\alpha} = V_0 \left[1 + \frac{L\alpha}{\phi r} \right]^{-1}, \\ \delta &= \frac{d\alpha}{\phi r + L\alpha}, \\ V_{\min} &= V_0^* \left(\frac{1+\beta}{1+\gamma'} \right) (1+\delta)^{-1}, \\ V_{\max} &= V_0^* \left(\frac{1-\beta}{1-\gamma''} \right) (1-\delta)^{-1}, \end{aligned}$$

α = angle to selector axis (Radians); and $\alpha > 0$ "adds" to helix angle, with all other quantities defined as before⁴⁶ (see also table II-1).

These equations (A1) are the basis for the computer simulations of the various velocity selector and velocity analyzer calibration experiments.

Note that the width of the selector transmission function, $(v_{\max} - v_{\min})$, is directly proportional to v_o^* which implies that the total selector transmission increases directly proportional to the rotation speed⁵⁴. Hence in analyzing a beam velocity distribution with a selector, the throughput intensity values must each be divided by the corresponding velocities to obtain the actual distribution incident upon the selector. An ideal case illustration is given in Table A-1 for a thermal effusive (Maxwell-Boltzmann) beam passing through a selector, then an analyzer.

1) Calibrating the analyzer and selector

Appendix A of Chapter III-B describes a calibration of the velocity analyzer with a low temperature effusive (M-B) K beam. The constant, k_A^* , that relates the analyzer rotation speed, ω_A , to the velocity transmitted, v_o^* ($v_o^* = k_A^* \omega_A$), is adjusted until the curve of experimental flux transmission (divided by rotation speed; see above) best matches the ideal M-B flux distribution. A comparison of k_A^* with the value, $k_A = L/\phi$, expected for zero misalignment angle gives:

$$k_A^* = k_A \left[1 + \frac{L\alpha}{\phi r} \right]^{-1}$$

so
$$\alpha = \frac{\phi r}{L} \left(\frac{k_A}{k_A^*} - 1 \right).$$

Table A-1 Relations of Velocity Distributions,
M-B beam; not normalized.

<u>Position</u>	<u>Density</u>	<u>Flux</u>
In oven	$v^2 \exp-(v^2/\alpha^2)$	
Beam entering selector	$v^2 \exp-(v^2/\alpha^2)$	$v^3 \exp-(v^2/\alpha^2)$
Beam transmitted through selector to analyzer	$v^3 \exp-(v^2/\alpha^2)$	$v^4 \exp-(v^2/\alpha^2)$
Beam finally transmitted through analyzer	$v^4 \exp-(v^2/\alpha^2)$	$v^5 \exp-(v^2/\alpha^2)$

$$\alpha = \left(\frac{2kT}{m}\right)^{1/2}$$

For the alignment of the velocity analyzer used in the $K + I_2$ experiments, $\alpha_A = + 0.18^\circ \pm 0.05^\circ$.

The α determined is from the center line of the detected beam to the selector axis.

For a velocity analyzer with a very narrow velocity bandpass and for narrow collimating slits and a thin detector, the experimental flux curve should be expected to match very well with the theoretical M-B form. This will prove to be the case for the velocity analyzer but not the velocity selector. Generally, the experimental flux transmission curve can be modified by a number of effects, separately, or in combination:

A) If the transmission function width $(v_{\max} - v_{\min})/v_0^*$ is not small compared to the velocity width of the beam scanned, then there will be a broadening of the transmitted flux curve due to the folding in of the transmission function at each v_0^* .

B) Any angular divergence in the beam leads to a broadening of the transmitted flux curve due to the dependence of $B(v)$ on the angle relative to the selector axis. (See Eqn. A1). Centered at the misalignment angle α , the detected beam has an angular divergence that can be estimated from the geometry of the detector and the collimating slits (See Fig. IV-1).

C) A selector with a broad transmission width (e.g., the present K beam selector) can have a bias towards high velocities in its transmission function (see "ideal" selector transmission function in Fig. 17 of Chapter III-B). This will give a shift in the

transmitted flux curve relative to the incident beam distribution; the shift is caused by the extra weighting of the transmitted flux from the high velocity portion of the transmission function.

D) The transmission function varies slightly from the bottom of the selector tooth to the top. Equation (A1) shows this effect through changes in $\eta = \frac{l_1}{l_1+l_2}$ as well as r . This effect can alter the breadth of the transmitted scan, especially if the slit height is not small compared to r .

To correct for the above effects in the various beam calibration experiments, a computer program (see Appendix C, Program DC) was written that folded selector transmission functions into beam distributions, integrating over both the angular distribution of the detected beam and the height of the beam from the bottom to the top of the selector slot. The calculated transmitted flux curves (broadened and shifted relative to the actual beam being characterized) could then be compared to the experimental scans.

For the case of the velocity analyzer with the effusive beam the calculated curve of flux vs. velocity was essentially identical to the M-B beam distribution. Fig. 16 of Chapter III-B shows a match of an experimental scan to the M-B distribution; no adjustment for the above-mentioned (A-D) effects is necessary. The velocity selector, however, has a wider and less symmetric transmission function yielding a velocity shift of approximately 1% in the computed transmission curve relative to the ideal M-B distribution (shown in Fig. A-1). The experimental points must be matched to the computed

Fig. A-1 Velocity Selector Calibration.

Calibration of the velocity selector with a thermal Maxwell-Boltzmann (M-B) K beam of known velocity distribution. The dashed curve represents on a reduced plot $(v^* = v / (\frac{3kT}{m})^{1/2})$ the M-B flux distribution incident upon the selector. The solid curve is a calculation of the ideal distribution into the selector (transmitted flux distribution divided by v^* to account for the velocity-dependent selector bandpass: $\Delta v \propto v$); the shift is due to a significant bias in the shape of the selector transmission function. The comparable experimental points are shown superimposed and are in excellent agreement with the calculated (solid) curve. All curves normalized to unity at peak.

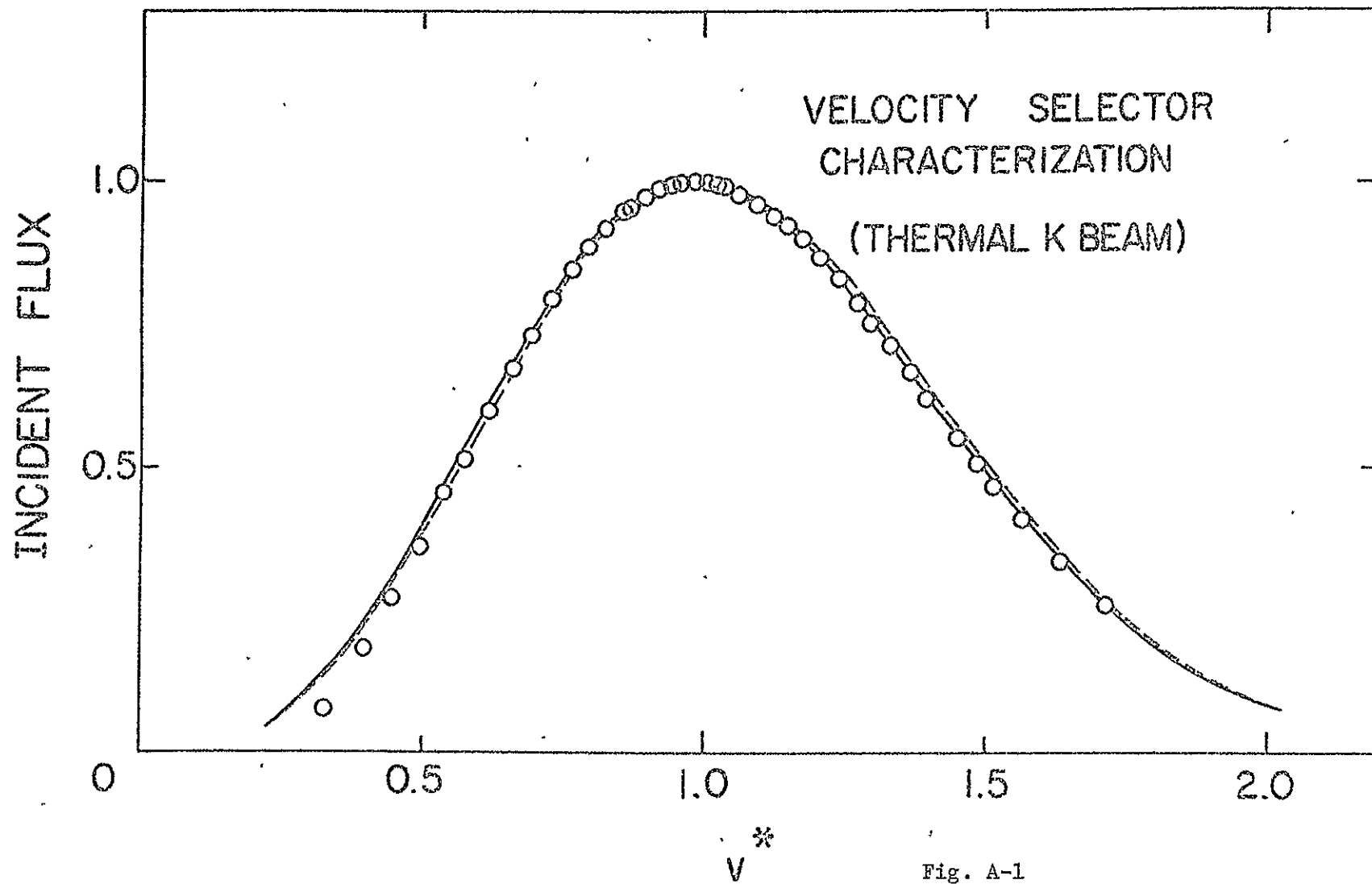


Fig. A-1

curve rather than the M-B; an example is shown in Fig. A-1. A comparison of k_s^* with the expected ($\alpha=0$) value yields the selector misalignment angle ($\alpha = +0.50^\circ \pm 0.05^\circ$ for the K + I₂ experiments). The value of α found may be put back into the computer simulation program to generate a better (iterated) computed flux curve for matching to the data; in the present example, iteration did not change the results.

There are two checks of these calibrations that have been used. First, a pin can be inserted at the center of rotation of the goniometer lid. Using a cathetometer to establish a line between this pin and the detector filament, one can lower the analyzer vertically approximately 1 cm; and using marker "shims" between the teeth on the front disk and on the back disk, one can optically determine the helix angle relative to the defined beam analysis axis. This gives a geometrical estimate of the analyzer constant, k_A^* , with somewhat less precision than the beam characterization method.

The other calibration check measures the self-consistency of the two constants k_A^* and k_s^* ; the analyzer is used to scan the selector transmission function with the goniometer set at 0.0 degrees. A computational simulation is then used for comparison. This type of consistency calibration check can then be done at other goniometer angles (and therefore different angles through the selector) to verify the change in selector constant k_s as a function of the angle through the selector. Accounting for the fact that a goniometer rotation of a specified angle corresponds to a smaller rotation (factor of 0.75) in the angle relative to the selector axis (see below) experimental measurements of the change in selector constant ($1.2 \pm 1\% / \text{degree}$)

agree well with the computed value (11.8%/degree: Prob. 7,8,9 in Program DC).

An example of an analyzer calibration of selector transmission is shown in Fig. A-2; the computational simulation (dashed curve (a)) uses the general formula of Equation (A-1) and supplants the earlier less complete calculational simulation of this type of calibration (e.g., Fig. 17 in Chapter III-B). Note that the new computation (Problem 7 in Program DC; dashed curve (a) in Fig. A-2) is somewhat more sharply peaked than the experimental data. The broadening of the experimental curve is due to an effect noted earlier; the first disk of the velocity selector has been eroded and thinned considerably, its slots widened significantly due to attack by the large amount of potassium deposited on this disk. Program DC has been run with corrections which approximately account for the "dissolving disk." Two curves of Fig. A-2 are computations which account for the thinned selector teeth curve (c) (solid line) corresponds to $\sim 20\%$ larger slots; curve (b) (dot-dash) uses $\sim 15\%$ larger slots than the ideal (dashed curve) calculation. The curve with 20% wider slots appears to represent well the actual situation for the selector transmission; measured slot widths concur approximately with this estimate. This cross-check between the selector and analyzer agreed (to better than $\pm 1\%$) with the two separate calibrations employing effusive M-B beams.

Fig. A-2 Analyzer Scan of Selector Transmission

A relative calibration of the velocity selector by the velocity analyzer. The points represent an experimental analyzer scan of the K beam flux vs. velocity transmission of the selector. The three curves are computational simulations of the experiment with full averaging over slit height and detector acceptance angle. Curve (a) is for the ideal selector with no alteration of the slot widths in the first selector disk. Curves (b) and (c) simulate 15% and 20% wider slots in the first selector disk due to cumulative erosion by alkali. Curve (c) appears to account well for the widened distribution. All distributions are arbitrarily normalized to unity at the peak.

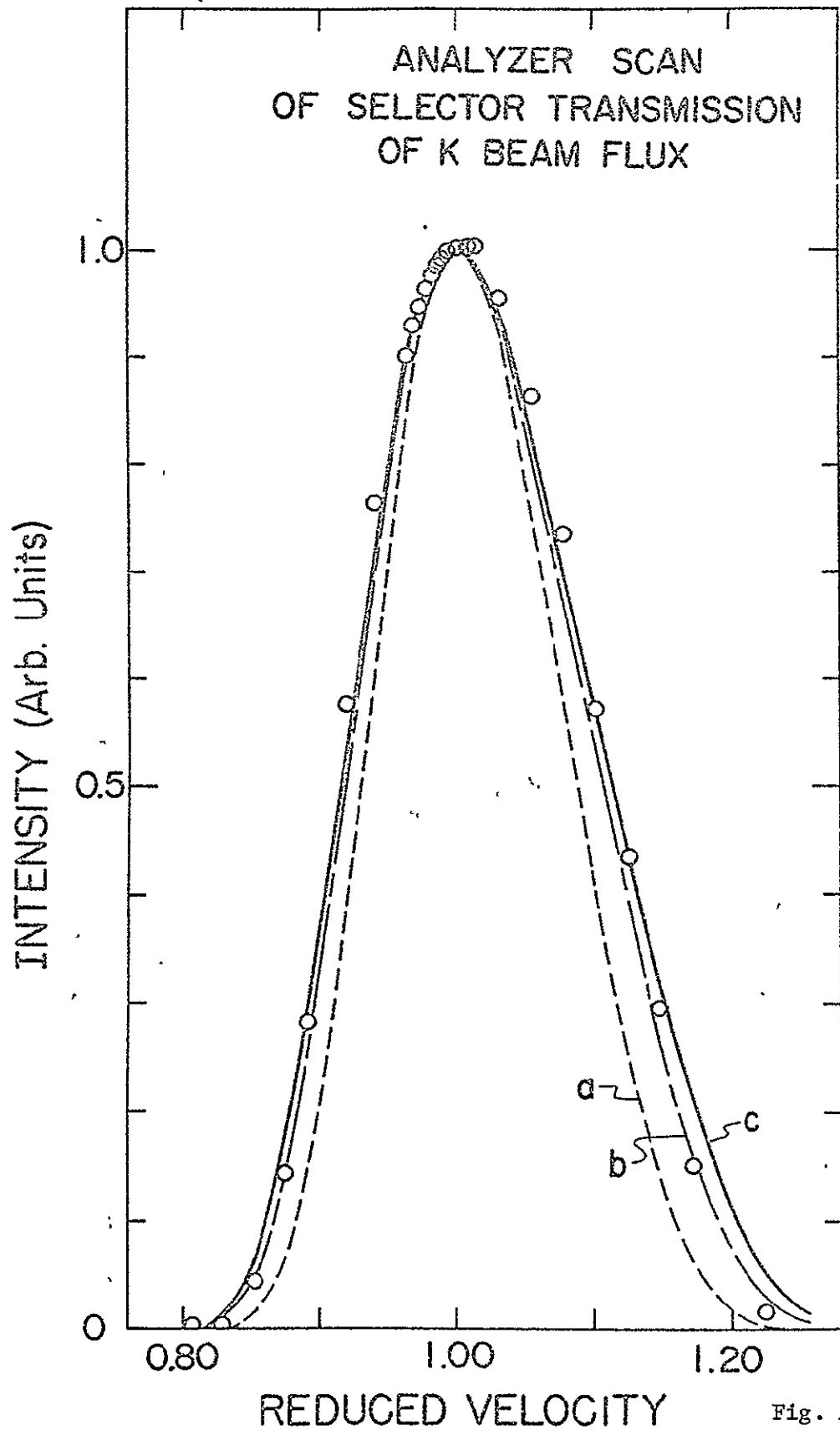


Fig. A-2

2) Velocity Distribution of the Laval K Beam.

The velocity distribution of the Laval K beam incident upon the selector can be estimated by a characterization of the velocity distribution using the selector as the scanning device. The distribution so characterized will, of course, be broader than the actual distribution incident upon the selector and will be shifted to slightly lower velocities, both effects due to folding in the selector transmission function (these effects are also seen in the selector calibration with a M-B beam). Fig. A-3 shows an assumed flux distribution (solid line) for a Laval K beam incident upon the selector; the dashed curve is a computer simulation (Problems 5 and 6 in Program DC) of the experimental data that would correspond to the assumed curve. Superimposed on these curves are the points from two typical experimental selector characterizations of the Laval K beam; the agreement with the dashed curve is good and suggests that the originally assumed solid curve is a good representation of the Laval K beam under the conditions of the experiments shown. No comparisons to theoretical Laval forms⁷² were made; but the density distribution agreed remarkably well with a distribution reported by Gordon et al.²¹ using similar Laval oven slits. It must be noted, however, that the observed Laval distribution was found to be very sensitive to oven conditions; this is reflected in day-to-day variations in the experimental characterization curves that can sometimes be larger even than the differences between the solid and the dashed curves. Hence, although the computer corrections are valid as a systematic correction, there are still random variations

Fig. A-3 Laval K Beam Flux Distribution

An assumed Laval K beam flux distribution (based on data, not on any theoretical form) incident upon the velocity selector (solid curve), compared to a computer simulation (dashed) of selector transmission/ v , which introduces a shift due to the bias in the shape of the selector transmission function. The points represent two experimental selector characterizations of the Laval distribution ($T(\text{slit}) = 705 \pm 5^\circ\text{K}$, $T(\text{oven}) = 625 \pm 5^\circ\text{K}$). The good agreement of the points with the dashed computed curve indicates that the (solid) assumed Laval K beam flux distribution is a reasonably good one. All curves arbitrarily normalized to unity at peak.

The energy marks (\bar{E}) show the average K beam velocities associated with the three relative collision energies used in the $\text{K} + \text{I}_2$ experiments. Note that the velocity dependent selector transmission ($\Delta v \propto v$) enhances the throughput beam intensity for the higher energy experiments relative to those at lower energies.

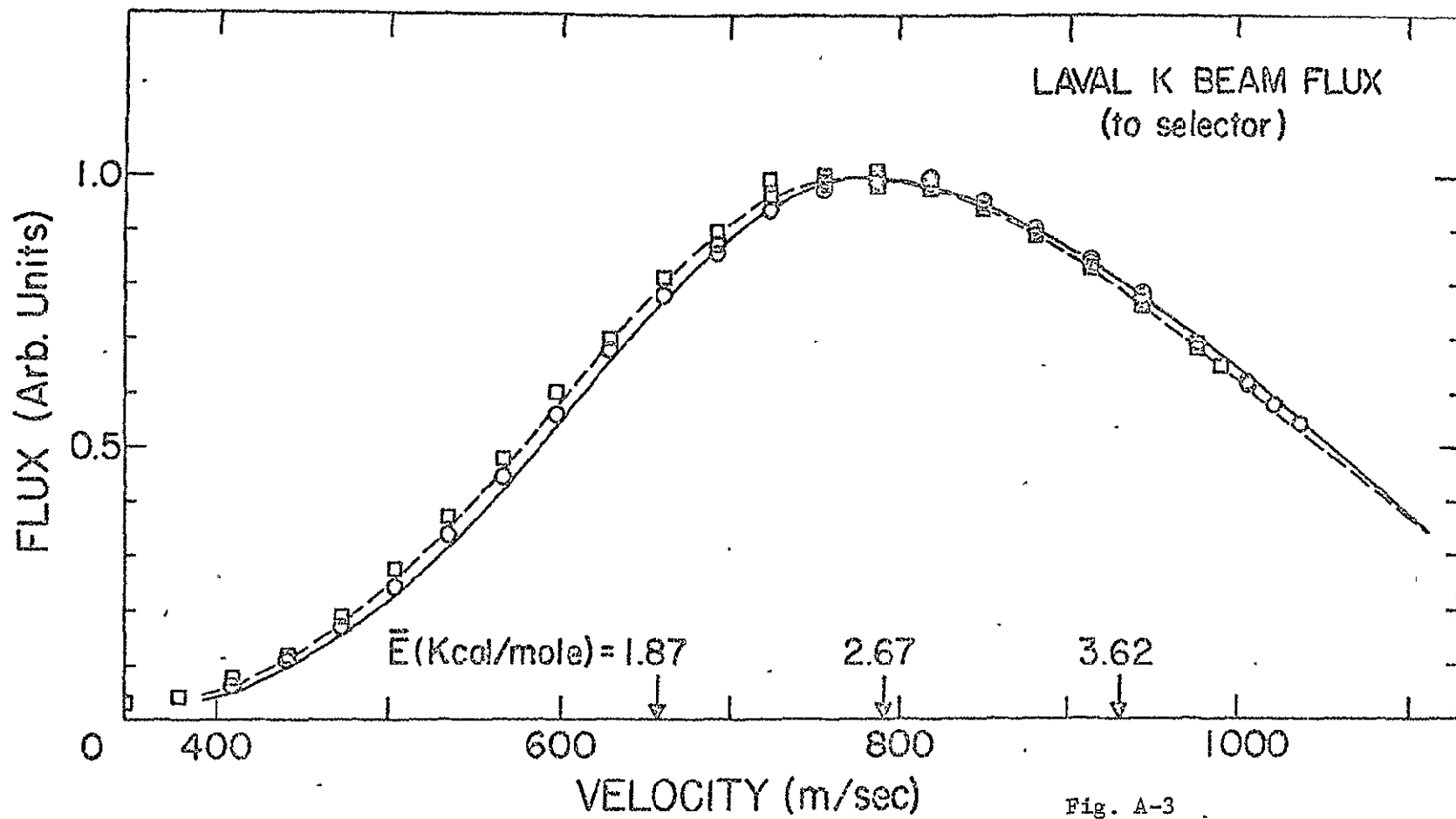


Fig. A-3

of about the same magnitude in the Laval beam. Fortunately in the scattering experiments the velocity selector set at a specified rotation speed defines a much narrower beam velocity distribution and the variations in the velocity distribution of the incident Laval beam become relatively unimportant.

3) Profile of K Beam Entering Scattering Center.

In the previous calibrations, the angular spread considered was determined by the geometry of the detector system (widths of analyzer entrance slit and detector and distance between them); the K beam entering the S.C. has a much larger angular spread determined by slit sizes and distances for the K beam geometry. The angular distribution can be determined by an angular profile of the K beam; a typical angular profile of a velocity-selected K beam is shown in Fig. A-4. Notice that the goniometer angle measured differs from the true angle to the selector axis; there is a shift of 0.5° due to misalignment, but in addition there is a scale change (factor of $-\frac{25.3}{33.9}$). This effect can be seen in the lower portion of Fig. A4. Potassium emitted (a) at an angle α to the center of the beam (defined as 0°) will not be detected when the goniometer is rotated (b) by an angle $-\alpha$; it will, however, be detected at a goniometer rotation angle of -1.34α as can be seen in (c).

The full-width-at-half-maximum (FWHM) of the beam measures 1.4° (beam angle); this compares well with a calculated value of 1.3° using the ideal geometry of Fig. IV-1, Chapter IV. The tails of the distribution are, however, much broader than expected; this is probably due

Fig. A-4 Angular Profile of K Beam

Upper: The experimental angular profile of the K beam flux distribution through the selector (at $v_K = 794$ m/sec) is plotted vs. goniometer rotation angle Θ . The curve passing through the data points is normalized to unity at its peak. The upper scale indicates the angle relative to the selector axis, α' , with $\alpha' = +0.5^\circ$ at $\Theta = 0.0^\circ$ (misalignment angle = 0.5°).

Lower: Representation of the difference in scale between Θ and α' .

(a) Rotation angle = 0.0° . Consider "beam" emitted at an angle α to the defining axis. S.C. = scattering center; DET. = detector.

(b) Rotation angle = $-\alpha$. Beam will not strike detector.

(c) Rotation angle = $\sim \alpha \times (1 + 8.6/25.3)$ necessary to detect the beam at an angle α .

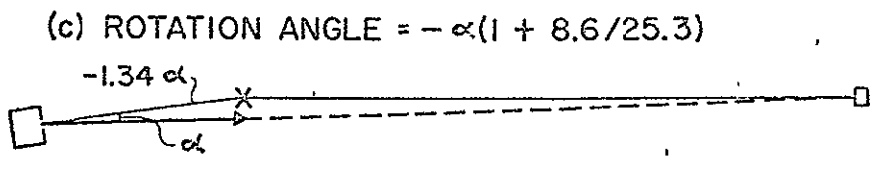
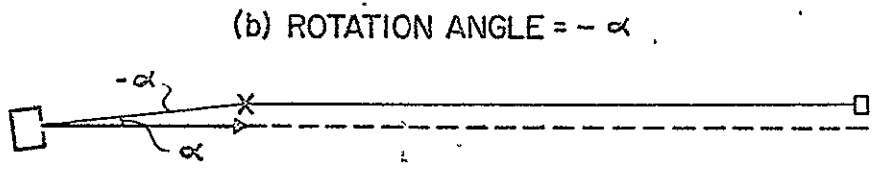
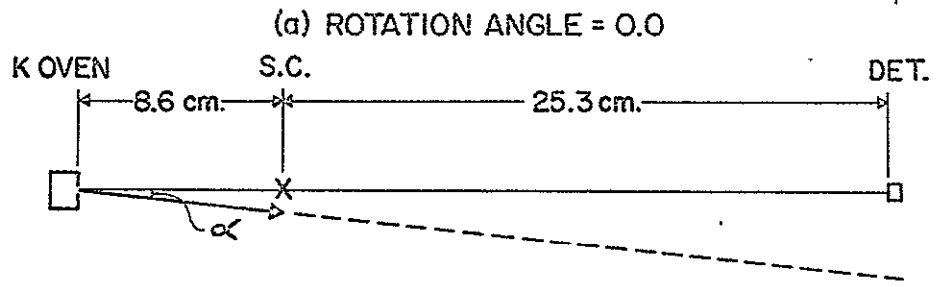
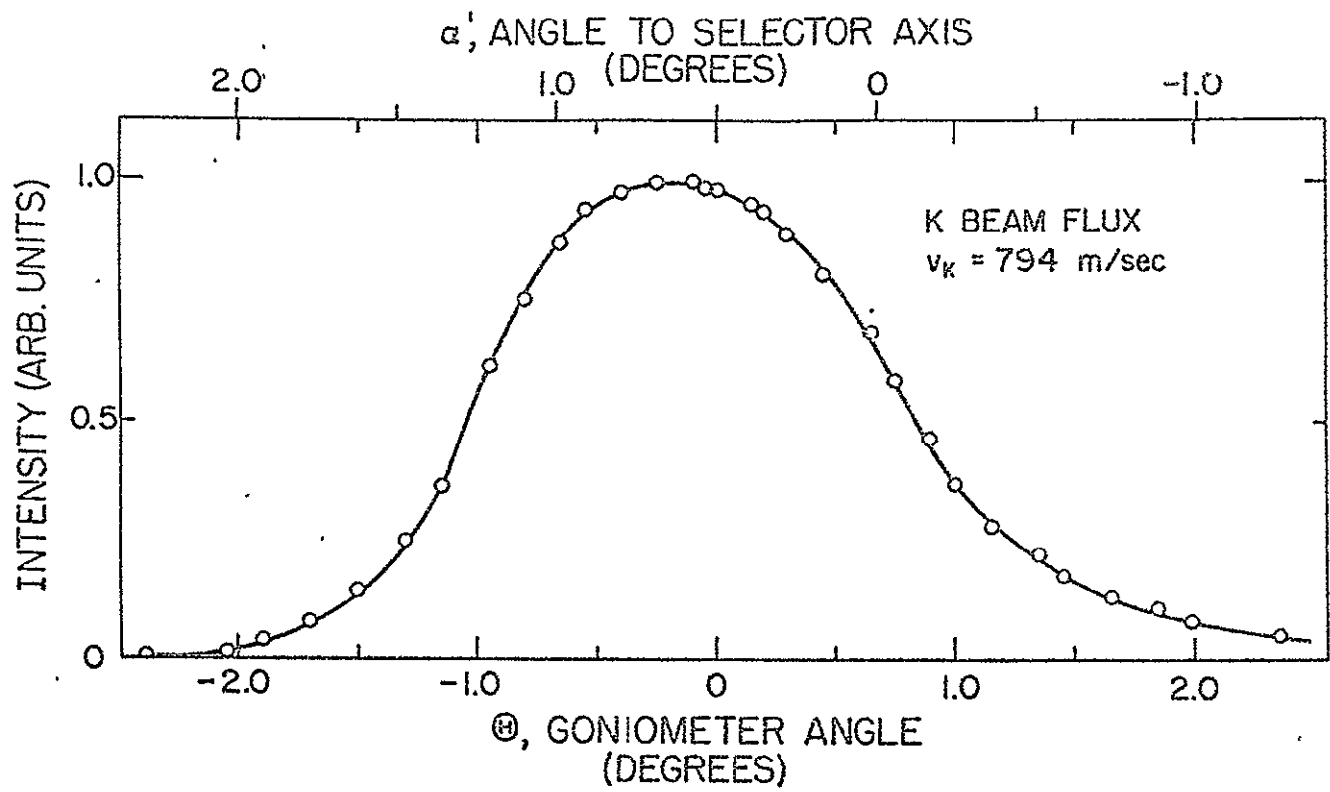


Fig. A-4

to a larger, more diffuse emission region (perhaps a cloud effect) than that associated with the ideal geometry.

Problem 10 of Program DC is a computational estimation of the K beam density vs. velocity distribution that enters the S.C.. The computation includes all the corrections (A-D) previously mentioned and also includes an internal iteration which adjusts for the fact that the experimental angular distribution is for a velocity selected beam and hence is not a true angular distribution of emitted potassium.

The narrowest (dashed) curve in Fig. A-5 is the density transmission curve associated with the ideal selector slot width. The "dissolving disk" curves of 15% (dot dash) and 20% (solid) wider slots correspond to the similar curves of Fig. A-2. Having seen in Fig. A-2 that the solid curve best matches the analyzer scan of selector transmission, one then concludes that the solid curve of Fig. A-5 is the best estimate of the selector transmission into the S.C.

The K beam density transmission produced has been adjusted so that it corresponds to the transmission associated with a beam of uniform flux vs. velocity incident upon the velocity selector. The density transmission produced by a Laval K beam can be found (for any given nominal velocity) by multiplying the Laval flux distribution curve by the (solid) K beam density transmission curve of Fig. A-5; the only assumption involved here is that there is negligible change in the shape of the Laval flux vs. velocity curve over the angular range ($\sim 3^\circ$) of the transmitted beam.

When the velocity selector is set at a speed significantly removed from the peak of the Laval flux curve, there may be a noticeable

Fig. A-5 Estimation of K Beam Density in Scattering Zone

Curve (c) depicts the best estimate of the K beam density distribution in the scattering zone associated with a uniform flux vs. velocity input to the selector. Deviations from uniform flux vs. velocity input in the Laval K beam can be accounted for by multiplying this curve by the proper Laval input distribution curve (e.g. Fig. A-3). The curve is plotted vs. reduced velocity ($v^* = 1.00$ at $\Theta = 0.0^\circ$ density peak); the shift to low velocities arises because the angular distribution is asymmetric with respect to 0.0° (Figure A-4). Curves (a), (b), and (c) have the same assumptions associated with the three curves of Fig. A-2; curve (c) is thought to be the best representation of the "dissolving disk syndrome". (cf. Fig. A-2 legend). All curves normalized to unity at peak.

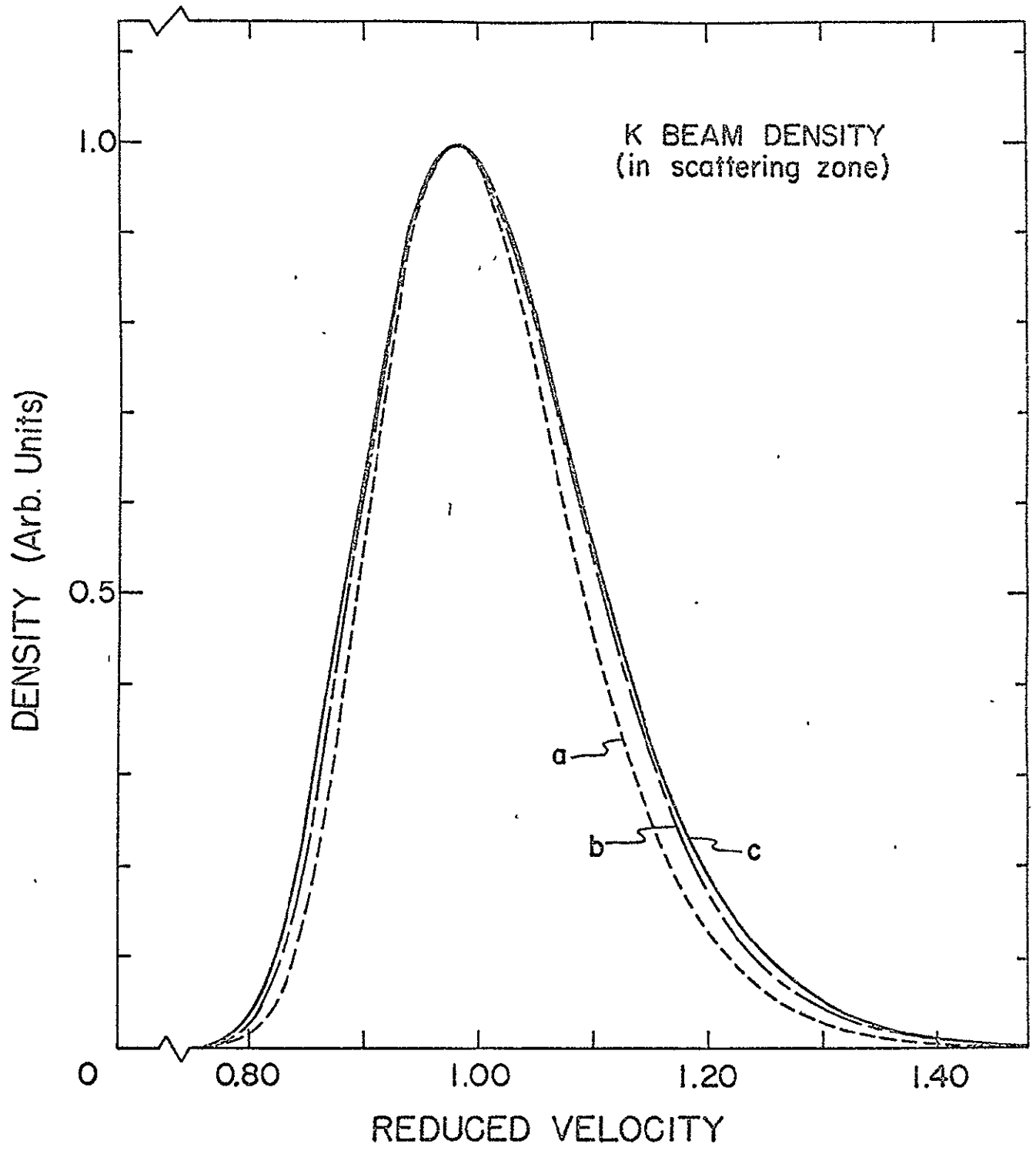


Fig. A-5

warping of the beam transmission into the S.C. relative to the solid curve of Fig. A-5. This effect must be accounted for in determining the average laboratory K velocity (and, therefore, also the average c.m. energy \bar{E}) associated with each reactive scattering experiment (Chapter IV).

Appendix B

Computational Inversion Methods

In the absence of a Maxwell demon riding with every c.m., one must find alternative methods for extracting the differential c.m. cross section (e.g. $\frac{d^3\sigma}{d^2\omega d\omega'}$) when the laboratory scattering intensities (e.g., $\frac{d^3\sigma}{d^2\Omega dv'}$) are known. All of the computational methods for inversion of scattering data from lab. to c.m. discussed below attempt to solve this problem; there are advantages and disadvantages in each. It is assumed that

- (a) the c.m. cross section is independent of ϕ , the azimuthal angle.
- (b) both beams are well collimated, at 90° incidence, and confined to the "detector plane".

Assumption a) is valid in the absence of aligning fields; assumption b) has been verified by observing that relaxation of this restriction in the computations does not significantly alter the results for the range of experimentally accessible incident angles.⁴⁴

1) "Nominal Inversion"

If one assumes that the two beams are monoenergetic, uses the average velocity for each beam, thereby determining a single "nominal" c.m. velocity, then one can immediately invert the laboratory distribution to the c.m. framework:

$$\left(\frac{d^3\sigma}{d^2\omega d\omega'}\right) = \left(\frac{w'}{v'}\right)^2 \left(\frac{d^3\sigma}{d^2\Omega dv'}\right), \text{ where } \left(\frac{w'}{v'}\right)^2 \text{ is the Jacobian}$$

of transformation from lab. to c.m.^{25,44}. This is the simplest inversion technique and works quite well when the range of vector velocities of the c.m. (determined by the velocity spreads in both beams) is small compared to the velocity spread in the experimental reactive product data (especially at product vector velocities far removed from the locus of centroids). Unfortunately, even for the quite favorable $K + I_2$ case, the velocity spread in the two beams is still large enough to cause a serious broadening of the laboratory KI distribution relative to that which would be produced by monoenergetic crossed beams. The "nominal inversion" thus gives a good first approximation to the KI c.m. distribution; but improvements that account for the beam distributions are definitely needed.

2) C.m. \rightarrow Lab. Computations.

The first approach to accounting for the beam distributions involves assuming (i.e., guessing) a c.m. differential cross section functionality and then integrating over the beam distributions to produce the associated lab. distribution. Comparing the results with the experimental lab. distribution, one then alters the assumed c.m. function to try for a better fit to the data. This is then repeated many times with the hope of eventually reproducing the data.

Two different methods of integration have been used at Wisconsin. The first method,²⁷ a "counting" method based on weighting a set of points in velocity space according to the chosen c.m. distribution function, has been replaced by a direct integration method.⁴⁴ (Another direct integration method has been developed by Entemann^{25,73}).

Computer Program KICM (Appendix C) encompasses the essence of the integration method described by Warnock and Bernstein⁴⁴ (with some modifications and embellishments). The integration over the beam distributions is accomplished by summing the contributions (properly weighted by the density distributions in the beams) from a set of velocity vector (Newton) diagrams. The choice of velocities v_1 and v_2 is based on a method of Zaremba,⁷⁴ which specifies an efficient way of evaluating a two-dimensional integral by computing the integrand at a set of properly spaced points.⁷⁵

There are three major limitations to this inversion technique:

- (a) In previous calculations of this sort, the angular and energy dependencies of the c.m. cross section function were assumed independent (i.e. factorizable):

$$\frac{d^3\sigma(\theta, w')}{d^2\omega dw'} \propto P_\omega(\theta) \times P_{w'}(w') ;$$

The method, in theory, allows the use of a general coupled functional form if it proves necessary; in practice, it is hard to parameterize one's visualization of the way in which a coupled function should be altered to achieve an improvement in the fit to the experiments. A "best uncoupled" fit to the data can eventually be obtained with this method; but coupling of the angle and velocity distributions (and nature is surely coupled!) usually complicates the problem beyond easy solution.

- (b) The second limitation is the fact that one must admit to

a certain personal prejudice in the choice of functional form (perhaps based simply on ease of computation-uncoupled functions, for example); hence, the proper c.m. cross section function may escape notice simply due to a lack of imagination during the search.

- (c) Finally, even though a number of assumed functions can be tried at one time, there is still a practical limit on the total number of functions that can be examined; time, patience, or money is eventually exhausted.

3) Linear Additivity

The third difficulty in the inversion method above can be removed by noting that the scattering produced by a given c.m. function can be added to the scattering from another function to give the resultant scattering from the sum of the two functions. In general, a set of c.m. functions can be added linearly to produce another function whose laboratory scattering intensities are just the equivalent linear sum of the intensities for the individual functions. In this way a large number of functions can be built up from a basis set of functions by a systematic variation of the coefficients in the linear sum. If this idea were taken no further, it would handle limitation (c) above, but neither (a) nor (b); the extension to a general inversion technique is described below.

4) Lab \rightarrow c.m. Inversion.⁷⁶

The disadvantages of the above methods are linked to the basic approach to the inversion problem; instead of using the lab. data to

produce the c.m. function directly, one works backward from an assumed c.m. cross section in an attempt to reproduce the experimental data. This is done because it is much easier to integrate over the beam distributions than to deconvolute these same distributions.

The more direct "inversion" from lab. to c.m. can be seen in a simple extension of the linear additivity approach already noted. A basis set of c.m. functions, $f_k(\theta, w')$ is chosen and the laboratory scattering map associated with each is computed in the normal way. The best linear combination of these basis functions

$$I_{cm}(\theta, w') = \sum_{k=1}^{\ell} b_k f_k(\theta, w') \quad (B1)$$

is found, not by a systematic variation of the coefficients in the sum, but by a general fitting routine which finds the expansion coefficients, b_k , which give the best (least-squares) fit to the experimental data. At n laboratory velocity-angle positions ($n > \ell$), the calculated laboratory intensities, I_n , are given by the sum

$$I_n = \sum_{k=1}^{\ell} b_k I_{nk},$$

where I_{nk} is the intensity at point n from the k^{th} c.m. distribution function. In these n equations, the coefficients b_k are determined which give a minimum in the quantity

$$\sum_n (I_n - I_n')^2,$$

where I_n is the experimental laboratory flux intensity at the n^{th} data point. The set of b_k 's found is then the set of expansion coefficients in Eqn. (B1). Least squares fitting programs are readily available; subroutine GAUSHAUS of the University of Wisconsin Computing Center is an example (see Appendix C); most X-ray crystallographers have similar packages.

If the basis set is a general expansion set in w' and θ , then any c.m. functional form can be obtained as a linear combination of the basis functions. This easily allows coupled c.m. functions without the problems associated with visualization, since the computer does the iteration to the best functional form. In practice for improved efficiency, an initial guess of the c.m. distribution is factored out of Eqn. (B1)

$$I_{\text{CM}}(\theta, w') = I_0(\theta, w') \sum_{k=1}^{\ell} b_k f_k(\theta, w')$$

the results are basically independent of the initial guess, as long as it is not a completely unreasonable function.

The first basis set used (for an unpublished re-analysis of the results of Chapter III for $K + \text{HBr}$ and $K + \text{DBr}$)⁴¹ was an uncoupled histogram function with typically 4 velocity and 5 angular intervals; the results were not encouraging, with many regions showing apparent negative c.m. cross section contributions (clearly unphysical). In an attempt to remove discontinuities from the functions, a Legendre basis set was tried next; the results also showed comparable regions of negative intensity and the fits to the data were not very good. Due to kinematic difficulties in the $K + \text{HBr}$ system (see Chapter III) and uncertainties as to the secondary beam velocity distribution, the

computations were abandoned without ever trying any coupled c.m. functions. P. Siska has recently and independently developed a similar inversion program and has used coupled c.m. functions to analyze the $K + \text{HBr}$, DBr data with somewhat greater success⁵⁷; unfortunately his results also had regions of negative c.m. intensity, suggesting that perhaps a still more accurate determination of the lab. scattering distribution might be needed for a good inversion.

For the $K + \text{I}_2$ system, however, kinematic considerations are far better; and less accurate lab. data are still adequate for obtaining a good inversion to the c.m. A coupled two-dimensional Legendre expansion was used:

$$I(\theta, w') = F_0(w') \times G_0(\theta) \sum_{i=0}^k \sum_{j=0}^m b_{ij} P_i(Y) P_j(X), \quad (\text{B2})$$

where $F_0(w') \times G_0(\theta)$ is an initial uncoupled starting guess,

$$Y = 2 \times \frac{w'}{1100} - 1, \quad (w' \text{ in m/sec}),$$

$$\text{and } X = 2 \times \theta/\pi - 1, \quad (\theta \text{ in Radians}),$$

with typically 30 coupled basis functions (6 velocity, 5 angle).

Computer program I2LEG (Appendix C) illustrates this calculation for the experimental data at $\bar{E} = 3.62$ kcal/mole.

5) Extensions*

There are a couple of ways of improving these calculations that should be mentioned. The most obvious extension is an increase in the number of basis functions used in the expansion. Unfortunately, when more Legendre terms are added to the expansion, the coefficients of all the previous terms change; this is due to a lack of orthonormality in the basis functions ($F_0(w) \times G_0(\theta)$ included!) and makes it hard to determine when a solution is "settling down". The best choice of basis functions, $S_j(x)$ and $T_i(y)$, for the expansion

$$I(\theta, w) = F_0(w) G_0(\theta) \sum_i \sum_j b_{ij} S_j(x) T_i(y)$$

is the "associated set" which satisfies the following orthonormality relations:

$$\int S_j(x) S_m(x) G_0(x) dx = \delta_{jm}$$

$$\int T_i(y) T_k(y) F_0(y) dy = \delta_{ik}$$

This is, in practice, difficult to satisfy except for very simple forms for F_0 and G_0 . When these orthogonality criteria are not met, any set of reasonably well-behaved basis functions is no better than any other. The Legendre expansion then has no particular merit over,

* Many stimulating discussions with R. A. LaBudde were very helpful in the development of this section.

for example, a power series solution in terms of $x^j y^i$. Such a power series was tried in one computation; the c.m. map deduced, the laboratory distribution it produced, and the least squares fit of that distribution to the experimental data were all virtually identical to the results using the Legendre expansion with the same number of terms. The power series saves a little computer time and is easier to handle; hence, if no attempt is made to simplify $F_0(w)$ and $G_0(\theta)$ so that an "associated basis set" can be used, it seems worthwhile to choose the simplest expansion set possible.

6) Narrowing Inversion*

Another, less satisfactory, approach to the inversion problem involves an iterative "narrowing" of the c.m. function. The first step is a "nominal inversion" (see (1) above) of the lab. map to produce a c.m. trial function. This c.m. function is then used to produce a laboratory distribution by a full averaging over the beam distributions (see (2) above). The lab. distribution produced is, of course, broader than the original one, due to the beam distribution averaging. Comparing the two lab. distributions (e.g. by subtracting) yields a difference function, which can be used as the lab. distribution for another cycle; hopefully, one would converge to the proper c.m. function (in this case, as a sum of the various terms) after a few

- - - - -

* This approach has been used by D. J. McDonald, Harvard Univ.
(Private communication).

iterations. A couple of peculiar difficulties arose with this method:

a) First, with only a partial data map, a fully defined c.m. map requires interpolation between data points and extrapolation to regions without data (note that the c.m. \rightarrow lab. integration, due to the motion of the c.m., uses a larger set of c.m. points than defined by the nominal inversion).

b) Second, every iteration necessitates a full averaging over the beam distributions; if a number of iterations are necessary, this can be very time consuming.

Program I2LEG does the beam integration only once (all basis functions at the same time); the iteration scheme simply "juggles" coefficients in a series of linear equations.

Appendix CComputer Programs1) DC

Program DC contains computational simulations of the various characterization experiments of the selector and analyzer, along with an estimation of the K beam distribution entering the scattering zone. The computations are based on the apparatus geometry and the general formulas of Appendix A and include integrations over resolution angles and slit heights. All integration subprograms in this (not subsequent) program are primitive trapezoidal rule summations. A comparison of the results of problems 1, 3, 5 (no angle, slit height averaging) with those of problems 2, 4, 6 (full averaging) shows that angle and slit height averaging were unnecessary in these three computations (selector characterization with M-B K beam, analyzer characterization with M-B beam, and selector characterization of Laval K beam, respectively). Problems 7-9 (selector-analyzer cross characterization at three different angles through the selector) require full averaging. This is also necessary in determining the K beam distribution entering the scattering zone (Problem 10). In the results described in Appendix A, a computational correction for the "dissolving" disk of the selector has also been made; the Fortran 63 program illustrated here does not contain this correction. This program (problems 1-10 incl.) took 3.5 minutes of computer time on a CDC 3600 computer.

```

PROGRAM DC
COMMON/TT/ANGD(49),ANGC(49),BOLTZ(300)
DIMENSION SIG(50),SRA(90),VNOM(50),VLAV(50),YANAL(90),YSEL(90,50)
DIMENSION SRAB(90)
C VLAV IS THE LAVAL K BEAM FLUX DISTRIBUTION INCIDENT UPON THE SEL.
C RANGE IS 90 TO 450 RPS (VELOCITY=3.14*RPS)
  DATA((VLAV(I),I=9,45)=.005,.01,.015,.025,.05,.09,.15,.22,.31,.41,
    1 .53,.66,.77,.87,.95,.99,1.,.99,.95,.91,.85,.78,.71,.63,.55,.46,
    2 .38,.32,.26,.21,.17,.14,.12,.1,.09,.08,.07)
C PROBLEM 1,2--SEL VS M-B BEAM
C PROBLEM 3,4-- ANAL VS M-B BEAM
C PROBLEM 5,6-- SEL VS LAVAL K BEAM
C 1,3,5 ARE WITH NO HT., ANGLE AVERAG.
C 2,4,6 HAVE 5 VALUES HT., .5 DEG. ANGULAR WIDTH
C 7,8,9 -- SEL VS ANAL, HT., ANGLE AVERAGED--
C 7 AT 0.0 DEG. 8 AT +.5(4/3) DEG. 9 AT -.5(4/3)
C PROBLEM 10 -- SEL FLUX, DENSITY TRANSMISSION VS VELOCITY AT LAVAL PEAK
C ACON*RPS= NOMINAL VELOCITY TRANSMITTED BY THE ANALYZER (ALONG CENTER
C OF BEAM), SELCON*RPS= NOMINAL K BEAM VELOCITY AT THE GIVEN ANGLE
C SELCON=3.14 AT .05 DEG E.Q., SELCON =3.15 AT ZERO DEGREES
  ACON=3.62 $ SELCON=3.15
  PI=3.1415926536 $ EX=EXPF(1.5) $ RAD=0.01745329252
C THE FOLLOWING CONSTANTS ARE EASILY UNDERSTOOD IN TERMS OF THEIR NAMES
C NOTE THAT SMALL PERTURBATIONS OF SPELLING IN CONSTANTS ARE EASILY
C IDENTIFIABLE-- S ASSOCIATED WITH SELECTOR, A WITH ANALYZER
C DIMENSIONS IN METERS/SEC ANGLES IN RADIANS
  APhi=.1695 $ SPhi=.0564 $ ABeta=.01628 $ SBeta=.05427
  Rmin=.072 $ Rave=.076 $ Rmax=.080 $ Nteeth=278
  Space=.000813 $ D=.001628 $ Alength=.1 $ Slength=.03
  Spaca=Space
C BUILDUP OF MAXWELL BOLTZMANN FLUX DISTRIBUTION
96 DO 11 J=1,300 $ U=J*.01 $ BOLTZ(J)=U**3*EXPF(-1.5*U**2)*EX
11 PRINT 6000,U,BOLTZ(J)
6000 FORMAT(F10.2,F10.4)
C SETTING UP PROBLEM 1
  NPROB=0 $ ANG=.5*RAD $ SL=.20 $ DS=.05 $ LL=36 $ NL=20 $ NH=30
  HFW=0. $ MM=1 $ JJ=1 $ XL=SLENGTH $ BETA=SBETA $ PHI=SPhi
  CON=SELCON
  17 DO 12 L=1,50
  12 SIG(L)=0. $ NPROB=NPROB+1 $ AINT=2./(MM+1)
  CALL KTIME(MIN,KSEC,KK) $ PRINT 5555,MIN,KSEC
5555 FORMAT(5X,I5,5H MIN,I5,5H SEC)
C SUMMING ALONG THE RADIAL DIRECTION
  DO 20 J=1,JJ $ R=RAVE+(RMAX-RMIN)*(2*J-JJ-1)/(2.*JJ)
  TOOTH=2.*PI/NTEETH*R-SPACE $ ETA=SPACE/(SPACE+TOOTH)
  ALPHA=ANG+HFW*RAD $ THETA=-HFW $ H=AINT*HFW*RAD
C SUMMING OVER ANGLE
  DO 19 M=1,MM $ ALPHA=ALPHA-H $ THETA=THETA+AINT*HFW
  GAMMAP=SPACE/((XL+D)*ALPHA+PHI*R) $ AL=ETA+ETA/GAMMAP
  GAMMADP=SPACE/((XL-D)*ALPHA+PHI*R) $ AH=ETA-ETA/GAMMADP
  DELTA=D*ALPHA/(PHI*R+XL*ALPHA)
C SCANNING THE BEAM DISTRIBUTION BY CHANGING ROTATION SPEED
  DO 10 L=1,LL $ VNOM(L)=SL+DS*L $ RPS=VNOM(L)/CON $ OMEGA=2*PI*RPS
  VZSTAR=XL*OMEGA*R/(PHI*R+XL*ALPHA)
  VMIN=VZSTAR*(1.+BETA)/(1+GAMMAP)/(1+DELTA) $ DELB=VZSTAR-VMIN
  VMAX=VZSTAR*(1.-BETA)/(1-GAMMADP)/(1-DELTA) $ DELT=VMAX-VZSTAR
  BL=-ETA*(1+BETA)*VZSTAR/GAMMAP/(1+DELTA)
  BH=ETA*(1-BETA)*VZSTAR/GAMMADP/(1-DELTA)
  IF(NPROB.GT.6) 18,9

```

```

C INTEGRATING OVER THE VELOCITY DISTRIBUTION
.9 TEML=0. $ TEMH=0. $ DO 13 I=1,NL $ V=VMIN+I/(NL+1)*DELB
13 TEML=TEML+(AL+BL/V)*BEAM(V)
   TEML=TEML+(AL+BL/VZSTAR)*BEAM(VZSTAR)*.5 $ TEML=TEML*DELB/(NL+1)
   DO 14 I=1,NH $ V=VZSTAR+I/(NH+1)*DELT
14 TEMH=TEMH+(AH+BH/V)*BEAM(V)
   TEMH=TEMH+(AH+BH/VZSTAR)*BEAM(VZSTAR)*.5 $ TEMH=TEMH*DELT/(NH+1)
   GO TO 10
18 DO 21 I=1,NV $ V=VZERO+I/100. $ IF(NPROB.GT.9) 27,26
C COMPUTING THE VELOCITY DISTRIBUTION OF THE SELECTOR TRANSMISSION
C INCIDENT UPON THE ANALYZER IN THE CROSS-COMPARISON EXPERIMENT
26 IF(V.LT.VMIN) 21,22
22 IF(V.LT.VZSTAR) 23,24
23 YSEL(I)=YSEL(I)+(AL+BL/V)*BEAM(V)*AR(THETA,HFW) $ GO TO 21
24 IF(V.LT.VMAX) 25,21
25 YSEL(I)=YSEL(I)+(AH+BH/V)*BEAM(V)*AR(THETA,HFW) $ GO TO 21
C SELECTOR TRANSMISSION COMPUTED AS A FUNCTION OF VELOCITY AND ANGLE--
C THIS MAKES POSSIBLE A LATER ADJUSTMENT OF THE BEAM ANGULAR PROFILE
C TO ACCOUNT FOR THE FACT THAT THE ACTUAL PROFILE TAKEN EXPERIMENTALLY
C WAS DONE FOR A VELOCITY-SELECTED BEAM AND THEREFORE WAS NOT A TRUE
C ANGULAR DISTRIBUTION OF THE K BEAM
27 IF(V.LT.VMIN) 21,28
28 IF(V.LT.VZSTAR) 29,30
29 YSEL(I,M)=YSEL(I,M)+(AL+BL/V)*BEAM(V)*EXPANG(THETA) $ GO TO 21
30 IF(V.LT.VMAX) 31,21
31 YSEL(I,M)=YSEL(I,M)+(AH+BH/V)*BEAM(V)*EXPANG(THETA) $ GO TO 21
21 CONTINUE $ GO TO 19
10 SIG(L)=SIG(L)+AR(THETA,HFW)*(TEMH+TEML)
19 CONTINUE
20 CONTINUE
   IF(NPROB.GT.6) 32,33
C SRA IS THE FLUX THROUGH THE SELECTOR DIVIDED BY VELOCITY--IT SHOULD
C BE COMPARED TO THE INCIDENT M-B BEAM(LAVAL BEAM IN PROB. 5,6)
33 DO 16 L=1,LL
16 SRA(L)=SIG(L)/VNOM(L)
C SEARCH FINDS THE LARGEST ELEMENT OF AN ARRAY FOR LATER NORMALIZATION
PRINT 7000,NPROB $ PRINT 7001 $ CALL SEARCH(0,SIG,LL,JK,APEX)
CALL SEARCH(0,SRA,LL,JK,TOP) $ DO 15 L=1,LL $ SRA(L)=SRA(L)/TOP
SIG(L)=SIG(L)/APEX $ W=BEAM(SL+L*DS)
PUNCH 6002,VNOM(L),SIG(L),SRA(L),W
15 PRINT 6002,VNOM(L),SIG(L),SRA(L),W
7001 FORMAT(5X,4HVNOM,6X,4HFLUX,6X,4HS/RA,5X,4HBEAM)
6002 FORMAT(F10.2,4F10.4)
7000 FORMAT(1H1,10X,6HNPROB=,I5)
C PROBLEMS 2 TO 6 ARE SET UP HERE
GO TO(51,52,51,54,51,56),NPROB
51 MM=9 $ HFW=.25 $ JJ=5 $ GO TO 17
52 MM=1 $ HFW=0. $ JJ=1 $ NL=10 $ NH=15 $ XL=ALENGTH $ ANG=.18*RAD
   BETA=ABETA $ PHI=APHI $ CON=ACON $ GO TO 17
C LAVAL K BEAM DISTRIB. IS SUBSTITUTED FOR THE M-B CURVE HERE (REDUCED
C VARIABLES) -- FOR PROBLEMS 5,6
54 DO 57 I=1,35
57 BOLTZ(I)=0. $ DO 58 I=36,180 $ J=U/I/4. $ V=(U-J)*4. $ W=4.-V
   JP=J+1
58 BOLTZ(I)=.25*(W*VLAV(J)+V*VLAV(JP)) $ PRINT 7002
7002 FORMAT(1H1,16HLAVAL FLUX INPUT)
DO 59 J=1,180 $ U=J/100.
59 PRINT 6000,U,BOLTZ(J)
95 MM=1 $ HFW=0. $ JJ=1 $ NL=20 $ NH=30 $ XL=SLENGTH $ ANG=.5*RAD
   BETA=SBETA $ PHI=SPHI $ CON=SELCON $ SL=.45 $ DS=.05 $ LL=19
   GO TO 17

```

```

C START OF PROBLEM 7
56 ANGS=.5*RAD $ ANGA=.18*RAD $ APPANG=0.
710 HFW=.25 $ MM=9 $ JJ=5 $ SL=.99 $ DS=.01 $ LL=1 $ NL=20 $ NH=30
93 ANG=ANGS $ NV=46 $ VZERO=.79 $ DO 60 I=1,90 $ YSEL(I)=0.
60 YANAL(I)=0. $ GO TO 17
32 IF(NPROB.GT.9) 34,35
C CARDS 35 THROUGH 120 ARE SIMILAR TO AN EARLIER SECTION OF THIS
C PROGRAM, CARDS 17 TO 20. THE DIFFERENCE IS THAT AVERAGING OVER THE
C SLIT HEIGHT, ANGLE, AND VELOCITY ARE DONE HERE FOR BOTH THE SELECTOR AND
C ANALYZER IN COMBINATION.
35 SL=VZERO $ DS=.01 $ LL=NV $ NL=10 $ NH=15
XS=SLENGTH $ XA=ALENGTH $ AINT=2./(MM+1)
DO 120 J=1, JJ $ R=RAVE+(RMAX-RMIN)*(2*J-JJ-1)/(2*JJ)
TOOTH=2*PI/NTEETH*R-SPACE $ ETA=SPACE/(SPACE+TOOTH)
RP=2.*RAVE-R $ TOOTHP=2.*PI/NTEETH*RP-SPACA
ETAP=SPACA/(SPACA+TOOTHP)
ALPHAS=ANGS+HFW*RAD $ THETA=-HFW
ALPHAA=ANGA-HFW*RAD $ H=AINT*HFW*RAD
DO 119 M=1, MM $ ALPHAS=ALPHAS-H $ ALPHAA=ALPHAA+H
THETA=THETA+AINT*HFW
GPS=SPACE/((XS+D)*ALPHAS+PHI*R) $ ALS=ETA+ETA/GPS
GPA=SPACA/((XA+D)*ALPHAA+PHI*RP) $ ALA=ETAP+ETAP/GPA
GDPS=SPACE/((XS-D)*ALPHAS+PHI*R) $ AHS=ETA-ETA/GDPS
GDPA=SPACA/((XA-D)*ALPHAA+PHI*RP) $ AHA=ETAP-ETAP/GDPA
DELS=D*ALPHAS/(PHI*R+XS*ALPHAS)
DELA=D*ALPHAA/(PHI*RP+XA*ALPHAA)
OMEGAS=2*PI/SELCON
VZSTARS=XS*OMEGAS*R/(PHI*R+XS*ALPHAS)
VMINS=VZSTARS*(1+SBETA)/(1+GPS)/(1+DELS)
VMAXS=VZSTARS*(1-SBETA)/(1-GDPS)/(1-DELS)
BLS=-ETA*(1+SBETA)*VZSTARS/GPS/(1+DELS)
BHS=ETA*(1-SBETA)*VZSTARS/GDPS/(1-DELS)
DO 110, L=1, LL $ VNOM(L)=SL+DS*L $ RPS=VNOM(L)/ACON
OMEGAA=2*PI*RPS $ VZSTARA=XA*OMEGAA*RP/(PHI*RP+XA*ALPHAA)
VMINA=VZSTARA*(1+ABETA)/(1+GPA)/(1+DELA) $ DELB=VZSTARA-VMINA
VMAXA=VZSTARA*(1-ABETA)/(1-GDPA)/(1-DELA) $ DELT=VMAXA-VZSTARA
BLA=-ETAP*(1+ABETA)*VZSTARA/GPA/(1+DELA)
BHA=ETAP*(1-ABETA)*VZSTARA/GDPA/(1-DELA) $ TEML=0. $ TEMH=0.
DO 113 I=1, NL $ V=VMINA+I/(NL+1)*DELB $ IF(V.LT.VMINS) 113,213
213 IF(V.LT.VZSTARS) 313,413
313 TEML=TEML+(ALA+BLA/V)*(ALS+BLS/V)*BEAM(V) $ GO TO 113
413 IF(V.LT.VMAXS) 513,113
513 TEML=TEML+(ALA+BLA/V)*(AHS+BHS/V)*BEAM(V)
113 CONTINUE $ DO 114 I=1, NH $ V=VZSTARA+I/(NH+1)*DELT
IF(V.LT.VMINS) 114,214
214 IF(V.LT.VZSTARS) 314,414
314 TEMH=TEMH+(AHA+BHA/V)*(ALS+BLS/V)*BEAM(V) $ GO TO 114
414 IF(V.LT.VMAXS) 514,114
514 TEMH=TEMH+(AHA+BHA/V)*(AHS+BHS/V)*BEAM(V)
114 CONTINUE
IF(VZSTARA.LT.VMINS) 115,215
215 IF(VZSTARA.LT.VZSTARS) 315,415
315 TEML=TEML+(ALA+BLA/VZSTARA)*(ALS+BLS/VZSTARA)*BEAM(VZSTARA)*.5
TEMH=TEMH+(AHA+BHA/VZSTARA)*(ALS+BLS/VZSTARA)*BEAM(VZSTARA)*.5
GO TO 115
415 IF(VZSTARA.LT.VMAXS) 515,115
515 TEML=TEML+(ALA+BLA/VZSTARA)*(AHS+BHS/VZSTARA)*BEAM(VZSTARA)*.5
TEMH=TEMH+(AHA+BHA/VZSTARA)*(AHS+BHS/VZSTARA)*BEAM(VZSTARA)*.5
115 TEML=TEML*DELB/(NL+1) $ TEMH=TEMH*DELT/(NH+1)
110 YANAL(L)=YANAL(L)+AR(THETA,HFW)*(TEMH+TEML)
119 CONTINUE

```

```

120 CONTINUE
C SRAB IS THE DISTRIBUTION ASSOCIATED WITH A UNIFORM FLUX INPUT TO THE
C SELECTOR
  DO 630 L=1,LL
    SRAB(L)=YANAL(L)/VNOM(L)/BEAM(VNOM(L))
  630 SRA(L)=YANAL(L)/VNOM(L) $ PRINT 7000,NPROB $ PRINT 8000,APPANG
8000 FORMAT(2X,11HSEL VS ANAL,10X,5HTLAB=,F5.2)
  PRINT 8001 $ CALL SEARCH(0,YSEL,LL,JK,APEX)
8001 FORMAT(5X,4HVRED,5X,5HAFLUX,6X,4HS/RA,3X,7HSELFLUX,5X,5HS/RAB)
  CALL SEARCH(0,SRAB,LL,JK,TOP)
  CALL SEARCH(0,YANAL,LL,JK,ZEN) $ CALL SEARCH(0,SRA,LL,JK,PEAK)
  DO 631 L=1,LL $ YSEL(L)=YSEL(L)/APEX $ YANAL(L)=YANAL(L)/ZEN
  SRA(L)=SRA(L)/PEAK $ SRAB(L)=SRAB(L)/TOP
  PUNCH 6002,VNOM(L),YANAL(L),SRA(L),YSEL(L),SRAB(L)
631 PRINT,6002,VNOM(L),YANAL(L),SRA(L),YSEL(L),SRAB(L)
  98 JK=NPROB-6 $ GO TO (700,701,702),JK
C PROBLEM 8 IS AT AN ANGLE 0.5 DEGREES CHANGED FROM PROBLEM 7
C 0.5 DEGREES RELATIVE TO THE SELECTOR AXIS IS 4/3*0.5 DEGREES ON THE
C ROTATING LID (GONIOMETER)
C APPARATUS GEOMETRY IS SUCH THAT GONIOMETER ROTATION OF 1. DEGREE IS
C EQUIVALENT TO 1.*3/4 DEGREES ANGLE RELATIVE TO THE SELECTOR AXIS
  700 ANGS=0. $ APPANG=.5*4./3. $ GO TO 710
C PROB. 9 IS 0.5 DEG. THE OTHER WAY
  701 ANGS=1.*RAD $ APPANG=-.5*4./3. $ GO TO 710
  702 ANG=.5*RAD $ RAD=RAD*.75 $ HFW=2.5 $ MM=49 $ JJ=5 $ SL=.99
C START OF PROB.10
  DS=.01 $ LL=1 $ NV=84 $ VZERO=.74
  DO 703 I=1,4500
  703 YSEL(I)=0. $ GO TO 17
C DETERMINING THE ANGULAR DISTRIBUTION PRODUCED BY THE INTEGRATION
  34 DO 400 I=1,NV
  400 ANGC(I)=0. $ DO 401 I=1,NV $ DO 401 M=1,MM
  401 ANGC(M)=ANGC(M)+YSEL(I,M) $ CALL SEARCH(0,ANGC,MM,JK,TOP)
  PRINT 9001
  DO 402 M=1,MM $ ANGC(M)=ANGC(M)/TOP
  THETA=(M-1)/10.-HFW+2*HFW/(MM+1)
  402 PRINT,9000,THETA,ANGD(M),ANGC(M)
9000 FORMAT(F10.2,2F10.3)
9001 FORMAT(1H1,4X,5HTHETA,6X,4HANGD,6X,4HANGC)
C AN ITERATION THAT CORRECTS FOR THE BIAS IN THE ANGULAR DISTRIBUTION
C CAUSED BY THE VELOCITY SELECTOR
  DO 403 I=1,NV $ DO 403 M=1,MM
  403 YSEL(I,M)=YSEL(I,M)*ANGD(M)/ANGC(M)
  DO 404 I=1,NV $ DO 404 M=2,MM
  404 YSEL(I,1)=YSEL(I,1)+YSEL(I,M)
  DO 706 I=1,NV
  XX=VZERO+I/100. $ SRA(I)=YSEL(I)/XX
  706 SRAB(I)=SRA(I)/BEAM(XX) $ PRINT 7000,NPROB $ PRINT 8002
8002 FORMAT(8X,1HV,7X,4HFLUX,6X,4HDENS,5X,5HS/RAB)
  CALL SEARCH(0,SRA,NV,JK,PEAK) $ CALL SEARCH(0,YSEL,NV,JK,APEX)
  CALL SEARCH(0,SRAB,NV,JK,TOP)
  DO 705 I=1,NV $ YSEL(I)=YSEL(I)/APEX $ SRA(I)=SRA(I)/PEAK
  SRAB(I)=SRAB(I)/TOP
  U=VZERO+I/100.
  PUNCH 6002,U,YSEL(I),SRA(I),SRAB(I)
  705 PRINT,6002,U,YSEL(I),SRA(I),SRAB(I)
  73 END
  FUNCTION BEAM(V)
C M-B FOR FIRST 4 PROBLEMS, THEN CHANGED TO AGREE WITH LAVAL K BEAM
  COMMON/TT/ANGD(49),ANGC(49),BOLTZ(300)
  U=100.*V $ I=U $ P=U-I

```

```

BEAM=BOLTZ(I)*(1.-P)+BOLTZ(I+1)*P
RETURN
END
FUNCTION AR(THETA,HFW)
C IDEALIZED ANGULAR DISTRIBUTION SEEN BY THE FILAMENT DETECTOR
AB=ABSF(THETA) $ IF(AB.LE..28*HFW) 1,2
1 AR=1. $ RETURN
2 AR=1.- (AB-.28*HFW)*10./7.2/HFW
RETURN
END
FUNCTION EXPANG(THETA)
C EXPERIMENTAL ANGLE SCAN AROUND ZERO DEGREES WITH SELECTOR AT
C LAVAL PEAK VELOCITY
COMMON/TT/ANGD(49),ANGC(49),BOLTZ(300)
DATA((ANGD(I),I=1,49)=.008,.01,.012,.013,.022,.04,.06,0.08,.11,
1 .15,.2,.26,.33,.43,.57,.68,.77,.86,.93,.97,.99,1.01,1.015,1.01,
2 1.,.98,.95,.91,.85,.79,.73,.65,.55,.47,.38,.32,.27,.23,.2,.17,
3 .15,.13,.11,.1,.08,.07,.06,.05,.04)
I=(THETA+2.4)*10.+1. $ EXPANG=ANGD(I)
RETURN
END
SCOPE
'LOAD
'RUN,TI=10,PR=5000,PL=1000,PU=1000

```

2) KICM

This is an improved version of the program of Warnock and Bernstein⁴⁴ which takes an assumed center-of-mass distribution (usually uncoupled angular and energy functions) and with proper averaging over the beam distributions transforms to a laboratory distribution. The example below contains only one assumed function and uses less than 2 minutes of computer time on a CDC 3600 computer; in practice, usually 7-10 different functions are tried simultaneously and the time is less than 3 minutes if the plotting section is removed (as is normally the case). The Zaremba numerical integration method⁷⁴ has been elucidated by T. T. Warnock.⁷⁵

```
PROGRAM KICM
COMMON/VELSLECT/V1NOM,V2NOM
COMMON/LINTERP/WCM(22)
C CM INTENSITY VS. VELOCITY DISTRIBUTION (POINTS SPACED EVERY 50 M/SEC)
C WHICH WILL BE USED AS A GUESS TO THE ACTUAL DISTRIBUTION--THE PROGRAM
C WILL LINEARLY INTERPOLATE ON THESE FUNCTION VALUES
C THE ANGULAR DISTRIB. USED IN THIS ATTEMPT(NOTE- UNCOUPLED) IS
C DEFINED IN SUBROUTINE XSECT
DATA((WCM(I),I=1,22)=.06,.27,.53,.76,.87,.87,.81,.75,.71,.67,.62,
1 .56,.49,.4,.29,.19,.11,.07,.03,.01,.005,.0)
DIMENSION VLAV(50)
C LAVAL K BEAM FLUX DISTRIB. FOR USE IN PROPER WEIGHTING OF BEAM DIST.
DATA((VLAV(I),I=13,45)=.05,.09,.15,.22,.31,.41,.53,.66,.77,.87,
1 .95,.99,1.,.99,.95,.91,.85,.78,.71,.63,.55,.46,.38,.32,.26,.21,
2 .17,.14,.12,.1,.09,.08,.07)
DIMENSION VEL(24),ANG(17),TEM(10),TOT(17,10),SIG(24,17,10)
DIMENSION GTOT(10)
DIMENSION ITAG(6)
DIMENSION BNORM(10)
COMMON/RETURNS/NUM,VALUES(10),LABLE(6,10)
COMMON/BETWEEN/VCM,VCMSQ,XI,ALPHA,VR,QMAX,E,WP
COMMON/STERN/THL,VP,EPC,EP,ETA,VPSQ,WPSQ
COMMON/BEEF/VV1,VV2,SQM1,SQM2,RMM,TMSQ,UC
DIMENSION V2(144),V1(144),WT(144)
DIMENSION ISY(100)
C ARRAY USED IN PLOTTING
DATA((ISY(I),I=1,100)= 2H01,2H02,2H03,2H04,2H05,2H06,2H07,2H08
1,2H09,2H10,2H11,2H12,2H13,2H14,2H15,2H16,2H17,2H18,2H19,2H20,2H21,
22H22,2H23,2H24,2H25,2H26,2H27,2H28,2H29,2H30,2H31,2H32,2H33,2H34,2
3H35,2H36,2H37,2H38,2H39,2H40,2H41,2H42,2H43,2H44,2H45,2H46,2H47,2H
448, 2H49,2H50,2H51,2H52,2H53,2H54,2H55,2H56,2H57,2H58,2H59,2H60,2H
561,2H62,2H63,2H64,2H65,2H66,2H67,2H68,2H69,2H70,2H71,2H72,2H73,2H7
64,2H75,2H76,2H77,2H78,2H79,2H80,2H81,2H82,2H83,2H84,2H85,2H86,2H87
7,2H88,2H89,2H90,2H91,2H92,2H93,2H94,2H95,2H96,2H97,2H98,2H99,2H00)
DATA(QMAX=41.5)
TYPE REAL M1,M2,M1P,M2P
C NUM=1 IMPLIES ONLY ONE CM FUNCTIONAL FORM TRIED HERE. THIS IS
C INEFFICIENT IN PRACTICE,BUT MAKES FOR EASIER ILLUSTRATION
C TEN ANGLES, 24 VELOCITIES USED FOR LAB. INTENSITY CALCULATIONS
NUM=1 $ NG=10 $ NV=24 $ SEL=300.
C SEL = SELECTOR ROTATION SPEED IN RPS
VINOM=3.15*SEL
M1=39.102 $ M2=253.81 $ M1P=166.00 $ M2P=126.90 $ V2NOM=152.0
SQM1=M1**2 $ SQM2=M2**2 $ RMM=M2/M1 $ TMSQ=(M1+M2)**2
UC=M1*M2/(M1+M2)*1.1950286807E-7
EPC=M1P/M2P*(M1P+M2P)*1.1950286807E-7
WMAS=SQRTF(M2*M1*M2P/M1P/TMSQ)
C ZAREMBA SPACING USES A FIBONACCI NUMBER OF POINTS--1,1,2,3,5,8,13,21,
C 34,55,89,144,... METHOD SPACES POINTS ALONG V1,V2 FOR NUMBER. INTEGR.
NTR=55 $ R=1./55. $ S=34./55. $ X=Y=0.0 $ XVS=.790*VINOM
C 55 DIFFERENT NEWTON DIAGRAMS USED IN INTEGRATING OVER THE BEAMS
XR=.63*VINOM $ YR=3.*V2NOM
C WEIGHTING THE VARIOUS NEWTON DIAGRAMS.
DO 1 I=1,NTR $ V1(I)=XVS+XR*X $ V2(I)=4.+YR*Y
WT(I)=PRV1(V1(I))*PRV2(V2(I)) $ Y=Y+S $ IF(Y.GT.1.) Y=Y-1.
U=V1(I)/3.15/10. $ LL=U $ P=U-LL
C T IS THE EFFECT DUE TO THE LAVAL DIST.
T=VLAV(LL)*(1.-P)+VLAV(LL+1)*P $ WT(I)=WT(I)*T
1 X=X+R
```

```

DO 2 I=1,24
2 VEL(I)=50.*(I+1) $ DO 3 J=3,10
3 ANG(I)=10.*(I-2) $ ANG(2)=-5.0 $ ANG(1)=-15.0
  ANG(11)=101. $ ANG(7)=49.5
  DO 4 J=1,170
4 TOT(I)=0.0 $ DO 5 I=1,4080
5 SIG(I)=0.
C DEFINING THE SIZE OF A LABORATORY SCATTERING BIN FOR EVENTUAL TWO-
C DIMENSIONAL ZAREMBA INTEGRATION OVER THE BIN
C THIS INTEGRATION IS NOT ALWAYS NECESSARY(IF KINEMATICS ARE FAVORABLE,
C AS IN K+I2)--- THE INTEGRATION HAS BEEN REMOVED IN THE COMPARABLE
C SECTION (INSIDE THE DO LOOP;ENDING AT CARD 100) OF PROGRAM I2LEG
  DV=10. $ DVSQ=100. $ DT=2.*.01745329252 $ DTSQ=DT*DT
  VHF=5. $ THF=1.
  DO 6 I=1,10
6 GTOT(I)=0.0
C MAIN INTEGRATION LOOP
120 DO 100 I=1,NTR $ VV1=V1(I) $ VV2=V2(I) $ CALL BEFORE
  WMX=SQRTF((QMAX+E)/E)*VR*WMAS
  DO 100 J=1,NG $ TLAB=(ANG(J)-THF)*.01745329252
  THL=ANG(J)*.01745329252 $ DO 100 K=1,NV $ VLAB=VEL(K)-VHF
  VP=VEL(K) $ CALL AFTER $ D=SQRTF(DVSQ+VEL(K)**2*DTSQ)
  IF(WP.GE.WMX+.5*D) 100,60
C FOR A BIN CLOSE TO CENTROID, NEED MORE INTEGRATION POINTS
60 IF(WP.LT.100.) 63,64
63 MP=4 $ X=R=1./5. $ Y=S=3./5. $ GO TO 70
64 MP=2 $ X=R=1./3. $ Y=S=2./3.
70 THL=TLAB+.5*X*DT $ VP=VLAB+.5*Y*DV $ CALL AFTER $ CALL XSECT
  DO 71 N=1,NUM
71 TEM(N)=VALUES(N) $ Y=.5*X+Y $ X=1.5*X $ DO 73 M=1,MP
  THL=TLAB+X*DT $ VP=VLAB+Y*DV $ CALL AFTER $ CALL XSECT
  DO 72 N=1,NUM
72 TEM(N)=VALUES(N)+TEM(N) $ Y=Y+S $ IF(Y.GT.1.) Y=Y-1.
73 X=X+R $ DO 74 N=1,NUM
74 SIG(K,J,N)=R*TEM(N)*WT(I)+SIG(K,J,N)
100 CONTINUE
C SUMMING, NORMALIZATION, PRINTING OF VARIOUS ARRAYS FOLLOWS
DO 200 N=1,NUM $ DO 200 J=1,NG $ DO 200 K=1,NV
200 TOT(J,N)=TOT(J,N)+SIG(K,J,N)
  DO 203 N=1,NUM
  DO 203 J=1,NG
203 GTOT(N)=GTOT(N)+TOT(J,N)
  DO 300 N=1,NUM $ CALL SEARCH(0,TOT(1,N),NG,L,A)
  CALL SEARCH(0,SIG(1,1,N),408,L,BNORM(N)) $ PRINT 7000,BNORM(N)
7000 FORMAT(E20.2)
  DO 300 J=1,NG
  TOT(J,N)=TOT(J,N)/A $ DO 300 K=1,NV
300 SIG(K,J,N)=SIG(K,J,N)/BNORM(N)
  DO 502 N=1,NUM
  PRINT 5000,(LABLE(I,N),I=1,6),(ANG(J),J=1,NG)
  PRINT 5001,(TOT(J,N),J=1,NG)
  DO 500 K=1,NV
500 PRINT 5003,VEL(K),(SIG(K,J,N),J=1,NG)
502 PRINT 5004,GTOT(N)
5000 FORMAT(1H1,40X,6A8,//10X,17F7.1)
5001 FORMAT(/,9X,17F7.3)
5003 FORMAT(2X,F5.0,3X,17F7.4)
5004 FORMAT(23HOTOTAL FLUX RECEIVED= ,E12.2)
C PLOTTING OF THE SCATTERING MAP GENERATED FROM THE ASSUMED CM FUNCTION
  V1=VINOM $ V2=V2NOM $ VCMX=V1*M1/(M1+M2) $ VCMY=V2*M2/(M1+M2)
  X1=V1/200.+2. $ Y1=V2/200.+2. $ XCM=VCMX/200.+2.

```

```

      YCM=VCMY/200.+2. $ CALL PLOT(15.,0.,-3)
      DO 805 N=1,NUM
810  CALL PLOT(2.,2.,3) $ CALL PLOT(X1,2.,2) $ CALL PLOT(2.,Y1,2)
      CALL PLOT(2.,2.,2) $ CALL SYMBOL(XCM,YCM,.04,29,0.,-1)
      DO 806 J=1,NG $ A=ANG(J)*.01745329252 $ PX=COSF(A) $ PY=SINF(A)
      DO 806 K=1,NV $ X=VEL(K)*PX/200.+2.-.05
      Y=VEL(K)*PY/200.+2.-.035
      M=100.* SIG(K,J,N)+.5 $ IF(M.EQ.0) 807,806
807  M=100.
806  CALL SYMBOL(X,Y,.07,ISY(M),0.,2)
      DO 811 L=1,6
811  ITAG(L)=LABLE(L,N)
      CALL SYMBOL(0.,9.7,.28,ITAG,0.,48)
      CALL NUMBER(.7,8.5,.56,SEL,0.,4HF5.1)
      CALL PLOT(15.,0.,-3)
805  CONTINUE
      END
      SUBROUTINE XSECT
C  COMPUTES THE SCATTERING INTENSITY IN THE LAB., USING THE ASSUMED CM
C  FUNCTIONS
      COMMON/LINTERP/WCM(22)
      DATA
      1 (LABLE(1,1)=48H BEST UNCOUPLED C.M. DISTRIBUTION FROM IZLEG
      *(EE=2.7182818284),(PI=3.1415926535)
      COMMON/RETURNS/NUM,VALUES(10),LABLE(6,10)
      COMMON/STERN/THL,VP,EPC,EP,THETA,VPSQ,WPSQ
      COMMON/BETWEEN/VCM,VCMSQ,XI,ALPHA,VR,QMAX,E,WP
      TYPE REAL JACK
      FX=EP/(E+QMAX) $ IF(FX.GT.1.0) GO TO 99
      Y=2.*WP/1100.-1.
      IF(THETA.GT.PI) THETA=2.*PI-THETA $ X=2.*THETA/PI-1.
      I=WP/50. $ IF(I.EQ.0) 1,2
C  QUADRATIC WP DEPENDENCE FROM 0 TO 50 M/SEC TO AVOID JACOBIAN BLOWUP
      1 JACK=VR*VPSQ*WCM(1)/50.**2*(.25-.2*X+.75*X*X) $ GO TO 3
C  JACK=JACOBIAN(CM TO LAB)* RELATIVE VELOCITY*ASSUMED ANGULAR DISTRIBUTION*
C  ASSUMED ENERGY DISTRIBUTION.(LINEAR INTERP.)
      2 P=WP/50.-I $ JACK=VR*VPSQ/WPSQ*(WCM(I)*(1.-P)+WCM(I+1)*P)*
      1 (.25-.2*X+.75*X*X)
      3 VALUES(1)=JACK
      14 RETURN
C  NUM=1 IMPLIES ONLY VALUES(1) IS USED IN MAIN PROGRAM
      99 VALUES(1)=VALUES(2)=VALUES(3)=VALUES(4)=VALUES(5)=VALUES(6)=VALUES
      *(7)=VALUES(8)=VALUES(9)=VALUES(10)=0. $ RETURN
      END
      FUNCTION PRV1(V)
      COMMON/VELSLECT/V1NOM,V2NOM
C  BEST K BEAM DENSITY TRANSMISSION FUNCTION FOR UNIFORM FLUX VS VELOCITY
C  INPUT TO SELECTOR .039 SEL. SLIT, NPROB=10, 11/19/69
C  REDUCED VELOCITY 0.78 TO 1.41
      DIMENSION WT(64)
      DATA((WT(I),I=1,64)=.011,.021,.037,.06,.094,.138,.192,.256,
      1 .327,.404,.485,.568,.649,.727,.799,.862,.914,.954,.981,.996,
      2 1.,.994,.978,.954,.923,.886,.844,.799,.751,.701,.651,.6,.551,
      3 .503,.458,.415,.375,.338,.306,.272,.243,.216,.192,.17,.15,
      4 .133,.116,.102,.089,.078,.068,.059,.052,.045,.039,.034,.03,
      5 .026,.023,.02,.017,.015,.013,.011)
      I=R/V/V1NOM*100. $ IF(I.GE.78.AND.I.LE.140) GO TO 1 $ PRV1=0.0
      RETURN
      1 P=R-I $ PRV1=WT(I-77)*(1.0-P)+WT(I-76)*P
      RETURN
      END

```

```

FUNCTION PRV2(V)
C MAXWELL-BOLTZMANN DENSITY DIST. ASSUMED FOR SECONDARY BEAM
COMMON/VELSLECT/V1NOM,V2NOM
PRV2=(V/V2NOM)**2/EXPF((V/V2NOM)**2)
RETURN
END
SUBROUTINE BEFORE
C COMPUTES VARIOUS QUANTITIES ASSOCIATED WITH A GIVEN NEWTON DIAGRAM
COMMON/BETWEEN/VCM,VCMSQ,XI,ALPHA,VR,QMAX,E,WP
COMMON/BEEF/V1,V2,SQM1,SQM2,RMM,TMSQ,UC
V1SQ=V1**2 $ V2SQ=V2**2 $ VRSQ=V1SQ+V2SQ $ VR=SQRTF(VRSQ)
ERASER=V2/V1 $ XI=ATANF(ERASER) $ ALPHA=ATANF(ERASER*RMM)
VCMSQ=(SQM1*V1SQ+SQM2*V2SQ)/TMSQ $ VCM=SQRTF(VCMSQ)
E=UC*VRSQ
RETURN
END
SUBROUTINE AFTER
C COMPUTES CM VELOCITY AND ANGLE ASSOCIATED WITH A PARTICULAR LAB
C VELOCITY AND ANGLE AND A PARTICULAR NEWTON DIAGRAM
COMMON/STERN/THL,VP,EPC,EP,ETA,VPSQ,WPSQ
COMMON/BETWEEN/VCM,VCMSQ,XI,ALPHA,VR,QMAX,E,WP
C SINCE THIS SUBROUTINE IS USED SO OFTEN, IT IS MORE EFFICIENT TO WRITE
C IT IN MACHINE LANGUAGE. THIS IS DONE IN PROGRAM IZLEG
DATA(PI=3.1415926536),(HALFPI=1.570796326)
VPSQ=VP**2
GAMMA=ALPHA-THL
WPSQ=-COSF(GAMMA)*VP*2.0*VCM+VCMSQ+VPSQ
WP=SQRTF(WPSQ)
CZETA=(WPSQ+VPSQ-VCMSQ)/(2.*WP*VP)
ZETA=HALFPI
IF(CZETA.LT.1.0) ZETA=ACOSF(CZETA)
IF(GAMMA.GT.0.0) ZETA=-ZETA
ETA=ABSF(ZETA+XI+THL)
EP=EPC*WPSQ
RETURN
END
SCOPE
'LOAD
'RUN, TI=60, PR=20000, DU=7, PL=1000, PU=5000

```

3) I2LEG

Program I2LEG is the general lab \rightarrow c.m. program which uses a least squares fitting routine to obtain a coupled (velocity-angle) c.m. distribution by determining, for a general set of expansion functions, those coefficients which give the best match to the experimental data (lab. contour map). In the program which follows, the basis set is a 30 term two-dimensional coupled Legendre expansion in w' and θ , each term of which is multiplied by an uncoupled angle-velocity function which was chosen to be a reasonable starting guess to the c.m. distribution (see Eqn. (B1), Appendix B). The 30 coefficients modify the starting guess ($F_0(w')G_0(\theta)$) in such a way as to obtain a c.m. function that when transformed to the laboratory frame of reference with proper averaging over the beam distributions, gives the best least squares fit to the experimental data. The Fortran program below used 4.5 minutes of CDC 3600 computer time; more than half of this time was for compiling and assembling, and for plotting of the results.

'JOB,2138,3411/GILLEN,5

248

'DEMAND,42276B

(BANK,(0),/100/

'FTN,L,X

PROGRAM IZLEG

COMMON/VELSLECT/VINOM,V2NOM

DIMENSION VLAV(45),V2(55),V1(55),WT(55)

COMMON/RETURNS/NHIST,G(5,6)

COMMON/MIST/EXA(250),EXI(250),EXV(250)

COMMON/BETWEEN/VCM,VCMSQ,XI,ALPHA,VR,QMAX,E,WP

COMMON/STERN/THL,VP,EPC,EP,ETA,VPSQ,WPSQ

COMMON/BEEF/VV1,VV2,SQM1,SQM2,RMM,TMSQ,UC

COMMON/LINTERP/WCM(22)

COMMON/THREE/SIG(250,5,6)

COMMON/SLICE/NOB

COMMON/EAT/ISY(102)

DIMENSION PSIGN(30),PDIFF(30),ABORT(9950)

COMMON/PIC/TH(30),NP

EXTERNAL LEGDEP

EQUIVALENCE(SIG,ABORT)

COMMON/100/SLEG(250,5,6),NA,NE,DEX(250)

DATA((ISY(I),I=1,100)= 2H01,2H02,2H03,2H04,2H05,2H06,2H07,2H08
1,2H09,2H10,2H11,2H12,2H13,2H14,2H15,2H16,2H17,2H18,2H19,2H20,2H21,
2H22,2H23,2H24,2H25,2H26,2H27,2H28,2H29,2H30,2H31,2H32,2H33,2H34,2
3H35,2H36,2H37,2H38,2H39,2H40,2H41,2H42,2H43,2H44,2H45,2H46,2H47,2H
448, 2H49,2H50,2H51,2H52,2H53,2H54,2H55,2H56,2H57,2H58,2H59,2H60,2H
561,2H62,2H63,2H64,2H65,2H66,2H67,2H68,2H69,2H70,2H71,2H72,2H73,2H
64,2H75,2H76,2H77,2H78,2H79,2H80,2H81,2H82,2H83,2H84,2H85,2H86,2H87
7,2H88,2H89,2H90,2H91,2H92,2H93,2H94,2H95,2H96,2H97,2H98,2H99,2H00)

DATA(ISY(101)=2HNE)

DATA(ISY(102)=2HPO)

DATA(QMAX=41.5)

C VLAV IS THE BEST ESTIMATE OF THE K BEAM FLUX DIST. INCIDENT UPON THE
C SELECTOR--RANGES FROM ROT. SPEED=130 TO 450 RPS (VEL.=3.14*ROT. SPEED)

DATA(VLAV(I),I=1,45)=.05,.09,.15,.22,.31,.41,.53,.66,.77,.87,
1 .95,.99,1.,.99,.95,.91,.85,.78,.71,.63,.55,.46,.38,.32,.26,.21,
2 .17,.14,.12,.1,.09,.08,.07)

C WCM IS THE FUNCTION CHOSEN TO REPRESENT, AS A FIRST GUESS, THE
C VELOCITY DISTRIBUTION IN THE C.M.

C DATA EVERY 50 M/SEC LINEAR INTERPOLATION USED IN SUBROUTINE XSECT
DATA(WCM(I),I=1,22)=.06,.27,.53,.76,.87,.87,.81,.75,.71,.67,.62,
1 .56,.49,.4,.29,.19,.11,.07,.03,.01,.005,.0)

TYPE REAL M1,M2,M1P,M2P

C 5X6 LEGENDRE ON ANGLE,ENERGY 30 COEFFICIENTS

NA=5 \$ NE=6 \$ NHIST=NP=30

C EXPERIMENTAL DATA--SEL ROT.SPEED,ANGLE,VELOCITY,INTENSITY

6 DO 516 J=1,250 \$ READ 1009,SEL,EXA(J),EXV(J),EXI(J)

IF(EXA(J).GT.900.)2,4

4 IF(EOF,60) 120,516

516 CONTINUE

1009 FORMAT(3F6.1,F6.3)

2 NBIN=NOB=J-1

PRINT 3006,SEL,NOB

3006 FORMAT(2X,4HSEL=,F5.0,10X,4HNOB=,I5)

CALL KTIME(MIN,KSEC,KK)

PRINT 5555,MIN,KSEC

5555 FORMAT(1H0,I5,5H MIN,I5,5H SEC)

DO 500 J=1,NBIN

500 PRINT 1009,SEL,EXA(J),EXV(J),EXI(J)

VINOM=3.14*SEL

M1=39.102 \$ M2=253.81 \$ M1P=166. \$ M2P=126.9 \$ V2NOM=152.0

```

SQM1=M1**2 $ SQM2=M2**2 $ RMM=M2/M1 $ TMSQ=(M1+M2)**2
UC=M1*M2/(M1+M2)*1.1950286807E-7
EPC=M1P/M2P*(M1P+M2P)*1.1950286807E-7
C ZAREMBA SPACING USES A FIBONACCI NUMBER OF POINTS--1,1,2,3,5,8,13,21,
C 34,55,89,144,... METHOD SPACES POINTS ALONG V1,V2 FOR NUMER. INTEGR.
NTR=55 $ R=1./55. $ S=34./55. $ X=Y=0.
XVS=.79*VINOM $ XR=.62*VINOM $ YR=3.*V2NOM
DO 5 I=1,7500
5 SIG(I)=0.
DENS=FLUX=0.
42 DO 1 I=1,NTR $ V1(I)=XVS+XR*X $ V2(I)=4.+YR*Y
C WT(I) IS THE WEIGHTING ON THE BEAM DISTRIBUTIONS IN THE INTEGRATION
C PRVIN(V) IS THE DENSITY WEIGHT OF THE K BEAM ASSUMING A UNIFORM FLUX
C VS. VELOCITY INCIDENT UPON THE SELECTOR. T ACCOUNTS FOR THE DEVIATIONS
C FROM THIS IDEAL INPUT THAT ARE DUE TO THE LAVAL K BEAM DISTRIB.
WT(I)=PRVIN(V1(I))*PRV2(V2(I)) $ Y=Y+S $ IF(Y.GT.1.) Y=Y-1.
U=V1(I)/3.14/10. $ LL=U $ P=U-LL
T=VLAV(LL)*(1.-P)+VLAV(LL+1)*P $ WT(I)=WT(I)*T
W=PRVIN(V1(I))*T $ DENS=DENS+W $ FLUX=FLUX+W*V1(I)
1 X=X+R
VRAT=FLUX/DENS/VINOM $ PRINT 3000,DENS,FLUX,VRAT
3000 FORMAT(2X,5HDENS=,E15.3,3X,5HFLUX=,E15.3,3X,5HVRAT=,F10.3)
C THE MAIN INTEGRATION FOLLOWS. IT IS A SUM OF THE RESULTS FOR THE NTR
C VELOCITY VECTOR TRIANGLES, EACH WEIGHTED PROPERLY BY WT(I).
DO 100 I=1,NTR $ VV1=V1(I) $ VV2=V2(I) $ CALL BEFORE
C COMPUTATIONS ARE MADE FOR SCATTERING INTENSITY AT THE NBIN DATA POINTS.
DO 100 J=1,NBIN $ THL=EXA(J)*.01745329252 $ VP=EXV(J)
CALL AFTER $ CALL XSECT $ DO 76 N=1,NE $ DO 76 K=1,NA
76 SIG(J,K,N)=G(K,N)*WT(I)+SIG(J,K,N)
100 CONTINUE
CALL KTIME(MIN,KSEC,KK)
PRINT 5555,MIN,KSEC
C POLYL: BUILDS UP THE LEGENDRE FUNCTIONS FROM THE POWER SERIES FUNCTIONS
C OF XSECT.
CALL POLYL
CALL KTIME(MIN,KSEC,KK)
PRINT 5555,MIN,KSEC
DO 436 J=1,NOB $ DO 436 K=1,NA $ DO 436 M=1,NE
436 SLEG(J,K,M)=SLEG(J,K,M)*5.0E-4
C PARAMETERS NECESSARY TO GAUSHAUS FOLLOW
DO 85 I=1,30 $ PSIGN(I)=0.
85 PDIFF(I)=.01 $ EPS1=EPS2=1.E-3
MIT=20
441 TH(1)=1.0 $ DO 439 J=2,30
439 TH(J)=.01 $ NPROB=1
C GAUSHAUS IS A LEAST SQUARES FITTING PROGRAM WHICH FINDS THE SET OF
C PARAMETERS FOR THE LEGENDRE EXPANSION WHICH GIVES THE BEST FIT TO
C THE EXPERIMENTAL DATA RESULTS
CALL GAUSHAUS(NPROB,LEGDEP,NBIN,EXI,NP,TH,PDIFF,PSIGN,EPS1,EPS2,
IMIT,.01,10.,ABORT)
C SEARCH FINDS THE MAXIMUM VALUE OF AN ARRAY FOR NORMALIZATION PURPOSES.
53 CALL SEARCH(0,TH,NP,LL,C)
DO 440 N=1,NP
440 TH(N)=TH(N)/C
PRINT 2006,(TH(N),N=1,NP)
PUNCH 2006,(TH(N),N=1,NP)
2006 FORMAT((10F8.5))
DO 437 J=1,NBIN
C DEX IS THE FIT TO THE DATA USING THE SET OF PARAMETERS GENERATED BY
C SUBROUTINE GAUSHAUS
PUNCH 6034,EXA(J),EXV(J),EXI(J),DEX(J)

```

```

437 PRINT 6034,EXA(J),EXV(J),EXI(J),DEX(J)
6034 FORMAT(2F10.1,2F10.2)
      CALL KTIME(MIN,KSEC,KK)
      PRINT 5555,MIN,KSEC
C VIEW PRINTS AND PLOTS OUT THE C.M. MAP
  CALL VIEW
  CALL KTIME(MIN,KSEC,KK)
  PRINT 5555,MIN,KSEC
C PLOTTING DEX (THE FIT TO THE LAB. DATA)
  20 CALL PLOT(2.,2.,3) $ CALL PLOT(10.,2.,2) $ CALL PLOT(2.,2.,2)
  CALL PLOT(2.,8.,2) $ DO 806 L=1,NOB
  A=EXA(L)*.01745329252
  PX=COSF(A) $ PY=SINF(A) $ X=EXV(L)*PX/200.+2.-.05
  Y=EXV(L)*PY/200.+2.-.035 $ M=100.*DEX(L)+.5
  IF(M.GT.100) M=102 $ IF(M.LT.0) M=101 $ IF(M.EQ.0) M=100
806 CALL SYMBOL(X,Y,.07,ISY(M),0.,2)
  CALL PLOT(15.,0.,-3)
120 END
      SUBROUTINE XSECT
C COMPUTES THE LAB. SCATTERING INTENSITY FOR THE NA*NE BUILD-UP FUNCTION
  DATA
  *(EE=2.7182818284),(PI=3.1415926535)
  COMMON/RETURNS/NHIST,G(5,6)
  COMMON/STERN/THL,VP,EPC,EP,THETA,VPSQ,WPSQ
  COMMON/BETWEEN/VCM,VCMSQ,XI,ALPHA,VR,QMAX,E,WP
  COMMON/LINTERP/WCM(22)
  COMMON/100/SLEG(250,5,6),NA,NE,DEX(250)
  TYPE REAL JACK
  FX=EP/(E+QMAX) $ IF(FX.GT.1.0) GO TO 99
  Y=2.*WP/1100.-1.
  IF(THETA.GT.PI) THETA=2.*PI-THETA $ X=2.*THETA/PI-1.
  I=WP/50. $ IF(I.EQ.0) 1,2
C QUADRATIC WP DEPENDENCE FROM 0 TO 50 M/SEC TO AVOID JACOBIAN BLOWUP
  1 JACK=VR*VPSQ*WCM(1)/50.**2*(.25-.2*X+.75*X*X) $ GO TO 3
C LAB INTENSITY EQUALS JACK*PRV2(V2)*PRV1(V1)-THESE DENSITY WEIGHTS
C ARE IN THE MAIN PROGRAM
C JACK CONTAINS VR*JACOBIAN*INITIAL UNCOUPLED GUESS OF CM CROSS SECTION
C JACOBIAN(C.M. TO LAB.) IS VPSQ/WPSQ, VR IS RELATIVE VELOCITY
  2 P=WP/50.-I $ JACK=VR*VPSQ/WPSQ*(WCM(I)*(1.-P)+WCM(I+1)*P)*
  1 (.25-.2*X+.75*X*X)
  3 G(1,1)=JACK $ G(2,1)=X*G(1,1) $ G(3,1)=X*G(2,1)
  G(4,1)=X*G(3,1) $ G(5,1)=X*G(4,1)
  DO 10 K=1,NA $ DO 10 N=2,NE
  10 G(K,N)=Y*G(K,N-1) $ RETURN
  99 DO 11 I=1,NHIST
  11 G(I)=0. $ RETURN
  END
      SUBROUTINE POLYL
C POLYL BUILDS UP THE LEGENDRE FUNCTIONS FROM POWER SERIES (2-D) IN
C ANGLE AND VELOCITY
  COMMON/MIST/EXA(250),EXI(250),EXV(250)
  COMMON/THREE/SIG(250,5,6)
  COMMON/Slice/NOB
  COMMON/100/SLEG(250,5,6),NAA,NE,DEX(250)
  DIMENSION A(10,5),L(10,5),NA(10),B(4,5)
  DATA((NA(J),J=1,10)=1,1,2,2,3,3,4,4,5,5)
  A(1,1)=A(2,1)=1. $ A(3,1)=1.5 $ A(3,2)=-.5 $ A(4,1)=2.5
  A(4,2)=-1.5 $ A(5,1)=4.375 $ A(5,2)=-3.75 $ A(5,3)=.375
  A(6,1)=7.875 $ A(6,2)=-8.75 $ A(6,3)=1.875
  L(1,1)=0 $ L(2,1)=1 $ L(3,1)=2 $ L(3,2)=0 $ L(4,1)=3 $ L(4,2)=1
  L(5,1)=4 $ L(5,2)=2 $ L(5,3)=0

```

```

L(6,1)=5 $ L(6,2)=3 $ L(6,3)=1
NX=5 $ NY=6
DO 91 M=1,NY $ DO 91 K=1,NX $ DO 91 J=1,NOB
91 SLEG(J,K,M)=0.0 $ DO 90 M=1,NY $ DO 90 K=1,NX
MM=M-1 $ KK=K-1 $ PRINT 2000, KK, MM
2000 FORMAT(2HOP, I2, 8H (X) * P, I2, 4H (Y))
NAY=NA(M) $ NAX=NA(K) $ DO 90 I=1,NAY $ DO 90 II=1,NAX
KZ=L(K,II)+1 $ MZ=L(M,I)+1
DO 96 J=1,NOB
96 SLEG(J,K,M)=SLEG(J,K,M)+A(K,II)*A(M,I)*SIG(J,KZ,MZ)
AP=A(K,II)*A(M,I) $ JX=L(K,II) $ JY=L(M,I)
90 PRINT, 2001, AP, JX, JY
2001 FORMAT(F12.6, 4H X**, I1, 4H Y**, I1)
RETURN
END
FUNCTION PRV1(V)
COMMON/VELSLECT/V1NOM,V2NOM
C BEST K BEAM DENSITY TRANSMISSION FUNCTION FOR UNIFORM FLUX VS VELOCITY
C INPUT TO SELECTOR .039 SEL. SLIT, NPROB=10, 11/19/69
C REDUCED VELOCITY 0.78 TO 1.41
DIMENSION WT(64)
DATA(WT(I), I=1,64)=.011,.021,.037,.06,.094,.138,.192,.256,
1 .327,.404,.485,.568,.649,.727,.799,.862,.914,.954,.981,.996,
2 1,.994,.978,.954,.923,.886,.844,.799,.751,.701,.651,.6,.551,
3 .503,.458,.415,.375,.338,.306,.272,.243,.216,.192,.17,.15,
4 .133,.116,.102,.089,.078,.068,.059,.052,.045,.039,.034,.03,
5 .026,.023,.02,.017,.015,.013,.011)
I=R=V/V1NOM*100. $ IF(I.GE.78.AND.I.LE.140) GO TO 1 $ PRV1=0.0
RETURN
1 P=R-I $ PRV1=WT(I-77)*(1.0-P)+WT(I-76)*P
RETURN
END
FUNCTION PRV2(V)
C MAXWELL-BOLTZMANN DENSITY FUNCTION WEIGHTS FOR SECONDARY BEAM.
COMMON/VELSLECT/V1NOM,V2NOM
PRV2=(V/V2NOM)**2/EXPF((V/V2NOM)**2)
RETURN
END
SUBROUTINE BEFORE
C COMPUTES SOME OF THE IMPORTANT CONSTANTS FOR A GIVEN VECTOR TRIANGLE.
COMMON/BETWEEN/VCM,VCMSQ,XI,ALPHA,VR,QMAX,E,WP
COMMON/BEEF/V1,V2,SQM1,SQM2,RMM,TMSQ,UC
VISQ=V1**2 $ V2SQ=V2**2 $ VRSQ=VISQ+V2SQ $ VR=SQRTF(VRSQ)
ERASER=V2/V1 $ XI=ATANF(ERASER) $ ALPHA=ATANF(ERASER*RMM)
VCMSQ=(SQM1*VISQ+SQM2*V2SQ)/TMSQ $ VCM=SQRTF(VCMSQ)
E=UC*VRSQ
RETURN
END
SUBROUTINE LEGDEP(NPROB,TH,FIT,NBIN,NP)
C SUBROUTINE CALLED BY GAUSHAUS SUPPLYING TO GAUSHAUS THE LABORATORY
C SCATTERING INTENSITIES FOR A GIVEN SET OF TRIAL PARAMETERS DURING THE
C COURSE OF A CALCULATION
DIMENSION TH(30),FIT(250)
COMMON/100/SLEG(250,5,6),NA,NE,DEX(250)
DO 50 J=1,NBIN
50 FIT(J)=0.0 $ DO 51 K=1,NA $ DO 51 M=1,NE
L=NA*(M-1)+K
DO 58 J=1,NBIN
58 FIT(J)=FIT(J)+TH(L)*SLEG(J,K,M)
51 CONTINUE
DO 55 J=1,NBIN

```

55 DEX(J)=FIT(J)

RETURN

END

252

SUBROUTINE VIEW

C COMPUTES THE C.M. SCATTERING INTENSITIES FOR THE FINAL SET OF
C PARAMETERS DETERMINED BY GAUSHAUS

COMMON/EAT/ISY(102)

DIMENSION SUM(15),SUMSIN(15)

COMMON/PIC/TH(30),NP

COMMON/100/SLEG(250,5,6),NAA,NE,DEX(250)

COMMON/LINTERP/WCM(22)

DIMENSION A(10,5),L(10,5),CUT(19,23),NA(10)

DATA((NA(J),J=1,10)=1,1,2,2,3,3,4,4,5,5)

A(1,1)=A(2,1)=1. \$ A(3,1)=1.5 \$ A(3,2)=-.5 \$ A(4,1)=2.5

A(4,2)=-1.5 \$ A(5,1)=4.375 \$ A(5,2)=-3.75 \$ A(5,3)=.375

A(6,1)=7.875 \$ A(6,2)=-8.75 \$ A(6,3)=1.875

L(1,1)=0 \$ L(2,1)=1 \$ L(3,1)=2 \$ L(3,2)=0 \$ L(4,1)=3 \$ L(4,2)=1

L(5,1)=4 \$ L(5,2)=2 \$ L(5,3)=0

L(6,1)=5 \$ L(6,2)=3 \$ L(6,3)=1

JW=1

DO 2 U=1,19 \$ DO 2 N=1,23

2 CUT(J,N)=0.0

DO 1 M=1,NE \$ NAY=NA(M) \$ DO 1 K=1,NAA \$ NAX=NA(K)

MM=NAA*(M-1)+K \$ DO 1 I=1,NAY \$ DO 1 II=1,NAX

JX=L(K,II) \$ JY=L(M,I) \$ DO 1 J=1,19 \$ X=(J-1)/9.-1.

DO 1 N=1,23 \$ Y=.1*(N-1)/1.1-1.

IF(JX.EQ.0) 5,6

5 UX=1 \$ GO TO 7

6 UX=X**JX

7 IF(JY.EQ.0) 8,9

8 UY=1 \$ GO TO 10

9 UY=Y**JY

10 CUT(J,N)=CUT(J,N)+A(K,II)*A(M,I)*TH(MM)*UX*UY

1 CONTINUE

3002 FORMAT(6H1THETA)

3000 FORMAT(10E12.3)

3001 FORMAT(6X,9E12.3)

DO 11 J=1,19 \$ X=(J-10.)/9. \$ DO 11 N=1,23 \$ U=50.*(N-1)

IF(U.EQ.0.) 15,16

15 CUT(J,N)=0. \$ GO TO 11

16 CUT(J,N)=CUT(J,N)*WCM(N-1)*(.25-.2*X+.75*X*X)

11 CONTINUE

C PRINTS,PUNCHES,AND PLOTS THE C.M. INTENSITIES

PRINT 3002

DO 12 N=1,23 \$ PRINT 3000,(CUT(J,N),J=1,10)

12 PRINT 3001,(CUT(J,N),J=11,19)

C LARGE ANGLE RESULTS(INVALID,BEYOND REACH OF EXPERIMENTAL DATA) ARE

C ZEROED TO AVOID RUINING NORMALIZATION

DO 17 N=1,23 \$ DO 17 J=16,19

17 CUT(J,N)=0.

CALL SEARCH(0,CUT,437,LL,AA) \$ DO 20 N=1,23 \$ DO 20 J=1,19

20 CUT(J,N)=CUT(J,N)/AA \$ PRINT 3002

DO 21 N=1,23 \$ U=50.*(N-1)

PRINT 3003,U,(CUT(J,N),J=1,19)

3003 FORMAT(3X,F5.0,4X,19F6.3)

PUNCH 3004,U,(CUT(J,N),J=1,10)

21 PUNCH 3004,U,(CUT(J,N),J=11,19)

3004 FORMAT(2X,F5.0,10F6.3)

42 CALL PLOT(0.,3.,3) \$ CALL PLOT(12.,3.,2)

CALL SYMBOL(6.,3.,.04,29,0.,-1)

DO 27 J=1,19 \$ A=(J-1)*10.*.01745329252 \$ PX=COSF(A) \$ PY=SINF(A)

```

DO 27 N=2,23 $ X=(N-1)*PX/4.+6.-.05
Y=(N-1)*PY/4.+3.-.035 $ M=100.*CUT(J,N)+.5
IF(M.GT.100) M=102 $ IF(M.LT.0) M=101 $ IF(M.EQ.0) M=100
27 CALL SYMBOL(X,Y,.07,ISY(M),0.,2)
CALL PLOT(15.,0.,-3)
IF(JW.EQ.1) 40,41
40 JW=2
C GENERATING CM MAP*SINF,= TO INTEGRATION OVER AZIMUTHAL ANGLE
DO 30 J=1,15 $ SUM(J)=0. $ DO 30 N=1,23
30 SUM(J)=SUM(J)+CUT(J,N) $ CALL SEARCH(0,SUM,15,LL,T) $ DO 31 J=1,15
31 SUM(J)=SUM(J)/T $ PRINT 3008,(SUM(J),J=1,15)
3008 FORMAT(2X,3HSUM,7X,19F6.3)
DO 26 J=1,15 $ A=SINF(10.*(J-1)*.01745329252)
SUMSIN(J)=A*SUM(J)
DO 26 N=1,23
26 CUT(J,N)=CUT(J,N)*A
CALL SEARCH(0,SUMSIN,15,LL,U) $ DO 32 J=1,15
32 SUMSIN(J)=SUMSIN(J)/U $ PRINT 3009,(SUMSIN(J),J=1,15)
3009 FORMAT(2X,6HSUMSIN,4X,19F6.3)
CALL SEARCH(0,CUT,437,LL,T) $ DO 24 M=1,437
24 CUT(M)=CUT(M)/T
PRINT 3007,T $ DO 28 N=1,23 $ U=50.*(N-1)
28 PRINT 3003,U,(CUT(J,N),J=1,13)
3007 FORMAT(1H1,E20.3)
GO TO 42
41 RETURN
END

```

IDENT AFTER
C COMPUTES THE CM ANGLE AND VELOCITY ASSOCIATED WITH A GIVEN LABORATORY
C VELOCITY AND ANGLE OF KI AND A GIVEN NEWTON DIAGRAM
C A FORTRAN VERSION OF THIS SUBROUTINE IS GIVEN IN PROGRAM KICM

EXIT.	ENTRY	AFTER
DICT.	XMIT	(*)*,(\$)Q8QDICT.
	OCT	0
	BCD	1,AFTER
STERN	BLOCK	
	COMMON	THL,VP,EPC,EP,ETA,VPSQ,WPSQ
BETWEEN	BLOCK	
	COMMON	VCM,VCMSQ,XI,ALPHA,VR,QMAX,E,WP
AFTER	UBJP	(*)
	XMIT	(*)*-1,(\$)Q8QDICT.
	XMIT	(*)*-2,(\$)DICT.
	LDA	VP
	FMU	VP
	STA	VPSQ
	LDA	ALPHA
	FSB	THL
	STA	GAMMA
	BRTJ	(\$)COSF,*,*
	SLJ	*+1
	OO	DICT.
	FMU,CM	VP
	FMU	VCM
	ADX	1
	FAD	VCMSQ
	FAD	VPSQ
	STA	WPSQ
	BRTJ	(\$)SQRTF,*,*
	SLJ	*+1
	OO	DICT.
	STA	WP

```

FMU          VP
ADX          1
STA         ZETA
LDA         WPSQ
FAD         VPSQ
FSB         VCMSQ
FDV         ZETA
FMU         GUARD
BRTJ        ($)ACOSF,*,*
SLU         *+1
00          DICT.
SSK         GAMMA
ROP,-      PZ,A,A
FAD         XI
FAD         THL
STA, MG    ETA
LDA         EPC
FMU         WPSQ
STA         EP
SLJ         EXIT.
GUARD      OCT      2000777777770000
ZETA       BSS      1
GAMMA      BSS      1
           EXT      ACOSF,COSF,SQRTF,Q8QDICT.
           END
           SCOPE

```

```

!LOAD
!RUN, TI=20, PR=20000, PL=1000, PU=2000

```

C	SEL	EXA	EXV	EXI
300.0	-15.0	150.0	0.011	
300.0	-15.0	200.0	0.144	
300.0	-15.0	250.0	0.245	
300.0	-15.0	300.0	0.288	
300.0	-15.0	350.0	0.317	
300.0	-15.0	400.0	0.343	
300.0	-15.0	450.0	0.357	
300.0	-15.0	500.0	0.354	
300.0	-15.0	550.0	0.335	
300.0	-15.0	600.0	0.311	
300.0	-15.0	650.0	0.286	
300.0	-15.0	700.0	0.256	
300.0	-15.0	750.0	0.222	
300.0	-15.0	800.0	0.186	
300.0	-15.0	850.0	0.135	
300.0	-15.0	900.0	0.087	
300.0	-15.0	950.0	0.053	
300.0	-15.0	1000.0	0.033	
300.0	-5.0	150.0	0.064	
300.0	-5.0	200.0	0.158	
300.0	-5.0	250.0	0.268	
300.0	-5.0	300.0	0.364	
300.0	-5.0	350.0	0.428	
300.0	-5.0	400.0	0.469	
300.0	-5.0	450.0	0.497	
300.0	-5.0	500.0	0.508	
300.0	-5.0	550.0	0.486	

```

C .....
C MUCH OF THE DATA HAS BEEN REMOVED HERE (TYPICALLY APPROX. 200 DATA PTS.)
300.0 999.9

```

4) GAUSHAUS

Below is the essential portion of the GAUSHAUS least-squares regression (fitting) package of the University of Wisconsin Computing Center.


```

      DO 150 I = 1, NP
      DO 151 J=1,I
      SUM = 0
      DO 160 K = 1, NOB
160  SUM = SUM + DELZ(K, I)*DELZ(K, J)
      TEMP= SUM/(P(I)*P(J))
      D(J,I)=TEMP
151  D(I,J)=TEMP
C      I
      D=XT*X (MOMENT MATRIX)
150  E(I)=SQRTF(D(I,I))
      GO TO KUWAIT
C
180  DO 200 I=1,NP
      DO 200 J = 1, I
      SUM=D(I,J)
      A(J,I)=SUM
200  A(I,J)=SUM
      CALL SYMEIG(A,NP,NP,0,P,TEMP,NP)
      PRINT 1006
      PRINT 2001, (P(I), I=1,NP)
      PRINT 1004,NIT
      ASSIGN 666 TO KUWAIT
C
      -END ITERATION 1 ON
666  DO 153 I=1,NP
      DO 153 J=1,I
      A(I,J)=D(I,J)/(E(I)*E(J))
153  A(J,I)=A(I,J)
C
      A= SCALED MOMENT MATRIX
      DO 155 I=1,NP
      P(I)=Q(I)/E(I)
      PHI(I)=P(I)
155  A(I,I)=A(I,I)+GA
      I=1
      CALL MATINV(A,NP,P,I,DET,NP)
C
      P/E = CORRECTION VECTOR
      PRINT 1005, DET
      STEP=1.0
      SUM1=0.
      SUM2=0.
      SUM3=0.
      DO 231 I=1,NP
      SUM1=P(I)*PHI(I)+SUM1
      SUM2=P(I)*P(I)+SUM2
231  SUM3=PHI(I)*PHI(I)+SUM3
      TEMP=SUM1/SQRTF(SUM2*SUM3)
      IF(TEMP .GT. 1)232,233
232  TEMP=1.0
233  TEMP=57.295*ACOSF(TEMP)
      PRINT 1041,TEMP
170  DO 220 I=1,NP
220  TB(I)=P(I)*STEP/E(I) +TH(I)
      PRINT 7000
7000  FORMAT(30H0TEST POINT PARAMETER VALUES
      PRINT 2006,(TB(I),I=1,NP)
      DO 2401 I=1,NP
      IF( SIGNS(I) .GT. 0 .AND. TH(I)*TB(I) .LE. 0 )663,2401
2401  CONTINUE
      SUMB=0
      CALL FOF(NPROB,TB,F,NOB,NP)
      DO 230 I=1,NOB
      R(I)=Y(I)-F(I)

```

```

230  SUMB=SUMB+R(I)*R(I)
      PRINT 1043,SUMB
      IF(SUMB/SSQ - 1 .LE. EPS1)662,663
663  IF( TEMP .LE. 30)665,664
665  STEP=STEP/2.0
      INTCOUNT=INTCOUNT+1
      IF(INTCOUNT .GE. 36) 2700,170
664  GA=GA*FNU
      INTCOUNT=INTCOUNT+1
      IF(INTCOUNT .GE. 36) 2700,666
662  PRINT 1007
      DO 669 I=1,NP
669  TH(I)=TB(I)
      CALL GAUSHS60(1,NP,TH,TEMP,TEMP)
      PRINT 1040,GA,SUMB
      GO TO IRAN
225  DO 240 I = 1, NP
      IF(ABSF(P(I))*STEP/E(I))/(1.0E-20+ABSF(TH(I)))-EPS2) 240,240,250
240  CONTINUE
      PRINT 1009, EPS2
      GO TO 280
250  GO TO JORDAN
265  IF( ABSF((SUMB-SSQ)/SSQ) .LE. EPS1)260,270
260  PRINT 1010, EPS1
      GO TO 280
270  SSQ=SUMB
      NIT=NIT+1
      IF(NIT .LE. MIT)100,280
2700 PRINT 2710
2710 FORMAT(//115H0**** THE SUM OF SQUARES CANNOT BE REDUCED TO THE SUM
      1OF SQUARES AT THE END OF THE LAST ITERATION - ITERATING STOPS /)
C
C
C
      END ITERATION
280  PRINT 1011
      PRINT 2001, (F(I), I = 1, NOB)
      PRINT 1012
      PRINT 2001, (R(I), I = 1, NOB)
      SSQ=SUMB
      IDF=NOB-NP
      PRINT 1015
      I=0
      CALL MATINV(D,NP,P,I,DET,NP)
      DO 7692 I=1,NP
7692  E(I)=SQRTF(D(I,I) )
      DO 340 I=1,NP
      DO 340 J = I, NP
      A(J,I)=D(J,I)/(E(I)*E(J))
      D(J,I)=D(J,I)/(DIFZ(I)*TH(I)*DIFZ(J)*TH(J))
      D(I,J)=D(J,I)
340  A(I,J)=A(J,I)
      CALL GAUSHS60(3,NP,TEMP,TEMP,A)
7057 PRINT 1016
      CALL GAUSHS60(1,NP,E,TEMP,TEMP)
      IF(IDF)7058,410
7058 SDEV=SSQ/IDF
      PRINT 1014,SDEV,IDF
      SDEV=SQRTF(SDEV)
      DO 391 I=1,NP
      P(I)=TH(I)+2.0*E(I)*SDEV
391  TB(I)=TH(I)-2.0*E(I)*SDEV

```

```

PRINT 1039
CALL GAUSHS6Q(2,NP,TB,P,TEMP)
DO 415 K=1,NOB
TEMP=0.0
DO 420 I=1,NP
DO 420 J=1,NP
420 TEMP=TEMP + DELZ(K,I)*DELZ(K,J)*D(I,J)
TEMP=2.*SQRTF(TEMP)*SDEV
R(K)=F(K)+TEMP
415 F(K)=F(K)-TEMP
PRINT 1008
IE=0
DO 425 I=1,NOB,10
IE=IE+10
IF(NOB-IE) 430,435,435
430 IE=NOB
435 PRINT 2001,(R(J),J=I,IE)
425 PRINT 2006,(F(J),J=I,IE)
410 PRINT 1033, NPROB
RETURN
99 PRINT 1034
GO TO 410
10000FORMAT(38HINON-LINEAR ESTIMATION, PROBLEM NUMBER 13, // 15,
114H OBSERVATIONS, 15, 11H PARAMETERS )
1001 FORMAT(/25H0INITIAL PARAMETER VALUES )
1002 FORMAT(/54HOPROPORTIONS USED IN CALCULATING DIFFERENCE QUOTIENTS )
1003 FORMAT(/25H0INITIAL SUM OF SQUARES = E12.4)
1004 FORMAT(/////45X,13HITERATION NO. I4)
1005 FORMAT(14H0DETERMINANT = E12.4)
1006 FORMAT(/52H0EIGENVALUES OF MOMENT MATRIX - PRELIMINARY ANALYSIS )
1007 FORMAT(/32HOPARAMETER VALUES VIA REGRESSION )
1008 FORMAT(/////54H0APPROXIMATE CONFIDENCE LIMITS FOR EACH FUNCTION VAL
LUE )
10090FORMAT(/62H0ITERATION STOPS - RELATIVE CHANGE IN EACH PARAMETER LE
1SS THAN E12.4)
10100FORMAT(/62H0ITERATION STOPS - RELATIVE CHANGE IN SUM OF SQUARES LE
1SS THAN E12.4)
1011 FORMAT(22H1FINAL FUNCTION VALUES )
1012 FORMAT(/////10H0RESIDUALS )
1014 FORMAT(//24H0VARIANCE OF RESIDUALS = ,E12.4,1H,I4,
120H DEGREES OF FREEDOM )
1015 FORMAT(/////19H0CORRELATION MATRIX )
1016 FORMAT(/////21H0NORMALIZING ELEMENTS )
1033 FORMAT(//19H0END OF PROBLEM NO. I3)
1034 FORMAT(/16HOPARAMETER ERROR )
10390FORMAT(/71H0INDIVIDUAL CONFIDENCE LIMITS FOR EACH PARAMETER (ON LI
1NEAR HYPOTHESIS) )
10400FORMAT(/9H0LAMBDA =E10.3,40X,33HSUM OF SQUARES AFTER REGRESSION =
1E15.7)
1041 FORMAT(25H0ANGLE IN SCALED COORD. = F5.2, 8H DEGREES )
1043 FORMAT(28H0TEST POINT SUM OF SQUARES = E12.4)
2001 FORMAT(/10E12.4)
2006 FORMAT(10E12.4)
END

```

Appendix D

Enlarged Views of Certain Important Figures.

Figures D-1,2,3

Enlargements of the laboratory KI flux contour maps of $\frac{d^3\sigma}{d^2\Omega dv'}$ shown in Fig. IV-27.

Figure D-1	$\bar{E} = 1.87$ kcal/mole
Figure D-2	2.67
Figure D-3	3.62

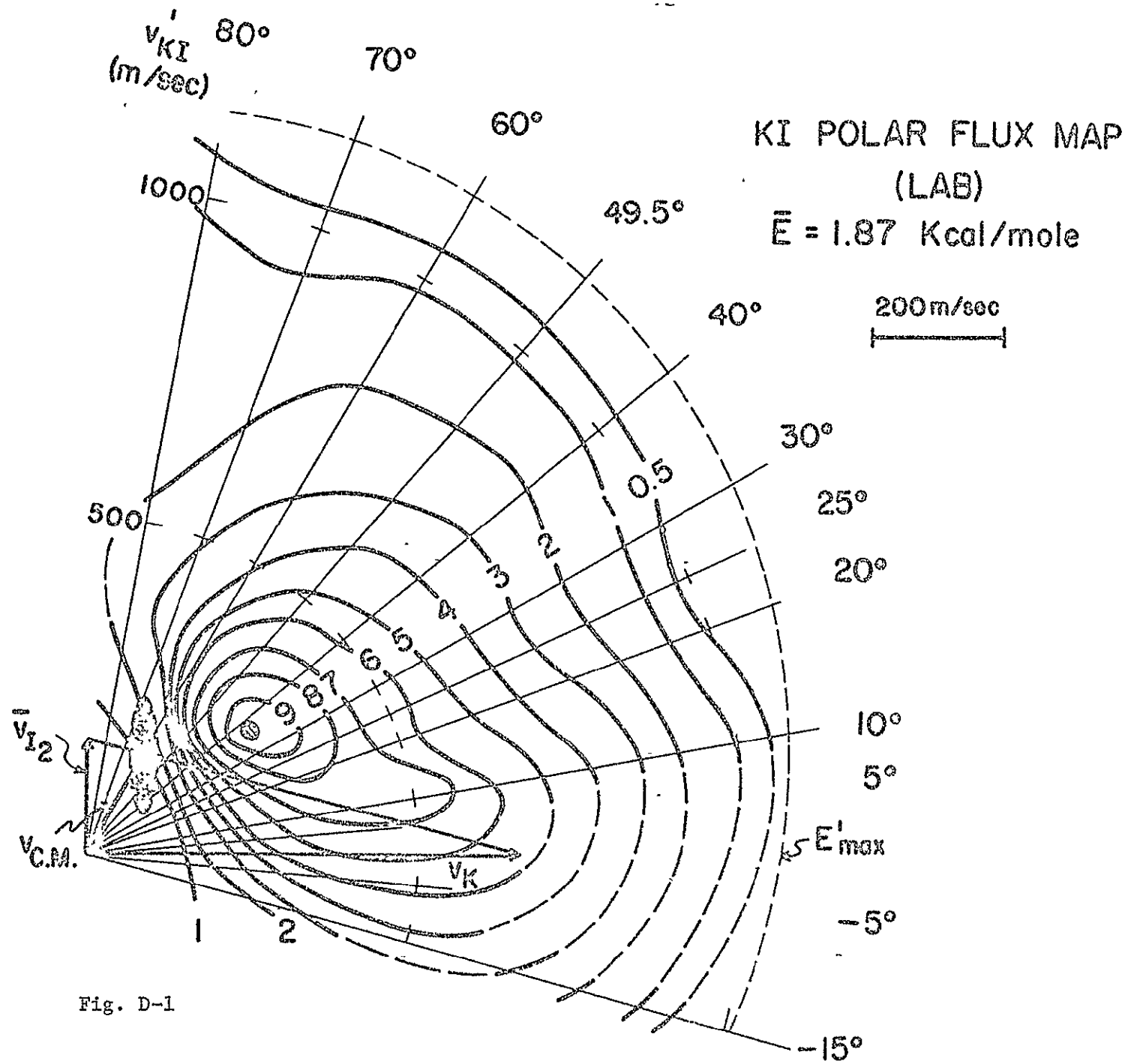


Fig. D-1

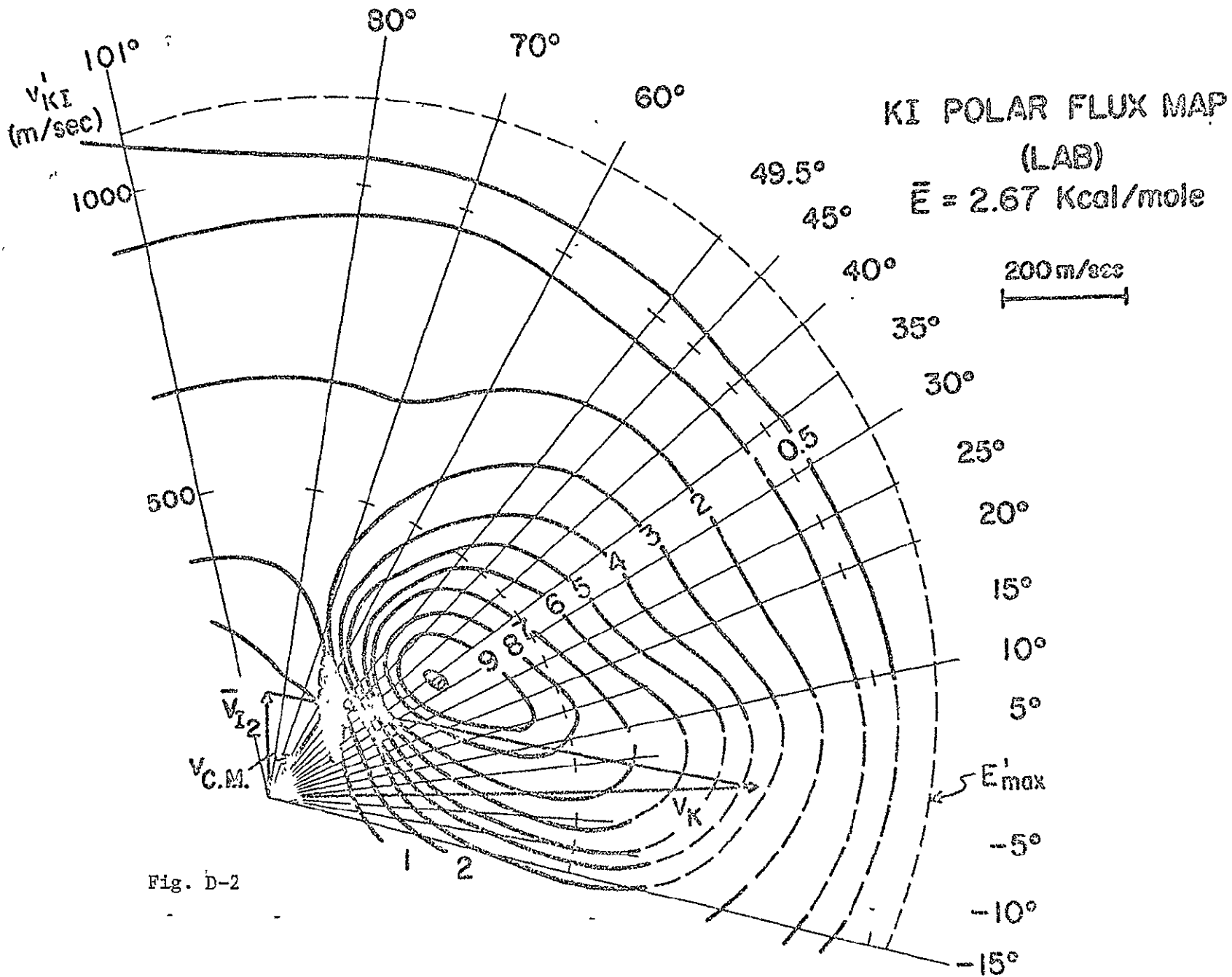


Fig. D-2

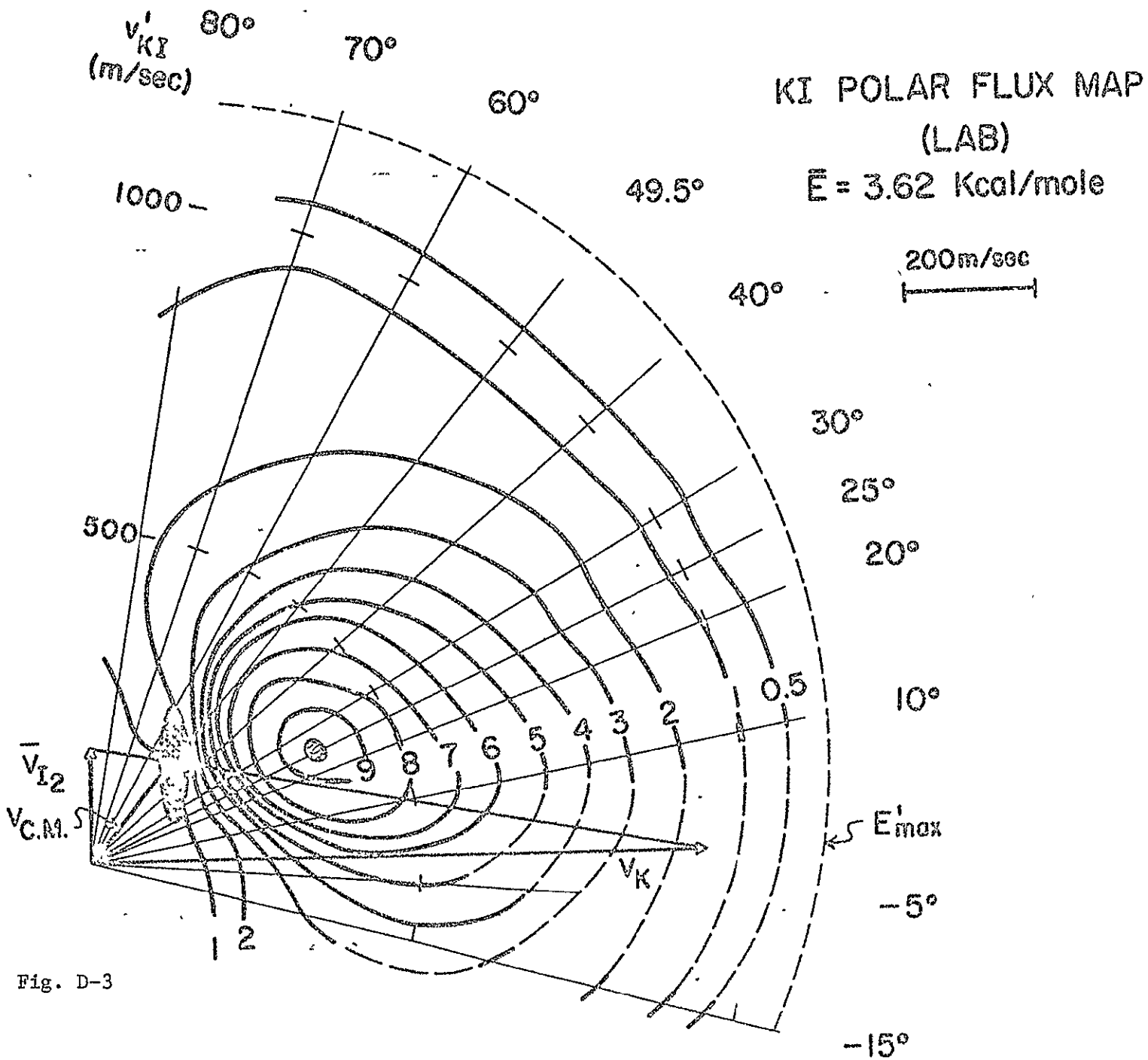


Fig. D-3

Figures D-4,5,6

Enlargements of the best c.m. KI flux contour maps of

$\frac{d^3\sigma}{d^2\omega d\nu}$ shown in Fig. IV-30

Figure D-4 , $\bar{E} = 1.87$ kcal/mole

Figure D-5 , 2.67

Figure D-6 3.62

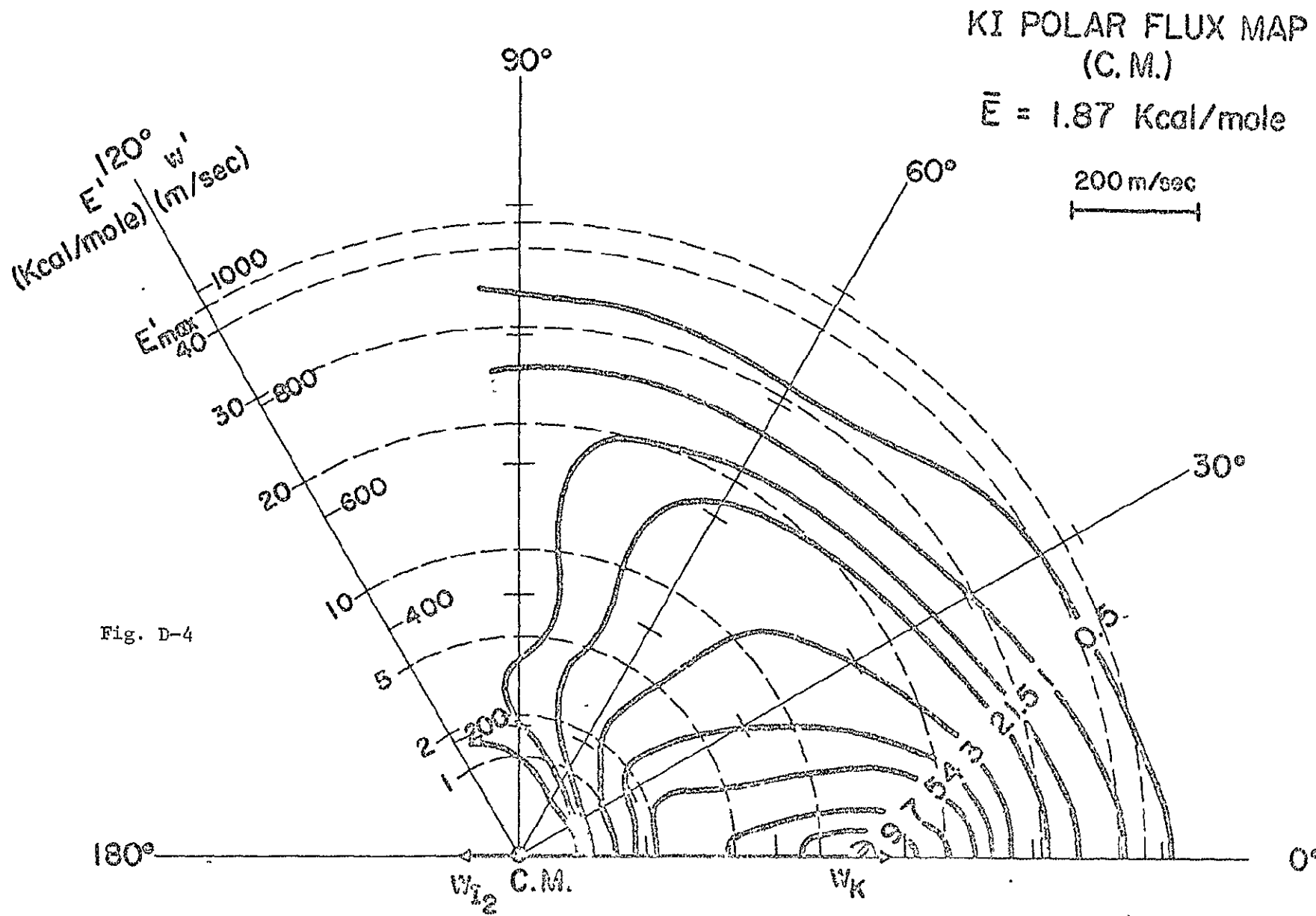


Fig. D-4

KI POLAR FLUX MAP
(C.M.)

$\bar{E} = 2.67$ Kcal/mole

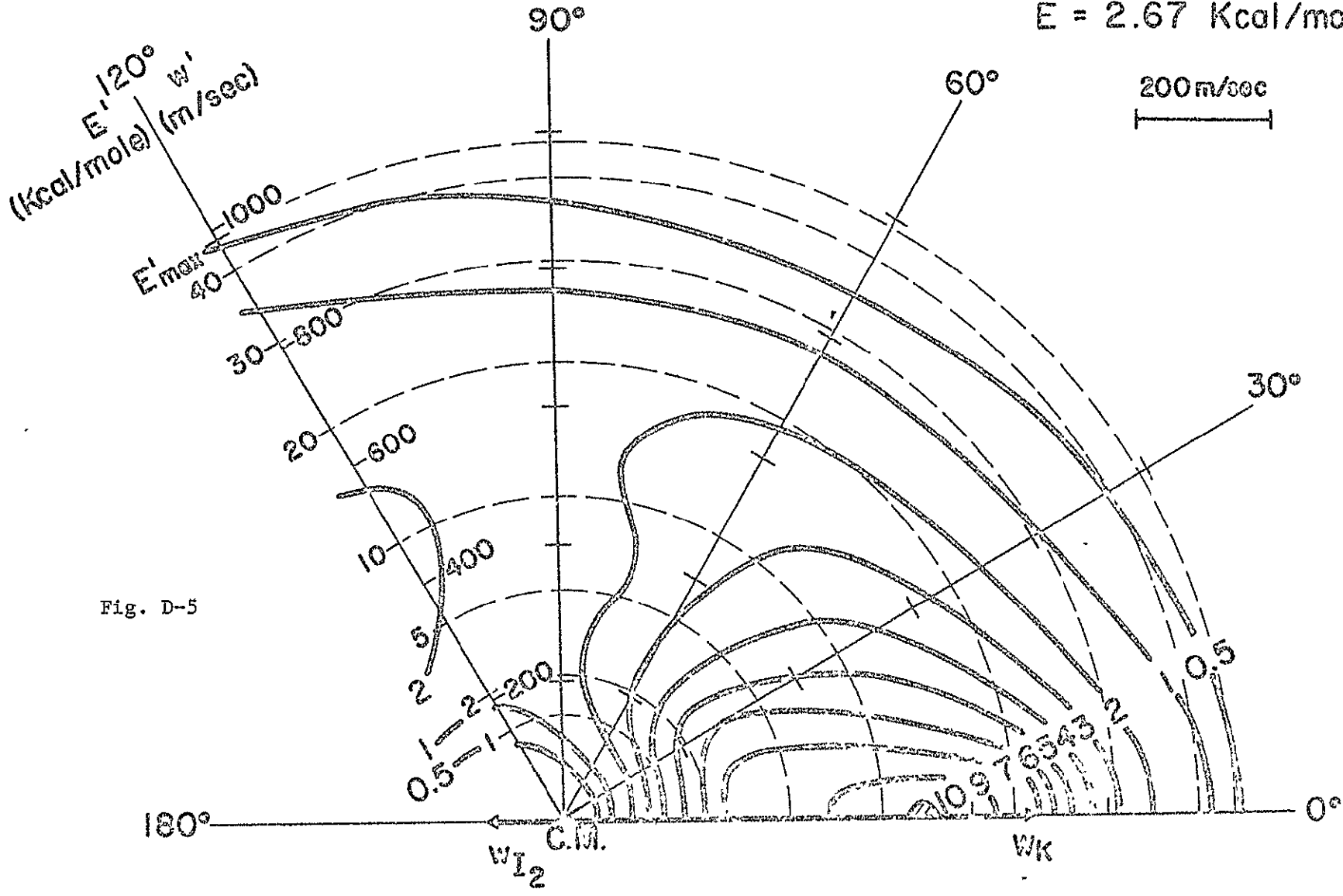


Fig. D-5

KI POLAR FLUX MAP
(C.M.)

$\bar{E} = 3.62$ Kcal/mole

200 m/csc
|-----|

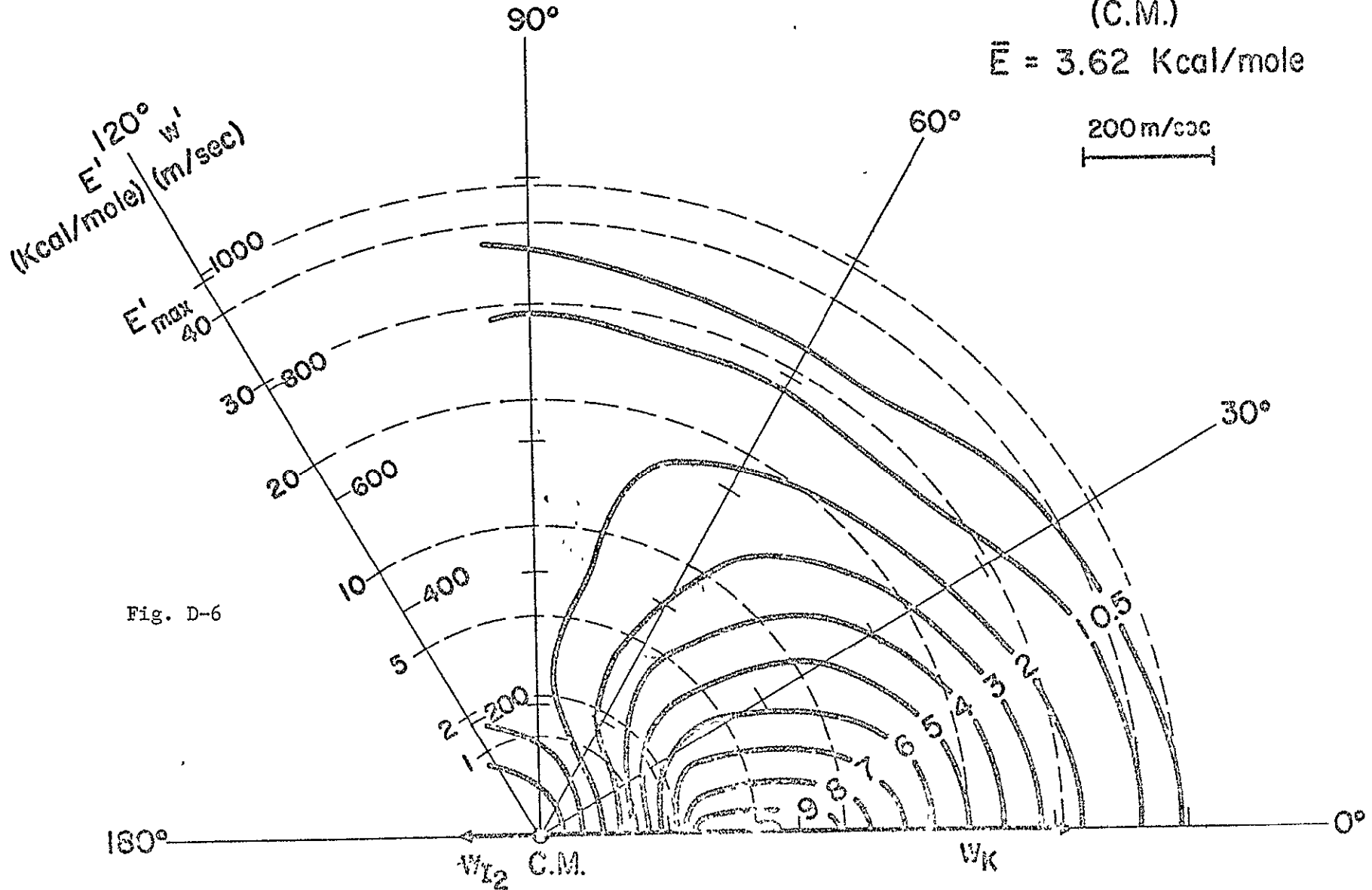


Fig. D-6

Appendix E

Coefficients for Legendre Expansion Functions

This appendix lists the Legendre expansion coefficients b_{ij} for the c.m. contour maps of $\frac{d^3\sigma}{d^2\omega dw'}$ $\propto I(\theta, w')$ defined by equation (B2).

For the three best c.m. functions (Figs. IV-30 and D-4,5,6):

- 1) $F_0(w')$ is a linear interpolation of function WCM(I), $I = 1,22$, defined in PROGRAM I2LEG (Appendix C);
- 2) $G_0(\theta) = (0.25 - 0.2 * X + 0.75 * X * X)$ defined in SUBROUTINE XSECT of PROGRAM I2LEG;
- 3) $m = 4$ (i.e. five Legendre terms in θ);
- 4) $k = 5$ (i.e. six Legendre terms in w');
- 5) and the three sets (each arbitrarily normalized) of 30 expansion coefficients b_{ij} are given below in the sequence $b_{00}, b_{01}, b_{02}, b_{03}, b_{04}, b_{10}, b_{11}, \dots, b_{54}$

a) $\bar{E} = 1.87$ kcal/mole

0.15951	0.21000	0.18072	0.09216	0.04013	0.34534	0.59431	0.51662	0.23812	0.11468
0.45961	0.85284	0.78517	0.43208	0.13984	0.50474	1.00000	0.99395	0.59121	0.24418
0.36739	0.76392	0.80324	0.51893	0.20268	0.12060	0.22349	0.24020	0.16235	0.09228

b) $\bar{E} = 2.67$

0.26501 0.33107 0.25381 0.11444 0.04239 0.51175 0.87932 0.70411 0.30920 0.07649
0.57578 1.00000 0.82666 0.45197 0.11189 0.46333 0.81161 0.71319 0.40498 0.05990
0.27514 0.46829 0.41166 0.25517 0.07511 0.09077 0.13992 0.13507 0.13312 0.04946

c) $\bar{E} = 3.62$

0.12559 0.25609 0.24372 0.12761 0.03586 0.32217 0.71659 0.68693 0.36468 0.10363
0.44232 1.00000 0.97409 0.53416 0.15491 0.42622 0.97204 0.96193 0.54370 0.15964
0.26173 0.59940 0.59454 0.33609 0.09842 0.07577 0.17361 0.17345 0.10273 0.03087

For the "compromise" (assumed energy-independent) c.m. contour map of Fig. IV-42:

1) $F_0(w') = w'^2 \exp(-w'^2/320^2)$, with w' in m/sec;

2) $G_0(\theta) = (0.65 - 0.7 * X + 1.05 * X * X)$

3) $m = 3$;

4) $k = 4$;

5) and the (arbitrarily normalized) 20 expansion coefficients b_{ij} are given below in the sequence $b_{00}, b_{01}, b_{02}, b_{03}, b_{10}, b_{11}, \dots, b_{43}$.

0.54635 0.13378-0.14677-0.55535 1.00000 0.28712-0.38055-1.30806 0.78742 0.19977
-0.40823-1.24687 0.31847 0.14459-0.16791-0.68054 0.05524 0.10505 0.01668-0.20574

REFERENCES

(References for Chapter V are contained within Chapter V)

1. E. H. Taylor and S. Datz, J. Chem. Phys. 23, 1711 (1955).
2. a. D. R. Herschbach, Adv. Chem. Phys. 10, 319 (1966);
b. E. F. Greene, A. L. Moursund, and J. Ross, Adv. Chem. Phys. 10, 135 (1966);
c. E. F. Greene and J. Ross, Science 159, 587 (1968);
d. J. P. Toennies, in Chemische Elementarprozesse, Ed. by H. Hartmann et al., Springer, Heidelberg (1968), p. 157;
e. H. Pauly and J. P. Toennies, in Methods of Experimental Physics, Ed. by L. Marton, Vol. 7 of Atomic and Electron Physics; Atomic Interactions, Part A, B. Bederson and W. L. Fite, Ed., Acad. Press, N. Y. (1968), p. 227;
f. J. P. Toennies, Ber. Bunsen. f. Phys. Chem. 72, 927 (1968).
3. S. Datz and E. H. Taylor, J. Chem. Phys. 25, 389 (1956).
4. S. Datz and E. H. Taylor, J. Chem. Phys. 25, 395 (1956).
5. T. R. Tow and J. W. Trischka, J. Appl. Phys. 34, 3635 (1963).
6. K. R. Wilson and R. J. Ivanetich, Lawrence Radiation Laboratory, Berkeley, Calif., UCRL Rept. 11606; 1964.
7. a. J. Penta, C. R. Mueller, W. Williams, R. Olson, and P. Chakraborti, Phys. Letters 25A, 658 (1967);
W. Williams, C. R. Mueller, P. McGuire, and B. Smith, Phys. Rev. Letters 22, 121 (1969);
W. Williams, J. Penta, C. R. Mueller, P. McGuire, P. Chakraborti, and B. Smith (to be published);

- b. Y. T. Lee, J. D. McDonald, P. R. LeBreton, and D. R. Herschbach, *J. Chem. Phys.* 49, 2447 (1968);
Y. T. Lee, P. R. LeBreton, J. D. McDonald, and D. R. Herschbach
J. Chem. Phys. 51, 455 (1969);
- c. J. B. Cross and N. C. Blais, *J. Chem. Phys.* 50, 4108 (1969);
- d. R. W. Bickes Jr. and R. B. Bernstein, *Chem. Phys. Letters* 4,
111 (1969);
- e. D. H. Winicur, L. R. Martin, A. L. Moursund, W. R. Devereaux,
and A. Kuppermann, Sixth International Conference on the
Physics of Electronic and Atomic Collisions, M.I.T. Cambridge,
Mass., July 28 - Aug. 2, 1969, p. 185;
- f. H. J. Loesch and D. Beck, *ibid.*, p. 587;
D. Beck, F. Engelke, and H. J. Loesch, *Ber. Bunsenges. Physik.*
Chem. 72, 1105 (1968).
8. a. M. Polanyi, Atomic Reactions, Williams and Norgate, Ltd.,
London, (1932);
- b. M. G. Evans and M. Polanyi, *Trans. Far. Soc.* 35, 178 (1939);
- c. C. E. H. Bawn, *Ann. Rpts. on Prog. Chem.* 39, 36 (1942);
- d. E. Warhurst, *Quart. Revs. Chem. Soc. (London)* 5, 44 (1951).
9. a. E. A. Gislason and G. H. Kwei, *J. Chem. Phys.* 46, 2838 (1967);
- b. R. K. B. Helbing and E. W. Rothe, *J. Chem. Phys.* 48, 3945
(1968).
10. R. B. Bernstein, *Adv. Chem. Phys.* 10, 75 (1966).
11. E. F. Greene, L. F. Hoffman, M. W. Lee, J. Ross, and C. E. Young,
J. Chem. Phys. 50, 3450 (1969).

12. a. E. A. Mason, *J. Chem. Phys.* 26, 667 (1957);
b. K. W. Ford and J. A. Wheeler, *Ann. Phys. N. Y.* 7, 259, 287 (1959).
13. S. Datz and R. E. Minturn, *J. Chem. Phys.* 41, 1153 (1964).
14. R. E. Minturn, S. Datz, and R. L. Becker, *J. Chem. Phys.* 44, 1149 (1966).
15. K. R. Wilson, G. H. Kwei, J. A. Norris, R. R. Herm, J. H. Birely, and D. R. Herschbach, *J. Chem. Phys.* 41, 1154 (1964).
16. J. H. Birely, R. R. Herm, K. R. Wilson, and D. R. Herschbach, *J. Chem. Phys.* 47, 993 (1967).
17. R. Grice and P. B. Empadocles, *J. Chem. Phys.* 48, 5352 (1968).
18. G. H. Kwei and D. R. Herschbach, *J. Chem. Phys.* 51, 1742 (1969).
19. J. H. Birely, E. A. Entemann, R. R. Herm, and K. R. Wilson, *J. Chem. Phys.* 51, 5461 (1969).
20. R. R. Herm, R. J. Gordon, and D. R. Herschbach, *J. Chem. Phys.* 41, 2218 (1964).
21. R. J. Gordon, R. R. Herm, and D. R. Herschbach, *J. Chem. Phys.* 49, 2684 (1968).
22. D. D. Parrish and R. R. Herm, *J. Chem. Phys.* 49, 5544 (1968).
23. D. D. Parrish and R. R. Herm, *J. Chem. Phys.* 51, 5467 (1969).
24. J. H. Birely and D. R. Herschbach, *J. Chem. Phys.* 44, 1690 (1966).
25. E. A. Entemann and D. R. Herschbach, *Disc. Far. Soc.* 44, 289 (1967).
26. A. E. Grosser and R. B. Bernstein, *J. Chem. Phys.* 43, 1140 (1965).
27. T. T. Warnock, R. B. Bernstein, and A. E. Grosser, *J. Chem. Phys.* 46, 1685 (1967).
28. R. R. Herm and D. R. Herschbach, *J. Chem. Phys.* 43, 2139 (1965).
29. C. Maltz and D. R. Herschbach, *Disc. Far. Soc.* 44, 176 (1967).

30. M. C. Moulton and D. R. Herschbach, *J. Chem. Phys.* 44, 3010 (1966).
31. E. Roth and G. Schay, *Z. physik. Chem.* B28, 323 (1935).
32. J. L. Magee, *J. Chem. Phys.* 8, 687 (1940).
33. S. Glasstone, K. J. Laidler, and H. Eyring, *The Theory of Rate Processes*, McGraw-Hill, New York, (1941).
34. R. W. Anderson, PhD. Thesis, Harvard Univ. (1968).
35. A. P. M. Baede, A. M. C. Moutinho, A. E. de Vries and J. Los, *Chem. Phys. Letters* 3, 530 (1969).
36. R. K. B. Helbing and E. W. Rothe, *J. Chem. Phys.* 51, 1607 (1969).
37. a. R. Bersohn and L. E. Brus, *Sixth International Conference on the Physics of Electronic and Atomic Collisions*, M.I.T., Cambridge, Mass., July 28 - Aug. 2, 1969, p. 603;
b. L. E. Brus (to be published).
38. D. C. Brodhead, P. Davidovits, and S. A. Edelstein, *J. Chem. Phys.* 51, 3601 (1969).
39. a. M. Godfrey and M. Karplus, *J. Chem. Phys.* 49, 3602 (1968);
b. N. C. Blais, *J. Chem. Phys.* 49, 9 (1968);
c. N. C. Blais, *J. Chem. Phys.* 51, 856 (1969);
d. P. J. Kuntz, E. M. Nemeth, and J. C. Polanyi, *J. Chem. Phys.* 50, 4607 (1969);
e. P. J. Kuntz, H. M. Mok, and J. C. Polanyi, *J. Chem. Phys.* 50, 4623 (1969).
40. a. Z. Herman, J. Kerstetter, T. Rose, and R. Wolfgang, *Disc. Far. Soc.* 44, 123 (1967);
b. Z. Herman, A. Lee and R. Wolfgang, *J. Chem. Phys.* 51, 452 (1969);
c. Z. Herman, P. Hierl, A. Lee and R. Wolfgang, *J. Chem. Phys.*, 51, 454 (1969);

- d. W. R. Gentry, E. A. Gislason, Y. Lee, B. H. Mahan, and C. Tsao, *Disc. Far. Soc.* 44, 137 (1967);
- e. W. R. Gentry, E. A. Gislason, B. H. Mahan, and C. Tsao, *J. Chem. Phys.* 49, 3058 (1968);
- f. E. A. Gislason, B. H. Mahan, C. Tsao, and A. Werner, *J. Chem. Phys.* 50, 142, 5418 (1969).
- 41. C. Riley, K. T. Gillen, and R. B. Bernstein, *J. Chem. Phys.* 47, 3672 (1967); (Chapter III A, this thesis).
- 42. K. T. Gillen, C. Riley, and R. B. Bernstein, *J. Chem. Phys.* 50, 4019 (1969); (Chapter III B, this thesis).
- 43. a. G. Herzberg, *Spectra of Diatomic Molecules* (2nd Edition) Van Nostrand, Princeton, New Jersey (1950);
b. L. Brewer and E. Brackett, *Chem. Rev.* 61, 425 (1961).
- 44. T. T. Warnock and R. B. Bernstein, *J. Chem. Phys.* 49, 1878 (1968);
Erratum *J. Chem. Phys.* 51, 4682 (1969).
- 45. H. U. Hostettler and R. B. Bernstein, *Phys. Rev. Letters* 5, 318 (1960).
- 46. H. U. Hostettler and R. B. Bernstein, *Rev. Sci. Inst.* 31, 872 (1960).
- 47. F. A. Morse, Ph.D. Thesis, Univ. of Michigan (1962).
- 48. F. A. Morse, R. B. Bernstein, and H. U. Hostettler, *J. Chem. Phys.* 36, 1947 (1962).
- 49. F. A. Morse and R. B. Bernstein, *J. Chem. Phys.* 37, 2019 (1962).
- 50. P. J. Groblicki, Ph.D. Thesis, Univ. of Michigan (1963).
- 51. P. J. Groblicki and R. B. Bernstein, *J. Chem. Phys.* 42, 2295 (1965).
- 52. R. B. Bernstein, *Science* 144, 141 (1964).
- 53. A. R. Blythe, A. E. Grosser, and R. B. Bernstein, *J. Chem. Phys.* 41, 1917 (1964).
- 54. A. E. Grosser, A. R. Blythe, and R. B. Bernstein, *J. Chem. Phys.* 42, 1268 (1965).

55. E. Hundhausen and H. Pauly, *Z. Naturforsch.* 20a, 625 (1965).
56. N. F. Ramsey, Molecular Beams, Oxford Univ. Press, London (1956).
57. P. Siska (Harvard University), Private Communication.
58. R. Wolfgang and R. J. Cross Jr., *J. Phys. Chem.* 73, 743 (1969).
59. R. E. Minturn, S. Datz, and E. H. Taylor, *J. Appl. Phys.* 31, 876 (1960).
60. E. F. Greene, M. H. Lau, and J. Ross, *J. Chem. Phys.* 50, 3122 (1969).
61. J. R. Airey, E. F. Greene, K. Koderá, G. P. Reck, and J. Ross, *J. Chem. Phys.* 46, 3287 (1967).
62. R. B. Bernstein, *Adv. Chem. Phys.* 10, 75 (1966);
 - a. Eqn. (II.6'),
 - b. Eqn. (X.9),
 - c. Eqn. (II.5).
63. F. T. Smith, R. P. Marchi, K. G. Dedrick, *Phys. Rev.* 150, 79 (1966).
64. R. B. Bernstein and R. D. Levine, *J. Chem. Phys.* 49, 3872 (1968).
65.
 - a. D. H. Maylotte, Ph.D. Thesis, Univ. of Toronto (1967);
 - b. D. H. Maylotte and J. C. Polanyi (to be published);
 - c. K. G. Anlauf, Ph.D. Thesis, Univ. of Toronto (1968);
 - d. K. G. Anlauf and J. C. Polanyi (to be published).
66. R. B. Bernstein, unpublished notes (1969).
67. P. Cadman and J. C. Polanyi, *J. Phys. Chem.* 72, 3715 (1968).
68. R. A. Berg and G. W. Skewes, *J. Chem. Phys.* 51, 5430 (1969).
69. R. S. Berry, *J. Chem. Phys.* 27, 1288 (1957);
70. P. Davidovits and D. C. Brodhead, *J. Chem. Phys.* 46, 2968 (1967).
71. K. R. Wilson and D. R. Herschbach, *J. Chem. Phys.* 49, 2676 (1968).

72. J. B. Anderson, R. P. Andres, and J. B. Fenn, *Advan. Chem. Phys.* 10, 275 (1966).
73. E. A. Entemann, Ph.D. Thesis, Harvard University (1967).
74. S. K. Zaremba, *Annali di Matematica* 4, 73 (1966).
75. T. T. Warnock, Theoretical Chem. Inst., Univ. of Wisconsin, Report # TCI-247G (1967).
76. Other comparable inversion methods exist:
 - a. P. Siska (Harvard University), Private Communication;
 - b. D. O. Ham and J. L. Kinsey, to be published.